Online ISSN 2716-9650
Print ISSN 2676-5837

Volume 3, Apr. 1, 2021

Journal of
Composites and Compounds

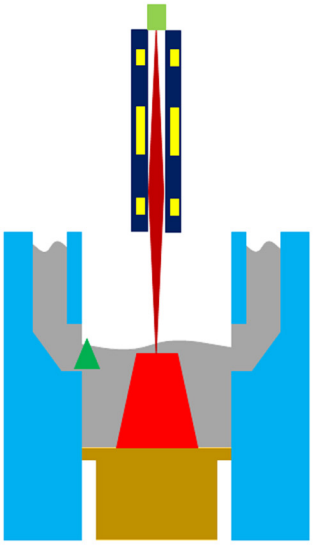

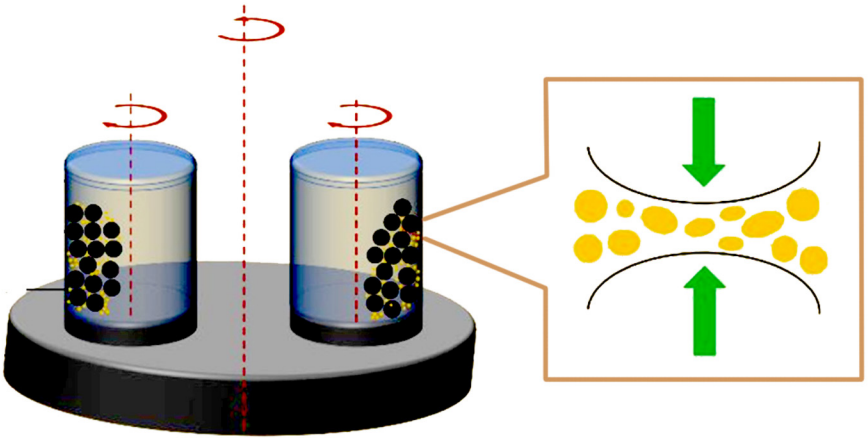

Editor-in-Chief: Prof. Dr. Hassan Karimi-Maleh

www.JOURCC.com

Journal of
Composites and Compounds

Online ISSN 2716-9650
Print ISSN 2676-5837
Mar. 28, 2021
Volume 3
No. 6

Available online at www.jourcc.com

Karoon St., Tehran, Iran

+982166897182

Journal of
Composites and Compounds

Online ISSN 2716-9650
Print ISSN 2676-5837
Mar. 28, 2021
Volume 3
No. 6

Table of contents

Development of hybrid electrodeposition/slurry diffusion aluminide coatings on Ni-based superalloy with enhanced hot corrosion resistance 1

Effect of powder manufacturing process on characteristics of nanostructured MCrAlY coatings: dry vs. wet ball milling 9

Electrical properties of polymer blend composites based on Silicone rubber/EPDM/clay for high voltage insulators 18

A review on the synthesis of the TiO_2-based photocatalyst for the environmental purification 25

Application of different Nanocatalysts in industrial effluent treatment: A review 43

Sol-gel: Uncomplicated, routine and affordable synthesis procedure for utilization of composites in drug delivery: Review 57

A review of additive manufacturing of Mg-based alloys and composite implants 71

Available online at www.jourcc.com

Karoon St., Tehran, Iran
+982166897182

Available online at www.jourcc.com

Journal homepage: www.JOURCC.com

Journal of Composites and Compounds

Development of hybrid electrodeposition/slurry diffusion aluminide coatings on Ni-based superalloy with enhanced hot corrosion resistance

Ali Zakeri[a]* , *Mohammadreza Masoumi Balashadehi*[a], *Alireza Sabour Rouh Aghdam*[a]

[a] *Department of Materials Engineering, Tarbiat Modares University, Tehran P.O. Box: 14115-143, Tehran, Iran*

A B S T R A C T

Ni/Co-modified aluminide coatings were prepared on the Hastelloy-X superalloy by a combined process of electrodeposition and slurry aluminizing. In this regard, pure layers of Ni and Ni-50wt.%Co were initially applied via electrodeposition process and successive aluminization was carried out by a slurry technique. The scanning electron microscopy (SEM) and X-ray diffraction (XRD) techniques were used for the microstructural and chemical composition characterization of the specimens. The results of these analyses revealed that a compact and dense aluminide coating was formed with a two-layered structure containing the outer Al-rich β phase and inner interdiffusion zone. Moreover, the presence of pre-electrodeposited layers inhibited the outward diffusion flux of elements from the substrate and effectively suppressed the formation of Kirkendall pores. The hot corrosion studies of the obtained coatings indicated that the addition of a pre-electrodeposited layer could enhance the high-temperature corrosion performance of the coatings when exposed to sulfate salt.

Peer review under responsibility of jourcc

A R T I C L E I N F O R M A T I O N

Article history:
Received 16 January 2021
Received in revised form 4 February 2021
Accepted 13 February 2021

Keywords:
Diffusion
Electrodeposition
Slurry
Aluminide
Hot corrosion

1. Introduction

Nickel-based superalloys have found extensive applications in gas turbine industries due to their excellent thermo-mechanical properties [1–4]. Oftentimes, these materials are employed in the manufacturing of turbine blades to combat the failure arising from the mechanical aspect, which is provided by increasing the content of refractory elements, such as W, Mo, and Re for creep strength improvement [1]. This, in turn, results in lower environmental degradation resistance due to the reduction in Al content (normally < 7 wt.%), which is critical for the formation of a protective oxide scale [5,6]. In this regard, the surfaces of these materials are typically protected by two types of coatings, namely overlay and diffusion coatings [7 16]. The former coatings are often applied by thermal spray methods which require sophisticated equipment and the operation cost is high. On the other hand, the diffusion coatings can be obtained by simple and cost-effective processes such as pack cementation and slurry aluminizing [17].

Application of the diffusion coatings for airfoils was first employed by using the pack cementation technique in the late 1960s [18]. This process is still considered the most widely used method for applying diffusion coatings and the formation mechanism of coating is well-studied [19,20]. Generally, the protection mechanism provided by the diffusion coatings relies on the enrichment of protective alloying elements at the surface of substrate, which leads to the formation of a uniform oxide scale during exposure to harsh conditions at high temperatures. For this purpose, the enrichment of surface layer with silicon (siliconizing), chromium (chromizing), and aluminum (aluminizing) elements were carried out. It should be mentioned that for applications at temperatures of higher than about 1000 ℃, the most crucial element is Al [21].

Currently, slurry aluminizing has received considerable attention as an alternative method [22,23]. This is because of the advantages in the processing compared to the conventional pack cementation. In addition, among the above mentioned processes, only the slurry aluminizing is capable of providing coatings for the interior surfaces (cooling passage) of the turbine blades [17]. In recent years, there are ongoing studies that are focused on the improvement of high-temperature corrosion behavior of the simple aluminide coatings by the addition of beneficial elements like Zr, Hf, Pt, and Co [24–28]. Chemical modification of the aluminide coatings is considered to be one of the efficient methods in improving the microstructural and oxidation/corrosion properties. A simple and effective strategy to fabricate the modified aluminide coatings is by incorporating an electrodeposited intermediate layer [29–32]. Karimzadeh and Sabour Rouhaghdam [33] investigated the influence of pre-plated Ni layer on the oxidation performance of aluminide coatings. They have pointed out that the presence of a primary electroplated Ni layer could inhibit the formation of Kirkendall pores during aluminizing, as well as improving its oxidation resistance. Furthermore, Safari et al. [34] have reported that the chemical modification of the aluminide coating through electrodeposition of Ni-CeO_2 layer could improve the cyclic oxidation resistance of the obtained coating. In another study by Qiao and Zhou [35], it has been shown that the addition of Co into the simple NiAl coating could lower the oxidation kinetics which was attributed to the formation of a thin and compact film of a-Al_2O_3 onto the coating sur-

* *Corresponding author: Ali Zakeri; E-mail: alizakeri@modares.ac.ir*
https://doi.org/10.52547/jcc.3.1.1

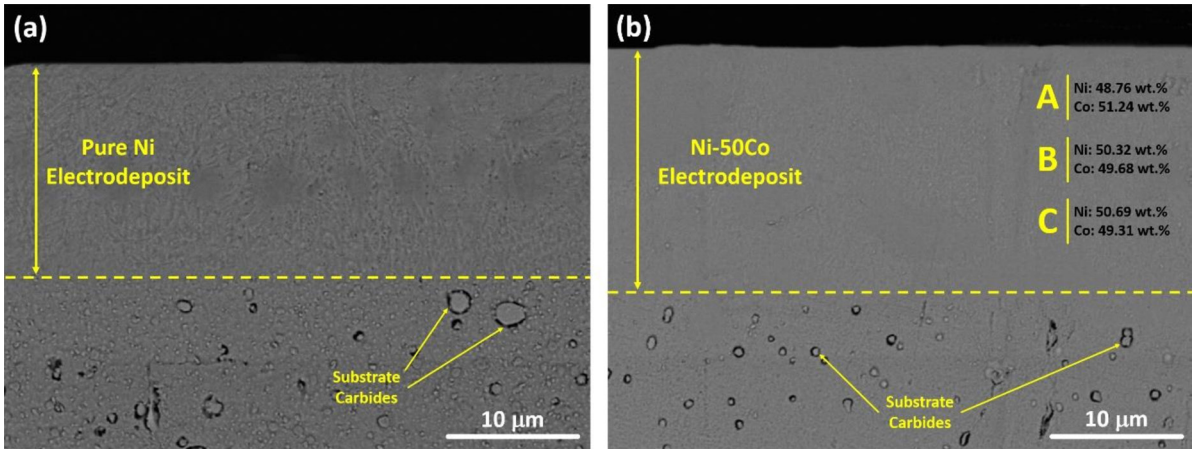

Fig. 1. Cross section of the (a) pure Ni and (b) Ni-50Co electrodeposited layers (the dashed line indicates the interface).

Table 1.
Chemical composition (wt. %) of Hastelloy® X

Element	Ni	Co	Cr	Fe	Mo	W	Al	C	Mn	Si	B
OES Values	Bal.	1.26	20.8	19.67	8.1	0.34	0.21	0.07	0.51	0.22	0.002

face. In a subsequent study conducted by the same authors, it has been found out that the Co-modified NiAl coating exhibited superior hot corrosion resistance and it was ascribed to the formation of a-Al_2O_3 scale promoted by the presence of cobalt [36]. The objective and novelty of this study are to propose a new and efficient approach to the fabrication of Ni/Co-modified aluminide coatings through a combined process of electrodeposition and slurry aluminizing. In addition, the hot corrosion performance of coatings is evaluated and discussed.

2. Materials and methods

2.1. Starting materials and sample preparation

A nickel-based superalloy Hastelloy® X was selected as the substrate material and its chemical composition, determined by the optical emission spectroscopy (OES), are given in Table 1. Several sets of coupons (15 x 5 x 2 mm^3) were cut by electro-discharge machining.

2.2. Electrodeposition process

At the first stage of experimental procedure, the coupons were prepared for electrodeposition by polishing to 600 grit SiC paper, degreasing by acetone and electrochemically activating by anodic oxidation at current density of 10.75 $A.dm^{-2}$ within H_2SO_4 solution for 60 seconds. A typical Watts-type bath, containing nickel sulfate ($NiSO_4.6H_2O$, 200 g/l), nickel chloride ($NiCl_2.6H_2O$, 35 g/l), cobalt sulfate ($CoSO_4.7H_2O$, 0-50 g/l), boric acid (H_3BO_3, 30 g/l), and sodium dodecyl sulfate as surfactant (SDS, 0.6 g/l) was used as the electrodeposition electrolyte. The operating conditions such as current density and temperature were adjusted as 5 $A.dm^{-2}$ and 50 ℃, respectively. Moreover, the pH of the electrolyte was kept constant at 4.0 and two pure Ni plates were used as anode. Afterward, two specimens with pure Ni and Ni-50Co pre-electrodeposited layers were produced.

2.3. Slurry aluminizing process

Initially, the samples were activated by immersion in an acidic solution comprised of 50 ml H_2SO_4, 75 ml HNO_3, 33 ml distilled water, and 1 g NaCl. Then, they were sprayed by a slurry containing spherical aluminum powder as the diffusion coating element source dispersed in a water/ polyvinyl alcohol (PVA) (10:1) mixture. The application of slurry layer was mass-controlled and adjusted in the range of 15-20 mg/cm^2. It should be noted that the application of slurry layer above this range would result in the spallation of slurry layer due to the thermal stresses generated during heating. Prior to placing the samples, the furnace chamber was circulated with argon for three times to eliminate oxygen. Subsequently, the coupons were placed in an alumina crucible and then heated to the processing temperature of 750 and 1050 ℃ for 2 and 1 h, respectively, followed by furnace cooling. An electric tube furnace operating at a heating rate of 10 ℃/min in an Ar atmosphere was used for slurry aluminizing process.

2.4. Hot corrosion test

A muffle furnace with an accuracy of ± 5 ℃ was used to perform the hot corrosion experiments in static air at 900 ℃. Prior to the experiment, all faces of the specimens were hand-brushed with a Na_2SO_4 saturated aqueous salt solution at about 1-2 mg/cm^2 and followed by hot airflow drying. In order to precisely control the mass/area ratio of the applied salt, the samples were weighed before and after supplying the salt. The salt composition used in this study is a typical approach to simulate the environment of materials exposed to regions with high levels of pollutants and it has been previously used by many researchers [37–40]. The samples were subjected to the hot corrosion test for 100 h and were withdrawn from the furnace after the cooling stage. In this study, the corrosion performance was evaluated by comparing the thickness of formed corrosion layer on the coatings' surface, which were measured by using ImageJ software [41]. This method does not involve the common errors associated with the mass change records due to the remaining salt deposits and formation of volatile compounds during the test [42].

2.5. Characterization techniques

The morphological assessment of the specimens was carried out by scanning electron microscopy (SEM, Zeiss, model Evo15) coupled with an X-ray energy dispersive (EDS) analyzer. The microstructure and chemical composition of the hot-corroded samples were also examined by SEM-EDS. In this regard, first the remaining salt was removed by washing the samples in boiling distilled water, then, one of the tested samples was warm-mounted in a plastic resin, ground with SiC abrasive papers (400-3000 grit) and polished to a mirror finish to reveal the cross-section microstructure of the coating and corrosion products layer. The phase analysis was performed by X-ray diffraction (XRD, Philips

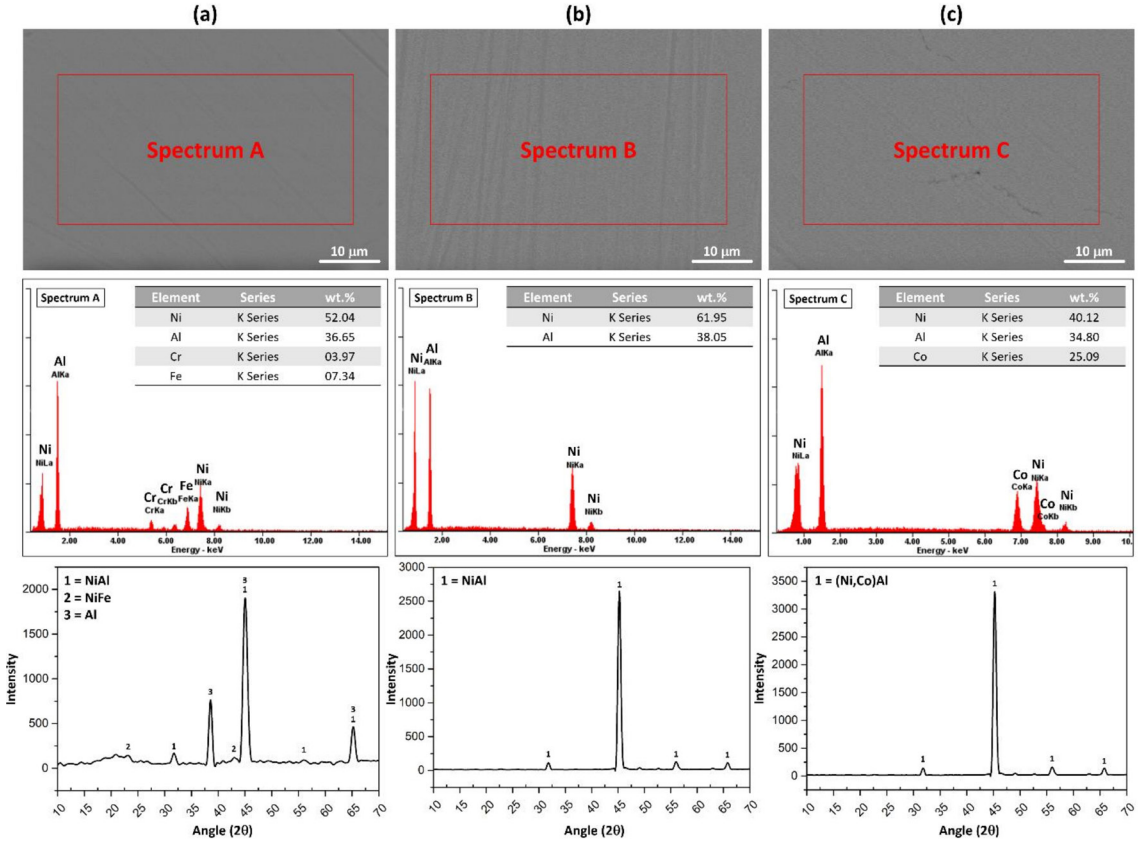

Fig. 2. Surface characteristics of the diffusion coatings; (a) simple, (b) Ni-modified, and (c) Ni/Co-modified aluminide coating.

PW1730, CuKα radiation) and the identification of XRD patterns was made on the basis of the ICDD database [43].

3. Results and discussion

3.1. As-electrodeposited samples

Among the surface engineering techniques, electrodeposition is a common and well-known method owing to its flexibility, moderate costs, and simple procedure [44–47]. Fig. 1 displays the cross-section of the electrodeposited coatings on the superalloy substrates. The average thickness of the mono-layer electrodeposited coatings was within the range of 15-18 mm. It can be noticed from the EDS analysis results that the chemical composition was homogeneous throughout the entire layer and was almost identical in upper, middle, and lower regions. The uniform structure of Ni-Co electrodeposits have been reported in other studies as well [48–50]. Although the samples were etched, no distinct interface between the substrate and the electrodeposited layer was evident from the SEM images. This is because of the nearly identical compositions of the two regions.

3.2. As-aluminized samples

The specimens were followed by slurry aluminizing. Fig. 2 shows the surface morphology images and the corresponding chemical compositions and crystalline structures determined by EDS and XRD analyses, respectively. According to the EDS analyses, it was revealed that only the modified samples showed the main elements of the β-(Ni,Co)Al intermetallic phase. This could be due to the presence of pre-electrodeposited layer onto the surface of the Hastelloy X, where only outward diffusion of Ni and Co occurred. On the other hand, concerning the simple aluminide coating, small amounts of Fe and Cr were detected. These observations may suggest that the electrodeposited layer hinders the outward diffusion from the substrate during slurry aluminizing process [33]. Moreover, the formation of β-phase was confirmed for all of the specimens by the XRD results. That being said, additional NiFe phase was detected for the simple aluminide coating, which may be the consequence of outward Fe diffusion. In addition, strong peaks of metallic Al were detected, which can be the result of un-reacted liquid Al in the slurry.

The formation of slurry diffusion coatings can be explained by the Ni-Al combustion synthesis process [18]. During this process, the melting of Al component is the initiating step. Afterward, through wetting of Ni by Al melt, it dissolves Ni from the surface and the Ni-Al reaction proceeds in the molten state. Based on the Ni concertation in the Al melt, which is dependent on the temperature of the process, one or more phases of $NiAl_3$, Ni_2Al_3, and NiAl can be formed. Taking into account that the processing temperatures used in this study were high and the maximum solubility of Ni in molten Al increases with temperature, the formation of NiAl as the thermodynamically stable phase was anticipated. This was true for the modified coatings, since at the initial stage, the liquid Al came in contact with the pure pre-electrodeposited layers instead of superalloy substrate. It has been reported that pure Ni substrates result in the higher exothermic reactions, which makes it easier for Al to react and form the intermetallic phases [18].

The cross-section SEM-EDS mapping and EDS line scan analyses of the aluminized samples are depicted in Fig. 3 and Fig. 4, respectively. All of the specimens exhibited the formation of a distinct outer NiAl layer with an interdiffusion zone (IDZ), which is a typical microstructure of the aluminide diffusion coatings [33]. This structure, in turn, provides the excellent adhesion of these coatings due to the metallurgical bonding with the substrate [17]. Moreover, the diffusion layer obtained by the slurry process was compact with no evident cracks or segmented parts. The EDS line scan analyses illustrate that the concentration of

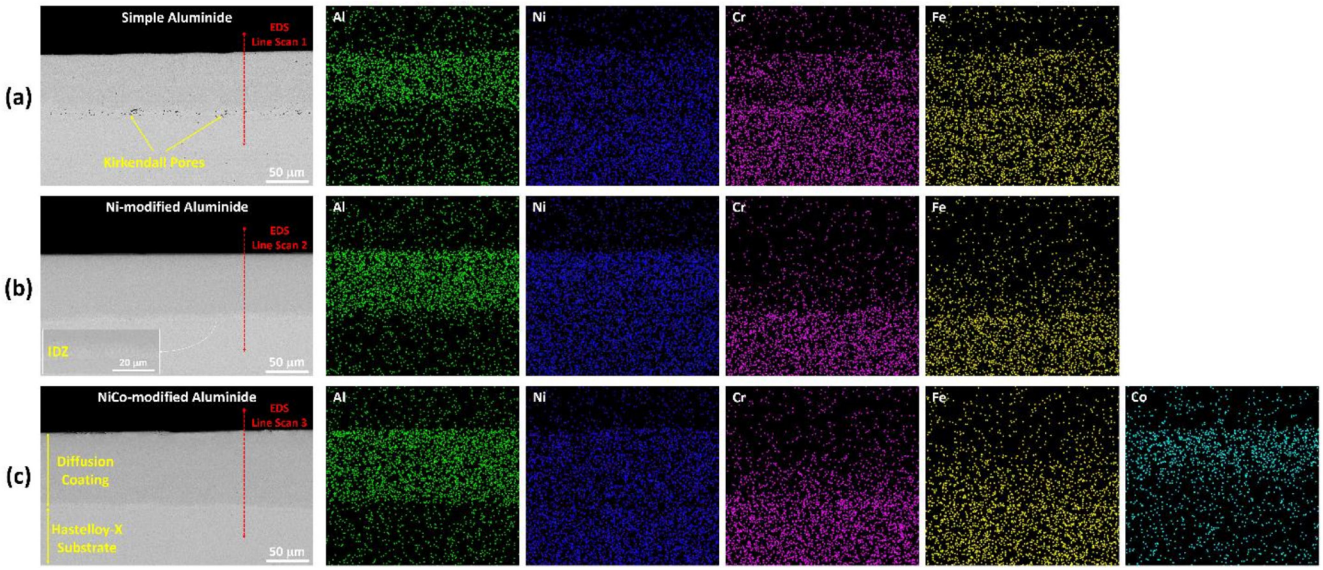

Fig. 3. Cross-section SEM-EDS mapping analyses of the coated samples; (a) simple, (b) Ni-modified, and (c) Ni/Co-modified aluminide coating.

Al was decreased from top surface toward the depth of the superalloy, which contains less Al content. The Al-rich zone indicates the formed aluminide coating and the average thickness was 68±2.71, 75±1.10, and 85±1.59 mm in the case of simple, Ni-modified, and Ni/Co-modified aluminide coatings. As previously mentioned, the presence of pure pre-electrodeposited layers makes the exothermic reactions easier in a Ni-Al diffusion couple, which may result in the increased thickness of the aluminide coating. Moreover, given the fine-grained microstructure of the electrodeposited layers in comparison with the pure substrate, the aluminizing kinetics could be enhanced for the samples with pre-electrodeposited layers, resulting in faster atomic diffusion and larger coating thickness [30].

The main microstructural differences between the simple and modified aluminide coatings can be attributed to the presence of Kirkendall pores and the outward diffusion of substrate elements (Cr and Fe). These phenomena have been reported in other cases of the diffusion aluminide coatings and are mainly related to the microstructural inhomogeneities in the substrate [33]. According to the EDS mapping analyses of the modified coatings, the pre-electrodeposited layers have effectively inhibited the outward diffusion of the major elements of the substrate. Moreover, the formation of Kirkendall pores were suppressed in the case of aforementioned coatings. A close-up of the interdiffusion zone for the Ni/Co-modified aluminide coating is shown in Fig. 5. According to the EDS point analyses, it is evident that the strip-like bright precipitates present in the IDZ are rich in Cr (Point 2) compared to the dark gray area of the diffusion coating, which is rich in Al (Point 1). Since the thickness of the outer diffusion coating is larger than the X-ray penetration depth; thus, the XRD results only indicate the presence of β-phase and identification of the phases present in the IDZ cannot be done via this technique. Based on the composition of the substrate, these phases can vary. Fan et al. explained the formation of Cr(W) enriched phases in the IDZ during the phase transformation from γ/γ' microstructure of the superalloy to the β-phase of diffusion coating [51]. It should be noted that the solubility of Cr and W in the dual phase γ/γ' microstructure is higher than that of β-phase [52].

3.3. Hot corrosion behavior

Fig. 6 displays the average thickness of the formed corrosion product layer on the coatings' surface and its phase identification. It is worth noting that the phase composition of the corrosion product revealed by the XRD analysis was similar in all three of the coatings and the only difference was noted on the peak intensities. With this in mind, further characterization was conducted by means of SEM-EDS analysis of the exposed samples.

According to Fig. 6, a considerable improvement in the hot corrosion behavior was observed for the modified coatings, with the NiCo-modified coating exhibiting the best performance. By comparing the XRD patterns before and after the hot corrosion test, it can be noticed that the singular dominant β-phase (Fig. 2c) has been replaced by the γ' phase. Moreover, the diffraction peaks of b phase are still detectable as well as Al_2O_3, indicating the consumption of Al to form the protective alumina layer [24]. In addition, some sulfides and spinels were revealed in the XRD pattern. This could signify the sulfur penetration into the coating; however, it should be studied form microscopic point of view to confirm. It should also be noticed that no peaks corresponding to the oxides of Ni or Co were detected. Although it is possible for these oxides to be formed at the early exposure times; however, they might have been deoxidized by Al (more active) or have been reacted with Al_2O_3, resulting in the formation of $(Ni,Co)(Cr,Al)_2O_4$ [7, 24].

Fig. 7 presents the SEM-EDS analyses of the hot-corroded samples after 100 h. These analyses clearly confirm the hot corrosion performance of the coatings, reported in Fig. 6. As is evident from Fig. 7c, the NiCo-modified coating exhibited the best resistance to the corrosion attack and a large part of the coating remained unaffected, which implies its capability of maintaining and reestablishing the protective alumina scale for prolonged exposure times [24]. In particular, the importance of scale healing is essential during hot corrosion. This is because catastrophic attack will proceed, if the molten salt comes in contact with the underlying depleted substrate, which is unable to reestablish a protective scale [40]. According to the XRD and EDS analyses' results, the corrosion product layer formed on the coatings was primarily consisted of Al_2O_3. This result was expected due to the alumina-forming nature of the diffusion coatings, which arise from their high Al content enabling its selective oxidation [53]. Furthermore, in addition to the sporadic Cr-rich bright precipitates detected within and near the IDZ (Fig. 5), a Cr-rich belt was observed for the NiCo-modified coating after the hot corrosion test (see the inset in Fig. 7c). It is possible that under the high-temperature condition, the Cr atoms have diffused towards the coating surface. Owing to the fact that the γ' phase has partially replaced the β-phase at the sub-surface regions, and considering the high solubility of Cr in the

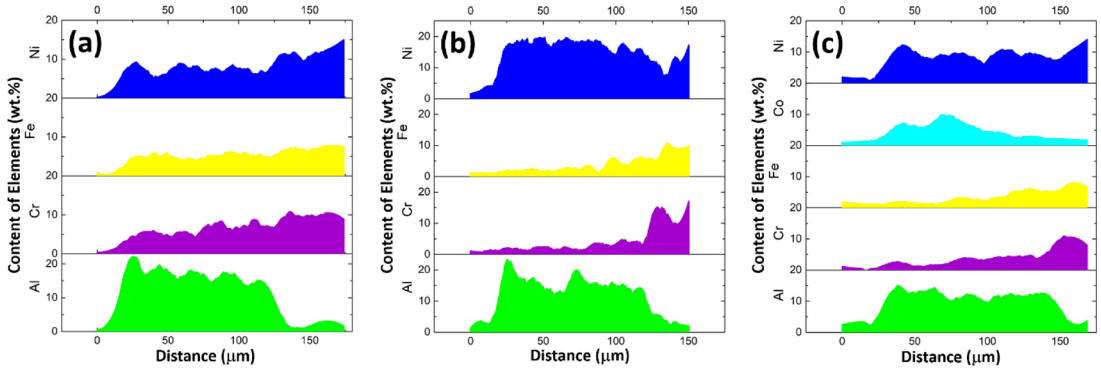

Fig. 4. EDS line scan analyses of the coated samples marked in Fig. 3; (a) simple, (b) Ni-modified, and (c) Ni/Co-modified aluminide coating.

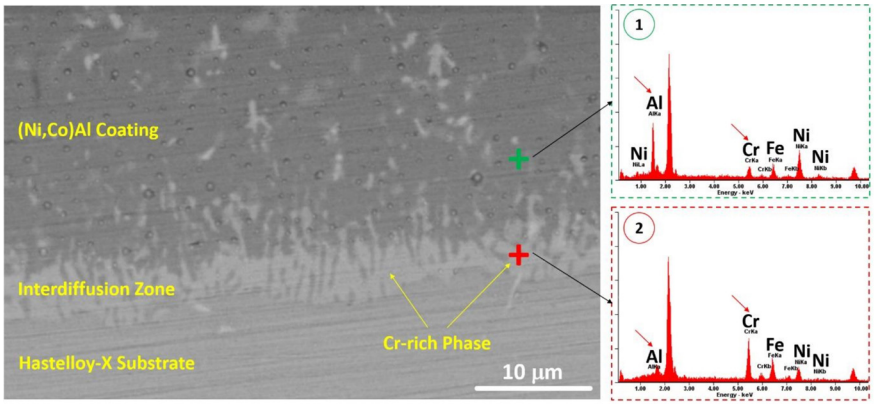

Fig. 5. Cross-section SEM-EDS analyses of the Ni/Co-modified aluminide coating (The arrows point out the peaks' intensities for Al and Cr).

former phase, no distinctive Cr enriched precipitates were found in the upper regions of the coating.

Both the simple aluminide and Ni-modified coatings have considerably suffered from corrosion damage in comparison to the NiCo-modified coating. The prominent mode of accelerated attack below the salt deposit occurs via the penetration of S, which can penetrate into the coating through cracks or voids [54]. It has been reported that S could penetrate as the SO_4^{2-} ions and then interact with alloy elements, especially Cr, to form internal sulfides (reaction 1) [51]. This phenomenon is in accordance with the high tendency of S to combine with Cr, which can be determined by the standard Gibbs free energy changes for the formation of CrS (reaction 2) [55]. Moreover, the consumption of S can accelerate the SO_4^{2-} decomposition (reaction 3), which in turn increases the basicity of the molten salt to a point where it can dissolve Al_2O_3 (reaction 4) [56]. The basic fluxing of Al_2O_3 is reported to be the main degradation mechanism of simple aluminide coatings [36]. Due to the concentration gradient, it is possible for AlO^{2-} to migrate from the salt deposit/oxide scale interface to the salt deposit/air interface, where Al_2O_3 can re-precipitate (reaction 5). However, the newly developed oxides are porous and prone to the transportation of the released O^{2-} back to the salt deposit/oxide scale interface. This process can lead to the increased alkalinity and further fluxing of the Al_2O_3 as a consequence [56]. In this study, a similar scenario was observed for the case of simple aluminide coating (Fig. 7a) and it seems that the discussed self-sustaining process is the reason for this sample's weak corrosion performance.

$$2Cr + 2SO_4^{2-} = 2O^{2-} + 2CrS + 3O_2 \quad (1)$$

$$2Cr + S_2 = 2CrS \ (\Delta G_0 = -405000 + 112.14T) \quad (2)$$

$$SO_4^{2-} = SO_3 + O^{2-} \quad (3)$$

$$Al_2O_3 + O^{2-} = 2AlO^{2-} \quad (4)$$

$$2AlO^{2-} = Al_2O_3 + O^{2-} \quad (5)$$

According to Fig. 7, internal sulfidation is discernible for the simple aluminide and Ni-modified coatings, which indicates a deep penetration of S. On the other hand, the internal sulfidation was significantly

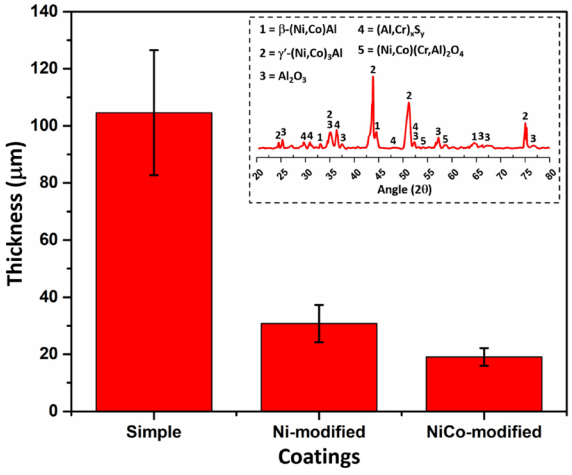

Fig. 6. The measured average thickness of the corrosion product layer for each specimen (the inset shows the XRD results for the NiCo-modified coating after being exposed to Na2SO4 for 100 h).

suppressed in the case of NiCo-modified coating. It is assumed that Co addition to the aluminide coatings can enhance their hot corrosion resistance due to its strong ability to fix S and prevent internal sulfidation [56]. According to the EDS mapping analysis shown in Fig. 7e, a high Co content was still present at the outer regions of the coating and presumably has participated in retarding the S transport. In addition, it has been proposed by Beltran and Shores that the diffusion rate of S in Co is lower than that in Ni by two orders of magnitude [57]. In view of this, the presence of Co in NiAl aluminide coating could alleviate the sulfidation reactions and reduce the internal sulfidation.

4. Conclusions

In this study, Ni/Co-modified aluminide coatings were successfully prepared on the Hastelloy-X superalloy by a combined process of electrodeposition and slurry aluminizing. The following conclusions can

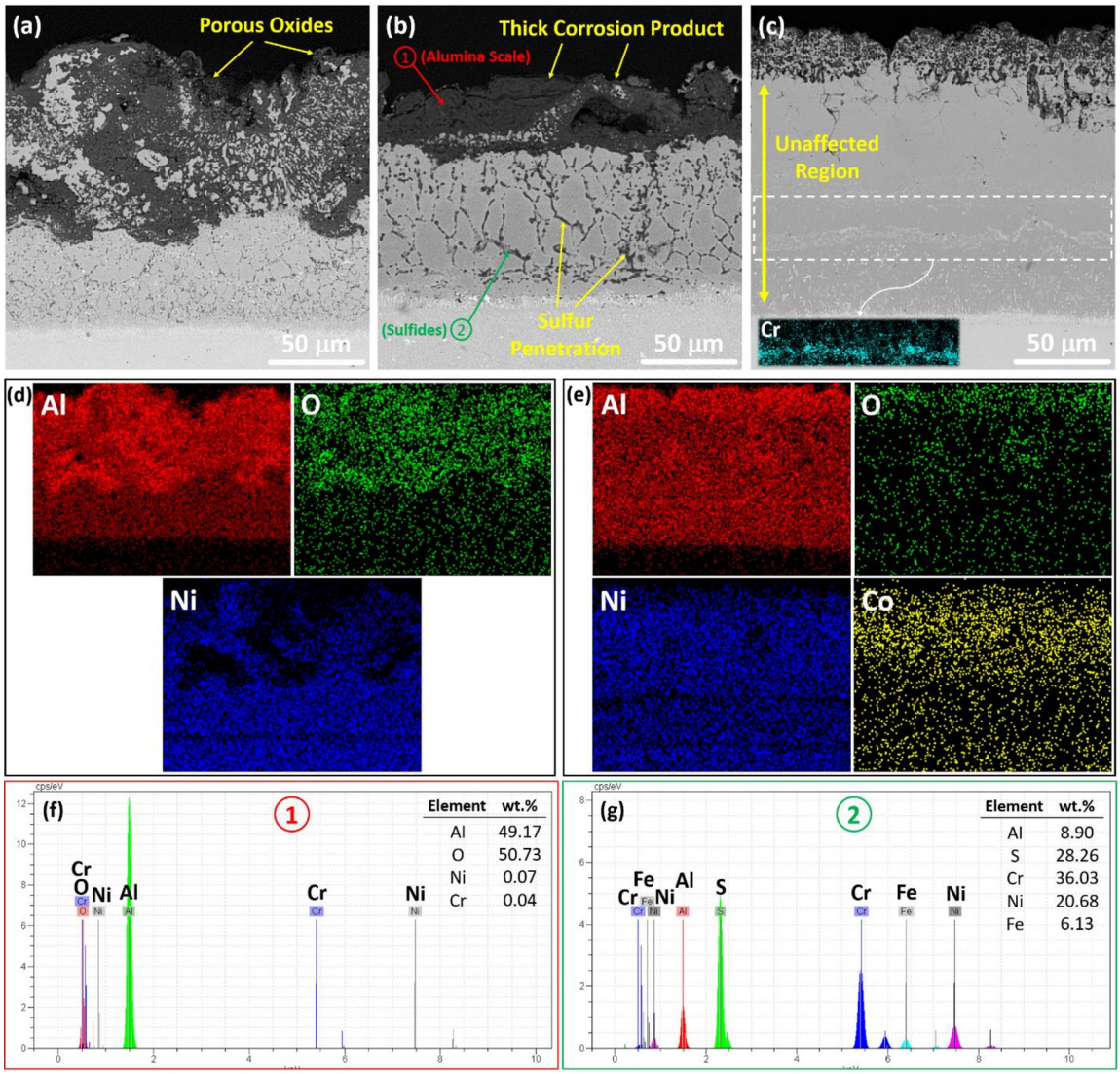

Fig. 7. Cross-section SEM-EDS analyses of the hot-corroded samples; (a) simple aluminide, (b) Ni-modified, (c) NiCo-modified, (d) EDS mapping performed on (a), (e) EDS mapping performed on (c), (f and g) EDS analyses from the marked points in (b).

be drawn from microstructural study and hot corrosion behavior of the obtained coatings:

1. It was established that pre-electrodeposition treatment can be utilized to develop modified slurry aluminide coatings.
2. Both simple and Ni-modified aluminide coatings were composed mainly of thermodynamically stable b-NiAl phase. A singular β-(Ni,Co)Al phase was detected in the case of NiCo-modified coating, in which some of the Ni atoms were replaced by Co. Moreover, some part of Al was remained un-reacted in the case of simple aluminide, which was attributed to the kinetics of aluminization.
3. It was shown that presence of the pre-electrodeposited layers inhibited the outward diffusion flux of elements from the substrate and effectively suppressed the formation of Kirkendall pores.
4. In terms of hot corrosion resistance, the NiCo-modified coating outperformed the other two coatings. This was mainly attributed to the beneficial effect of Co in preventing the internal sulfidation.

Declaration of conflicting interests

The authors declare that there is no conflict of interest.

Acknowledgments

The authors would like to thank Dr. Mohammad Hossein Allahyarzadeh Bidgoli for his valuable help and advice.

REFERENCES

[1] T.M. Pollock, S. Tin, Nickel-based superalloys for advanced turbine engines: Chemistry, microstructure, and properties,Journal of Propulsion and Power 22 (2006) 361–374.

[2] R.C. Reed, The superalloys: fundamentals and applications, Cambridge university press, 2008.

[3] M. Vajdi, F. Sadegh Moghanlou, F. Sharifianjazi, M. Shahedi Asl, M. Shokouhimehr, A review on the Comsol Multiphysics studies of heat transfer in advanced ceramics, Journal of Composites and Compounds 2 (2020) 35–44.

[4] M. Alehojat, R. Jafari, P. Karimi, E. Sadeghi, Electron beam-powder bed fusion of Alloy 718: Effect of hot isostatic pressing and thermal spraying on microstructural characteristics and oxidation performance, Surface and Coatings Technology 404 (2020) 126626.

[5] A. Zakeri, E. Bahmani, A. Sabour Rouh Aghdam, B. Saeedi, M. Bai, A study on the effect of nano-CeO_2 dispersion on the characteristics of thermally-grown oxide (TGO) formed on NiCoCrAlY powders and coatings during isothermal oxidation, Journal of Alloys and Compounds 835 (2020) 155319.

[6] M. Bai, Fabrication and Characterization of Thermal Barrier Coatings, (2015) 182. https://www.researchgate.net/publication/287347007_Fabrication_and_characterization_of_thermal_barrier_coatings.

[7] A. Zakeri, E. Bahmani, A.S.R. Aghdam, Impact of MCrAlY feedstock powder modification by high-energy ball milling on the microstructure and high-temperature oxidation performance of HVOF-sprayed coatings, Surface and Coatings Technology (2020) 125935.
[8] A. Zakeri, E. Bahmani, A. Sabour Rouh Aghdam, B. Saeedi, A comparative study on the microstructure evolution of conventional and nanostructured MCrAlY powders at high-temperature, Surface and Coatings Technology 389 (2020) 125629.
[9] A. Zakeri, F. Ghadami, A. Sabour Rouhaghdam, B. Saeedi, Study on production of modified MCrAlY powder with nano oxide dispersoids as HVOF thermal spray feedstock using mechanical milling, Materials Research Express 7 (2019) 015030.
[10] M. Masoumi Balashadehi, P. Nourpour, A. Sabour Rouh Aghdam, M.H. Allahyarzadeh, A. Heydarzadeh, M. Hamdi, The formation, microstructure and hot corrosion behaviour of slurry aluminide coating modified by Ni/Ni-Co electrodeposited layer on Ni-base superalloy, Surface and Coatings Technology 402 (2020) 126283.
[11] F. Ghadami, A. Zakeri, A.S.R. Aghdam, R. Tahmasebi, Structural characteristics and high-temperature oxidation behavior of HVOF sprayed nano-CeO_2 reinforced NiCoCrAlY nanocomposite coatings, Surface and Coatings Technology 373 (2019) 7–16.
[12] F. Ghadami, A. Sabour Rouh Aghdam, A. Zakeri, B. Saeedi, P. Tahvili, Synergistic effect of CeO_2 and Al_2O_3 nanoparticle dispersion on the oxidation behavior of MCrAlY coatings deposited by HVOF, Ceramics International 46 (2020) 4556–4567.
[13] M. Bai, L. Reddy, T. Hussain, Experimental and thermodynamic investigations on the chlorine-induced corrosion of HVOF thermal sprayed NiAl coatings and 304 stainless steels at 700 °C, Corrosion Science 135 (2018) 147–157.
[14] M. Bai, B. Song, L. Reddy, T. Hussain, Preparation of MCrAlY–Al_2O_3 Composite Coatings with Enhanced Oxidation Resistance through a Novel Powder Manufacturing Process, Journal of Thermal Spray Technology 28 (2019) 433–443.
[15] H. Chi, M.A. Pans, M. Bai, C. Sun, T. Hussain, W. Sun, Y. Yao, J. Lyu, H. Liu, Experimental investigations on the chlorine-induced corrosion of HVOF thermal sprayed Stellite-6 and NiAl coatings with fluidised bed biomass/anthracite combustion systems, Fuel 288 (2021) 119607.
[16] A. Abuchenari, H. Ghazanfari, M. Siavashi, M. Sabetzadeh, S. Talebi, Z. Karami Chemeh, A. Jamavari, A review on development and application of self-healing thermal barrier composite coatings, Journal of Composites and Compounds 2 (2020) 147–154.
[17] A. Firouzi, K. Shirvani, The structure and high temperature corrosion performance of medium-thickness aluminide coatings on nickel-based superalloy GTD-111, Corrosion Science 52 (2010) 3579–3585.
[18] M.C. Galetz, X. Montero, M. Mollard, M. Günthner, F. Pedraza, M. Schütze, The role of combustion synthesis in the formation of slurry aluminization, Intermetallics 44 (2014) 8–17.
[19] Z.D. Xiang, J.S. Burnell-Gray, P.K. Datta, Aluminide coating formation on nickel-base superalloys by pack cementation process, Journal of Materials Science 36 (2001) 5673–5682.
[20] Y. Wang, J. Wang, H. Hu, J. Meng, X. Zhao, Effect of Y_2O_3 content in the pack mixtures on the cyclic-oxidation of Y_2O_3-modified low temperature aluminide coatings on 309 stainless steel, Vacuum 158 (2018) 101–112.
[21] G.W. Goward, Progress in coatings for gas turbine airfoils, Surface and Coatings Technology 108–109 (1998) 73–79.
[22] T. Kepa, F. Pedraza, F. Rouillard, Intermetallic formation of Al-Fe and Al-Ni phases by ultrafast slurry aluminization (flash aluminizing), Surface and Coatings Technology 397 (2020) 126011.
[23] J.T. Bauer, X. Montero, M.C. Galetz, Fast heat treatment methods for al slurry diffusion coatings on alloy 800 prepared in air, Surface and Coatings Technology 381 (2020) 125140.
[24] Q.X. Fan, S.M. Jiang, H.J. Yu, J. Gong, C. Sun, Microstructure and hot corrosion behaviors of two co modified aluminide coatings on a ni-based superalloy at 700 c, Applied Surface Science 311 (2014) 214–223.
[25] M. Zagula-Yavorska, J. Morgiel, J. Romanowska, J. Sieniawski, TEM analysis of the hafnium-doped aluminide coating deposited on Inconel 100 superalloy, Vacuum. 116 (2015) 115–120.
[26] M. Zagula-Yavorska, J. Morgiel, J. Romanowska, J. Sieniawski, Nanoparticles in zirconium-doped aluminide coatings, Materials Letters 139 (2015) 50–54.
[27] W. Ren, C. Xiao, Q. Li, J. Song, L. He, C. Cao, Microstructure evolution of cobalt aluminide coating on nickel-based superalloys during exposure at 1050 °c, Vacuum. 106 (2014) 39–45.
[28] S.A. Azarmehr, K. Shirvani, A. Solimani, M. Schütze, M.C. Galetz, Effects of Pt and Si on the low temperature hot corrosion of aluminide coatings exposed to Na_2SO_4 -60 mol% V_2O_5 salt, Surface and Coatings Technology 362 (2019) 252–261.
[29] Y. Zhou, X. Zhao, C. Zhao, W. Hao, X. Wang, P. Xiao, The oxidation performance for Zr-doped nickel aluminide coating by composite electrodepositing and pack cementation, Corrosion Science 123 (2017) 103–115.
[30] Y. Wang, Y. Zhang, G. Liang, Q. Ding, Low temperature formation of aluminide coatings on the electrodeposited nanocrystalline Ni and its oxidation resistance with La_2O_3/CeO_2 nanoparticle dispersion, Vacuum 173 (2020) 109148.
[31] Y.B. Zhou, H.T. Hu, H.J. Zhang, Oxidation behavior of aluminide coatings on carbon steel with and without electrodeposited Ni-CeO_2 film by low-temperature pack cementation, Vacuum 86 (2011) 210–217.
[32] M.H. Allahyarzadeh, M. Aliofkhazraei, A.S. Rouhaghdam, ELectrodeposition on superalloy substrates: A review, Surface Review and Letters 23 (2016) 1630001.
[33] A. Karimzadeh, A.S. Rouhaghdam, Effect of Nickel Pre-Plated on Microstructure and Oxidation Behavior of Aluminized AISI 316 Stainless Steel, Materials and Manufacturing Processes 31 (2016) 87–94.
[34] M. Safari, F. Shahriari Nogorani, Formation mechanism of high activity aluminide coating on Ni-CeO_2 coated Rene 80 alloy, Surface and Coatings Technology 329 (2017) 218–223.
[35] M. Qiao, C. Zhou, Codeposition of Co-Al-Y on nickel base superalloys by pack cementation process, Corrosion Science 75 (2013) 454–460.
[36] M. Qiao, C. Zhou, Hot corrosion behavior of Co modified NiAl coating on nickel base superalloys, Corrosion Science 63 (2012) 239–245.
[37] S. Mahini, S. Khameneh Asl, T. Rabizadeh, H. Aghajani, Effects of the pack Al content on the microstructure and hot corrosion behavior of aluminide coatings applied on Inconel-600, Surface and Coatings Technology 397 (2020) 125949.
[38] D. He, H. Guan, X. Sun, X. Jiang, Manufacturing, structure and high temperature corrosion of palladium-modified aluminide coatings on nickel-base superalloy M38, Thin Solid Films. 376 (2000) 144–151.
[39] M. Salehi Doolabi, B. Ghasemi, S.K. Sadrnezhaad, A. Habibollahzadeh, K. Jafarzadeh, Hot corrosion behavior and near-surface microstructure of a "low-temperature high-activity Cr-aluminide" coating on inconel 738LC exposed to Na_2SO_4, Na_2SO_4 + V_2O_5 and Na_2SO_4 + V_2O_5 + NaCl at 900 °C, Corrosion Science 128 (2017) 42–53.
[40] M.N. Task, B. Gleeson, F.S. Pettit, G.H. Meier, Compositional effects on the Type I hot corrosion of β-NiAl alloys, Surface and Coatings Technology 206 (2011) 1552–1557.
[41] C.A. Schneider, W.S. Rasband, K.W. Eliceiri, NIH Image to ImageJ: 25 years of image analysis, Nature Methods 9 (2012) 671–675.
[42] R. Jafari, E. Sadeghi, High-temperature corrosion performance of HVAF-sprayed NiCr, NiAl, and NiCrAlY coatings with alkali sulfate/chloride exposed to ambient air, Corrosion Science 160 (2019).
[43] P.D.F. ICDD, International Centre for Diffraction Data, Microscopy Today 21 (2013) 8–8.
[44] A. Brenner, Electrodeposition of alloys: principles and practice, Elsevier, 2013.
[45] M. Ferdosi Heragh, S. Eskandarinezhad, A. Dehghan, Ni-Cu matrix composite reinforced with CNTs: preparation, characterization, wear and corrosion behavior, inhibitory effects, Journal of Composites and Compounds 2 (2020) 123–128.
[46] E. Bahmani, A. Zakeri, A. Sabour Rouh Aghdam, A fast and efficient approach to fabricate tarnish-resistant nanocrystalline Ag-Ge thin films by direct current electrodeposition, Materials Letters 274 (2020) 127991.
[47] E. Bahmani, A. Zakeri, A. Sabour Rouh Aghdam, Microstructural analysis and surface studies on Ag-Ge alloy coatings prepared by electrodeposition technique, Journal of Materials Science (2021) 1–21.
[48] A. Karimzadeh, A.S. Rouhaghdam, M. Aliofkhazraei, R. Miresmaeili, Sliding wear behavior of Ni–Co–P multilayer coatings electrodeposited by pulse reverse method, Tribology International 141 (2020) 105914.
[49] A. Karimzadeh, M. Aliofkhazraei, F.C. Walsh, A review of electrodeposited Ni-Co alloy and composite coatings: Microstructure, properties and applications, Surface and Coatings Technology 372 (2019) 463–498.
[50] M.S. Safavi, M. Tanhaei, M.F. Ahmadipour, R.G. Adli, S. Mahdavi, F.C. Walsh, Electrodeposited Ni-Co alloy-particle composite coatings: a comprehensive review, Surface and Coatings Technology 382 (2020) 125153.
[51] R.D. Liu, S.M. Jiang, H.J. Yu, J. Gong, C. Sun, Preparation and hot corrosion behaviour of Pt modified AlSiY coating on a Ni-based superalloy, Corrosion Science 104 (2016) 162–172.
[52] C.C. Jia, K. Ishida, T. Nishizawa, Partition of alloying elements between γ (A1), γ′ (L12), and β (B2) phases in Ni-Al base systems, Metallurgical and Materials Transactions A 25 (1994) 473–485.

[53] T.J. Nijdam, L.P.H. Jeurgens, W.G. Sloof, Promoting exclusive α-Al_2O_3 growth upon high-temperature oxidation of NiCrAl alloys: Experiment versus model predictions, Acta Materialia 53 (2005) 1643–1653.
[54] M. Bai, H. Jiang, Y. Chen, Y. Chen, C. Grovenor, X. Zhao, P. Xiao, Migration of sulphur in thermal barrier coatings during heat treatment, Materials & Design 97 (2016) 364–371.
[55] C.Y. Jiang, Y.F. Yang, Z.Y. Zhang, Z.B. Bao, M.H. Chen, S.L. Zhu, F.H. Wang, A Zr-doped single-phase Pt-modified aluminide coating and the enhanced hot corrosion resistance, Corrosion Science 133 (2018) 406–416.
[56] Q.X. Fan, S.M. Jiang, D.L. Wu, J. Gong, C. Sun, Preparation and hot corrosion behaviour of two Co modified NiAl coatings on a Ni-based superalloy, Corrosion Science 76 (2013) 373–381.
[57] A.M. Beltran, D.A. Shores, Hot Corrosion, The Superalloys, CT Sims and WC Hagel, Eds, (1972).

Available online at www.jourcc.com

Journal homepage: www.JOURCC.com

Journal of Composites and Compounds

Effect of the powder manufacturing process on characteristics of nanostructured MCrAlY coatings: dry vs. wet ball milling

Ali Zakeri [a], Pouya Tahvili [a], Elnaz Bahmani [a], Alireza Sabour Rouh Aghdam [a]*

[a] *Department of Materials Engineering, Tarbiat Modares University, Tehran P.O. Box: 14115-143, Tehran, Iran*

ABSTRACT

Metallic MCrAlY coatings have been widely utilized to protect the high-temperature materials operating in aggressive conditions of gas turbines. However, with more demands on the turbine inlet temperature rise for efficiency gains, there is a need to further improve the high-temperature performance of the MCrAlY coatings. A possible way to meet this challenge is by microstructure modification. The aim of this study is to produce nanocrystalline MCrAlY powders via wet and dry mechanical milling techniques and deposit the obtained feedstock powders by the high-velocity oxygen fuel (HVOF) spraying method. Comprehensive characterization and comparison of the different powder processing techniques and the corresponding coatings were studied. It was established that the nano-scaled MCrAlY feedstock powder with low contamination levels could be achieved by mechanical milling. Moreover, the powder samples were well-deposited by the HVOF process and the correlation between powder properties and coating characteristics was investigated.

Peer review under responsibility of jourcc

ARTICLE INFORMATION

Article history:
Received 15 January 2021
Received in revised form 5 February 2021
Accepted 3 February 2021

Keywords:
MCrAlY
Ball milling
Thermal spray
HVOF

1. Introduction

In today's modern world, it is well-known that the gas turbines have dominated the electricity generation and aerospace industries [1]. The incentive and driving force for further developing the advanced gas turbines arise from the society's increasing demand for aviation and electricity industries [2]. This could be achieved through increasing the inlet temperature of these engines, which translates to their higher efficiency. In addition, the higher efficiency plays a key role in the carbon emission reduction due to lower fossil fuel consumption. That being said, higher operating temperatures lead to more aggressive conditions for engine components; therefore, new materials with enhanced thermo-mechanical properties along with more efficient protective coatings are vital for successful prolonged operation of the engines [3–6].

It has been reported that up to 50% of the total weight of a gas turbine powered aircraft is manufactured from Ni-based superalloys [7]. However, it should be taken into account that the primary role of these alloys is to endure the heavy mechanical loads at the elevated temperatures; therefore, the design strategy is to maximize the mechanical strength at the expense of environmental degradation resistance [8]. In this respect, the protective coatings came into being. The most commonly used coatings for the protection of superalloy components consist of chromia- and alumina-forming alloys. Oftentimes, these coatings are applied via diffusion treatments and thermal spraying methods, which have gained popularity in the industry [9–12]. MCrAlY-type alloys (M: Ni and/or Co) are considered the state-of-the-art materials for thermal spray coatings and have proven to be effective in most engine applications [13]. Furthermore, it has been shown that MCrAlY coatings can be deposited by HVOF process, which enjoy equivalent, and sometimes superior, protection properties compared to the plasma-sprayed counterparts [14–16].

Although utilizing the conventional coatings have enabled the superalloy components to serve at harsh conditions, further advancements in gas turbine efficiency are conditional to the development of thermostable and oxidation-resistant coatings [17]. One of the practical approaches for this purpose is the microstructural modification of coatings. In this regard, some routes have been proposed and pursued by other researchers, some good examples of which are: powder processing, laser treatment, and shot peening [18–21]. Among these approaches, the powder processing via mechanical milling technique has been widely adapted due its simplicity and versatility [14, 22].

The mechanical milling is a solid-state powder processing technique which is applicable to a number of purposes, including grain refinement, inducing preferred orientation, and homogeneous dispersion of reinforcements in a multicomponent powder system [22]. In a study by Tahari et al., CoNiCrAlY/YSZ composite powders with nanocrystalline structure and uniform dispersion of strengthening ceramic particles were produced via mechanical milling process [23]. Studies conducted by Ajdelsztajn et al. have confirmed the capability of HVOF process to produce the nanostructured MCrAlY coatings by virtue of its high kinetic energy and low spraying temperature [24–26]. Despite research efforts highlighting the characteristics of nanostructured MCrAlY powders and coatings, it is essential to examine the effects of mechanical milling conditions and their influence on the quality of final coatings in terms of the desired microstructure and oxidation performance. Given this

* *Corresponding author: Ali Zakeri; E-mail: alizakeri@modares.ac.ir*

https://doi.org/10.52547/jcc.3.1.2

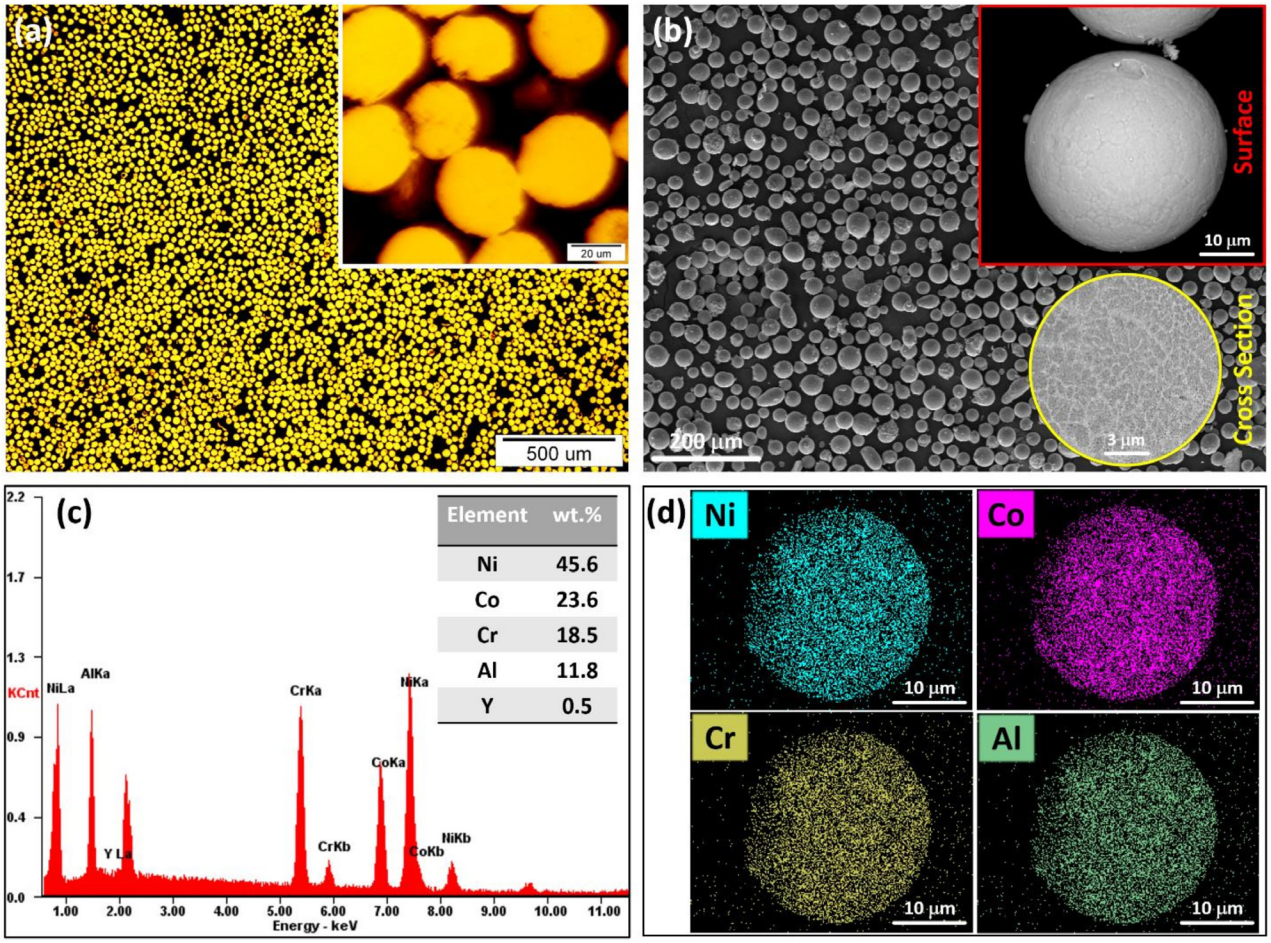

Fig. 1. Morphology and chemical composition of the as-received NiCoCrAlY powder; (a) optical light micrographs of powder cross-section, (b) SEM images (the inset images show the secondary electron (SE) and backscattered electron (BSE) mode images from the surface and cross-section, respectively), (c) EDS analysis, and (d) EDS elemental mapping.

background, the objective of current work concerns with the feedstock powder characteristics-microstructural evolution relationship of the nanostructured MCrAlY coatings produced by the mechanical milling.

2. Material and methods

2.1. Powder materials and processing

A commercially available gas-atomized MCrAlY powder supplied by Oerlikon Metco was used as the starting powder material (Fig. 1). The preparation of the nanostructured feedstock powder was carried out by using a two-body planetary ball milling machine. Prior to the milling, the vials were purged with argon gas to prevent possible powder oxidation. Two modes of milling, namely dry and wet milling, were conducted. The sample coding along with the milling conditions of each powder are given in Table 1. As is known from the selected milling parameters, the only difference is the amount of process control agent, also known as surfactant or lubricant, used for each mode. Typically, PCAs are organic compounds commonly used in the milling processes. Basically, these compounds are surface-active agents which can be adsorbed on the powder particles' surfaces, by which they control the milling mechanism [22]. As will be discussed in the next section, the WM powder was followed by an additional spray drying process to provide the suitable morphology of the powder for thermal spraying. This process was performed using a high-speed centrifugal spray drier with the inlet and outlet temperature values of 350 and 120 ℃, respectively. The rotating speed of the atomizing disc was set to 10500 rev/min. It worth noting that no binder was added to the powder slurry before feeding into the spray dryer and the final product was used as the feedstock powder without any post calcination treatments.

Table 1.
Sample coding and milling conditions for the powder specimens.

Sample (Code) / Parameter	Revolution Speed (RPM)	Ball to Powder Ratio (wt.%)	Process Control Agent (PCA)	Milling Time (h)
Conventional (CN)	-	-	-	-
Dry Milled (DM)	200	20:1	Ethanol (1 wt.%)	10
Wet Milled (WM)	200	20:1	Ethanol (5 wt.%)	10

2.2. HVOF thermal spraying

A commercial HVOF system was used for the deposition of MCrAlY coatings. Ground and degreased mild steel coupons (60 x 30 x 2 mm^3) were used as the substrate. Owing to the fact that in this study, the coatings were characterized in the free-standing form, no traditional preparation of the substrate, such as grit blasting, was conducted prior to the thermal spraying. The spraying parameters, for all three types of the powders, were chosen based on the conventional powder manufacturer's recommendation. With this respect, the thermal spraying was carried out with an oxygen flow rate of 200 l/min, propane flow rate of 55 l/min, and at a spraying distance of about 28 cm. It is worth noting that the maximum flame temperature of 2828 ℃ can be reached using the

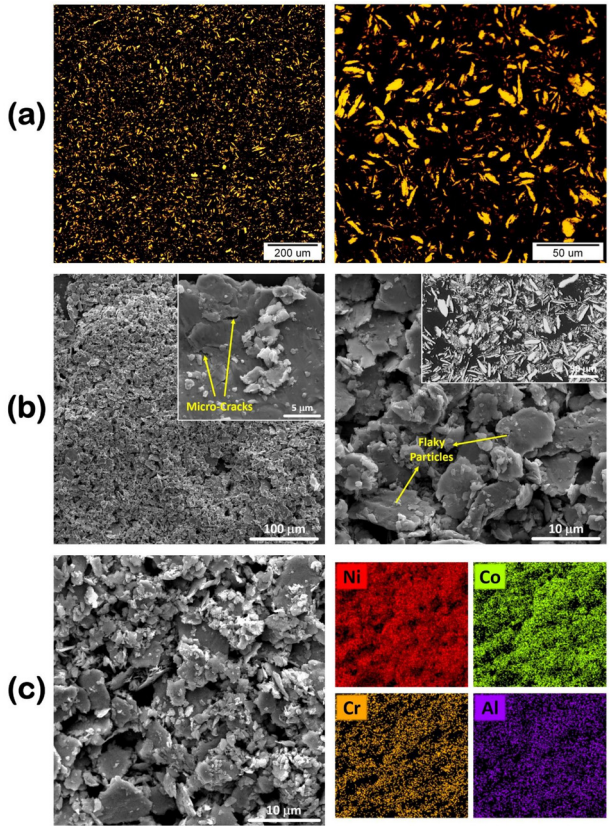

Fig. 2. As-milled WM powder; (a) OM images, (b) secondary electron SEM images (the inset image in the right presents the BSE-SEM image from the cross-section), and (c) SEM images with the corresponding EDS elemental mapping.

propane-oxygen mixture with the oxygen to propane ratio of 4.5 [27].

2.3. Characterization techniques

The microstructure of the obtained powders and coatings were observed by optical light microscopy (OM, Olympus BX51, Olympus Optical Co., Ltd., Japan). The surface morphology and cross-section examinations were performed by scanning electron microscopy (SEM, Ziess EVO MA15) equipped with an EDS detector (EDAX Genesis and Oxford Instruments). In addition, the high-magnification images were taken with a field-emission scanning electron microscope (FESEM, Nova NanoSEM 450). According to the ASTM E-384 standard, a microhardness tester instrument (MicroMet 1, Buehler) was used for the hardness measurements, using a load of 300 g [28]. The reported values are based on the average of at least ten measurements.

3. Results and discussion

3.1. Powder characterization

Fig. 2 shows the OM and SEM-EDS analyses of as-milled WM powder. Compared to the original spherical morphology, severe particle deformation can be clearly observed with the morphological transformation to the flaky particles. Despite the fact that the NiCoCrAlY powder is consisted of a ductile g-matrix with FCC crystal structure, the typical tendency for cold-welding was inhibited, primarily due to the active presence of ethanol [14]. Also, some micro-cracks were observed on the surface of particles (Fig. 2b) which indicates the fracturing stage as the dominant mechanism controlling the milling process. A combined effect of the ethanol inhibiting the cold welding and the work-hardening of particles through the milling process led to the dominance of fracturing stage. According to the EDS mapping analysis (Fig 2c), the milling process did not affect the chemical composition homogeneity. Further, it has been confirmed that high-energy ball milling could induce nanocrystallization in the milled powder samples [22]. This is true in the case of as-milled WM powder and the nano-scale structure of the powder particles were confirmed through high-magnification FESEM images (Fig. 3). As is well-known, the nanocrystalline materials have significantly higher diffusion rates in comparison to the materials with conventional grains size; typically, greater than 1 mm. This specific property favors the oxidation performance of MCrAlY coatings owing to the fact that the protective oxide former element (Al) benefits the higher diffusion flux to the coatings surface and developing a protective alumina scale in less time [29 31].

Analyzing the microscopic morphologies shows that the as-milled WM powder particles do not satisfy the suitable powder properties for the HVOF spraying process, namely the spherical morphology with a size distribution of 10–45 mm [32]. This is because the small-sized particles have small mass inertias and they might not track the motion of HVOF jet stream, which in turn reduces the deposition efficiency [33]. With this in mind, a subsequent spray drying process was utilized to obtain powder particles which meet the requirements of HVOF feeding system. Fig. 4 depicts the OM and SEM images of the spray-dried WM powder. It can be seen that the obtained granules are composed of semi-spherical shaped particles with diameters in the range of 10-50 mm. With respect to these characteristics, it is reasonable to predict that the spray-dried powder particles benefit from good flowability in the HVOF jet stream. Moreover, it is evident that each particle contains building blocks of flaky-shaped fractures shown in Fig. 2b. Based on the cross-section and surface morphology of the particles, it is clear that the granules are not completely dense and compact. Since the particle formation during the spray drying process involves the agglomeration of small particles, some hollow or porous particles might be observed in the final product [34].

Fig. 5 displays the OM and SEM images of the DM powder. As can be observed, the milling process in the dry condition has resulted in the semi-spherical powder particles. As opposed to the spray-dried sample, DM powder particles are compact and intensely cold-welded. It should be taken into account that the amount of PCA used for the milling of DM powder was lower than that of WM powder; therefore, the milling medium was dry for most of the milling time. Considering this, it appears that the absence of ethanol has promoted the cold-welding mechanism, producing the semi-spherical agglomerates which did not require any granulation process for using as the HVOF feedstock powder.

Despite the advantages of the mechanical milling, powder contamination has been remained as one of the main limitations of this process. Owing to the nanostructure characteristics of milled powder particles, namely large surface area and small size of the particles, some precautions should be taken to minimize the introduction of impurities. That being said, it can be surmounted by optimizing the milling parameters and using the proper materials as the PCA and grinding medium. The different results reported by the researchers, showing different levels of impurities, indicate the significant role of the milling conditions, including atmosphere, intensity and time of milling. The inherent properties of the powder samples, such as strength and hardness, influence the powder contamination as well [13]. Fig. 6 reports the EDS analysis results from the final powder samples in this study. It is apparent that the level of Fe impurity is higher in the case of dry milling condition. This can be attributed to the wear of the grinding balls and vials, which occur at a higher rate in the dry milling conditions. It should be noted that the impurity levels detected in this study are relatively low; hence, it would neither affect the microstructure nor the oxidation properties of the MCrAlY coatings [16, 35].

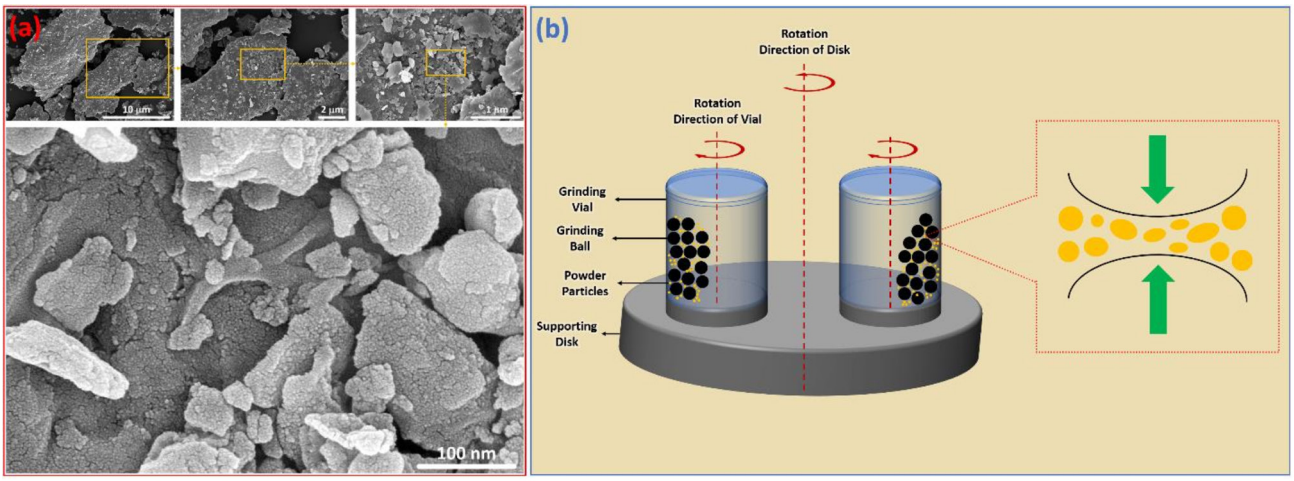

Fig. 3. (a) High-magnification FESEM images of the as-milled WM powder and (b) a schematic representing the mechanical milling process.

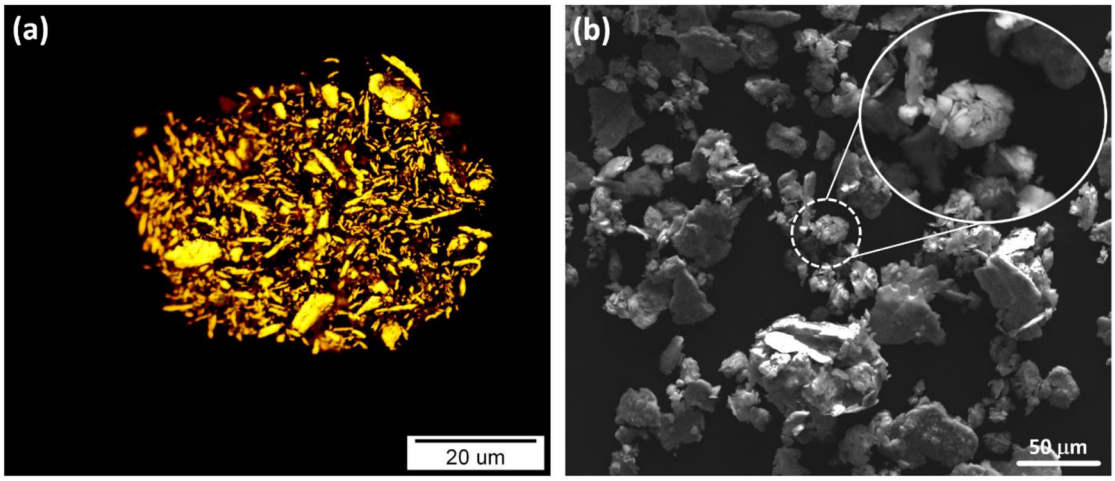

Fig. 4. Spray-dried WM powder; (a) cross-sectional OM image and (b) secondary electron SEM image.

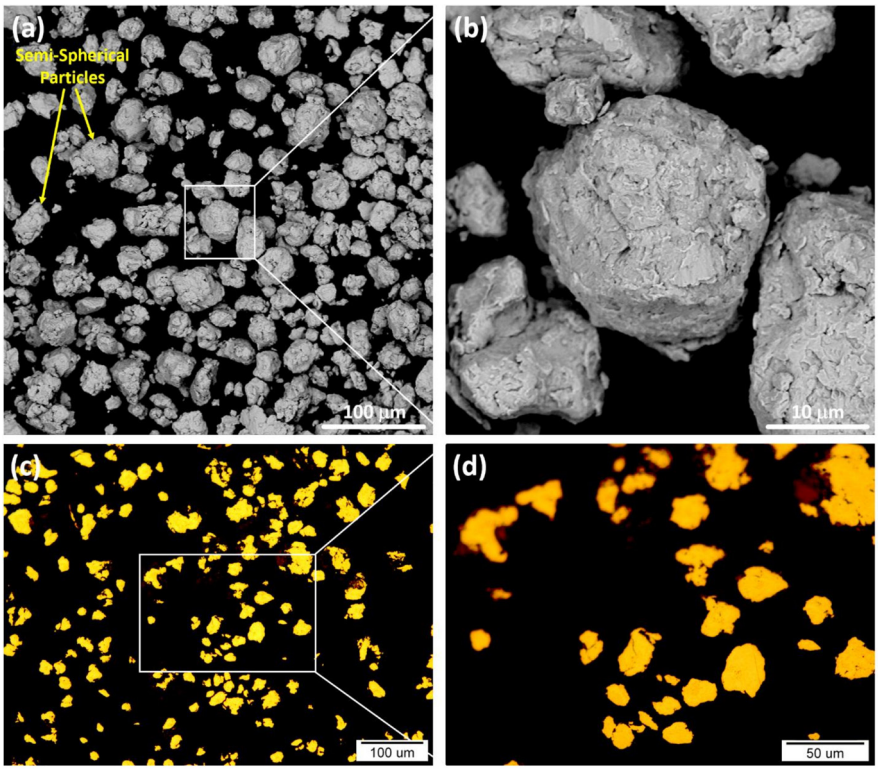

Fig. 5. DM powder; (a, b) secondary electron SEM images and (c, d) cross-sectional OM images.

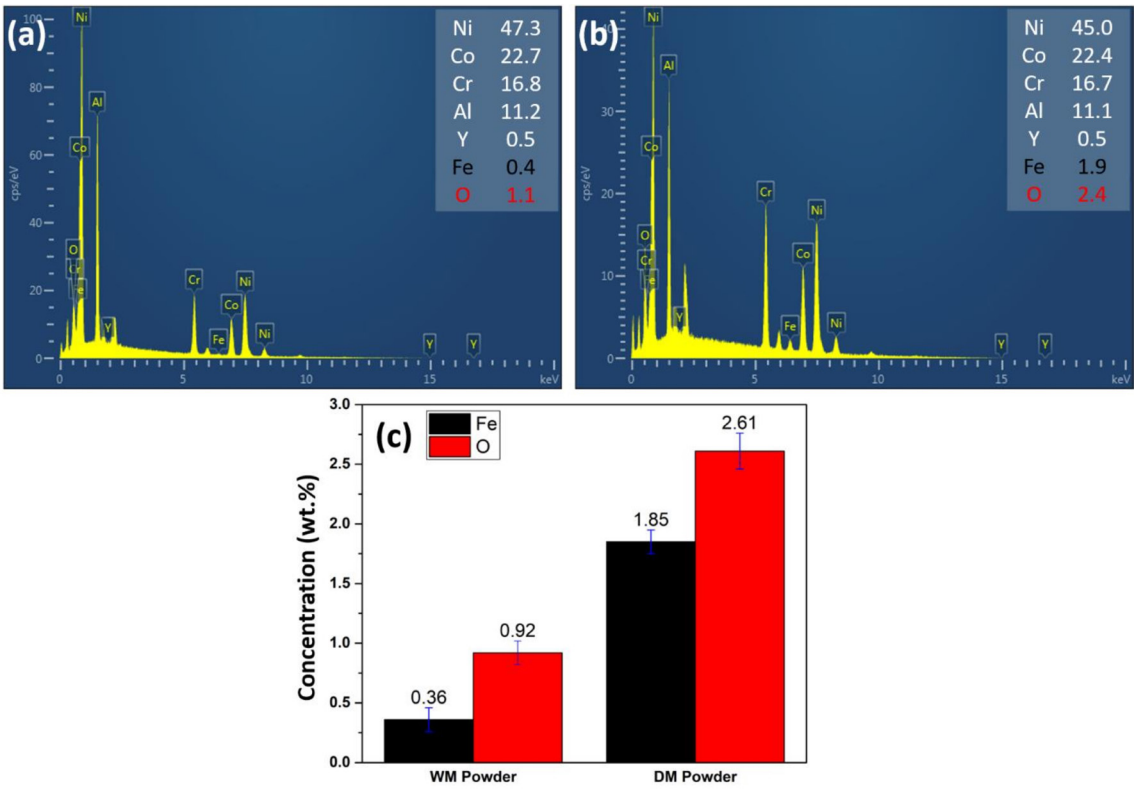

Fig. 6. EDS analysis results from (a) WM and (b) DM powders with a comparison of mean values of O and Fe contents shown in (c).

3.2. Coating characterization

The conventional NiCoCrAlY powder as well as the milled powders were sprayed by HVOF technique. Fig. 7 presents the characteristics of the CN coating. To better explain the coating characteristics, the HVOF deposition mechanism is briefly reviewed. In HVOF process, the desired feedstock material is injected into a high-velocity jet stream and heated up to get fully and/or partially melted. This is accompanied by the acceleration of the powder particles, followed by propelling onto the substrate and impinging in a semi-solid state. Upon the impact, the bonding of coating material takes place by mechanical interlocking. After the solidification of the impacted particles, they form splats in a lamellar manner [36].

Based on the Fig. 7a, it can be seen that a number of un-melted particles have maintained their original spherical morphology. This is mostly true for the larger particles which do not get as easily melted as the smaller ones. It is worth noting that the surface particles lack the impact pressure from the subsequent deposition pass; therefore, there is a higher possibility for the particles to experience a minor degree of deformation [14]. Moreover, splashed regions were also observed on the coating surface, as a result of molten particle impingement. The EDS point analysis from these areas showed a higher content of oxygen, which is probably due to the oxygen pick-up during the atmospheric spraying [37].

The cross-sectional investigations were performed in both SE and BSE modes of SEM. The SE-SEM image confirms the highly compact structure of the deposited coating, without any large pores. It should be mentioned that the pores are associated with some depth in the SE mode SEM images [38]. Some dark veins can be observed in the BSE-SEM image, indicating the splat boundaries. These dark lines were formed as a consequence of slight in-flight oxidation and are mainly composed of Al oxide. Moreover, the gray-colored b precipitates were remained within the splats. These precipitates are rich in Al, as detected by the EDS analysis, and are present in the as-received powder as well (see the inset in Fig. 1b).

The characteristics of the coating obtained from depositing the spray-dried WM powder are depicted in Fig. 8. It is clear that a surface with less roughness level compared to the CN coating has been formed. Moreover, the cross-section images exhibit a considerable number of dark veins between the splats, known as the oxide stringers. This has to do with the excessive heating of the small powder particles, resulting in significant in-flight oxidation. Further, the small splat sizes may imply the scattering of the spray-dried powder particles within the HVOF jet stream. More precisely, the high-velocity of the jet stream causes a drop in the pressure, which in turn, can lead to the scattering of porous powder particles [39].

Fig. 9 shows the characteristics of the coating attained from spraying the DM powder. Similar lamellar structure was formed due to the spreading of splats; however, slightly higher content of inter-particle pores was notable for the DM coating. This is mainly due to the insufficient localized particle deformation. The lower deformability of the DM powder particles originates from their high work-hardening level during the milling process. As can be seen from the coating surface, presence of the un-deformed particles leads to the formation of pin-holes. It should be mentioned that these pores are not inter-connected; therefore, they would not exacerbate the penetration of corrosive elements through the coating [40].

When looked at in detail, a sporadic distribution of dark dots was observed for the DM coating (Fig. 10). According to the EDS elemental mapping analysis, these dots are rich in Al and O. Aside from the dark veins in the splat boundary regions, it appears that the dispersed dots stem from the alumina formation and dispersion during the milling process. It should be noted that based on the EDS analysis, it was revealed that the DM powder exhibited higher oxygen content (Fig. 6c). Although the milling process was conducted in a high-purity Ar ambient, the slight powder oxidation occurred due to the temperature rise during milling. The generated temperature is dependent on the energy input into the powder, which can be up to 30 kJ/mol [41]. It has been reported that the addition of fine-grained alumina particles strengthens the high-tem-

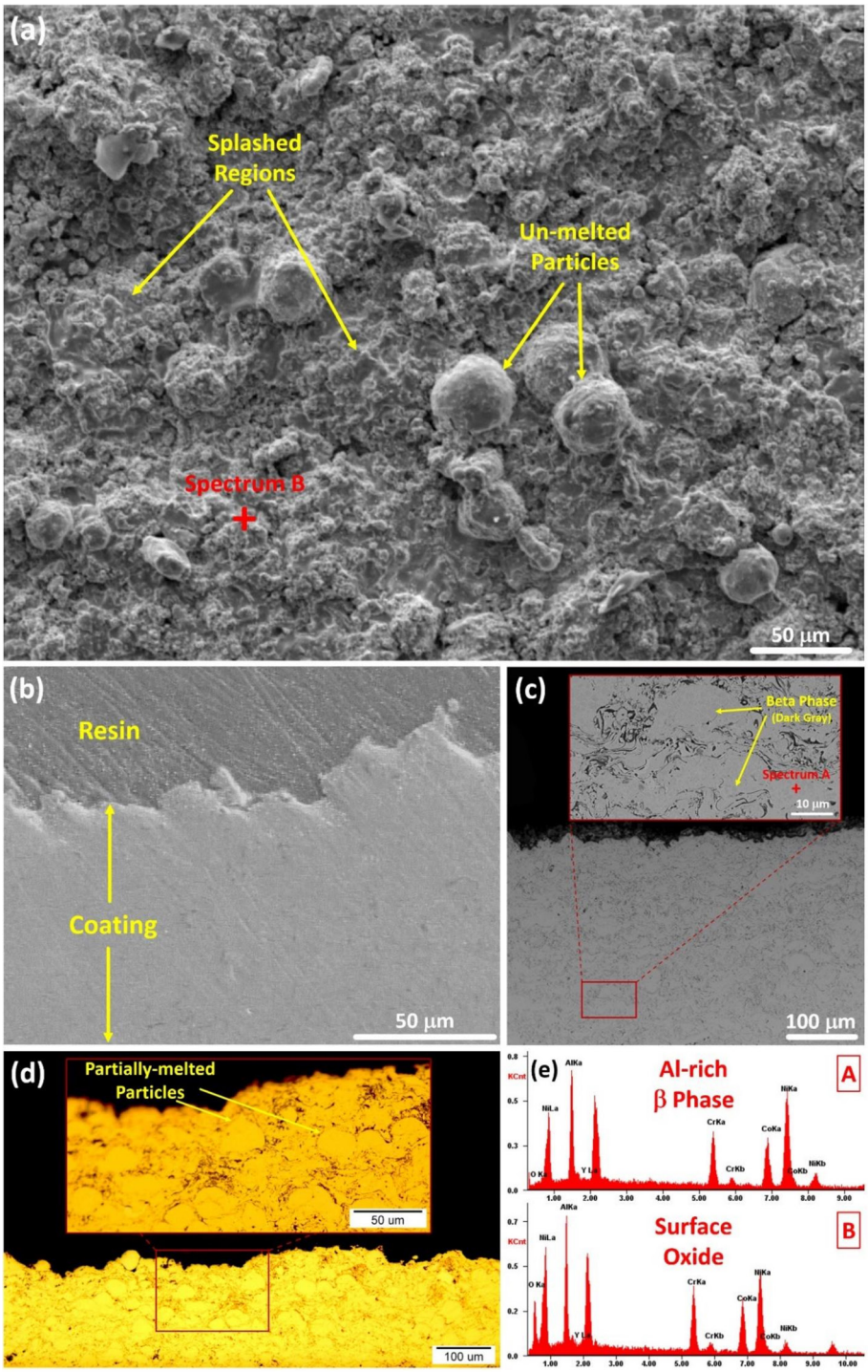

Fig. 7. Characteristics of the CN coating; (a) surface SE-SEM image, (b) cross-section SE-SEM image, (c) cross-section BSE-SEM image, (d) cross-section OM image, and (e) EDS analysis performed on the marked spots.

perature wear and oxidation resistance of the MCrAlY coatings [4, 42].

The Vickers hardness results of the coatings with a typical OM image showing indents from hardness measurements are shown in Fig. 11. As is apparent from Fig. 11b, the measured hardness values vary across the cross-section of the coating. This is due to the discrepancies in the resistance of different regions to the indenter force and the standard deviations in the measurements were indicated by the error bars. Both of the coatings obtained from the milled powders, exhibited higher hardness values compared to the CN coating. The DM coating owns the highest hardness of 519±21 HV_{300}. This is attributable to the combined effect of the presence of work-hardened powder particles and alumina dispersoids within the coating. Furthermore, as discussed earlier, the near-surface regions of the coating lack the hammering effect from the subsequent deposition pass; thus, exhibit slightly lower hardness values (note the large indent size shown in Fig. 11b).

4. Conclusions

The main objective of the work presented in this paper concerned the development of nanocrystalline NiCoCrAlY coatings. In this regard, mechanical milling approach was taken to produce nano-scaled NiCoCrAlY feedstock powder, and then the coatings were applied by means of HVOF spraying method. The key findings are as follows:

1. The wet milling process resulted in the small-sized flaky particles, which required an additional agglomeration step to be used as a sprayable powder. With this in mind, a spray dry-

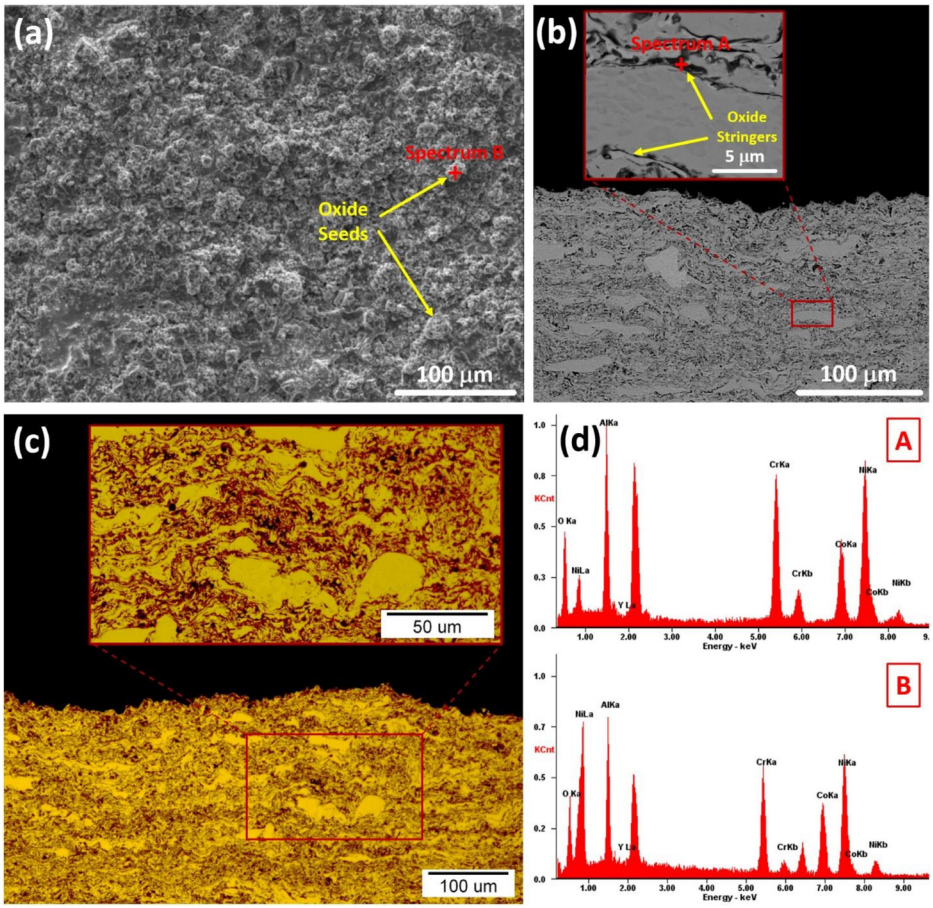

Fig. 8. Characteristics of the WM coating; (a) surface SE-SEM image, (b) cross-section BSE-SEM image, (c) cross-section OM image, and (d) EDS analysis performed on the marked spots.

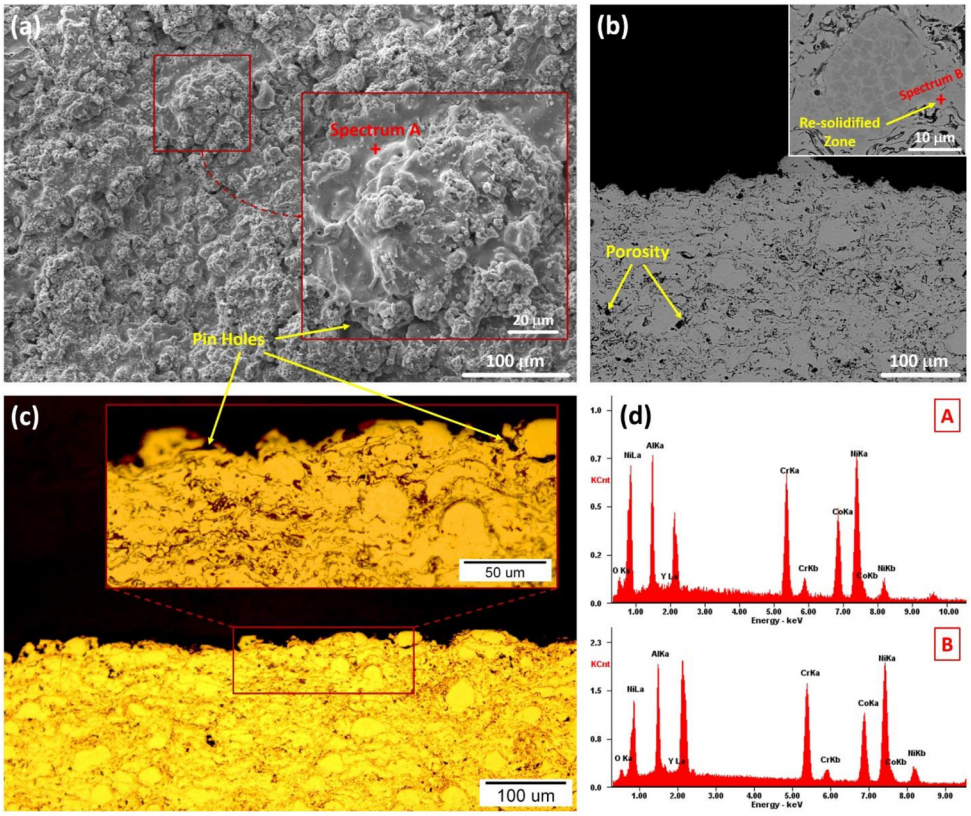

Fig. 9. Characteristics of the DM coating; (a) surface SE-SEM image, (b) cross-section BSE-SEM image, (c) cross-section OM image, and (d) EDS analysis performed on the marked spots.

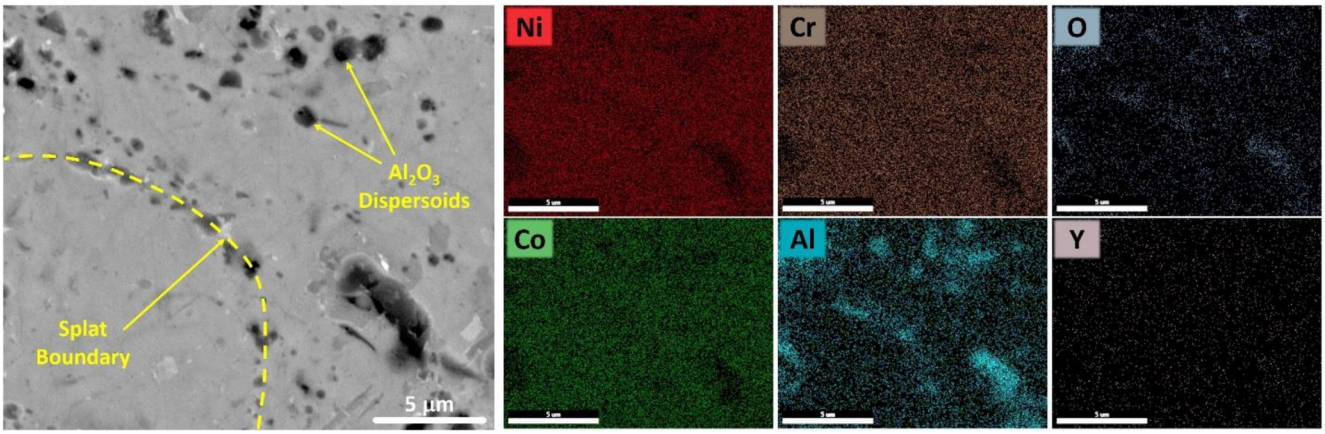

Fig. 10. BSE-SEM image and corresponding EDS elemental mapping from DM coating.

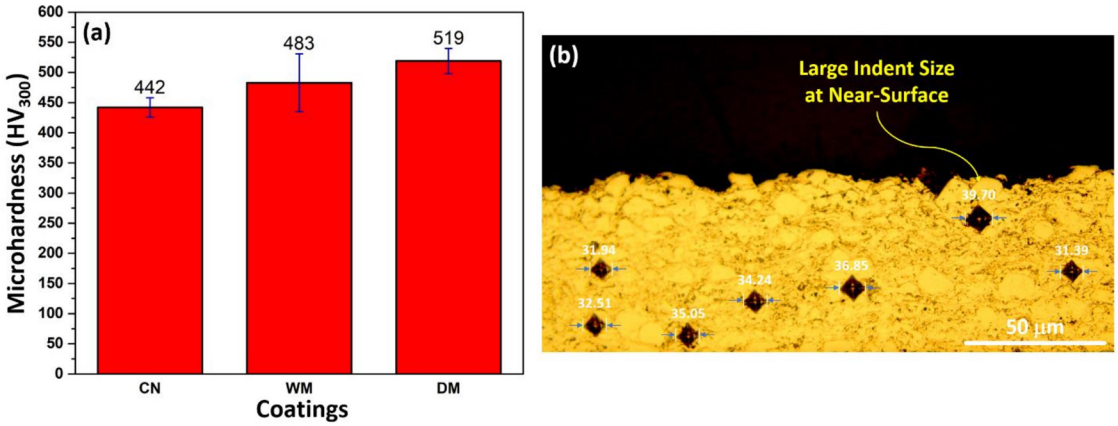

Fig. 11. (a) Average values of hardness measurements and (b) OM image showing indents from hardness measurements for the DM coating.

ing process was conducted, by which porous particles with semi-spherical morphology were achieved.

2. The powder particles obtained by dry milling process were compact with semi-spherical morphology, which met the suitable properties for thermal spraying. It appeared that the dry medium gave rise to a higher energy input into the powder.
3. A slightly higher contamination level was observed for the dry milled powder and it was attributed to the higher wear rates associated in this condition.
4. The coatings' investigations exhibited some discrepancies in terms of porosity and oxide content. These differences were mainly ascribed to the deformability and in-flight oxidation of the powder particles.
5. The coating obtained from spraying the dry milled powder (DM) showed the highest hardness values. This is due to the combined effect of powder particle work-hardening during the milling process and the presence of alumina dispersion within the coating.

Declaration of conflicting interests

The authors declare that there is no conflict of interest.

REFERENCES

[1] N.P. Padture, M. Gell, E.H. Jordan, Thermal barrier coatings for gas-turbine engine applications, Science (80). 296 (2002) 280–284.

[2] R.C. Reed, The superalloys: fundamentals and applications, Cambridge university press, 2008.

[3] F. Ghadami, A. Zakeri, A.S.R. Aghdam, R. Tahmasebi, Structural characteristics and high-temperature oxidation behavior of HVOF sprayed nano-CeO_2 reinforced NiCoCrAlY nanocomposite coatings, Surf. Coatings Technol. 373 (2019) 7–16.

[4] F. Ghadami, A. Sabour Rouh Aghdam, A. Zakeri, B. Saeedi, P. Tahvili, Synergistic effect of CeO_2 and Al_2O_3 nanoparticle dispersion on the oxidation behavior of MCrAlY coatings deposited by HVOF, Ceram. Int. 46 (2020) 4556–4567.

[5] M. Bai, H. Jiang, Y. Chen, Y. Chen, C. Grovenor, X. Zhao, P. Xiao, Migration of sulphur in thermal barrier coatings during heat treatment, Mater. Des. 97 (2016) 364–371.

[6] M. Bai, Fabrication and Characterization of Thermal Barrier Coatings, (2015) 182. https://www.researchgate.net/publication/287347007_Fabrication_and_characterization_of_thermal_barrier_coatings.

[7] T.M. Pollock, S. Tin, Nickel-based superalloys for advanced turbine engines: Chemistry, microstructure, and properties, J. Propuls. Power. 22 (2006) 361–374.

[8] W. Xia, X. Zhao, L. Yue, Z. Zhang, Microstructural evolution and creep mechanisms in Ni-based single crystal superalloys: A review, J. Alloys Compd. 819 (2020) 152954.

[9] M. Masoumi Balashadehi, P. Nourpour, A. Sabour Rouh Aghdam, M.H. Allahyarzadeh, A. Heydarzadeh, M. Hamdi, The formation, microstructure and hot corrosion behaviour of slurry aluminide coating modified by Ni/Ni-Co electrodeposited layer on Ni-base superalloy, Surf. Coatings Technol. 402 (2020) 126283.

[10] A. Zakeri, E. Bahmani, A. Sabour Rouh Aghdam, B. Saeedi, M. Bai, A study on the effect of nano-CeO_2 dispersion on the characteristics of thermally-grown oxide (TGO) formed on NiCoCrAlY powders and coatings during isothermal oxidation, J. Alloys Compd. 835 (2020) 155319.

[11] B. Song, M. Bai, K.T. Voisey, T. Hussain, Role of Oxides and Porosity on High-Temperature Oxidation of Liquid-Fueled HVOF Thermal-Sprayed Ni50Cr Coatings, J. Therm. Spray Technol. 26 (2017) 554–568.

[12] C. Liu, Y. Chen, L. Qiu, H. Liu, M. Bai, P. Xiao, The al-enriched γ'-Ni3Al-base bond coat for thermal barrier coating applications, Corros. Sci. 167 (2020) 108523.

[13] A. Zakeri, E. Bahmani, A. Sabour Rouh Aghdam, B. Saeedi, A comparative study on the microstructure evolution of conventional and nanostructured MCrAlY powders at high-temperature, Surf. Coatings Technol. 389 (2020) 125629.

[14] A. Zakeri, F. Ghadami, A. Sabour Rouhaghdam, B. Saeedi, Study on produc-

tion of modified MCrAlY powder with nano oxide dispersoids as HVOF thermal spray feedstock using mechanical milling, Mater. Res. Express. 7 (2019) 015030.
[15] W. Brandl, D. Toma, H.J. Grabke, The characteristics of alumina scales formed on HVOF-sprayed MCrAlY coatings, Surf. Coatings Technol. 108–109 (1998) 10–15.
[16] B. Saeedi, A. Sabour Rouh Aghdam, G. Gholami, A study on nanostructured in-situ oxide dispersed NiAl coating and its high temperature oxidation behavior, Surf. Coatings Technol. 276 (2015) 704–713.
[17] A.H. Pakseresht, Production, properties, and applications of high temperature coatings, 2018.
[18] A.H. Pakseresht, A. Kimiayi, M. Alizadeh, H. Nuranian, A. Faeghinia, Microstructural study and hot corrosion behavior of bimodal thermal barrier coatings under laser heat treatment, Ceram. Int. 46 (2020) 19217–19227.
[19] A.C. Karaoglanli, K.M. Doleker, B. Demirel, A. Turk, R. Varol, Effect of shot peening on the oxidation behavior of thermal barrier coatings, Appl. Surf. Sci. 354 (2015) 314–322.
[20] Q. Zhang, C.J. Li, C.X. Li, G.J. Yang, S.C. Lui, Study of oxidation behavior of nanostructured NiCrAlY bond coatings deposited by cold spraying, Surf. Coatings Technol. 202 (2008) 3378–3384.
[21] K.M. Doleker, A.C. Karaoglanli, Comparison of Oxidation Behavior of Shot-Peened Plasma Spray Coatings with Cold Gas Dynamic Spray Coatings, Oxid. Met. 88 (2017) 121–132.
[22] C. Suryanarayana, Mechanical alloying and milling, Prog. Mater. Sci. 46 (2001) 1–184.
[23] M. Tahari, M. Shamanian, M. Salehi, Microstructural and morphological evaluation of MCrAlY/YSZ composite produced by mechanical alloying method, J. Alloys Compd. 525 (2012) 44–52.
[24] L. Ajdelsztajn, J.A. Picas, G.E. Kim, F.L. Bastian, J. Schoenung, V. Provenzano, Oxidation behavior of HVOF sprayed nanocrystalline NiCrAlY powder, Mater. Sci. Eng. A. 338 (2002) 33–43.
[25] J.A. Picas, A. Forn, L. Ajdelsztajn, J. Schoenung, Nanocrystalline NiCrAlY powder synthesis by mechanical cryomilling, Powder Technol. 148 (2004) 20–23.
[26] L. Ajdelsztajn, F. Tang, G.E. Kim, V. Provenzano, J.M. Schoenung, Synthesis and oxidation behavior of nanocrystalline MCrAlY bond coatings, J. Therm. Spray Technol. 14 (2005) 23–30.
[27] O. Maranho, D. Rodrigues, M. Boccalini, A. Sinatora, Influence of parameters of the HVOF thermal spray process on the properties of multicomponent white cast iron coatings, Surf. Coatings Technol. 202 (2008) 3494–3500.
[28] ASTM E384-05a, Standard Test Method for Microindentation Hardness of Materials, ASTM Int. 14 (2005) 1–24.
[29] A. Zakeri, E. Bahmani, A.S.R. Aghdam, Impact of MCrAlY feedstock powder modification by high-energy ball milling on the microstructure and high-temperature oxidation performance of HVOF-sprayed coatings, Surf. Coatings Technol. (2020) 125935.
[30] D. Guo, L. Zhao, B. Jodoin, Cold Spray for Production of In-Situ Nanocrystalline MCrAlY Coatings – Part II: Isothermal Oxidation Performance, Surf. Coatings Technol. (2021) 126828.
[31] Y. Chen, X. Zhao, P. Xiao, Effect of microstructure on early oxidation of MCrAlY coatings, Acta Mater. 159 (2018) 150–162.
[32] S. Hong, Y. Wu, G. Li, B. Wang, W. Gao, G. Ying, Microstructural characteristics of high-velocity oxygen-fuel (HVOF) sprayed nickel-based alloy coating, J. Alloys Compd. 581 (2013) 398–403.
[33] Z. Khodsiani, H. Mansuri, T. Mirian, The effect of cryomilling on the morphology and particle size distribution of the NiCoCrAlYSi powders with and without nano-sized alumina, Powder Technol. 245 (2013) 7–12.
[34] M.R. Loghman-Estarki, M. Pourbafrany, R. Shoja Razavi, H. Edris, S.R. Bakhshi, M. Erfanmanesh, H. Jamali, S.N. Hosseini, M. Hajizadeh-Oghaz, Preparation of nanostructured YSZ granules by the spray drying method, Ceram. Int. 40 (2014) 3721–3729.
[35] K. Ma, F. Tang, J.M. Schoenung, Investigation into the effects of Fe additions on the equilibrium phase compositions, phase fractions and phase stabilities in the Ni-Cr-Al system, Acta Mater. 58 (2010) 1518–1529.
[36] M. Bai, B. Song, L. Reddy, T. Hussain, Preparation of MCrAlY–Al_2O_3 Composite Coatings with Enhanced Oxidation Resistance through a Novel Powder Manufacturing Process, J. Therm. Spray Technol. 28 (2019) 433–443.
[37] B. Rajasekaran, G. Mauer, R. Vaßen, Enhanced characteristics of HVOF-sprayed MCrAlY bond coats for TBC applications, J. Therm. Spray Technol. 20 (2011) 1209–1216.
[38] S. Deshpande, S. Sampath, H. Zhang, Mechanisms of oxidation and its role in microstructural evolution of metallic thermal spray coatings - Case study for Ni-Al, Surf. Coatings Technol. 200 (2006) 5395–5406.
[39] H. Wang, Y. Liu, X. Ning, Q. Wang, F. Wang, D. Chen, The influence of milling parameters on the characteristics of milled and spray-dried NiCoCrAlY–Al_2O_3 composite powders, Powder Metall. 60 (2017) 15–21.
[40] P. Richer, M. Yandouzi, L. Beauvais, B. Jodoin, Oxidation behaviour of CoNiCrAlY bond coats produced by plasma, HVOF and cold gas dynamic spraying, Surf. Coatings Technol. 204 (2010) 3962–3974.
[41] C. Borchers, T. Stoltenhoff, M. Hahn, M. Schulze, H. Assadi, C. Suryanarayana, F. Gärtner, T. Klassen, Strain-induced phase transformation of MCrAlY, Adv. Eng. Mater. 17 (2015) 723–731.
[42] H.Y. Wang, D.W. Zuo, M. Di Wang, G.F. Sun, H. Miao, Y.L. Sun, High temperature frictional wear behaviors of nano-particle reinforced NiCoCrAlY cladded coatings, Trans. Nonferrous Met. Soc. China (English Ed. 21 (2011) 1322–1328.

Available online at www.jourcc.com

Journal homepage: www.JOURCC.com

Journal of Composites and Compounds

Electrical properties of polymer blend composites based on silicone rubber/EPDM/clay hybrid for high voltage insulators

Leila Bazli [a], Sara Eskandarinezhad [b], Naresh Kakur [c], Velmurugan Ramachandran [d], Alejandro Bacigalupe [e], Marcela Mansilla [e,f], Mariano Escobar [e,f]*

[a] *Rubber Group, Iran Polymer & Petrochemical Institute, Nano and Smart Polymers Center of Excellence, Tehran-Karaj Hwy, Iran*
[b] *Department of Mining and Metallurgy, Yazd University, Yazd, Iran*
[c] *Department of Mechanical Engineering, Indian Institute of Technology Madras, Chennai, India*
[d] *Department of Aerospace Engineering, Indian Institute of Technology Madras, Chennai, India*
[e] *Center of Advanced Materials, National Institute of Industrial Technology (INTI), Buenos Aires, Argentina*
[f] *National Scientific and Technical Research Council (CONICET), Buenos Aires, Argentina*

ABSTRACT

Silicone rubber (SR) and ethylene-propylene-diene monomer (EPDM) are widely-used polymers as housing for high voltage insulators. In this work, SR/EPDM/clay nanocomposites were obtained by two-roll mill mixing for outdoor polymeric insulators. Morphology, dielectric properties, dielectric breakdown strength (DBS), and surface and volume resistivity of different weight contents of nanoclay (Cloisite 15A) incorporated in SR, EPDM, and SR/EPDM hybrid nanocomposites were characterized. In addition, the distribution of breakdown voltages was fit to the distribution of Weibull and estimated the scale and shape parameters. The polar groups of the clay particles enhanced the polarization capability of the nanocomposites. Moreover, DBS results showed an enhancement of the dielectric strength proportional to clay content. Finally, the surface and volume resistance of all nanocomposites decreases but maintains very high electrical resistance. The experimental data presented in this study will be useful for designing and manufacturing the outdoor insulators.

Peer review under responsibility of jourcc

ARTICLE INFORMATION

Article history:
Received 26 January 2021
Received in revised form 22 February 2021
Accepted 25 March 2021

Keywords:
EPDM
Silicone rubber
Clay
Nanocomposite
Dielectric properties

1. Introduction

In dry environments, fiberglass has a high mechanical and electrical performance. Nevertheless, under humid conditions, it retains moisture and serves as a weak insulator [1]. Because of its potential to have enhanced thermal, electrical, and mechanical characteristics and offering promising properties related to each component [2-6], polymer nanocomposites design is an exciting field of advanced science [7]. While employing polymer nanocomposites in the electrical insulating technology sector has started recently, due to their strong dielectric capabilities, lightweight, better pollution efficiency, low price, and easy production, polymeric materials have provided various benefits to external insulation systems [8].

Silicon rubber (SR), ethylene-propylene-diene monomer (EPDM), and ethylene-propylene rubber (EPR) are widely used polymeric components for electrical insulators. Notably, owing to affordable price, a high percent of elongation, being lightweight, thermal resilience, and improved wear resistance, the use of EPDM rubber materials has been expanded in tire sidewalls, wires, vibration, and noise isolation, cables, and outdoor insulation system products. It also exhibits superior temperature, oxygen, and ozone resistance [9, 10]. However, because of its low rigidity, EPDM rubber cannot be employed for primary structural uses without including fillers such as carbon nanotubes (CNTs) or clay particles [2, 11]. Insulators made of SR exhibit excellent characteristics of hydrophobicity transference in action. As a result, SR insulators exhibit high electrical efficiency in damp and contaminated areas and they are commonly used in toxic settings. However, they struggle with cost, mechanical characteristics, and resistance to tracking [12, 13]. The electrical and mechanical characteristics of EPDM/SR blends in various proportions were analyzed by Raja Prabhu et al. [14]. In addition to dissipation factor, due to silicone's low freezing temperature, low surface tension, and high oxidation resistance, an improvement in electrical properties including tracking resistance, comparable tracking index, dielectric constant, and surface and volume resistivity was observed with increasing amounts of SR. Due to their promising mechanical and physical characteristics, rubber/layered silicate (such as montmorillonite (MMT)) nanocomposites have recently attracted much interest . The distribution of MMT clay particles could lead to either exfoliated and/or intercalated structures in the polymer matrix [15]. Rana et al. [9] studied the crystallographic, thermal, electrical, and mechanical behavior of out-

* *Corresponding author: Leila Bazli; E-mail: leilabazli64@gmail.com*
https://doi.org/10.52547/jcc.3.1.3

door insulating EPDM/clay nanocomposites and found that these qualities are improved by incorporating clay into the composite. Vijayalekshmi [16] studied the mechanical, electrical, and thermal characteristics of organically modified MMT (OMMT) clay distributed in an EPDM/SR (50:50) blend nanocomposites with variable clay content (1, 3, 5 and 7 phr). Increasing OMMT loading to 5 phr was shown to improve electrical and mechanical properties, and a further increase in the filler content led to the reduced properties, which could be related to a low particle dispersion at high clay loadings. Although there are some studies on mechanical and electrical properties of EPDM/SR/clay nanocomposites, to the best of our knowledge, limited researches were made to characterize the electrical and dielectric properties of nanocomposites based on EPDM, SR, and hybrid SR/EPDM matrices [17, 18]. Therefore, the main purpose of the present study is to compare the electrical and dielectric characteristics of these blend composites for high-voltage insulators.

2. Materials and method

2.1. Materials

Vinyl methyl siloxane (HD-9170, Hongda Co., Ltd, China) was the employed silicone rubber. The hardness and density of SR were 70 (Shore A) and 1.18 g/cm^3, respectively. EPDM (commercial name: KEP 270) was supplied from Kumho Polychem Co., Ltd., Korea; its Mooney viscosity (ML (1 + 4) at 125 °C) was 70 along with a density of 0.86 g/cm^3, with a 4.5%ethylene norbornene content and ethylene content of 57.0%. Dicumyl peroxide (DCP; Hercules Inc., USA) with 98% purity was used as the curing agent and the nanoclay was Cloisite 15A fabricated by Southern Clay, USA.

2.2. Preparation of the samples

To prepare the samples, EPDM gum was first softened on a two-roll mill manufactured by Polymix 200L, Schwabenthan, Germany, for 3 min at 50 °C (rotor speed=15 rpm, friction ratio=1.6), followed by the SR addition and blending for a further 3 min. Subsequently, the addition of 3, 6, or 9 phr nanoclay and mixing for 3 min were done. Eventually, 1 phr of DCP was added for 2 min. In a 100-ton hydraulic hot press fabricated by Bucher, Switzerland, the mixture was molded by compression and cured for 15 min at 160 °C. Specimens were later post-cured at 150 °C for 2 hours in an oven. Prior to testing, the samples were allowed to rest for 24 h at 25°C. Table 1 presents the composition and coding of the nanocomposites.

Table 1.
Composition of the composites

Sample code*	EPDM	SR	Cloisite 15A
Q100C0	0	100	0
Q100C3	0	100	3
Q100C6	0	100	6
Q100C9	0	100	9
E100C0	100	0	0
E100C3	100	0	3
E100C6	100	0	6
E100C9	100	0	9
Q70E30C0	30	70	0
Q70E30C3	30	70	3
Q70E30C6	30	70	6
Q70E30C9	30	70	9

*Curing of all the samples was performed with 1 phr of DCP

2.3. Microstructural studies

Microstructural images were obtained from cross-sections of different samples fractured in liquid nitrogen by a VEGA TESCAN scanning electron microscope (SEM), operating at 10 kV. An ion-sputter device was employed to gold-coat the specimens in order to minimize charging and enhance electrical conductivity.

2.4. Surface and volume resistivity

The measurements of the surface and volume resistivity of the nanocomposites were performed by a high-insulation resistance meter device from Shanghai Precision & Scientific Instrument Co., Ltd, following the procedure indicated in the IEC 60093 standard, The determination of surface resistivity was done by placing the electrodes on the surface and volumetric resistivities were measured applying 500 V for 60 s to the opposite surfaces of the samples. Specific volume resistance was calculated by the following equation (Eq. 1):

$$\rho = R_x \frac{A}{h} \quad (1)$$

where R_x, A, and h denote the measured resistance, surface area of the electrode, and thickness of the specimen, respectively.

2.5. Dielectric properties

Dielectric spectroscopy specifies the dielectric characteristics of materials, including permittivity (ε') and loss tangent (tan δ), based on the interaction of the applied field and the specimen's internal electric dipole moments. Dielectric properties were measured in an E4980A Precision LCR meter (Agilent Technologies, Inc.). The ε' and tan δ of the nanocomposites were assessed at low frequency (50 Hz).

2.6. Dielectric breakdown strength

The characterization of the DBS was carried out according to IEC 60243-1 using a semiautomatic dielectric test set (DTS90, BAUR), equipped with copper parallel plates as electrodes. For the room temperature estimation, insulating oil was used as an embedding medium. Between the two electrodes, the specimen with a thickness of 1 mm was held, and an incremental alternating voltage of 3 kV/s was applied until the specimen could no longer withstand the flow of current, therefore the electrical breakdown takes place. The breakdown voltage was determined as the value at which the electric breakdown (represented by sparking) occurs. Notice that all of the reported values were the peak voltage (Vp). For every sample, 20 different locations were measured.

3. Results and discussion

3.1. Microstructural studies

As shown in our previous report [19], nanoclay was efficiently distributed and due to good compatibility between EPDM rubber chains and Cloisite 15A surfactant (2M2HT1), an exfoliated morphology was obtained in the dispersed EPDM phase. Consequently, higher filler-rubber interaction leads to clay migration into the EPDM phase by blending, enhancing its elasticity. The polarity differences between Cloisite 15A and SR, on the other hand, caused nanoclay particles to become agglomerated. As shown in Fig. 1, In the Q70E30C0 sample that is a blend of SR and EPDM blend has a droplet-matrix morphology and good dis-

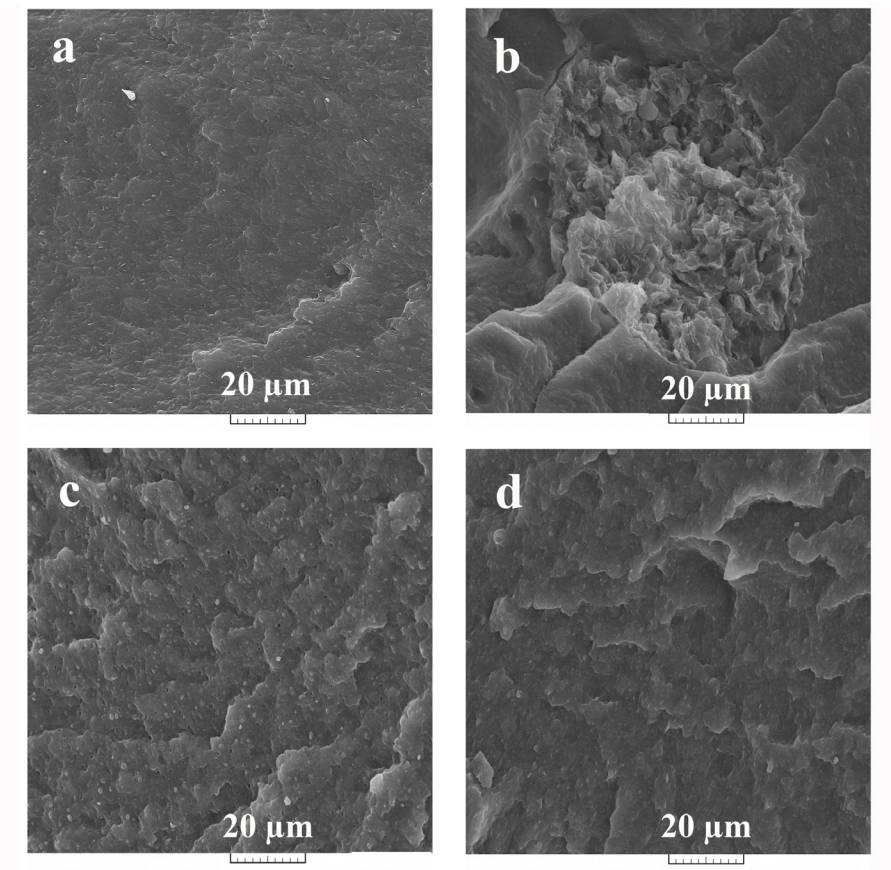

Fig. 1. SEM images of the samples, a) E100C9, b) Q100C9, c) Q70E30C0, d) Q70E30C9.

persion of EPDM is observed in the SR matrix. The incorporation of nanoclay filler into the SR/EPDM blend led to an enhanced distribution of the dispersed phase of EPDM in the SR matrix (Q70E30C9). The stabilization effect of the nanoclay in the blend could be inferred to be the result of a decrease in interfacial tension; moreover, the rigid layer of nanoclay prohibits the dispersed droplets from coalescing through steric hindrance [20, 21].

The change from spherical EPDM droplets to oval shapes could be described by the relationship of elasticity and viscosity of the phases. The morphology evolves towards a co-continuous configuration because of the nanoclay presence in the dispersed phase and matrix and the consequent drop in viscosity. Additionally, owing to their high interactions, the trapping of nanoclay in EPDM led to an increase in the elasticity of this phase, a decrease in shape relaxation associated with the droplets, and maintaining the oval-shaped droplets. Therefore, nanoclay showed a potential compatibilizing effect in these nanocomposites [22].

3.2. Surface and volume resistivity

Besides analyzing the electrical performance of different components to define industrial applications, the electrical characterization can be used as a suitable complement to study the molecular behavior of polymers, as well as their thermal and optical properties in combination with mechanical properties. The key electrical properties that determine the characteristics of insulating material are dielectric constant, dielectric strength, and surface and volumetric resistance.

As observed in Fig. 2, the surface and volume resistance of all samples were decreased with increasing filler content but were still maintaining a high value. No polymer is entirely free of conduction mechanism; therefore, all of them are able to have a low number of charge carriers. Conduction is often carried out by impurities that introduce charge carriers in the form of electrons or ions. Therefore, the addition of impurities such as clay, which can supply ions and electrons in the bulk of materials, reduces its electrical resistance. In addition, the electrical resistance of EPDM is about 10 times that of SR, and adding it to the mixture increases its electrical resistance. Khodaparast et al. [23] reported that the reason for the decrease in electrical resistance of TiO_2/PVDF nanocomposite obtained from in situ method compared to commercial nanocomposite was the presence of ion and electron supply introduced from impurities left by the sol-gel method. By studying the electrical properties of EPDM and clay nanocomposites, Kang et al. [24] showed that the addition of impurities plays an important role in electrical conductivity.

Hidayah et al. [25] observed that the addition of nanofillers reduced the volume resistivity of low-density polyethylene (LLDPE)/SR nanocomposites, regardless of the kind of filler. The volume resistivity of all forms of nanocomposites also decreased significantly with increasing SR content. Nevertheless, the addition of a larger amount of nanofiller had a negligible influence on its volume resistivity. Rajini et al. [26] produced reinforced hybrid polyester composites using coconut sheath/clay. The findings revealed that resistivity values were reduced with the inclusion of MMT nanoclay. It was discussed that, owing to the conductive properties of crystalline clay materials, the inclusion of clay allows the movement of electrons in the clay/polyester blend.

3.3. Dielectric constant

According to Fig. 3, the dielectric constant of all nanocomposites has increased with the increase of nanoparticles due to the high number of polar groups and the increase of polarization capability. Applying an electric field to a polymer causes the redistribution of any charge on the polymer, which makes them mobile enough to respond within the period of the applied field. If some moving charges can penetrate through the sample and migrate through the interface of sample and electrode, a DC conduction is often created, and if the penetration of moving charges under the field is spatially limited, polymers can be polarized by the field and DC conduction is not observed. The dielectric constant (ε') of a material is the relationship between the capacity of a capacitor in

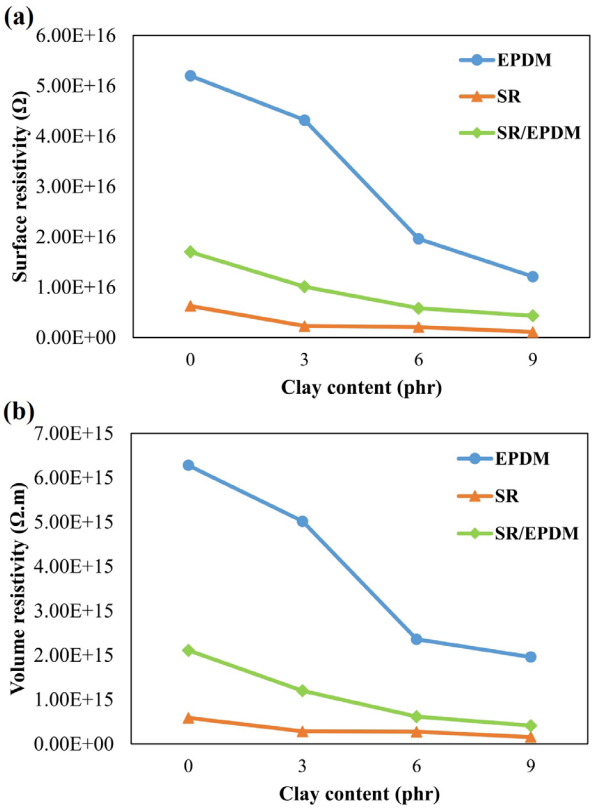

Fig. 2. The surface and volume resistance of samples.

the presence of that material and the same capacitor in the vacuum. The capacity of a capacitor measures its ability to store charges. For a non-polar material, the increase in capacity is related to the charges on the capacitor, which polarizes the molecules and absorbs the positive charges on the molecules at one end and the negative charges at the other end, resulting in an increase in charges on the surface. Therefore, the greater the polarization capacity of the molecules, the greater the dielectric constant of the material. The improvement in nanocomposite dielectric features attributed to the addition of nanoclays depends on the quality and proportion of the nanoclay [27]. The filler is polarized by the introduction of an external electric field, causing a charge disturbance in the nanoclays. In this situation, on the surface of the filler, the charge carriers could be redistributed, and hence the nanocomposite interface becomes polarized, resulting in interfacial polarization. The density of the interfacial polarized electrical charge relies on both the filler and matrix properties.

Khodaparast et al. [23] also observed that a better filler distribution and no agglomeration in the samples increased the effective interface between the nanoparticles and the polymer, and there is evidence that a greater interface formed between the filler and polymer chains leads to increased dielectric constant and it can trap charge carriers. Su et al. [28] reported the improvement of dielectric constant in EPDM composites filled with graphite flakes due to interfacial polarization. Razzaghi et al. [29] worked on SR/clay nanocomposites and showed an increase in the dielectric constant by the addition of nanoclay due to the interfacial polarization between clay and SR. Arya et al. [30] also reported the improvement of the dielectric constant by adding MMT to polymer nanocomposite films based on blend poly(ethylene oxide)-polyvinyl chloride (PEO-PVC).

Clay-filled SR composites were designed by Sarkarat et al. [31] and their electrical characterizations revealed that the neat SR dielectric constant was about 2.9 over the frequency spectrum implemented. The relaxation peak in the dielectric loss was detected along with an increase in

Table 2.
Weibull parameters for the composites

Samples	Scale parameter α (V)	Shape parameter β	R^2
Q100C0	2.87	9.33	0.97
Q100C9	3.00	8.09	0.87
E100C0	3.57	8.49	0.96
E100C9	3.63	19.14	0.95
Q70E30C0	3.08	10.98	0.97
Q70E30C9	3.20	14.35	0.95

dielectric permittivity at a frequency <100 Hz with the inclusion of 2.5 % of clay in the SR mixture. Rana et al. [9] also found that the conductivity values and dielectric constant of nanocomposites are higher than those of neat EPDM rubber. Thus, it has been shown that adding clay to rubber matrices improves the electrical characteristics.

3.4. Dielectric breakdown strength

Fig. 4 illustrates the dielectric strength (dielectric breakdown) of the composites. As mentioned above, in insulating materials, a low level of conduction can exist in different ways. This is usually due to the presence of impurities that introduce low charge carrier concentrations, such as ions or electrons, into materials. In strong electric fields, new charge carriers may also be injected into the polymer by the electrodes, hence, with the increase in voltage, the current will increase more rapidly compared to what is expected based on Ohm's law. In very intense fields, this phenomenon, besides other processes, often leads to surface conduction and hence, the complete polymer failure as a dielectric material (dielectric breakdown). The maximum voltage that a dielectric material is able to tolerate for a long time without failure is known as dielectric strength and can be defined as the voltage divided by the thickness of the material. In other words, dielectric strength is the maximum electric field that the material can withstand indefinitely. As Fig. 4 shows, increasing the amount of clay increases the dielectric strength of the nanocomposites. This can be explained by the fact that more obstacles and traps are created in the path of space charges. Spatial charge in a dielectric material means the accumulation of electric charges near its interface with the electrode. The accumulation of charge creates an internal electric field and reduces the current. Electrons can be trapped in a solid, therefore, trapping more charges in the material results in increasing the opposite electric field, and reducing the flow of electrons from the electrode to the material, thus increasing the dielectric strength [32, 33].

The scheme of the spatial charge phenomenon is shown in Fig. 5. Since EPDM has a higher dielectric strength than SR (almost double), its addition to SR has significantly enhanced the blend's dielectric strength and nanocomposite. Dong et al. [32] reported that increasing the amount of TiO_2 nanoparticles in silicon rubber reduced the electrical resistance due to the increase of the impurity content by introducing ions and electrons in the polymer matrix. Additionally, the dielectric strength increased due to the increase of obstacles in the way of electrons and, consequently, the increase of the space charge. Also, Hidaya et al. [25] reported that the DBS of LLDPE/SR loaded with Si, BN, and Zn nanofillers are better in all blended formulations relative to the related compositions without nanofillers. Dutta et al. [34] studied polyethylene octene elastomer/ethylene-vinyl acetate copolymer (POE/EVA) reinforced with organoclay particles. The findings revealed that the nanocomposite containing 0.5 wt% of organoclay showed an improvement in the breakdown voltage value from 6 kV to 10 kV. Besides, Shah et al. [35]

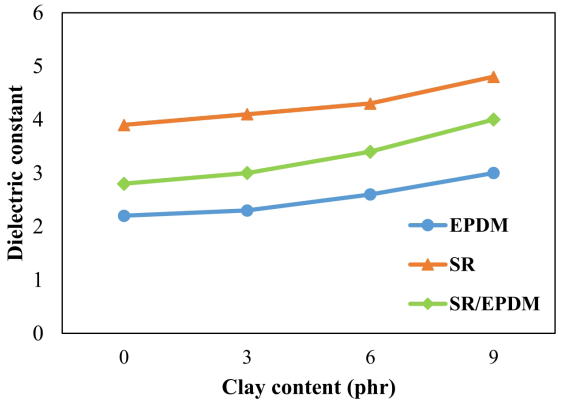

Fig. 3. The dielectric constant of the nanocomposites.

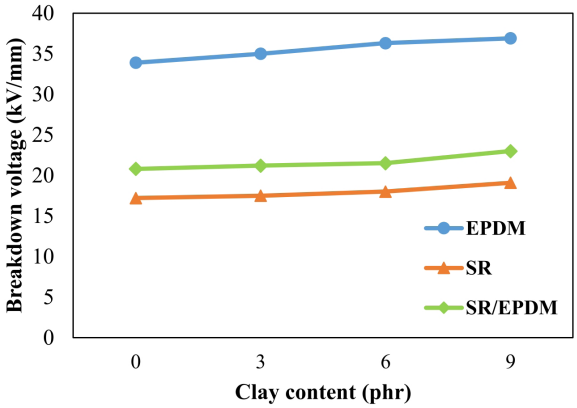

Fig. 4. The dielectric strength (dielectric breakdown) of the nanocomposites.

observed a noticeable increase in high-density polyethylene (HDPE) dielectric breakdown strength from 33 kV/mm to 68 kV/mm after processing organic clay with the mixture of titanate and silane coupling agents.

The distribution of breakdown voltages was fit to the distribution of Weibull. The value F is the Weibull cumulative distribution function, which [36, 37] is obtained from Eq. 2:

$$F(V_{BD}) = 1 - \exp[-(\frac{V_{BD}}{\alpha})] \quad (2)$$

where the scale parameter of α denotes the voltage at which 63% of all capacitors have broken down, and the Weibull module indicating the distribution width is represented by the shape parameter β. Usually, by taking two logarithms, the function of Weibull cumulative distribution is rearranged as:

$$lnln\left[-lnln(1-F)\right] = \beta lnln(V_{BD}) - \beta lnln\,\alpha \quad (3)$$

Using Eq. 3, the y-intercept (-β ln α) and slope (β) are easily measured from a plot of ln[-ln(1- F)] versus ln (V_{BD}). Results that match the distribution of Weibull would fall along a line (Fig. 6). As reported in Table 2, linear regression was utilized to evaluate alpha and β for the specimens. For low probability events (low V_{BD}), the transformed data inspection indicates deviations from the Weibull distribution. This tail, which comprising below 10% of the results, could imply the presence of a separate low-voltage breakdown dominant mechanism or the presence of a threshold voltage under which the samples do not experience a breakdown.

The competitive advantage associated with nanocomposites may be

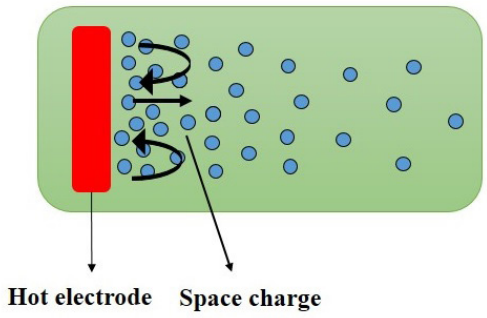

Fig. 5. Schematic of the spatial charge phenomenon.

described by the nanofiller effect, which was assumed to interfere with the consistency of the pathway given to the charge carriers, leading to increased breakdown strength. The significant number of small particles and the vast interfacial area could also serve as scattering sites for electrons, decreasing their momentum and raising the breakdown voltage [38]. The decrease in the inner bulk charge in the nanocomposite structure may also be a potential explanation for enhancing the DBS of SR/EPDM nanocomposite after nanofillers have been added. It was attributed to the addition of a regional conducting route by the overlap of nanometric double layers or localized charge flow. This could keep inner localized fields low and help to increase DBS [39].

The most remarkable point was that the Weibull shape variable, β, was increased for the nanocomposites, as shown in Table 2. The findings indicate that in nanocomposites rather than the unfilled SR/EPDM blend, a less disparate or relatively consistent dielectric breakdown process happened indicating an improvement in the uniformity of the sample (material with a lower weak point, typically composed of macrovoids). The existence of nanoclays could have pervaded the formed voids in the SR/EPDM. Li et al. [40] reported that the incorporation of aligned nanoplatelet fillers, in addition to any enhancements attributable to the crystal orientation, produced an extra and complementary boost in the dielectric breakdown strength. Thus, in the nanostructured matrix, with the coordinated fillers and arranged polymer crystals functioning as a macroscopic shield formed across the specimen, a significantly enhanced breakdown strength could be achieved. The findings of Hiziroglu et al. [41] also showed that the breakdown strength of the natural polypropylene filled with nanoclay was greater than that of the unfilled polypropylene, and the optimal nanoclay density tended to be 2% by weight. A substantial variation in DBS value was found from the findings of the nanocomposite specimens produced by various blending processes. The DBS value has been found to be overly reliant on the relative dispersion of nanofillers in the composite mixture [14]. Furthermore, it is commonly assumed that new gaps or defects can be formed into polymers by introducing nano-or micro-particles [42]. Therefore, to boost DBS, it is crucial to monitor the distribution of nanofillers when they are introduced into the composite.

4. Conclusions

SR, EPDM, and SR/EPDM hybrid nanocomposites containing organically modified clay (Cloisite 15A) were developed. Thus, the specimen morphology, surface and volume resistivity, and dielectric properties of different SR/clay, EPDM/clay, and SR/EPDM/clay hybrid nanocomposites were studied. The findings were as follows:

The addition of nanoclay leads to a fine EPDM distribution in the SR matrix. The stabilization effect of the nanoclay is followed by an interfacial tension reduction; also, the rigid layer of nanoclay prohibits the dispersed droplets from coalescing and offers steric hindrance.

If the filler content increases, the volume and surface electrical resis-

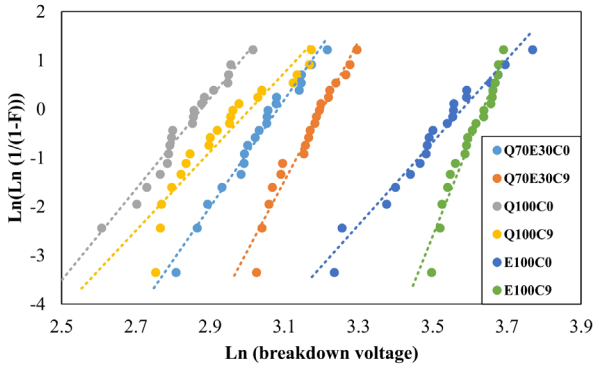

Fig. 6. Weibull distribution of breakdown voltages of the nanocomposites.

tance of all specimens are reduced, but they still maintain fairly strong electric resistance. The presence of impurities, including clay, which can provide the bulk of materials with electrons and ions, decreases their electrical resistance.

The increase in polar groups produced by a larger quantity of nanoparticles increases the dielectric constant of all nanocomposites.

An increase in the clay content improves the dielectric strength of the nanocomposite since the route of space charges develops more barriers and traps. In a dielectric substrate, spatial charging implies the storage of electrical charges along with its electrode interface.

REFERENCES

[1] D. Tsalagkas, Z. Börcsök, Z. Pásztory, Thermal, physical and mechanical properties of surface overlaid bark-based insulation panels, European Journal of Wood and Wood Products 77(5) (2019) 721-730.

[2] A.S. Rana, M.K. Vamshi, K. Naresh, R. Velmurugan, R. Sarathi, Effect of nanoclay on mechanical, thermal and morphological properties of silicone rubber and EPDM/silicone rubber hybrid composites, Advances in Materials and Processing Technologies (2020) 1-8.

[3] J. Sun, F. Cai, D. Tao, Q. Ni, Y. Fu, Enhanced Thermal Insulation of the Hollow Glass Microsphere/Glass Fiber Fabric Textile Composite Material, Polymers 13(4) (2021) 505.

[4] P. Abasian, M. Radmansouri, M.H. Jouybari, M.V. Ghasemi, A. Mohammadi, M. Irani, F.S. Jazi, Incorporation of magnetic NaX zeolite/DOX into the PLA/chitosan nanofibers for sustained release of doxorubicin against carcinoma cells death in vitro, International journal of biological macromolecules 121 (2019) 398-406.

[5] M. Radmansouri, E. Bahmani, E. Sarikhani, K. Rahmani, F. Sharifianjazi, M. Irani, Doxorubicin hydrochloride-Loaded electrospun chitosan/cobalt ferrite/titanium oxide nanofibers for hyperthermic tumor cell treatment and controlled drug release, International journal of biological macromolecules 116 (2018) 378-384.

[6] L. Bazli, M.H. Bagherian, M. Karrabi, F. Abbassi-Sourki, H. Azizi, Effect of starch ratio and compatibilization on the viscoelastic behavior of POE/starch blends, Journal of Applied Polymer Science 137(29) (2020) 48877.

[7] B.F. Dizaji, M.H. Azerbaijan, N. Sheisi, P. Goleij, T. Mirmajidi, F. Chogan, M. Irani, F. Sharafian, Synthesis of PLGA/chitosan/zeolites and PLGA/chitosan/metal organic frameworks nanofibers for targeted delivery of Paclitaxel toward prostate cancer cells death, International Journal of Biological Macromolecules 164 (2020) 1461-1474.

[8] J.E. Contreras, E.A. Rodriguez, J. Taha-Tijerina, Recent trends of nanomaterials for high-voltage applications, Handbook of Nanomaterials for Industrial Applications, Elsevier2018, pp. 724-738.

[9] A.S. Rana, M.K. Vamshi, K. Naresh, R. Velmurugan, R. Sarathi, Mechanical, thermal, electrical and crystallographic behaviour of EPDM rubber/clay nanocomposites for out-door insulation applications, Advances in Materials and Processing Technologies 6(1) (2020) 54-74.

[10] S. Bhavya, U. Mahesh, R. Velmurugan, R. Sarathi, Comparative Study of Nano and Micro Fillers in EPDM/Silicone Rubber for Outdoor Insulator Application, Springer Singapore, Singapore, 2021, pp. 761-769.

[11] A.V. Shaw, P. Ketsamee, T. Andritsch, A.S. Vaughan, Effect of organoclay loading on the dielectric properties and charge dynamics of a PP-rubber nanocomposite, High Voltage 5(6) (2020) 662-668.

[12] L. Bazli, A. Khavandi, M.A. Boutorabi, M. Karrabi, Correlation between viscoelastic behavior and morphology of nanocomposites based on SR/EPDM blends compatibilized by maleic anhydride, Polymer 113 (2017) 156-166.

[13] P. Song, J. Song, Y. Zhang, Stretchable conductor based on carbon nanotube/carbon black silicone rubber nanocomposites with highly mechanical, electrical properties and strain sensitivity, Composites Part B: Engineering 191 (2020) 107979.

[14] R.R. Prabu, S. Usa, K. Udayakumar, M.A. Khan, S.A. Majeed, Electrical insulation characteristics of silicone and epdm polymeric blends. i, IEEE Transactions on Dielectrics and Electrical Insulation 14(5) (2007) 1207-1214.

[15] S. Bhavya, U. Mahesh, R. Velmurugan, R. Sarathi, Comparative Study of Nano and Micro Fillers in EPDM/Silicone Rubber for Outdoor Insulator Application, Recent Advances in Mechanical Engineering, Springer2021, pp. 761-769.

[16] V. Vijayalekshmi, S.A. Majeed, Mechanical, thermal and electrical properties of EPDM/Silicone blend nanocomposites, International Journal of Engineering Research and Applications 3(2) (2013) 1177-1180.

[17] V. Vijayalekshmi, Dielectric properties of compatibilised EPDM/silicone rubber nanocomposites, Int J Eng Res Appl 7 (2017) 54-61.

[18] P. Intanoo, A. Sirivat, R. Kunanuruksapong, W. Lerdwijitjarud, Electromechanical properties of ethylene propylene diene elastomers: Effect of ethylene norbornene content, Materials Sciences and Applications 2(05) (2011) 307.

[19] L. Bazli, A. Khavandi, M.A. Boutorabi, M. Karrabi, Morphology and viscoelastic behavior of silicone rubber/EPDM/Cloisite 15A nanocomposites based on Maxwell model, Iranian Polymer Journal 25(11) (2016) 907-918.

[20] F. Fenouillot, P. Cassagnau, J.-C. Majesté, Uneven distribution of nanoparticles in immiscible fluids: Morphology development in polymer blends, Polymer 50(6) (2009) 1333-1350.

[21] L. Elias, F. Fenouillot, J.C. Majesté, G. Martin, P. Cassagnau, Migration of nanosilica particles in polymer blends, Journal of Polymer Science Part B: Polymer Physics 46(18) (2008) 1976-1983.

[22] P. Van Puyvelde, P. Moldenaers, Rheology and morphology development in immiscible polymer blends. Rheol Rev: 101–145, 2005.

[23] P. Khodaparast, Z. Ounaies, On the impact of functionalization and thermal treatment on dielectric behavior of low content TiO 2 PVDF nanocomposites, IEEE Transactions on Dielectrics and Electrical Insulation 20(1) (2013) 166-167.

[24] D. Kang, D. Kim, S.H. Yoon, D. Kim, C. Barry, J. Mead, Properties and dispersion of EPDM/modified-organoclay nanocomposites, Macromolecular materials and engineering 292(3) (2007) 329-338.

[25] N. Hidayah, M. Mustapha, H. Ismail, and Mohamad Kamarol, Journal of Elastomers & Plastics 1 (2017) 22.

[26] N. Rajini, J.W. Jappes, S. Rajakarunakaran, C. Bennet, Effects of chemical modifications and MMT nanoclay addition on transport phenomena of naturally woven coconut sheath/polyester nanocomposites, Chinese Journal of Polymer Science 31(8) (2013) 1074-1086.

[27] A. Eshraghian, M. Kamkar, M. Asgari, M. Arjmand, U. Sundararaj, X-band dielectric properties of hybrid nanocomposites of nitrogen-doped carbon nanotube/functionalized nanoclay/polyvinylidene fluoride nanocomposite, Polymer Composites n/a(n/a) (2020).

[28] J. Su, J. Zhang, Improvement of mechanical and dielectrical properties of ethylene propylene diene monomer (EPDM)/barium titanate ($BaTiO_3$) by layered mica and graphite flakes, Composites Part B: Engineering 112 (2017) 148-157.

[29] M. Razzaghi-Kashani, N. Gharavi, S. Javadi, The effect of organo-clay on the dielectric properties of silicone rubber, Smart materials and structures 17(6) (2008) 065035.

[30] A. Arya, A. Sharma, Investigation on enhancement of electrical, dielectric and ion transport properties of nanoclay-based blend polymer nanocomposites, Polymer Bulletin 77(6) (2020) 2965-2999.

[31] M. Sarkarat, M. Lanagan, D. Ghosh, A. Lottes, K. Budd, R. Rajagopalan, High field dielectric properties of clay filled silicone rubber composites, Materials Today Communications 23 (2020) 100947.

[32] Z.-M. Dang, Y.-J. Xia, J.-W. Zha, J.-K. Yuan, J. Bai, Preparation and dielectric properties of surface modified TiO_2/silicone rubber nanocomposites, Materials Letters 65(23-24) (2011) 3430-3432.

[33] T. Andritsch, R. Kochetov, P.H. Morshuis, J.J. Smit, Dielectric properties and space charge behavior of MgO-epoxy nanocomposites, 2010 10th IEEE International Conference on Solid Dielectrics, IEEE, 2010, pp. 1-4.

[34] S. Dutta, S. Sengupta, J. Chanda, A. Das, S. Wiessner, S.S. Ray, A. Bandyopadhyay, Distribution of nanoclay in a new TPV/nanoclay composite prepared through dynamic vulcanization, Polymer Testing 83 (2020) 106374.

[35] K. Shah, R. Jain, V. Shrinet, A. Singh, D. Bharambe, High density polyeth-

ylene (HDPE) clay nanocomposite for dielectric applications, IEEE Transactions on Dielectrics and Electrical Insulation 16(3) (2009) 853-861.
[36] K. Naresh, K. Shankar, R. Velmurugan, Reliability analysis of tensile strengths using Weibull distribution in glass/epoxy and carbon/epoxy composites, Composites Part B: Engineering 133 (2018) 129-144.
[37] K. Naresh, K. Shankar, R. Velmurugan, N. Gupta, Statistical analysis of the tensile strength of GFRP, CFRP and hybrid composites, Thin-Walled Structures 126 (2018) 150-161.
[38] I. Hidayah, M. Mariatti, H. Ismail, M. Kamarol, Effect of selective localization on dielectric properties of boron nitride nanofiller filled linear low density polyethylene (LLDPE)/silicone rubber (SR) blends, Polymer Testing 56 (2016) 131-139.
[39] M. Takala, Electrical insulation materials towards nanodielectrics, (2010).
[40] B. Li, P.I. Xidas, E. Manias, High Breakdown Strength Polymer Nanocomposites Based on the Synergy of Nanofiller Orientation and Crystal Orientation for Insulation and Dielectric Applications, ACS Applied Nano Materials 1(7) (2018) 3520-3530.
[41] H.R. Hiziroglu, I.E. Shkolnik, Electrical characteristics of polypropylene mixed with natural nanoclay, Polymers 10(9) (2018) 942.
[42] L. Gong, S.-h. Chen, Y. Yu, B. Yin, M.-b. Yang, Breakup promotion of deformed EPDM droplets by the migration of nanoparticles during extrusion, Polymer Testing 86 (2020) 106445.

Available online at www.jourcc.com

Journal homepage: www.JOURCC.com

Journal of Composites and Compounds

A review on the synthesis of the TiO_2-based photocatalyst for the environmental purification

Naghmeh Aboualigaledari [a], Mohammad Rahmani [b]*

[a] *Department of Nanoscience, Joint School of Nanoscience and Nanoengineering (JSNN), University of North Carolina at Greensboro, Greensboro, North Carolina, United States*

[b] *Department of Chemical Engineering, Amirkabir University of Technology, Tehran, Iran*

A B S T R A C T

TiO_2 as a photocatalyst has been widely investigated and applied in many fields such as fuel cells, sterilization, and environmental decontamination. Some efforts, such as operation pa-rameters, synthesis techniques, and improvements by doping have been made to improve its performance. To have a photocatalyst with high photocatalytic activity for environmental purification, the most important step is to know about the synthesis methods and the pa-rameters and conditions that lead to preparing a highly photocatalytic active photocatalyst. This article paves the way in selecting the best synthesizing technique. In this article, the most common synthesis techniques of TiO_2-based photocatalysts, including sol-gel, hydro-thermal, solvothermal, chemical vapor deposition, and physical vapor deposition have been reviewed. The most important results that have been achieved in the field of synthesis were collected.

Peer review under responsibility of jourcc

A R T I C L E I N F O R M A T I O N

Article history:
Received 27 December 2020
Received in revised form 21 February 2021
Accepted 27 February 2021

Keywords:
TiO_2-based photocatalyst
Liquid-phase processing
Physical production techniques
Environmental application

Table of contents

1. Introduction 25
2. Synthesis method 26
2.1. Sol-gel method 26
2.1.1. Modified sol-gel method 27
2.1.2. Preparation of photocatalysts with sol-gel method 27
2.2. Hydrothermal method 28
2.2.1. Photocatalysts preparation via hydrothermal method 30
2.3. CVD method 31
2.3.1. Preparation of photocatalysts by CVD method 35
2.4. PVD method 35
2.4.1. Pulsed laser deposition (PLD) 36
2.4.2 Electron-beam and ion-assisted electron-beam evaporation 36
2.4.3 Magnetron and reactive magnetron sputtering 36
2.4.4 Preparation of photocatalysts by PVD Method 36
3. Conclusions 37

1. Introduction

In the last decades, environmental purification has been one of the major challenges facing researchers [1-3]. Among the various methods used for environmental purification, semiconductor photocatalysis has been known as an effective and environmentally friendly method. TiO_2 has received increasing attention for photocatalysts application due to its nontoxicity, low cost, high oxidation power, and high chemical stability [4-25].

The recent nanotechnology development has shown that nanomaterials like nano-sized TiO_2 photocatalysts can exhibit high performance in environmental purification. A fast-developing field in environmental engineering is TiO_2 heterogeneous photocatalyst which has excellent potential for environmental purification. Fujishima and Honda discovered the photocatalyst performance of TiO_2 with the application of TiO_2-anode in the hydrolysis of water to hydrogen and oxygen [26, 27].

The metal of TiO_2 is present in nature in various forms. The oxygens of TiO_2 have three various molecule structures including brookite, anatase, and rutile. Rutile is a pigment in white paints that has revealed

* *Corresponding author: Naghmeh Aboualigaledari; E-mail: naghmeh.abuali@gmail.com*
https://doi.org/10.52547/jcc.3.1.4

low photocatalytic performance, and anatase is more favorable in using as the photocatalytic cell. UV-light with 387 nm wavelength or lower is required for applying anatase.[28]

Air conditioning (air purification), water purification, white tents, tunnel lightning, mirrors (anti-condensation), textile (anti-odor), ceramic tiles (self-cleaning, antibacterial), and self-cleaning glazing are some of the application of TiO_2 as photocatalyst. In addition to anti-septical action and air purifying in which the pollutants are reduced or oxidized, it is also used to prepare a self-cleaning material. This is because of the high surface hydrophilicity of TiO_2 which is the result of activation by UV-light [29].

Up to now, different methods have been reported to prepare TiO_2 and TiO_2-based photocatalyst, including physical vapor deposition (PVD) [30], chemical vapor deposition (CVD) [31], solvothermal [32], hydrothermal [33-35], and sol-gel method [34]. Indeed, photocatalytic performance is especially influenced by some factors such as crystallinity, light adsorption ability, pore size, shape, and porosity. Since these factors are ultimately influenced by the preparation method, significant consideration should be done to study the effect of preparation methods, conditions, and parameters on photocatalytic performance [36]. Some reviews on the synthesis of TiO_2-based materials exist [37-41], the works that have been done before 2011.

In this study, we review the latest advances in both liquid-phase processing and physical production techniques. Also, the precursors, surfactants, and solvents used in the synthesis process, as well as the operating parameters of synthesis were extensively studied. The results obtained from the publications, which can help to select the promotional materials and operating parameters in the synthesis process are shown.

2. Synthesis method

2.1 Sol-gel method

The sol-gel process is a wet chemical, a low-temperature method that is used for the synthesis of various nanostructures, especially metallic oxide nanoparticles. In this method, the precursors are dissolved in solvents and then converted into a gel via hydrolysis and polycondensation reactions, with or without the use of a catalyst, under heating and stirring conditions. Inorganic metal salt, metal-organic compounds, and miscellaneous titanium-containing [42] are the most common precursors used for TiO_2 nano photocatalyst synthesis. Principally, the sol-gel process includes the following steps: (a) preparation of the initial homogeneous solution, which is consisted of dissolution of the precursors in solvents (e.g., water, alcohol, and organic solvent). Sometimes it is necessary to use the combination of two solvents with a certain ratio, to get a homogeneous solution. For example, some metal alkoxides precursors (e.g. titanium tetraisopropoxide (TTIP)) are dissolved in an organic solvent (e.g. isopropyl alcohol) that is miscible with water and then dissolved in water [43]. (b) Hydrolysis of the initial homogeneous solution by adding water, under acidic, neutral, or basic conditions to provide a sol. Hydrolysis replaces an alkoxide ligand with a hydroxyl ligand or oxo ligands. Depending on the amount of water and catalyst present, hydrolysis reaction can be complete or partial. The sol complete hydrolysis forms a rigid gel, which can be heat-treated to form powders. The sol partial hydrolysis will provide a polymeric viscous liquid, which deposited on a substrate by dip coating or spin coating and thermally processed to obtain dense crystalline films [44]. Also, when the viscosity of the sol is adjusted into a specific range, ceramic fibers are produced. (c) Conversion of sol by changing the concentration or pH of the sol into a gel which can be an integrated discrete particles network or network polymer. Generally, gelation is involved condensation of hydroxyl and/or alkoxy groups that lead to the release of water or alcohol and then polymerization. A gel that is produced from these processes is a nanostructure material. When the by-products (e.g., water or alcohol) are removed from this nanostructure via evaporation or the porosity of the gel is improved around the surfactant such as hexadecyltrimethyl, nanoporose structure material is produced. The structure of the polymeric gel can be rigid with large void area (macropores) or weak with smaller void area (micropores). Different kinds of surfactants have been used for photocatalysts preparation, for instance, polyethylene glycol sorbitan monooleate surfactant has been used for the preparation of highly porous TiO_2 films. Another type of surfactant is lauryl amine hydrochloride (LAHC), which has been used to prepare mesoporous-assembled nano titania (TiO_2) thin films [45, 46]. As a different method, the gel can be formed from stabilized sol, in which the solvent of the precursor is usually water and very fast hydrolysis happen as a result of high water/alkoxide molar ratio, in this condition the synthesized nanoparticles agglomerate very rapidly, these aggregates can be broken up by peptizing agents such as HCl or NH_3 and as a result, the colloidal suspension is produced [47-51]. Complete (Eqs. (1)-(3)) and partial condensation and hydrolysis reactions (Eqs. (4)-(6)) of titanium alkoxide precursors are described by the following reactions:

$$\text{Ti-OR}+H_2O\rightarrow\text{Ti-OH}+\text{ROH (hydrolysis)} \quad (1)$$

$$\text{Ti-OH}+\text{OR-Ti}\rightarrow\text{Ti-O-Ti}+\text{ROH (alcohol condensation)} \quad (2)$$

$$\text{Ti-OH}+\text{HO-Ti}\rightarrow\text{Ti-O-Ti}+H_2O\text{ (water condensation)} \quad (3)$$

$$Ti(OR)_n+H_2O\rightarrow Ti(OR)_{(n-1)}(OH)+\text{ROH (hydrolysis)} \quad (4)$$

$$Ti(OR)_n+Ti(OR)_{(n-1)}(OH)\rightarrow Ti_2O(OR)_{(2n-2)}+\text{ROH (alcohol condensation)} \quad (5)$$

$$Ti(OR)_{(n-1)}(OH)+Ti(OR)_{(n-1)}(OH)\rightarrow Ti_2O(OR)_{(2n-2)}+H_2O\ \text{(water condensation)} \quad (6)$$

Important factors that can affect the kinetics of the condensation and hydrolysis reactions of titanium alkoxide and titanium chlorides and will ultimately lead to the production of material with different structure, size, and morphology are water/titanium ratio, alcohol/titanium ratio, concentration, and nature of the precursors (alkoxy groups), pH, temperature, etc. According to the studies, the type of the alkoxy groups affects the size of the cluster formed [52]. The hydrolysis and diffusion rate of the alkoxides with higher alkyl groups is slow. Since polymerization is partial hydrolysis and diffusion-reaction, alkoxides with this property lead to the formation of oxide components with smaller sizes [53]. Hydrolysis and condensation rate are both influenced by pH. At acidic media, the hydrolysis reaction is improved, and hydrolysis is faster than condensation. Also, pH can influence the porosity, surface area, and pore size of the producing oxides. The water/titanium ratio has the greatest effect on the particle size and a higher water/titanium ratio leads to the faster gel formation of sol [48, 54]. (d) Aging: when the solvents are removed from the gel, keeping the pore structure stability is difficult. Normally in order to improve the strength of the links between particles, aging step, which takes a few hours or several days is necessary before draying step. (e) Drying: This step has involved the removal of solvent from the gel. There are two different methods for removing the solvent: 1- Drying the gel under ambient conditions. In this method shrinkage is obvious and the resulted material is called Xerogel which is a dense material with low porosity. 2- Drying the gel under hypercritical conditions. In this method, solid network collapse is minimized and the resulting material is called Aerogel which has high porosity. (f) Thermal treatment: To improve the structural stability and mechanical property, different kinds of thermal treatment such as sintering, densification, and calcinations are used. In a study done by Wetchakun et al, TiO_2 nanopar-

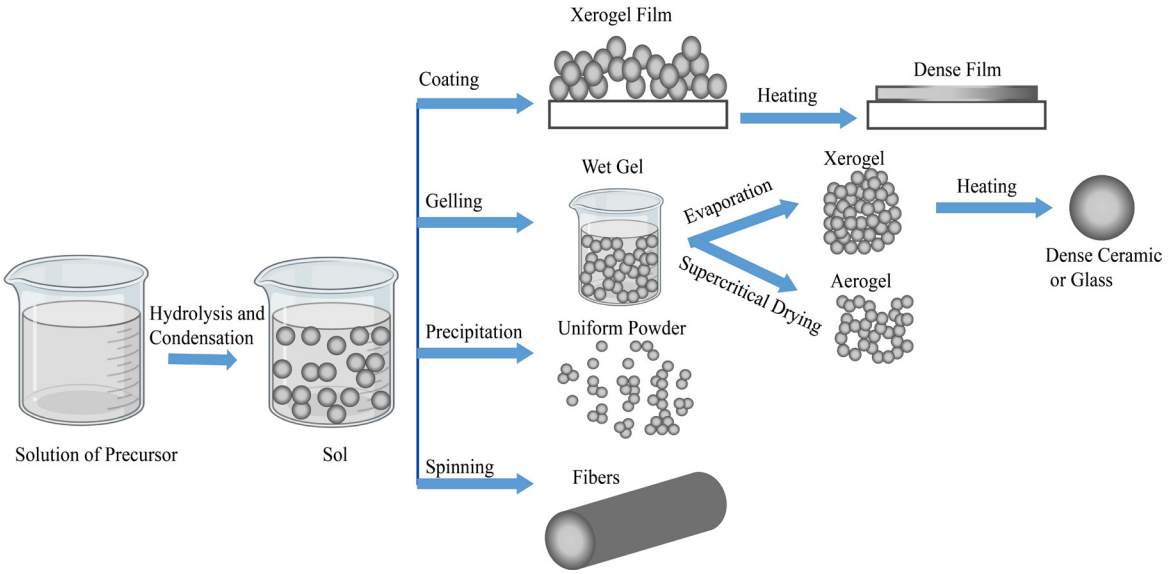

Fig. 1. Different sol-gel process steps to control the final morphology of the product.

ticles were prepared via the sol-gel method by titanium tetraisopropoxide as the titanium precursor, the results show that the calcination temperature can affect the average particle sizes of the nanoparticles and anatase to rutile transformation [55]. Different sol-gel process steps to control the final morphology of the product depicted in Fig 1.

2.1.1 Modified sol-gel method

Generally, highly reactive titanium alkoxide precursors undergo aggressive and exothermic hydrolysis reaction and condensation reaction leads to the formation of the Ti-O-Ti network. This process can lead to the precipitation of undesired phases with particles of large size and uncontrolled structure. Also in the synthesis of nanosized TiO_2 powder, the high hydrolysis rate of titanium tetraisopropoxide can cause loss of optical and photocatalytic properties of nanosized TiO_2 material [56, 57]. To control the kinetics of hydrolysis and polycondensation reactions of titanium alkoxide precursors, some modifier ligands such as a diol, the carboxylic acid (e.g. acetic acid), and diketones (e.g. acetylacetone) compounds or other complex ligands are used [58, 59]. The most common modifiers used in the modification of the titanium alkoxide precursors are acetylacetone and acetic acid. Generally, the role of modifier ligands is to chemically react with alkoxide precursors and as a result, the reactivity of precursors is modified, and a new precursor is produced. Also, the shape and size of the primary particles which formed in the sol-gel of metal alkoxides are described by the interactions on the phase boundary, that is directed to the properties of ligand [60]. Acetyl acetone is a kind of hydroxylated strong complexing ligands (SCL) that has a reactive hydroxyl group. Due to this property, the reaction between acetylacetone and titanium alkoxide precursor results in the protonation of the oxygen atom in the alkoxide ligand, and as a result alcohol and a modified alkoxide precursor are produced. The reactions of titanium tetraisopropoxide with acetylacetone (enolic form) are described in Eq. (7) [58, 60, 61]. Another modifier is acetic acid. As it is shown in Eq. (8)-(9) the reactions of titanium tetraisopropoxide with acetic acid lead to the production of new precursors. In this reaction, due to the replacement of the alkoxy groups bonded to titanium by acetate groups, Ti-OAc and ROH are formed. Modification of titanium tetraisopropoxide $Ti(O-Pr^i)_4$ with glacial acetic acid decrease the availability of groups which condense and hydrolyze easily by stable complex formation, which its structure was specified to be $Ti(OCOCH_3)(OPr^i)_2$ [58, 62]. Esterification reaction (Eq. (10)) of AcOH with alcohol leads to the releasing of water in the solution. In the esterification reaction, titanium alkoxide precursor can be hydrolyzed with water molecules through esterification reaction followed by condensation reaction to form Ti-O-Ti [63, 64]. The esterification reaction has several drawbacks for example: if the reaction is not controlled the generated water can lead to precursor condensation reaction. The hydrolysis and direct condensation reaction which is another route of the formation of Ti-O-Ti condensed bridge is described in Eqs. (11)-(12) [56-58, 65].

$$Ti(OPr^i)+x(acacH)\rightarrow Ti(OPr^i)+xPr^iOH \quad (7)$$

$$Ti(OPr^i)+AcOH\rightarrow Ti(OPr^i)(OAc)+Pr^iOH \quad (8)$$

$$Ti\text{-}OR+AcOH\rightarrow TiOAc+ROH \quad (9)$$

$$ROH+AcOH\rightarrow ROAC+H_2O \quad (10)$$

$$Ti\text{-}OAc+ROH\rightarrow ROAc+Ti\text{-}OH \quad (11)$$

$$TiOR+TiOAc\rightarrow ROAc+Ti\text{-}O\text{-}Ti \quad (12)$$

2.1.2 Preparation of photocatalysts with sol-gel method

Several investigations have been done due to the photocatalyst preparation via the sol-gel method, some of these synthesis processes are described as following:

Titanium sol was prepared by $TiCl_4$ acid hydrolysis, in this route pH of the medium was adjusted by NH_4OH, at pH=6 to 7, followed by peptization of precipitates with HNO_3. Stable titania sol was prepared at the molar ratio $[H+]/[Ti]=0.5$, 1, 1.5, and 2 with strong stirring at 70 °C for 24 h. To prepared SiO_2-TiO_2 (the content of SiO_2 was 10 wt%) nanoparticles photocatalyst, the appropriate amount of tetraethylorthosilicate (TEOS) solution was dropped in the sol of titania followed by drying and calcination at 400-700 °C for 1-3 h [66]. TiO_2 based catalyst exhibited the highest photocatalytic performance because of lowest crystallite size, highest surface area, and better crystallization, at calcination temperature of 400 °C for 3 h. The optimum condition of $[H^+]/[Ti]$ ratio is taken at 0.5. When the pH value increased from 6 to 7, this led to an increase in surface area.

Both Ni, Co, and Fe-doped TiO_2 and pure TiO_2 samples were prepared by the alkoxide route of the method of sol-gel. The precursor of TiO_2 was tetraethyl orthotitanate and the solvent was the absolute ethanol. The titanium alkoxide hydrolysis took place at room temperature with a final pH=6 of the solution. Undoped TiO_2 and 0.5, 1, and 2 wt% Co, Fe, or/and Ni-doped nanopowders of TiO_2 were synthesized. The

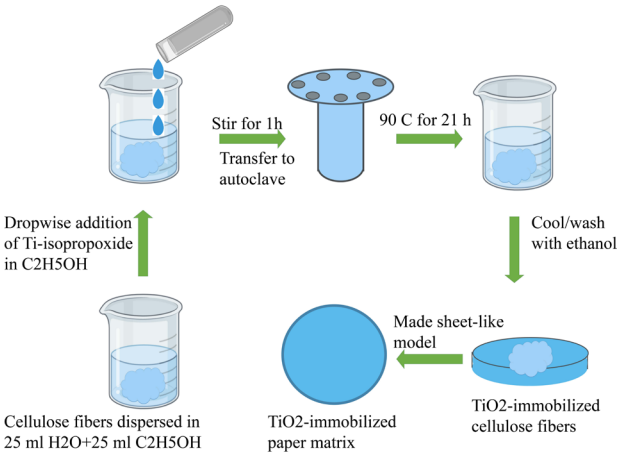

Fig. 2. Schematic diagram of a hydrothermal method.

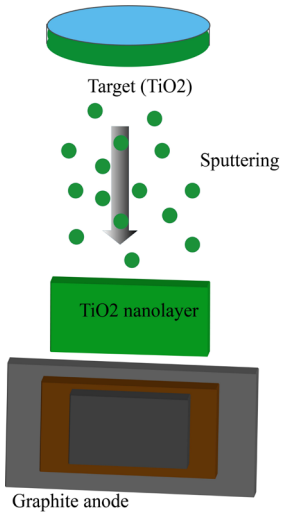

Fig. 3. Chemical vapor deposition mechanism.

compositions with 0.5 wt% dopants were chosen for this work. The prepared sols dried at 80 °C and the xerogels were thermally treated with a heating rate of 1 °C/min at 400 °C (1 h plateau). The sample with 0.5 wt% Fe dopant concentration thermally treated at 400 °C showed the best photocatalytic performance for nitrobenzene removal from water [67].

To prepare N-doped TiO_2 samples decorated with N-doped graphene, 17 mL of tetrabutyl titanate was mixed with 30 mL of ethanol with stirring for 30 min (solution A). A mixture of 28.32 mL absolute ethyl alcohol, 7.2 mL distilled water, 20 mL of acetic acid, a specified proportion of carbamide and graphene oxide with various graphene proportion of 0.5wt%, 1wt%, 3wt%, and 5wt% before adding another 20 mL of acetic acid was added to solution A with 30 min of stirring. The aging and drying condition was 24 h and100 °C, respectively. The samples were calcination at (400, 500, and 600 °C) in the furnace under the N_2 atmosphere for 2.5 h. The results suggested that N-RGO (0.5wt%)/N-TiO_2-400 °C showed the best photocatalytic efficiency for the decomposition of methylene blue (MB) [68]. In another work, the preparation of mesoporous Fe_2O_3/TiO_2 in the presence of Pluronic P123 as the structure-directing agent was done by addition of iron (III) nitrate nonahydrate (1.52 g) and titanium tetraisopropoxide (5.18 mL) into a mixture of Pluranic P123 (1 g) and ethanol (60 mL). In this method pH of the medium was adjusted by a solution of ammonia (8 mL) and distilled water (36 mL), to pH around 10. After 24 h stirring, the obtained mixture for nucleation the precipitated was hold in the dark overnight. To get a fine powder, the product was centrifuged and dried at 100 ºC and then calcination at 400 °C for 5 h in an N_2 atmosphere. Meso-30 wt% Fe_2O_3/TiO_2 showed highest photocatalytic activity for 4-chlorophenol degradation [69]. A summary of TiO_2 and TiO_2-based photocatalysts prepared via sol-gel or modified sol-gel method are reported in Table1.

2.2 Hydrothermal method

The hydrothermal synthesis can be defined as any heterogeneous reaction in an aqueous media performed at a pressure higher than 1 atm and above room temperature [70]. It should be noticed that with a non-aqueous solvent (e.g., n-butyl alcohol, ethanol, methanol, toluene, etc), the process is referred to as the solvothermal method. In comparison to the other methods, the solvothermal method involves much milder conditions and softer chemistry conducted at lower temperatures [71]. Hydrothermal and solvothermal are techniques to produce TiO_2 and TiO_2-based nano photocatalysts with different morphology such as nanosheets [72], nanofibers [73], nanotubes [74], films [75], nanoparticles [76, 77], nanorods [78, 79], powder [80, 81], and to process nanocomposites materials [82-86]. The common Ti-source used in the synthesis process of nano photocatalysts via hydrothermal and solvothermal methods are titanyl sulfate ($TiOSO_4$) [83], titanium (IV) butoxide (TBOT, $Ti(OC_4H_9)_4$) [72, 82, 87], $TiCl_4$ [76, 79, 81, 88], titanium tetraisopropoxide (TTIP, $(Ti(OCH(CH_3)_2)_4)$ [73, 89], $Ti(SO_4)_2$ [80, 90], titanium (IV) n-butoxide (TNB, $Ti(OBu)_4$) [91], TiO_2-P25 [92] and $TiCl_3$ [93]. Precursors which are used in the hydrothermal method are administered in the form of solutions, gels, and suspensions. These precursors are heated at a temperature range between (100-200 °C) and pressure (P < 100 bars), in autoclaves usually with Teflon liners. After the reaction occurred in the autoclave, the autoclave is cooled and some process such as centrifuging, drying, washing, etc is done.

In the hydrothermal method, some organic or inorganic mineralizers are used to control pH, also mineralizers with high concentrations (e.g., 10 m), used to promote solubility. For example, mineralizers such as NaOH, KOH, HCl, HNO_3, HCOOH, and H_2SO_4 are used in the synthesis of TiO_2 nanoparticles. Also, to control the shape of the nanomaterial, some other additives or shape control agents are used [94-97]. For instance, to prepare TiO_2 with a specific nanostructure, some surfactant molecules such as ammonia, diamine, dodecane diamine (DDA) [98], and triethanolamine [99] are used. As another example, in a system based on ethylene glycol and titanium tetra isopropoxide, the hydrothermal method of the base system could fabricate nanowires. In this system, the addition of ethylenediamine (EDA) with different concentrations led to a change in the shape of nanomaterial from nanowire to nanorods, nanofibers, and arrays [71]. To enhance the reaction kinetics or make a new material, the hydrothermal techniques can be hybridized with other processes such as microwaves, ultrasound, electrochemistry, etc [95].

A technique to prepare thin films or porous TiO_2 powder is the sol-gel method which has a drawback that involves deposition or calcined sol-gel-synthesized TiO_2 can readily form particles aggregates rather than a periodic and continuous inorganic framework. The hydrothermal method with low reaction temperature has been specified to solve this problem. The other advantage of the hydrothermal method for nanocrystalline state synthesis is the possibility to produce the material with uniform composition, phase, and microstructure [75, 76, 100]. Although the Hydrothermal synthesis process seems to be very simple, some pa-

Table 1.
Summary of TiO_2 and TiO_2 -based photocatalysts prepared via sol-gel or modified sol-gel method

Catalyst-shape	Method	The material used for the preparation	Model compound	Operating condition	Main results	Ref
Nanoparticles of TiO_2-CS, Pd/TiO_2, as well as Pd/TiO_2-CS	Modified sol-gel	**TiO_2 Precursor:** $TiC_{16}H_{36}O_4$ (titanium sec-butoxide) **The material used in the synthesis process:** Solvent for TiO_2 precursor: ethanol, HCl, and double-distilled water Precipitation agent: ammonia solution Pd source and solvent: $PdCl_2$ (Pd to TiO_2 molar ratio: 0.03), distilled water (50 mL) CS source and solvent: 1 g of CS (CS to TiO_2 molar ratio: 0.03), aqueous acetic acid solution (100 mL of 5%) pH controller (pH 9): ammonia solution	MB	Pd/TiO_2: Drying: at 100 °C overnight Calcination: for 5 h at 550 °C TiO_2-CS: Draying: at 100 °C for 24 h Calcinnation: at 550 °C for 5 h in air Light source: Xenon lamp	• Chitosan can prevent the agglomeration of TiO_2 nanoparticles • Photocatalytic activity: Pd/ TiO_2 < TiO_2-CS < Pd/ TiO_2-CS.	[168]
TiO_2-P25-nanocomposite films	Peroxotitanic acid (PTA) modified sol-gel	**TiO_2 Precursor:** TTIP (5 mL) **The material used in the synthesis process:** Solvents for TiO_2 Precursor: isopropanol (20 mL) Hydrolysis agent: deionized water (100 mL) PTA sol: dissolving the precipitate in 20 mL of aqueous H2O2 Surface modifier: 0.3 g 10% PEG solution TiO_2–P25 film preparation: substrate based on borosilicate glass with the dimension of 4.5 × 39.5 × 0.2 cm and sol of P25 (4 wt.%)	Reactive Red 222 (RR222)	Drying:100 °C in the oven for 1h Calcination: 500 °C for 2 h Light source: UV-C lamp	The photocatalytic efficiency of TiO_2-P25 increase due to effective charge transfer	[169]
CNS-TiO_2-nanoparticles	Sol-gel	**TiO_2 Precursor:** TTIP **The material used in the synthesis process:** Solvents for TiO_2 precursor: isopropyl alcohol solution Hydrolysis agent: deionized water Precursor and solvents for CNS-TiO_2 preparation: thiourea, double distilled water.	Amidoblack-10B dye (AB-10B)	Drying: 80 °C, in oven Calcination: 400 °C Light source: solar light	Co-doped TiO_2 activity under visible light irradiation is higher compared to pure TiO_2	[43]
N-doped TiO_2	Sol-gel reverse micelle (SGRM)	**TiO_2 precursor:** titanium (IV) 2-ethyl-1,3-hexanediolate (15.71 g) The material used in the synthesis process: Solvents for TiO_2 precursor: isopropyl alcohol (30 mL) Material for micelle reverse solution preparation: cyclohexane (16 mL), aqueous solution of Na2EDTA (14 mL) and TritonX100 (50 µliter)	MB	Heating: 70 °C for 60 min Aging: 24 h Drying: 80 °C for 8 h Calcination: for 1 h at 500 °C in static air with a 5 °C/min heating rate Light source: Mercury/ Xenon lamp (λ=400 nm)	Optimum condition: N/Ti atomic ratio=0.05	[42]
TiO_2- fibers	Sol-gel	**TiO_2 Precursor:** TBOT **The material used in the Synthesis process:** Solvent for TiO_2 precursor: anhydrous alcohol (TBT to EtOH molar ratio: 1:3) Surfactant: solution of PVP and HCl (26 mL) in absolute alcohol	Formaldehyde	Stirring: 2h Oil bath temperature: 110-140 °C Calcination: 500 °C for 90 min Light source: UV (λ=254 nm)	Optimum condition: H_2O:TBOT molar ratio ≤ 2	[170]
H-PVA/TiO_2-composite films	Sol-gel	**TiO_2 Precursor:** TBOT **The material used in the synthesis process:** Solvent for TiO_2 precursor: EtOH, AcOH Hydrolysis agent: deionized water (100 mL) and HCl (0.3 mL) Preparation of glass slides based on H-PVA/TiO_2: (75 mm × 25 mm × 1 mm), the mass ratio of PVA/ TiO_2: 1/5	Rhodamine B (RhB)	TiO_2 preparation: Stirring: 2h, 70 °C Aging: 48 h at room temperature Preparation of H-PVA/ TiO_2: Heat-treating: at 12-240°C for 4h in an N_2 gas flow Light source: Tungsten-Halogen lamp	Optimum condition: 180 °C and 16.7 mass% of polymer content	[167]
TiO_2-powder	Sol-gel	**TiO_2 Precursor:** $TiCl_4$ **The material used in the synthesis process:** Solvent for TiO_2 precursor: Ethanol/water (volume ratio of 4:1) **Hydrolysis agent:** Ammonia (pH=7.5)	Phenol	Calcination: 450 °C for 4 h Drying: 80 °C Light source: sunny day of summer (April–May)	19.6 nm species size demonstrate good photocatalytic activity under solar irradiation	[171]

Table 1. (Continued)

Catalyst-shape	Method	The material used for the preparation	Model compound	Operating condition	Main results	Ref
TiO_2-Fe_2O_3	Sol-gel	**TiO_2 Precursor:** $TiOCl_2$ **The material used in the synthesis process:** $FeCl_3.6H_2O$ and $FeCl_2.4H_2O$ (Fe^{3+}: Fe^{2+}=1:2) were added in distilled water and then added to 20 mL $TiOCl_2$. Ammonia solution was used to control pH at 9	MB	Aging: at 80 °C for 4 h and then settled at room temperature for 12 h with gentle stirring Drying: 80 °C for 24 h in the thermal oven Calcination: for 2 h at 400, 600 and 800 °C in a box furnace Light source: 100 W Halogen lamp emitting wavelengths=350-1050 nm	Optimum condition: 5 wt% Fe_2O_3 and calcination at 600 °C	[172]
Zirconium doped TiO_2-nanopowder	Controlled sol-gel route based on halide free non-aqueous solvent	**Precursor:** TTIP (20 mL) **The material used in the synthesis process:** Solvents for TiO_2 precursor: 2-methoxy ethanol (40 mL) Zirconium precursor: Zirconium-oxy-nitrate-hydrate (0.831 g, 1.754 g, and 2.785 g) Quenchers: potassium iodide (KI), sodium azide (NA), parabenzoquinone (BQ), and dimethyl sulphoxide (DMSO) pH controller (pH 3): HNO_3 and KOH	MB, RhB	Drying: using IR lamp (250 watt) and then pulverization Calcination: 450 °C for 1 h Light source: high-pressure ultra vitalux lamp (300 W, peak wavelength: 365 nm)	Doping of 10 at.% Zr leading to obtaining TiO_2 nano-powder with the size of 11 nm rendering energy gap of 3.33 eV increase photocatalytic efficiency	[173]
TiO_2-ZnO	Sol-gel	**TiO_2 Precursor:** TBOT **The material used in the synthesis process:** **ZnO precursor:** zinc nitrate ($Zn(NO_3)_2$. $6H_2O$) **Catalyst:** citric acid **Solvent:** deionized water	H_2 generation	Heating: 100 °C on a hot plate Annealing: for 5 h at 500 °C in a static atmosphere using a 1 °C/min heating rate Light source: UV	Optimum condition:10% ZnO-TiO_2	[174]
TiO_2/activated carbon	Sol-gel	**TiO_2 Precursor:** TTIP (2.87 mL) **The material used in the synthesis process:** Solvents for TiO_2 precursor: anhydrous isopropanol (10 mL) Activated carbon: 250 mg, Solvent for activated carbon: water (5 mL)	Tetracycline	Stirring: 5 min at room temperature Drying: 100 °C for 12 h Pyrolysis: under N2 gas flow for 2 h at 500 °C Drying: 100 °C for 24 h Light source: UV (18 W)	•Better electronic and structural features were observed in TiO_2/AC • Bandgap energy:3.04 eV anatase phase crystal size: 8.53 nm, and SBET:129 m^2/g	[175]
N-doped TiO_2	Sol-gel	**TiO_2 Precursor:** TBOT (10 mL) **The material used in the synthesis process:** Solvent for TiO_2 precursor: anhydrous ethanol (20 mL) Stabilizer: acetylacetone (2.5 mL) N source: ethylenediamine (N:Ti molar ratios: 0, 3.65, 5.21, 7.29, 18.23, 36.47, 72.94, 109.41)	MO and H_2 evolution	Stirring: 4 h Aging: 3 days Drying: 60 °C for 5days Calcination: 300-600 °C for 1-3 h	Optimum condition: ethylenediamine to sintering temperature of 500 °C and sol volume ratio of 1:1	[34]

rameters such as the type and source of precursors, the hydrothermal condition (e.g. reaction temperature and time), and the washing procedure, play important roles in controlling the structure of the produced photocatalysts. [74]. The schematic diagram of a hydrothermal method of synthesis TiO_2 matrix is depicted in Fig.2.

2.2.1 Photocatalysts preparation via hydrothermal method

F-doped anatase TiO_2 nanoparticles were prepared by adding dropwise 2.2 mL $TiCl_4$ to a solution of 2 mL HF (40%) and 36 mL solution of HCl (1.0 M) under vigorous stirring for 30 min. Then the resulted solution was placed in a 50 mL stainless-steel autoclave and maintained at 120-180 °C for 4-12 h. After the autoclave was cooled to room temperature, the resulted sample was collected by centrifugation, washed with distilled water various times, and dried in an oven at 80 °C. The presence of HF led to the formation of the F-doped shuttle-like anatase nanostructures of TiO_2 [76].

In another study, nanoparticles of TiO_2 were synthesized by titanium tetraisopropoxide hydrolysis using tetramethylamine (TMA) as a peptizer in the hydrothermal technique. In this route, white precipitates of hydrous oxides were prepared by adding titanium isopropoxide solution (water/TTIP molar (R) ratio=100) into a solution of trimethylamine and water with vigorous stirring at 25°C. The mixture was stirred for 2 h. Then the resulted solution (200 mL) was placed in a 250 mL Teflon container maintained in a vessel and heated for 4 h at 120-200 °C. The resulted in TiO_2 particles were separated using a centrifuge at 10,000 rpm for 10 min, after that washed in distilled water, and dried for 12 h at 105 °C, at last calcined for 3 h at 200-800 °C. The result showed that titania particles synthesized at 170 °C and calcined at 600 °C, have the highest performance in the orange II photocatalytic decomposition under UV light [77].

In yet another study, nanofibers were synthesized from low-cost (0.5-0.7 dollar/kg) natural ilmenite mineral ($FeTiO_3$) by a simple hydrothermal method. In this route, ilmenite mineral (5 g) and 10 M aqueous solution of NaOH (200 mL) were placed in an autoclave, heated, and stirred for 72 h at 120 °C. Then the mixture was cooled to room temperature, and washed with 0.1 M aqueous solution of HCl and deionized water (DI) several times, and dried at 100 °C for 12 h. The nanofibers calcined

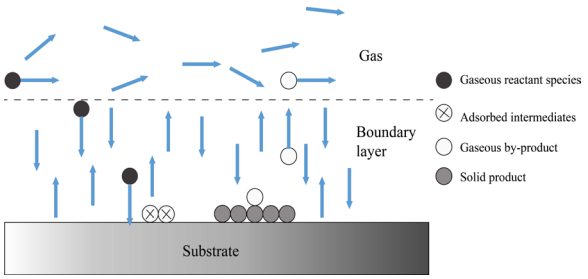

Fig. 4. Schematic of physical vapor deposition for TiO_2 coating.

at 300-400 °C presented TiO_2 , the nanofibers calcined at 500 °C presented a mixture of anatase and TiO_2 and the nanofibers calcined at 600-1000 °C presented the mixture of Fe_2O_3, tri-crystalline of anatase, and rutile [73]. A summary of TiO_2 and TiO_2-based photocatalysts synthesized via hydrothermal and solvothermal method are reported in Table 2.

2.3 CVD method

Chemical vapor deposition (CVD) is one of the photocatalyst preparation methods. In this process, one or more volatile precursors are evaporated to the carrier gasses and transfer into the reaction chamber. Depending on the reactions, which can occur in the gas phase (homogeneous reaction) or near/on a heated substrate (heterogeneous reaction), either powder or solid thin films are formed. Thermal decomposition or reaction of gas or vapor phase species occurs at a temperature range between (500-1000 °C) [101-103]. Preparation of powder and film includes several steps. It can be noticed that the main steps for nanoparticle formation are: (a) nucleus formation, (b) nucleus growth, and (c) collection of nanosized powder [104]. Also, the main steps for thin film deposition on the substrate can be described as follow: (a) volatile precursors are evaporated into carrier gas and then transferred by the gas into the reactor; (b) gaseous reactions happen in the reaction zone; (c) the mass transfer of the reactants is occurred to the heated substrate; (d) adsorption of the reactants occurs on the substrate; (e) surface diffusion of sediments is occurred and cussed by surface chemical reactions, nucleation, and layers growth and (f) deposition of unreacted precursors and by-products from the reaction zone.

There are different parameters, which can control the deposition rate and quality of a film resulting from a CVD process, such as 1- Carrier gas (reactant gas or inert gas including H_2, N_2, and Ar). These kinds of gases have different prominent features and any of these features have a typical effect. For instance, the gas flow rate has an effect on the deposition rate, source temperature (effect on the deposition rate and dispersion of supporting materials), total pressure gas flows, and carrier gas composition. 2- Type of the precursors and type and temperature of the substrates, which have effects on the temperature of crystal structure transition through TiO_2 preparation process. 3- Experimental conditions such as deposition time (long deposition time can cause several problems, for example, energy consumption) and synthesis temperature (influence on the visible light performance of TiO_2 photocatalyst, species of supporting material, and percentage of anatase and rutile content). 4- Reactor design [105-110].

The selection of a suitable precursor is an essential requirement of the metalorganic chemical vapor deposition (MOCVD) process. To select a suitable precursor, several parameters should be considered. For instance, adequate volatility, thermal stability, conventionally, low hazardous risk, high chemical purity, clean decomposition, and long shelf life. The common Ti-precursors used to synthesis the TiO_2 and TiO_2-based photocatalysts by the CVD method are halides such as $TiCl_4$ [111-

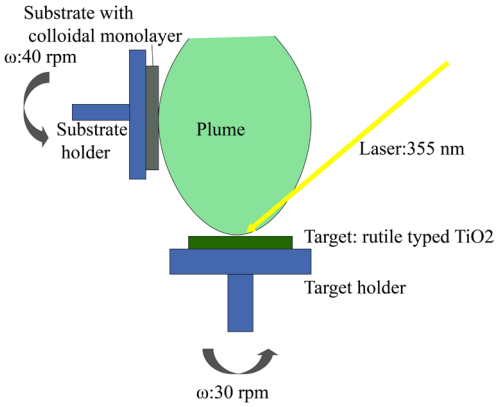

Fig. 5. Schematic illustration of PLD process.

114], alkoxides such as TTIP [105, 115-124], TBOT [101], and titanium nitrate. The metalorganic precursors such as titanium isopropoxide ($Ti(OPr^i)_4$), are less toxic and pyrophoric and offer the advantage of lower deposition and reaction temperatures than halides. Titanium isopropoxide includes an unsaturated four-coordinate Ti(IV) center, that is very reactive to moisture and air, and can cause problems in handling and storage, particularly in solution-based liquid injection MOCVD applications. $TiCl_4$ is toxic and needs safety installations and particular equipment. Its use can result in severe chloride contamination in CVD films. Several ligands such as ß-ketoesters, ß-keto amides, malonates, and aminoalkoxides have been used to synthesize the mixed alkoxide complexes of titanium. These ligands increase the sublimation rate and decrease the decomposition temperature. Also to reduce the sensitivity of moisture of the Ti-alkoxide precursors, chelating ß-diketone groups and bidentate donor functionalized ligands including 2-dimethylaminoethanol or diolates including 2-methyl pentane-2, 4-diolate, have been inserted to improve the Ti(IV) coordination sphere saturation [125-127]. As an example of the photocatalysts, which are produced from complex precursors in a chemical vapor deposition and photo-assisted CVD process, titania thin films were synthesized by titanium isopropoxide ($Ti(OPr^i)_4$) and titanium [bis (dipiraloymethanate) diisopropoxide] ($Ti(DPM)_2(OPri)_2$) complex compound precursors. The result showed that two crystalline forms, anatase and rutile, could be synthesized by these precursors, and also it has been observed that surface composition is different from that of the bulk in the film [128].

As mentioned above, chemical reactions can happen in both the gas phase (homogeneous reactions), which leads to powder formation (poor film morphology) and on the surface of the substrate (heterogeneous process). As the decomposition reaction is strongly dependent on the pressure, it is true to say that the selection of the low pressure (~Torr) can lead to heterogeneous reactions. Various types of CVD reactions consist of thermal decomposition reactions (pyrolysis reactions), reduction reaction, oxidation, hydrolysis, oxidation, nitride and carbide formation, and disproportionation [90]. Pyrolysis is involved the thermal dissociation of a gaseous compound into solid material and a gaseous reaction product. This reaction does not attack the substrate chemically. Pyrolysis reaction of a halide is described in Eq. (13). According to reduction reaction (Eq. (14)), in the presence of an adequate amount of reducing agent such as hydrogen, chemistry occurs primarily on the substrate. Oxidation (Eq. (15)) and hydrolysis reactions (Eq. (16)) is greatly used to deposit oxide materials. The most common oxidizing agent which is used in these reactions is oxygen and water. In disproportionation reaction (Eq. (17)), the oxidation number of an element both increases and decreases through the formation of two new species.

$$TiI_4(g) \rightarrow Ti(s) + 2I_2 \quad (13)$$

Table 2.
Summary of TiO_2 and TiO_2 -based photocatalysts synthesized via hydrothermal and solvothermal method

Photocatalyst-shape	Method	The material used for the preparation	Model compound	Operating condition	Main results	Ref.
WO_3/TiO_2	Hydrothermal	**TiO_2 Precursor:** titanyl sulfate ($TiOSO_4$) **The material used in the synthesis process:** double distilled water, titanyl sulfate (weight ratio= 4:5:1), and absolute ethanol WO_3 precursor: ammonium tungstate	MO and 2, 4-dichlorophenol (2, 4-DCP)	Stirring: 24 h at 25 °C Autoclave conditions:140 °C, 16 h, Teflon-inner-liner stainless steel Washing: water and ethanol Drying: 40-50 °C (overnight) Calcination: 500 °C Light source: visible and UV light ($\lambda < 420$ nm)	Optimum condition: 5.0% composite	[83]
SnS_2/TiO_2	Solvothermal	**TiO_2 Precursor:** TBT **Material used in the synthesis process:** $SnCl_4.5H_2O$ (5 mmol), thioacetamide (10 mmol) and 5 vol% acetic acid aqueous solution (40 mL). SnS_2 nanoparticles (0.4 g), TBT (0.5–2.0 mL) and a solution (38.0–39.5 mL) of ethanol (34.0 mL) and acetic acid (4.0 mL)	Aqueous Cr (VI)	The hydrothermal reaction for SnS2: 150 °C for 24 h Autoclave conditions: 180 °C, 12 h Cooling: at room temperature Washing: deionized water Drying: 100 ºC, 4 h, in vacuum Light source: visible light ($\lambda >$ 420 nm)	Optimum condition: SnS2/ TiO_2-B with the TiO_2 content of 25.5 mass%	[82]
TiO_2 -nanosheets	Hydrothermal	**TiO_2 Precursor:** TBOT **The material used in the synthesis process:** distilled water (80 mL), NH_3OH, and a solution of titanium (IV) butoxide mixing with acetylacetone	concentration	Stirring: 5 minutes Autoclave conditions: 120 ºC for 12 h, Thai made Cooling: at room temperature Washing: distilled water and 0.1 M of HCl Drying: 100 ºC for 12 h in an oven Heating: 300, 400, 500, 600, 700 and 800 ºC for 2 h	Specific surface area: 360.28 m2/g, average pore diameter: 3-5nm , pore volume 0.275 cm3/g	[72]
N, S-doped TiO_2 -powders	Hydrothermal	**TiO_2 Precursor:** $Ti(SO_4)_2$ **Materials used in the synthesis process:** CS $(NH_2)_2$, and an of $Ti(SO_4)_2$ (12.0 g), and distilled water (100 mL) solution	MO	Oil-bath temperature: 120 °C Hydrothermal treatment: 24 h Washing: distilled water Drying: 60 °C for 10 h, in a vacuum Calcination: 400, 500, 600, and 700 °C in the air for 3 h Light source: sunshine irradiation	Optimum condition: 3% N, S-TiO_2 calcined at 500 °C	[80]
Core–shell TiO_2 @ $ZnIn_2S_4$	Hydrothermal- ultrasonication	**TiO_2 Precursor:** TiO_2 **Materials used in the synthesis process:** TiO_2, deionized water (60 mL), $ZnCl_2$ (1 mmol), $In(NO_3)_3$ $4.5H_2O$ (2 mmol), and excessive thioacetamide (TAA, 6 mmol)	MB	Autoclave conditions: 160 °C for 6 h Cooling: at room temperature Washing: distilled water and absolute ethanol Drying: 80 °C for 6 h in a vacuum Light source: visible light ($\lambda =$ 420 nm)	Compared to TiO_2, Core-shell TiO_2 @ ZnIn2S4 showed higher photocatalytic activity	[176]
La/TiO_2-graphene composites	Hydrothermal	**TiO_2 Precursor:** TBT **Materials used in the synthesis process:** a suspension of TBT (15 mL), ethanol (80 mL), distilled water (40 mL at pH 3.0), and $La(NO_3)_3.6H_2O$. A solution of graphene oxide (20 mg), distilled water (80 mL), ethanol (40 mL), and TiO_2 (200 mg)	MB	Synthesis of TiO_2 nanopowder: Stirring:1 h Autoclave condition: 180 °C for 6 h Washing: deionized water Driying:100 °C in the vacuum oven for 12 h Calcination: 450 °C Synthesis of La/TiO_2 graphene composites: Stirring: 2 h Autoclave conditions:120 °C for 3 h Washing: deionized water Drying: 70 °C for 12 h. Light source: Visible light ($\lambda \geq$ 420 nm)	Photocatalytic activity of La/TiO_2-graphene composites was higher than TiO_2	[177]

Table 2. (Continued)

Photocatalyst-shape	Method	The material used for the preparation	Model compound	Operating condition	Main results	Ref.
(N−F) codoped TiO_2-nanobelts	Solvothermal	**TiO_2 Precursor:** TBT **Materials used in the synthesis process:** Step1: TBT (2.2 mL), a mixture of sodium chloride solution (0.4 mL 0.1 M) and ethanol (100 mL). Step2: TiO_2 (0.8 g), ammonium fluoride (0.37 g), 10 M sodium hydroxide solution (50 mL)	MO	Step1: Aging: for 24 h in a static condition Drying: 80 °C in air Step 2: Stirring: about 30 min Autoclave conditions:180 °C for 72 h Cooling: down to room temperature Washing: with ethanol and deionized water Drying: in the air at 80 °C Light source: visible solar irradiation ($\lambda \geq 420$ nm).	Mesopores like a prison, wormhole-like, enhanced absorption of light and larger surface area in the case of N-F codoping increasing the photocatalytic performance	[178]
Ag/TiO_2/ZnO composite particles	Hydrothermal	**TiO_2 Precursor:** P25(TiO_2) **Materials used in the synthesis process:** aqueous suspension of the mixture of TiO_2 (20 mg) in ethanol (10 mL), 0.058 M bis-hexamethylene triamine (40 mL), 5.8810- 3 M $AgNO_3$ (10 mL), and 0.063 M zinc nitrate hexahydrate (40 mL)	The aqueous solution of reactive black 5	Stirring: for 1 h Autoclave condition:140 °C for 2 h Cooling: at room temperature Washing: alcohol and distilled water Drying: 130 °C for 12 h	Ag/TiO_2/ZnO composite decrease the rate of electron-hole separation and prevent the loss of photocatalyst during recovery	[179]
Anatase nano-TiO_2 -powder	Hydrothermal	**TiO_2 Precursor:** $TiCl_4$ **Materials used in the synthesis process:** $TiCl_4$ (20 mL), ethanol (200 mL), H_2O_2 (80 mL), and 10 wt% ammonia	RhB	Autoclave condition:140 °C for 2 h Drying: 60 °C in vacuum Washing: distilled water Light source: (λ_{max}=553 nm)	Increasing the hydrothermal synthesis time and the sol concentration lead to an increase in particle size	[81]
Nitrogen-doped titania -nanoparticles	Microwave-assisted solvothermal process	TiO_2 Precursor:$TiCl_3$ **Materials used in the synthesis process:** hexamethylenetetramine (HMT, 2 g) and 20 wt% $TiCl_3$ solutions (10.75 cm3), 12.5 cm3 of distilled water, methanol, and ethanol	MO	Autoclave condition: 160-230 °C for 5min using a 1000 W microwave reaction apparatus Washing: distilled water and acetone Vacuum drying: at 80 °C overnight Light source: simulated solar radiation Xenon-lamp (λ_{max}=465 nm)	The reaction time could be reduced resulting from the high microwave irradiation heating	[93]
Urchin-like titania	One-step hydrothermal method	**TiO_2 precursor:** TiO_2 particles **Materials used in the synthesis process:** 10 M NaOH solution with TiO_2: NaOH molar ratio of 1:333	MO	Stirring: 10 min at room temperature Autoclave condition: 100 mL Teflon autoclave and an H_2O_2 solution (30 wt%) was added followed by rinsing with hydrochloric (0.1 M) Drying: 10 h at 50 °C Annealing: at 550 °C for 2 h in air and reducing atmospheres (10% H_2 + 90% Ar) respectively	• At temperatures of 130 and 150 °C, thick and small holes were present on the urchin-like surface. • Adding H_2O_2 form finer urchin-like surface and hydrogenation increase photocatalytic efficiency	[180]
TiO_2/graphene quantum dots	One-step hydrothermal	**TiO_2 precursor:** TiO_2 particles **Materials used in the synthesis process:** 0.5 g of TiO_2 nanoparticles, a suspension of 15 mg of 1,3,6-trinitropyrene (TNP), and 0.2 M NaOH aqueous solution (80 mL)	Hydrogen evolution	Ultrasonication: (150W, 50 kHz) for 4 h and additional sonication for 2 h Autoclave condition: Teflon-lined autoclave (100 mL), 200 °C for 10 h Washing: water and ethanol Drying: in the air for overnight Light source: 250 W high-pressure mercury lamp	TiO_2/graphene quantum dots H_2 evolution rate and photocurrent response at optimal GQDs content is 7 and 3 times higher than TiO_2	[181]
G-C_3N_4/TiO_2 heterojunction composites	Hydrothermal	**TiO_2 precursor:** $TiCl_4$ **Materials used in the synthesis process:** 0.5 mL of $TiCl_4$, a solution of melamine containing 0.5, 1, 2, 3, or 4 g melamine, and 60 mL of DI	RhB	Stirring: 30 min and then at 3-5 °C for 2 h in an ice bath Autoclave condition: stainless steel autoclave lined with Teflon (100 mL). 180 °C for 4 h Drying: 100 °C for 10 h and then heating in the crucible for 2 h at 550 °C at a 5 °C/ min rate in a muffle furnace under air atmosphere	• For 0.5 mL of $TiCl_4$, optimum melamine content was 3 g • Specific surface area: up to 115.6 m2/g	[182]

Table 2. (Continued)

Photocatalyst-shape	Method	The material used for the preparation	Model compound	Operating condition	Main results	Ref.
Bi-TiO_2 nanotube/graphene composites	One-step hydrothermal	**TiO_2 precursor:** Degussa P25 **Materials used in the synthesis process:** 1 g of Degussa P25, a suspension of GO (2 wt%), and 30 mL of double distilled. various amount of bismuth nitrate and NaOH	Dinoseb (phenolic herbicide) and MB	Autoclave condition: Teflon-lined autoclave and heated for 24 h at 140 °C Washing: double distilled water followed by acid washing with HCl (0.1 M) Drying: 80 °C for 16 h, dry overnight at 80 °C Annealing process: 350 °C for 6 h Light source: visible light 500 W (9500 lumens) linear halogen lamp	2-wt% bismuth shows improvement in photocatalytic activity	[6, 183]
Graphene/TiO_2/CdS nanocomposites	Hydrothermal	**TiO_2 precursor:** TBT **Materials used in the synthesis process:** GO (15 mg), TBT (2.63 mmol), diethylene glycol (60 mL). A solution of acetone (180 mL) and deionized water (600 µL). A suspension of $Cd(NO_3)_2.4H_2O$/L-cysteine (0.2/0.6, 0.4/1.2, 0.6/1.8 mmol) and deionized water (80 mL)	MB and parachlorophenol (4-CP)	Stirring: 12 h at room temperature another stirring 1.5 h Washing: water/ethanol Autoclave condition: 120 °C for 12 h Light source: a visible-light	The surface area of GO-TiO_2-0.55CdS (157.5 m^2/g) result in higher photocatalytic activity	[184]

$$SiCl_4\ (g)+2H_2\ (g)\rightarrow Si\ (s)+4HCl\ (g) \quad (14)$$

$$TiCl_4\ (g)+2O_2\ (g)\rightarrow TiO_2\ (s)+Cl_2\ (g) \quad (15)$$

$$TiCl_4\ (g)+2H_2O\ (g)\rightarrow TiO_2\ (s)+4HCl\ (g) \quad (16)$$

$$2TiCl_2\ (g)\rightarrow Ti\ (s)+TiCl_4\ (g) \quad (17)$$

The CVD process can be operated in either a close or open system. Closed systems can be utilized for reversible reactions, for example, metal purification. However, it can be said that close systems are less common in comparison with open systems. In open systems, the carrier gasses flow through the reactor and after deposition, by-products and unreacted precursors are carried by carrier gas, and then go out from the reactor [129]. Main equipment in the open systems can be classified into three basic components:1- Delivery system, which is used to produce vapor precursors and deliver them to the reactor. 2- The effluent gas handling system. To provide the low pressure or high vacuum pressure for the CVD method, some systems such as a mechanical pump (van pump) are used [105]. Many precursors used in the CVD method are toxic and pyrophoric, in this respect, a liquid nitrogen trap is employed to neutralize or entrap the hazardous by-product and unreacted precursors, before being released to the environment [107, 130]. 3- CVD reactor.

Conventional CVD reactors including distributing and delivering reactive gases through a substrate, and a system of heating with temperature control. Regarding the performance of CVD reactors, it is highly important to be considered, that precursors must be injected into the reactor, also carrier gasses with a certain flow rate and temperature must be injected into the reactor. The volatile precursors are carried out by carrier gas toward the substrate and then decomposed on the surface of the substrate, after that the extra vapor precursors and exhausted gasses are removed from the reactor, then the reactor is purged by inert gas [105-108, 131]. There are several types of CVD methods, which are classified based on the activation energy of the reaction. Various activation energies can be included: thermal (RF heating, infrared radiation, and resistive heating), photons (UV lamp-laser), and plasma (DC current-frequency, pulses-microwave). Thermally activated CVD is called TCVD, photonic activated CVD is called LCVD and plasmatic activated CVD is called PECVD (plasma-enhanced CVD). Another type of CVD method is metalorganic CVD (MOCVD) which uses metalorganics as the precursor. The pressure for MOCVD is usually around 10^3-10^5 Pa and the temperature range is between~300-800 °C. In this type of reactor, reactants are volatile at relatively low temperatures.

Thermally activated CVD is a usual CVD process in which thermal energy in a cold wall or hot-wall reactor by inorganic chemical precursors led to the initiation of the chemical reactions. A hot wall reactor is usually tubular and surrounded by an isothermal furnace and is used mostly for an exothermic reaction. The advantage of this reactor is close temperature control and the disadvantage is that deposition can occur on the wall of the reactor because the wall and the substrate have the same temperature. The cold wall reactor is bell-jar shaped and used for endothermic reactions. In this reactor, the substrate is heated directly either by electricity (induction) or by glowing heating, as a result, the rest of the reactor remains cold and the substrate has the highest temperature. The processes of thermally activated CVD can be subdivided based on the pressure range of deposition. The operating pressure can be considered as (a) low-pressure CVD (LPCVD), the pressure range is between 10-1000 Pa; (b) atmosphere pressure (APCVD) and (c) high vacuum pressure (HPCVD), the pressure is less than 10^{-5} Pa. The difference between LPCVD/UHVCVD and APCVD is the ratio of the mass transport velocity and the velocity of reaction on the surface. It can be said that the diffusion of a gas is inversely proportional to the pressure [125, 132].

In PECVD temperature is between 100-700 °C and pressure is 1-80 Pa. PECVD processes by metal-organic precursors have gained attention due to their potential in lowering the deposition temperatures, as a result, this process is used in the coating of the temperature-sensitive substrates. In a DC plasma-assisted and thermally activated CVD process by titanium isopropoxide as a precursor, the TiO_2 film deposition has been under investigation. The result shows that the pulsed DC plasma has several advantages such as: nanostructured of crystalline TiO_2 are deposited at a lower temperature, the plasma-assisted CVD produced dense microstructure even in amorphous deposits and enhanced desorption of residual surface contamination [123].

The LCVD is a CVD derivative in which the global heat source for the furnace is replaced with a localized spot heated by a laser [133].

The use of precursors with better deposition routes is more important than the utilization of less volatile precursors, in this respect, some

Table 3.
Summary of TiO_2 and TiO_2 -based photocatalysts prepared via CVD method

Photocatalyst-shape	Reactor design	Model compound	Operating conditions	Main results	Ref.
TiO_2 films covered by noble metal nanoparticles silver, platinum	Radiofrequency (RF) low-pressure PECVD reactor	Acid Orange 7 (AO7)	Precursor: TTIP Substrate: glass slide and silicon wafer Temperatures: 40, 300 °C Liquid heated evaporator temperature: 50 °C Oxygen flow rate: 25 to 200 sccm Working gas: a TTIP vapors and oxygen mixture Pressure: 8-20 Pa Bias on the substrate: about -50V at 20 W Light source: UV-A lamp (15 W, λ=365 nm)	Treated or untreated films synthesized at higher temperature (300 °C) showed enhanced antibacterial properties	[122]
TiO_2 thin film deposited on silica gel powder	Radiofrequency circulating fluidized bed PECVD reactor	MB	Precursor: TTIP Deposition temperature: 250 °C Supplying power: 13.56 MHz Bubbler temperature: 95 °C Light source: ultraviolet lamp (15 W/cm^2, λ=365 nm)	The optimum condition for anatase phase deposition was 3.6 vol.% of O2, 0.4 g/min of TTIP, and 8.18 vol.% of Ar	[121]
TiO_2 coating of activated carbon	AP-MOCVD (hot-wall reactor)	MO	Precursor: TBOT Deposition temperature: 600 °C Light source: UV lamp (1.2 15 mW/cm^2, λ=356 nm)	• The particles size is ranging from 10 to 50 nm • The optimum loading of TiO_2 was 12 wt%	[101]
N-doped titanium thin film	APCVD (custom-built, horizontal cold wall reactor)	Stearic acid	Precursor: $TiCl_4$ Deposition temperature:500 °C Bubbler temperature: 40 °C and 70 °C	Selective doping at the interstitial site (ionization 400 eV by XPS) shows a dominant impact on the enhancement of photocatalysis	[112]
Needle-like TiO_2 / WO_{3-x}	APCVD-cold wall reactor	Stearic acid	Precursor: TiCl4 Deposition temperature: 500 °C Bubbler temperature: 200 °C Light source: UVC light (200 W Xenon lamp, λ=254 nm)	The increase in activity of films is explained in terms of effective vectorial charge separation at the interface of the two oxide semiconductors	[113]

delivery systems are used to generate vapor precursors and deliver them to the reactor. Different types of delivery systems are classified based on the phase of the precursors (liquid, solid, and gas). The method for gas precursor delivery is to use a cylinder containing the right composition of the precursor with a mass flow controller to control the vapor phase concentration. The liquid precursors with low pressures must be heated in an oil bath or placed in a bubbling chamber, to evaporate to their evaporation temperature. Also, carrier gasses must be used to deliver volatile precursors to the reactor [132, 134]. It can be said that the precursor's flow rate should be controlled by adapting the temperature of the bubbling chamber or/and the flow rate of carrier gasses [103]. If the vapor pressure of the liquid reactant is specified, its partial pressure may be designed and controlled by controlling the flow rate and volume of the carrier gas. On the other hand, like a flash vaporization method, the flow rate of the precursors must be controlled by a syringe pump or other equipment, and carrier gas with mass flow controlled can be used to deliver volatile precursors towards the reactor [105, 132]. If the phase of the precursors is solid precursors, the precursor must be sublimated and then transferred by the carrier gas to the reactor [107].

2.3.1 Preparation of photocatalysts by CVD Method

TiO_2 nanoparticles were coated onto a glass bead using a CVD method with T-junction apparatus and using TTIP as a precursor. The precursor was vaporized in a bubbler using argon gas at 90 °C and then carried with carrier gasses (argon and nitrogen) through an alumina tube which was heated at 900 °C and connected to a horizontal T-junction containing soda lime glass beads. The deposition time was regulated to 10, 30, 60, and 120 min. The result showed that the sample with the 60 min coating time had the best photocatalytic performance (~52%) for the decomposition of acetaldehyde. Another result is that TiO_2 nanoparticles were deposited with a uniform shape onto the glass bead, and the coating time was decreased with this simple process [116].

TiO_2 /silica gel photocatalyst was synthesis by the CVD method, according to three steps: (a) the support materials pretreatment by adding water dropwise to silica gel and then drying for 20 min at 110 °C; (b) CVD reaction and (c) calcination at 500 °C for 3 h in airflow. In the synthesis process, TTIP was stored in a separate container (bubbler at 80 °C) and introduced into the reactor of CVD (300 °C) by the carrier gas (nitrogen) under vacuum. The result showed that the size for all the TiO_2 /silica gel samples is uniform in the 10-20 nm range [120]. The mechanism of chemical vapor deposition is illustrated in Fig.3. A summary of TiO_2 and TiO_2-based photocatalysts prepared via the CVD method is reported in Table 3.

2.4 PVD method

In processes of physical vapor deposition (PVD), the coating is deposited in a vacuum using condensation from a flux of ionized or neutral metal atoms. The basic PVD processes fall into two general categories: (a) thermal methods (evaporation and electron-beam evaporation) and (b) mechanical methods (cathodic sputtering). For the evaporation process, the substance to be evaporated is heated in an evacuated chamber so that it attains a gaseous state. The coating material is moved along the transport area and condenses on the substrate surface. For sputtering, atoms are ejected mechanically from a target with the ions impact or energetic neutral atoms.

Electron-beam evaporation (EBE) [135-137], ion-assisted electron-beam evaporation [138-140], pulsed laser deposition (PLD) [31, 141], radio frequency (RF) magnetron sputtering [142-145], direct current (DC) magnetron sputtering [146-148], and pulse magnetron sputtering [149, 150] are the common PVD methods, which are used to synthesis photocatalysts. Fundamental of PVD process is like CVD, except that in PVD method the raw materials, which are going to be deposited

start in solid form. Also in comparison with the CVD method, the PVD process does not produce harmful by-products and it can be noticed that the operating temperature of the PVD method (200 to 300 °C) is less than the CVD method [151, 152]. The main disadvantage of processes of PVD (with EB-PVD exception) is the low deposition rates. The schematic of physical vapor deposition for TiO_2 coating is depicted in Fig.4.

2.4.1 Pulsed laser deposition (PLD)

In the PLD method, a focused pulsed-laser beam illuminates one or more targets and thin films are prepared by the ablation of these targets. There are different parameters affecting film properties such as laser fluence, pressure, background gas, substrate temperature, target-to-substrate distance, wavelength, and pulse duration [153]. The experimental apparatus used in the PLD method contains: a deposition chamber that is evacuated to a base pressure using a mechanical pump and a Cryopump and the chamber is filled with gasses (e.g., oxygen, nitrogen, etc). Other components are a pulsed laser (Nd: YAG laser, KrF laser), which is used to irradiate the target, and a substrate (part to be coated) that is set apart from the target and heated by an instrument (e.g., IR lamp or laser). The advantages of the PLD technique are that this method causes the growth of high-quality thin-film materials. PLD as a thin film deposition technique possesses some disadvantages including droplet deposition on the film and the formation of non-homogeneous films [154]. Several investigations have been done on photocatalyst synthesis via the PLD method. For example, nitrogen-doped titanium oxide photocatalyst was synthesized using PLD. With this regard, the TiN target in a gas mixture of N_2/O_2 was used. According to the results, the N_2 ratio in the gas mixture and target material have significant effects on the film structure and properties. Additionally, the absorption edges of the films shifted from 320 nm to 360 nm for TiO_2 and $TiO_{2-x}N_x$ films, respectively [155]. Mn-doped ZnO/TiO_2 multilayer nanostructures (photocatalyst) were deposited on Si (100) substrates by this method. To prepare the nanostructure, a multi-target carousel system was used following by post-growing annealing in O_2 or N_2 atmosphere at a pressure of 1 bar and temperatures of 400-800 °C. It was found that the thicknesses of grown nanostructures by the pulsed laser deposition technique were about 2 and 15 nm [156]. Fig.5 shows a schematic illustration of the PLD process.

2.4.2 Electron-beam and ion-assisted electron-beam evaporation

In EBE, to evaporate the material, a beam of electrons with high kinetic energy is directed to the target material. On the surface of the components or substrates, the evaporated material is condensed causing the formation of a deposit. In the EBE method, the deposition rate can be varied simply by adjusting the beam current and during the deposition process also it does not particularly need the specific gas atmosphere. The other advantages of the EBE method are the high deposition rate, excellent economy, and practicability [157-159]. EBE is one of the methods that are preferred among different physical vapor deposition techniques to deposit TiO_2 films to achieve high-quality optical thin films [140]. An annealing treatment is essentially required after deposition to control the morphology, structure, and thereafter photocatalytic activity of the films that have been prepared [158]. EBE unit consists of main components namely, EB-gun assembly, a substrate that is usually held with a rotating substrate holder, a (vacuum) chamber, and a target [160]. EBE method is used in the deposition of thin films on a substrate. For example, on a substrate of quartz glass with a temperature of 200 °C, TiO_2 thin-film was deposited at oxygen gas pressure accounting for 6.7 × 10−3 Pa. TiO_2 was used as a target, and the base pressure of the chamber was 8.0 × 10−4 Pa. The results exhibited higher photocatalytic activity of GO/TiO_2 in the UV-violet compared to the visible range [136]. Using an ion-assisted EBE system, TiOxCy films were deposited by using carbon monoxide (CO) and the source material of rutile TiO_2 powder flowing through a dopant source (ion gun). According to the results, the CO ion beam can produce TiO_xC_y films with visible-light responsiveness [139]. Another result is that the film crystallinity deteriorated because of the increasing ion-beam current.

2.4.3 Magnetron and reactive magnetron sputtering

In the sputtering method, materials are eliminated from objects by transferring energy in energetic atomic projectile collisions. In magnetron sputtering, the magnetron field can be created by permanent magnets, electromagnets, or a combination of both [161]. Magnetron sputtering of TiO_2 films is one of the most favorable techniques because this industrial process provides the ability of large-area deposition rendering good adhesion to substrates. Also, with this technique, high-quality TiO_2 films could be obtained even at low substrate temperatures. Both DC and RF sputtering techniques have attracted extensive attention recently because of the very smooth surface that is achieved by sputtering [143, 161-163]. In the magnetron sputtering technique, the sputtering gas is an inert gas (e.g., Ar) and in the reactive magnetron sputtering a second gas (O_2), which can react with the target material is added to the sputtering gas. In DC reactive sputtering method, plasma is created between the anode (substrate holder) and the cathode, and positive ions in plasma sputter off the atoms from a target (cathode) that is connected to a potential source. These atoms react further with the particles of the reactive gas and deposit on the substrate under an oxidized form [164]. Properties and structure of the DC-magnetron-sputtered TiO_2 films can be controlled and modified by regulating process parameters including coating thickness, sputtering gas Ar: O_2 ratio, sputtering power, and sputtering pressure [165].

2.4.4 Preparation of photocatalysts by PVD Method

Pansila et al. [166] used the DC reactive magnetron sputtering method with a variation in the sputtering power to synthesize TiO_2 films. The Ti target (120 mm) was sputtered in the Ar + O_2 gas mixture. In this study, the deposition of the TiO_2 thin films was carried out on the unheated substrate (silicon wafer) at 210 W and 230 W sputtering power. The deposition happened in the vacuum chamber (at 3 h, base pressure: 5.0×10^{-5} mbar and total pressure: 5.0×10^{-3} mbar). The result showed that the sputtering power strongly affected the TiO_2 thin film crystalline structure. With an increase in the sputtering power of the cathode, the TiO_2 thin film structure was transformed from anatase to mixed structure of anatase/rutile.

In a work done by Huang et al. [143], the influence of the deposition parameters, such as substrate temperature, argon-oxygen ratio (O_2/(Ar + O_2), RF power, and deposition time, on the decomposition of methylene blue, was studied. In this study, titanium oxide films were applied on non-alkali glass (temperature: 100 °C) by RF magnetron sputtering with the base pressure of 0.67×10^{-3} Pa and sputtering power of 20 W using a Ti metal target. Sputtering and reactive gases were Ar and O_2. It was found that parameters that had a dominant influence on the absorbance of MB were argon-oxygen ratio and RF power.

In another study done by Nair et al. [142], the deposition of TiO_2 thin films was performed onto cleaned quartz substrates by RF magnetron sputtering method following post-annealing at 873 K using TiO_2 ceramic target, which was synthesized by pelletized TiO_2 powder sintering for 4 h at 1673 K. The authors investigated the influence of sputtering pressure and the RF power on the optical and structural properties of the films. The results indicated that the films contain anatase phase, also the results show that a decrease in sputtering pressure and the increase in RF power leads to a decrease in the optical bandgap.

Su-Shia et al. [167] employed the simultaneous DC magnetron sputtering of W and RF magnetron sputtering of TiO_2 to heavy doping of the TiO_2 films with W (TiO_2 :W). This type of deposition method offers

Table 4.
Summary of TiO_2 and TiO_2 -based photocatalyst prepared by PVD method

Photocatalyst	Method	Model compound	Synthesis condition	Main results	Ref.
TiO_2 thin films deposited on quartz glass	Electron-beam evaporation	MB	Target: TiO_2 (99.99% pure) Substrate-to-target distance: 650 mm Evaporator pressure: 6×10^{-6} Torr Working oxygen gas pressure: 5×10^{-5}Torr Deposition temperature: 200 °C The voltage of electron gun: 7.0 kV Current: 200 mA Substrate rotate vertical axis: 15 rpm Deposition rate: 1.50-2.05 A°/s, at an incident angle of 0-75° Annealing: 600 °C in air, 1 h Light source: black-light lamps (20 W) with λ=352 nm	Incident deposition angle up to 60° led to the enhanced photocatalytic activity while a further increase to 75° decreased the photocatalytic activity resulted from a lack of the crystalline phase	[135]
TiO_2/SiO_x/TiO_x multi-layers deposited on quartz glass	Electron-beam evaporation	MB	Deposited temperature: 200 °C Distance between the substrate and target: 580 mm Base pressure: 6.0×10^{-6} Torr The partial pressure of oxygen: 2.5×10^{-5} Torr for the TiO_x layer, 6.0×10^{-5} Torr for the SiO_2 layer, and 5.0×10^{-5} Torr for the TiO_2 layer deposition The voltage of electron gun: 7.0 kV Current: 110 mA for SiO_2, and 220 mA for TiO_2 Substrate rotate vertical axis: 15 rpm Deposition rate: 0.25 nm/s, 1.00 nm/s and 0.25 nm/s Annealing: in air and at 600 °C for 1 h Light source: 20W-black-light lamps, λ=352 nm	Due to more trap levels in the SiO_x (80 nm) inter-layer and higher surface roughness, the TiO_2/SiO_x (80 nm)/TiO_x multi-layer showed promising photocatalytic activity	[137]
Thin films based on Bi: TiO_2	Pulsed laser deposition and thermal evaporation	Malachite green solution	Laser: Nd: YAG with emission at the third harmonic (355 nm), pulse duration: 10 ns, focal length spherical lens: 60 cm, incidence angle: 45°, laser fluence: 10.0 J/cm^2 Base pressure: 2×10^{-5} Torr Substrate-to-target distance: 5 cm Light source: Hg lamp, λ=404 nm	Bi: TiO_2 thin films reduced the bandgap energy and also favored the formation of segregated anatase and b-Bi_2O_3 phases	[31]
TiO_2 films deposited on non-alkali glass	RF magnetron sputtering	MB	Target: TiO_2 with 50.8 mm diameter and 99.995% purity Deposition time: 180 min Base pressure: 5.0×10^{-6} Torr Gas: O_2 (99.995%), Ar (99.995%) Distance between the substrate and target: 8 cm Rotate vertical axis of substrate: 10 rpm Light source: blacklight lamp, λ=365 nm	The optimal condition was 10 mTorr sputtering pressure, power of 200 W, 50% argon-oxygen ratio, and 450 °C for substrate temperature	[185]
Boron-doped titanium dioxide (B-TiO_2) films	Reactive magnetron co-sputtering	MB	Target and power: 99.99% titanium (SDIC) metal, 200 W. 99.5% TiB_2, 30, 60, 90, 120, 150 and 180 W Substrates: glass or fused quartz slides and polished Si (100) wafers Distance between the substrate and the targets: 100 mm Base pressure: 4.0×10^{-5} Pa or lower Substrate temperature: 100 °C Gas flow rates and pressure: 8 sccm for O_2 and 20 sccm for Ar. 4.0×10^{-1} Pa (3.0×10^{-3} Torr). Thicknesses of the films: 300 nm Light Source: UV	Ti_2BO_2 enhanced the photocatalytic activity of TiO_2 under visible-light	[186, 187]

the capability of changing the W content in a wide range. A summary of TiO_2 and TiO_2-based photocatalyst prepared by the PVD method are reported in Table 4.

3. Conclusions

TiO_2 is a promising material for environmental applications. Several parameters such as suitable pore size, high specific surface area, good crystallinity, and porosity, also shape can be very effective to achieve more efficient photocatalytic activity of TiO_2. Also, modification of TiO_2 with various materials is a good method to achieve better photoactivity and enhance the visible light absorption ability. The photocatalytic activity and light absorption ability are influenced by preparation methods, parameters, and conditions. In the future researchers can focus on physical production techniques. As these techniques still need effort and investigation.

Acknowledgment

This research did not receive any specific grant from funding agencies in the public, commercial, or not-for-profit sectors.

REFERENCES

[1] A. Jafari Rad, Synthesis of copper oxide nanoparticles on activated carbon for pollutant removal in Tartrazine structure, Journal of Composites and Compounds 2(3) (2020).
[2] A. Abuchenari, K. Hardani, S. Abazari, F. Naghdi, M. Ahmady Keleshteri, A. Jamavari, A. Modarresi Chahardehi, Clay-reinforced nanocomposites for the

slow release of chemical fertilizers and water retention, Journal of Composites and Compounds 2(3) (2020).
[3] S. Askari, M. Ghashang, G. Sohrabi, Synthesis and mechanical properties of Bi_2O_3-$Al_4Bi_2O_9$ nanopowders, Journal of Composites and Compounds 2(5) (2020).
[4] B. Cheng, Y. Le, J. Yu, Preparation and enhanced photocatalytic activity of Ag@TiO_2 core–shell nanocomposite nanowires, Journal of Hazardous Materials 177(1–3) (2010) 971-977.
[5] H. Jing, Q. Cheng, J.M. Weller, X.S. Chu, Q.H. Wang, C.K. Chan, Synthesis of TiO_2 nanosheet photocatalysts from exfoliation of TiS_2 and hydrothermal treatment, Journal of Materials Research 33(21) (2018) 3540-3548.
[6] H. Mao, Z. Fei, C. Bian, L. Yu, S. Chen, Y. Qian, Facile synthesis of high-performance photocatalysts based on Ag/TiO_2 composites, Ceramics International 45(9) (2019) 12586-12589.
[7] S. Liu, Y. Zhang, Synthesis of CPVC-modified SnS_2/TiO_2 composite with improved visible light-driven photocatalysis, Materials Research Bulletin 135 (2021) 111125.
[8] S. Narzary, K. Alamelu, V. Raja, B.M. Jaffar Ali, Visible light active, magnetically retrievable Fe_3O_4@SiO_2@g-C_3N_4/TiO_2 nanocomposite as efficient photocatalyst for removal of dye pollutants, Journal of Environmental Chemical Engineering 8(5) (2020) 104373.
[9] Y. Shen, P. Zhou, S. Zhao, A. Li, Y. Chen, J. Bai, C. Han, D. Wei, Y. Ao, Synthesis of high-efficient TiO_2 /clinoptilolite photocatalyst for complete degradation of xanthate, Minerals Engineering 159 (2020) 106640.
[10] S. Alberti, V. Caratto, D. Peddis, C. Belviso, M. Ferretti, Synthesis and characterization of a new photocatalyst based on TiO_2 nanoparticles supported on a magnetic zeolite obtained from iron and steel industrial waste, Journal of Alloys and Compounds 797 (2019) 820-825.
[11] S. Ali, Z. Li, S. Chen, A. Zada, I. Khan, I. Khan, W. Ali, S. Shaheen, Y. Qu, L. Jing, Synthesis of activated carbon-supported TiO_2-based nano-photocatalysts with well recycling for efficiently degrading high-concentration pollutants, Catalysis Today 335 (2019) 557-564.
[12] J.C. Lopes, M.J. Sampaio, B. Rosa, M.J. Lima, J.L. Faria, C.G. Silva, Role of TiO_2-based photocatalysts on the synthesis of the pharmaceutical precursor benzhydrol by UVA-LED radiation, Journal of Photochemistry and Photobiology A: Chemistry 391 (2020) 112350.
[13] S. Saroj, L. Singh, S.V. Singh, Solution-combustion synthesis of anion (iodine) doped TiO_2 nanoparticles for photocatalytic degradation of Direct Blue 199 dye and regeneration of used photocatalyst, Journal of Photochemistry and Photobiology A: Chemistry 396 (2020) 112532.
[14] H. Zhang, X. Wang, N. Li, J. Xia, Q. Meng, J. Ding, J. Lu, Synthesis and characterization of TiO_2 /graphene oxide nanocomposites for photoreduction of heavy metal ions in reverse osmosis concentrate, RSC Advances 8(60) (2018) 34241-34251.
[15] X. Yu, H. Qiu, B. Wang, Q. Meng, S. Sun, Y. Tang, K. Zhao, A ternary photocatalyst of all-solid-state Z-scheme TiO_2 –Au–BiOBr for efficiently degrading various dyes, Journal of Alloys and Compounds 839 (2020) 155597.
[16] N. Yaacob, G.P. Sean, N.A.M. Nazri, A.F. Ismail, M.N. Zainol Abidin, M.N. Subramaniam, Simultaneous oily wastewater adsorption and photodegradation by ZrO_2–TiO_2 heterojunction photocatalysts, Journal of Water Process Engineering 39 (2021) 101644.
[17] B. Zhang, X. He, X. Ma, Q. Chen, G. Liu, Y. Zhou, D. Ma, C. Cui, J. Ma, Y. Xin, In situ synthesis of ultrafine TiO_2 nanoparticles modified g-C_3N_4 heterojunction photocatalyst with enhanced photocatalytic activity, Separation and Purification Technology 247 (2020) 116932.
[18] N. Sedaghati, A. Habibi-Yangjeh, S. Asadzadeh-Khaneghah, S. Ghosh, Integration of oxygen vacancy rich-TiO_2 with BiOI and $Ag_6Si_2O_7$: Ternary p-n-n photocatalysts with greatly increased performances for degradation of organic contaminants, Colloids and Surfaces A: Physicochemical and Engineering Aspects 613 (2021) 126101.
[19] J. Abdi, M. Yahyanezhad, S. Sakhaie, M. Vossoughi, I. Alemzadeh, Synthesis of porous TiO_2 /ZrO_2 photocatalyst derived from zirconium metal organic framework for degradation of organic pollutants under visible light irradiation, Journal of Environmental Chemical Engineering 7(3) (2019) 103096.
[20] X. Wei, C. Wang, S. Ding, K. Yang, F. Tian, F. Li, One-step synthesis of Ag nanoparticles/carbon dots/TiO_2 nanotube arrays composite photocatalyst with enhanced photocatalytic activity, Journal of Environmental Chemical Engineering 9(1) (2021) 104729.
[21] D. Boczar, T. Łęcki, M. Skompska, Visible-light driven FexOy/TiO_2 /Au photocatalyst – synthesis, characterization and application for methyl orange photodegradation, Journal of Electroanalytical Chemistry 859 (2020) 113829.
[22] Y.P. Bhoi, F. Fang, X. Zhou, Y. Li, X. Sun, J. Wang, W. Huang, Single step combustion synthesis of novel Fe_2TiO_5/α-Fe_2O_3/TiO_2 ternary photocatalyst with combined double type-II cascade charge migration processes and efficient photocatalytic activity, Applied Surface Science 525 (2020) 146571.
[23] A. Shahnazi, M.R. Nabid, R. Sedghi, B. Heidari, A thermosensitive molecularly imprinted poly-NIPAM coated MWCNTs/TiO_2 photocatalyst for the preferential removal of pendimethalin pesticide from wastewater, Journal of Photochemistry and Photobiology A: Chemistry 402 (2020) 112802.
[24] M. Sabri, A. Habibi-Yangjeh, H. Chand, V. Krishnan, Activation of persulfate by novel TiO_2 /FeOCl photocatalyst under visible light: Facile synthesis and high photocatalytic performance, Separation and Purification Technology 250 (2020) 117268.
[25] J. Xie, M. Xu, R. Wang, S. Ye, X. Song, Three-Dimensional Porous Spherical TiO_2 –Bi_2WO_6 Decorated Graphene Oxide Nanosheets Photocatalyst with Excellent Visible Light Catalytic Degradation of Ethylene, Ceramics International (2021).
[26] A. Beeldens, An environmental friendly solution for air purification and self-cleaning effect: the application of TiO_2 as photocatalyst in concrete, Proceedings of transport research arena Europe–TRA, Göteborg, Sweden (2006).
[27] H. Won Jang, A. Zareidoost, M. Moradi, A. Abuchenari, A. Bakhtiari, R. Pouriamanesh, B. Malekpouri, A. Jafari Rad, D. Rahban, Photosensitive nanocomposites: environmental and biological applications, Journal of Composites and Compounds 2(2) (2020).
[28] L. Bazli, M. Siavashi, A. Shiravi, A review of carbon nanotube/TiO_2 composite prepared via sol-gel method, Journal of Composites and Compounds 1(1) (2019).
[29] I. Ali, M. Suhail, Z.A. Alothman, A. Alwarthan, Recent advances in syntheses, properties and applications of TiO_2 nanostructures, RSC Advances 8(53) (2018) 30125-30147.
[30] M. Zhou, S. Roualdès, J. Zhao, V. Autès, A. Ayral, Nanocrystalline TiO_2 thin film prepared by low-temperature plasma-enhanced chemical vapor deposition for photocatalytic applications, Thin Solid Films 589 (2015) 770-777.
[31] L. Escobar-Alarcón, D.A. Solís-Casados, J. Perez-Alvarez, S. Romero, J.G. Morales-Mendez, E. Haro-Poniatowski, Preparation of Bi:TiO_2 thin films by an hybrid deposition configuration: pulsed laser deposition and thermal evaporation, Appl. Phys. A (2014) 1-5.
[32] H. Wang, X. Liu, X. Liu, Q. Guan, P. Huo, Y. Yan, Enhancement of photocatalytic activity on salicylic acid by nonmetal-doped TiO_2 with solvothermal method, Desalination and Water Treatment 54(9) (2015) 2504-2515.
[33] D. Li, M. Wang, C. Luo, C. Pan, Preparation of TiO_2-Coated Mo Powders for High Photocatalytic Property, Journal of the American Ceramic Society (2015) n/a-n/a.
[34] R. Mohammadi, B. Massoumi, H. Eskandarloo, Preparation and characterization of Sn/Zn/TiO_2 photocatalyst for enhanced amoxicillin trihydrate degradation, Desalination and Water Treatment 53(7) (2015) 1995-2004.
[35] D. Li, M. Wang, C. Luo, C. Pan, Preparation of TiO_2-Coated Mo Powders for High Photocatalytic Property, Journal of the American Ceramic Society 99(1) (2016) 79-83.
[36] M. Huang, S. Yu, B. Li, D. Lihui, F. Zhang, M. Fan, L. Wang, J. Yu, C. Deng, Influence of preparation methods on the structure and catalytic performance of SnO_2-doped TiO_2 photocatalysts, Ceramics International 40(8, Part B) (2014) 13305-13312.
[37] S.M. Gupta, M. Tripathi, A review on the synthesis of TiO_2 nanoparticles by solution route, Central European Journal of Chemistry 10(2) (2012) 279-294.
[38] Y.M. Evtushenko, S.V. Romashkin, V.V. Davydov, Synthesis and properties of TiO_2-based nanomaterials, Theoretical Foundations of Chemical Engineering 45(5) (2011) 731.
[39] X. Chen, S.S. Mao, Titanium Dioxide Nanomaterials: Synthesis, Properties, Modifications, and Applications, Chemical Reviews 107(7) (2007) 2891-2959.
[40] T.L. Thompson, J.T. Yates, Surface Science Studies of the Photoactivation of TiO_2 New Photochemical Processes, Chemical Reviews 106(10) (2006) 4428-4453.
[41] M. Ferdosi Heragh, S. Eskandarinezhad, A. Dehghan, Ni-Cu matrix composite reinforced with CNTs: preparation, characterization, wear and corrosion behavior, inhibitory effects, Journal of Composites and Compounds 2(4) (2020).
[42] K. Elghniji, M. Ksibi, E. Elaloui, Sol–gel reverse micelle preparation and characterization of N-doped TiO_2 : Efficient photocatalytic degradation of methylene blue in water under visible light, Journal of Industrial and Engineering Chemistry 18(1) (2012) 178-182.
[43] E.K.K.a.G.A.G. RAJ, Preparation, Characterization and Photocatalytic Behaviour of Codoped Nanophotocatalyst, Chemical Science Transactions 2(4) (2013) 1282.
[44] Ramona- Crina Suciu, Marcela Corina Roşu, Teofil Dănuţ Silipaş, Emil Indrea, Violeta Popescu, G.L. Popescu, Fe_2O_3 – TiO_2 THIN FILMS PREPARED BY

SOL-GEL METHOD, Environmental Engineering and Management Journal 10(2) (2011) 187-192.
[45] H. Choi, E. Stathatos, D.D. Dionysiou, Synthesis of nanocrystalline photocatalytic TiO_2 thin films and particles using sol–gel method modified with nonionic surfactants, Thin Solid Films 510(1–2) (2006) 107-114.
[46] P. Kunwanlee, T. Puangpetch, S. Chavadej, Preparation and photocatalytic activity of mesoporous-assembled nano-titania thin films derived from a laurylamine hydrochloride surfactant-aided sol–gel method, Materials Science in Semiconductor Processing 26(0) (2014) 567-574.
[47] G. Oskam, A. Nellore, R.L. Penn, P.C. Searson, The Growth Kinetics of TiO_2 Nanoparticles from Titanium(IV) Alkoxide at High Water/Titanium Ratio, The Journal of Physical Chemistry B 107(8) (2003) 1734-1738.
[48] H.H. Kung, E.I. Ko, Preparation of oxide catalysts and catalyst supports — a review of recent advances, The Chemical Engineering Journal and the Biochemical Engineering Journal 64(2) (1996) 203-214.
[49] C.J. Brinker, R. Sehgal, S.L. Hietala, R. Deshpande, D.M. Smith, D. Loy, C.S. Ashley, Sol-gel strategies for controlled porosity inorganic materials, Journal of Membrane Science 94(1) (1994) 85-102.
[50] J.D. Mackenzie, E.P. Bescher, Chemical Routes in the Synthesis of Nanomaterials Using the Sol–Gel Process, Accounts of Chemical Research 40(9) (2007) 810-818.
[51] Z. Goudarzi, N. Parvin, F. Sharifianjazi, Formation of hydroxyapatite on surface of SiO_2– P_2O_5–CaO–SrO–ZnO bioactive glass synthesized through sol-gel route, Ceramics International 45(15) (2019) 19323-19330.
[52] M. Simonsen, E. Søgaard, Sol–gel reactions of titanium alkoxides and water: influence of pH and alkoxy group on cluster formation and properties of the resulting products, J Sol-Gel Sci Technol 53(3) (2010) 485-497.
[53] B. Yoldas, Hydrolysis of titanium alkoxide and effects of hydrolytic polycondensation parameters, J Mater Sci 21(3) (1986) 1087-1092.
[54] J. Sekulic, J.E. ten Elshof, D.H.A. Blank, Synthesis and Characterization of Microporous Titania Membranes, J Sol-Gel Sci Technol 31(1-3) (2004) 201-204.
[55] N. Wetchakun, B. Incessungvorn, K. Wetchakun, S. Phanichphant, Influence of calcination temperature on anatase to rutile phase transformation in TiO_2 nanoparticles synthesized by the modified sol–gel method, Materials Letters 82(0) (2012) 195-198.
[56] H. Choi, E. Stathatos, D.D. Dionysiou, Sol–gel preparation of mesoporous photocatalytic TiO_2 films and TiO_2 /Al_2O_3 composite membranes for environmental applications, Applied Catalysis B: Environmental 63(1–2) (2006) 60-67.
[57] E. Stathatos, P. Lianos, C. Tsakiroglou, Highly efficient nanocrystalline titania films made from organic/inorganic nanocomposite gels, Microporous and Mesoporous Materials 75(3) (2004) 255-260.
[58] A. Attar, M. Ghamsari, F. Hajiesmaeilbaigi, S. Mirdamadi, Modifier ligands effects on the synthesized TiO_2 nanocrystals, J Mater Sci 43(5) (2008) 1723-1729.
[59] C. Su, B.Y. Hong, C.M. Tseng, Sol–gel preparation and photocatalysis of titanium dioxide, Catalysis Today 96(3) (2004) 119-126.
[60] V. Kessler, G. Spijksma, G. Seisenbaeva, S. Håkansson, D.A. Blank, H.M. Bouwmeester, New insight in the role of modifying ligands in the sol-gel processing of metal alkoxide precursors: A possibility to approach new classes of materials, J Sol-Gel Sci Technol 40(2-3) (2006) 163-179.
[61] E. Scolan, C. Sanchez, Synthesis and Characterization of Surface-Protected Nanocrystalline Titania Particles, Chemistry of Materials 10(10) (1998) 3217-3223.
[62] R. Parra, M.S. Góes, M.S. Castro, E. Longo, P.R. Bueno, J.A. Varela, Reaction Pathway to the Synthesis of Anatase via the Chemical Modification of Titanium Isopropoxide with Acetic Acid, Chemistry of Materials 20(1) (2007) 143-150.
[63] M. Ivanda, S. Musić, S. Popović, M. Gotić, XRD, Raman and FT-IR spectroscopic observations of nanosized TiO_2 synthesized by the sol–gel method based on an esterification reaction, Journal of Molecular Structure 480–481(0) (1999) 645-649.
[64] C. Wang, Z.-X. Deng, Y. Li, The Synthesis of Nanocrystalline Anatase and Rutile Titania in Mixed Organic Media, Inorganic Chemistry 40(20) (2001) 5210-5214.
[65] V. Salimian Rizi, F. Sharifianjazi, H. Jafarikhorami, N. Parvin, L. Saei Fard, M. Irani, A. Esmaeilkhanian, Sol–gel derived SnO_2/Ag_2O ceramic nanocomposite for H_2 gas sensing applications, Materials Research Express 6(11) (2019) 1150g2.
[66] F.A. Harraz, O.E. Abdel-Salam, A.A. Mostafa, R.M. Mohamed, M. Hanafy, Rapid synthesis of titania–silica nanoparticles photocatalyst by a modified sol–gel method for cyanide degradation and heavy metals removal, Journal of Alloys and Compounds 551(0) (2013) 1-7.
[67] M. Crişan, N. Drăgan, D. Crişan, A. Ianculescu, I. Niţoi, P. Oancea, L. Todan, C. Stan, N. Stănică, The effects of Fe, Co and Ni dopants on TiO_2 structure of sol–gel nanopowders used as photocatalysts for environmental protection: A comparative study, Ceramics International 42(2, Part B) (2016) 3088-3095.
[68] R. Tang, Q. Jiang, Y. Liu, Preparation and Study on Photocatalytic Activity of N-doped TiO_2 Decorated N-doped graphene, Procedia Engineering 205(Supplement C) (2017) 573-580.
[69] B. Palanisamy, C.M. Babu, B. Sundaravel, S. Anandan, V. Murugesan, Sol–gel synthesis of mesoporous mixed Fe_2O_3/TiO_2 photocatalyst: Application for degradation of 4-chlorophenol, Journal of Hazardous Materials 252–253(0) (2013) 233-242.
[70] R. Roy, Accelerating the Kinetics of Low-Temperature Inorganic Syntheses, Journal of Solid State Chemistry 111(1) (1994) 11-17.
[71] R.-C. Xie, J. Shang, Morphological control in solvothermal synthesis of titanium oxide, J Mater Sci 42(16) (2007) 6583-6589.
[72] A. Simpraditpan, T. Wirunmongkol, W. Boonwatcharapunsakun, S. Pivsa-art, C. Duangduen, S. Sakulkhaemaruethai, S. Pavasupree, Preparation of High Photocatalyst Mesoporous TiO_2 from Nanosheets Using Autoclave Unit (Thai Made), Energy Procedia 9(0) (2011) 440-445.
[73] A. Simpraditpan, T. Wirunmongkol, S. Pavasupree, W. Pecharapa, Effect of calcination temperature on structural and photocatalyst properties of nanofibers prepared from low-cost natural ilmenite mineral by simple hydrothermal method, Materials Research Bulletin 48(9) (2013) 3211-3217.
[74] N. Liu, X. Chen, J. Zhang, J.W. Schwank, A review on TiO_2-based nanotubes synthesized via hydrothermal method: Formation mechanism, structure modification, and photocatalytic applications, Catalysis Today 225(0) (2014) 34-51.
[75] X. Zhao, M. Liu, Y. Zhu, Fabrication of porous TiO_2 film via hydrothermal method and its photocatalytic performances, Thin Solid Films 515(18) (2007) 7127-7134.
[76] G. Ren, Y. Gao, X. Liu, A. Xing, H. Liu, J. Yin, Synthesis of high-activity F-doped TiO_2 photocatalyst via a simple one-step hydrothermal process, Reac Kinet Mech Cat 100(2) (2010) 487-497.
[77] Y.B. Ryu, M.S. Lee, S.S. Park, G.-D. Lee, S.-S. Hong, Effect of synthesis temperature on the preparation of titanium dioxides by the hydrothermal method. Photocatalytic activity, React Kinet Catal Lett 84(1) (2005) 101-108.
[78] Y. Li, M. Zhang, M. Guo, X. Wang, Hydrothermal growth of well-aligned TiO_2 nanorod arrays: Dependence of morphology upon hydrothermal reaction conditions, Rare Metals 29(3) (2010) 286-291.
[79] Y. Wang, L. Zhang, K. Deng, X. Chen, Z. Zou, Low Temperature Synthesis and Photocatalytic Activity of Rutile TiO_2 Nanorod Superstructures, The Journal of Physical Chemistry C 111(6) (2007) 2709-2714.
[80] J. Ju, X. Chen, Y. Shi, J. Miao, D. Wu, Hydrothermal preparation and photocatalytic performance of N, S-doped nanometer TiO_2 under sunshine irradiation, Powder Technology 237(0) (2013) 616-622.
[81] X. Shi, X. Yang, S. Wang, S. Wang, Q. Zhang, Y. Wang, Photocatalytic degradation of rhodamine B Dye with high purity anatase nano-TiO_2 synthesized by a hydrothermal method, J. Wuhan Univ. Technol.-Mat. Sci. Edit. 26(4) (2011) 600-605.
[82] J. Li, T. Wang, X. Du, Preparation of visible light-driven SnS_2/TiO_2 nanocomposite photocatalyst for the reduction of aqueous Cr(VI), Separation and Purification Technology 101(0) (2012) 11-17.
[83] S.A.K. Leghari, S. Sajjad, F. Chen, J. Zhang, WO3/TiO_2 composite with morphology change via hydrothermal template-free route as an efficient visible light photocatalyst, Chemical Engineering Journal 166(3) (2011) 906-915.
[84] I. Tajzad, E. Ghasali, Production methods of CNT-reinforced Al matrix composites: a review, Journal of Composites and Compounds 2(2) (2020).
[85] S. Saadi, B. Nazari, Recent developments and applications of nanocomposites in solar cells: a review, Journal of Composites and Compounds 1(1) (2019).
[86] F.S. Jazi, N. Parvin, M. Tahriri, M. Alizadeh, S. Abedini, M. Alizadeh, The Relationship Between the Synthesis and Morphology of SnO_2-Ag_2O Nanocomposite, Synthesis and Reactivity in Inorganic, Metal-Organic, and Nano-Metal Chemistry 44(5) (2014) 759-764.
[87] J. Liu, T. An, G. Li, N. Bao, G. Sheng, J. Fu, Preparation and characterization of highly active mesoporous TiO_2 photocatalysts by hydrothermal synthesis under weak acid conditions, Microporous and Mesoporous Materials 124(1–3) (2009) 197-203.
[88] S. Ding, L. Wang, S. Zhang, Q. Zhou, Y. Ding, S. Liu, Y. Liu, Q. Kang, Hydrothermal synthesis, structure and photocatalytic property of nano-TiO_2-MnO_2, Sc. China Ser. B-Chem. 46(6) (2003) 542-548.
[89] S.-H. Lee, M. Kang, S.M. Cho, G.Y. Han, B.-W. Kim, K.J. Yoon, C.-H. Chung, Synthesis of TiO_2 photocatalyst thin film by solvothermal method with a small amount of water and its photocatalytic performance, Journal of Photochemistry and Photobiology A: Chemistry 146(1–2) (2001) 121-128.
[90] Y.-r. Wang, W.-y. Li, B. Zhou, X. Zhao, Synthesis and characterization of SnO_2-TiO_2 nanocomposite with rutile-phase via hydrothermal method at low tem-

perature, Chem. Res. Chin. Univ. 29(4) (2013) 617-620.
[91] W. Kongsuebchart, P. Praserthdam, J. Panpranot, A. Sirisuk, P. Supphasrirongjaroen, C. Satayaprasert, Effect of crystallite size on the surface defect of nano-TiO_2 prepared via solvothermal synthesis, Journal of Crystal Growth 297(1) (2006) 234-238.
[92] CHAU THANH NAM, W.-D. YANG, a.L.M. DUC, Study on photocatalysis of TiO_2 nanotubes prepared by methanol-thermal synthesis at low temperature, Bull. Mater. Sci. 36(5) (2013) 779-788.
[93] Bin Liu, Yuhua Wang, Yongji Huang, P. Dong, a.S. Yin, Morphological Control and Photocatalytic Activities of Nitrogen-doped Titania Nanoparticles by Microwave-assisted Solvothermal Process, Journal of the Australian Ceramic Society Volume 48(2) (2012) 249-252.
[94] K. Byrappa, T. Adschiri, Hydrothermal technology for nanotechnology, Progress in Crystal Growth and Characterization of Materials 53(2) (2007) 117-166.
[95] R.E. Riman, W.L. Suchanek, M.M. Lencka, Hydrothermal crystallization of ceramics, Annales de Chimie Science des Matériaux 27(6) (2002) 15-36.
[96] S. Sōmiya, R. Roy, Hydrothermal synthesis of fine oxide powders, Bull Mater Sci 23(6) (2000) 453-460.
[97] A. Moghanian, F. Sharifianjazi, P. Abachi, E. Sadeghi, H. Jafarikhorami, A. Sedghi, Production and properties of Cu/TiO_2 nano-composites, Journal of Alloys and Compounds 698 (2017) 518-524.
[98] T. Sugimoto, X. Zhou, A. Muramatsu, Synthesis of uniform anatase TiO_2 nanoparticles by gel–sol method: 3. Formation process and size control, Journal of Colloid and Interface Science 259(1) (2003) 43-52.
[99] F. Wang, Z. Shi, F. Gong, J. Jiu, M. Adachi, Morphology Control of Anatase TiO_2 by Surfactant-assisted Hydrothermal Method, Chinese Journal of Chemical Engineering 15(5) (2007) 754-759.
[100] M.S.N. Shahrbabak, F. Sharifianjazi, D. Rahban, A. Salimi, A Comparative Investigation on Bioactivity and Antibacterial Properties of Sol-Gel Derived 58S Bioactive Glass Substituted by Ag and Zn, Silicon 11(6) (2019) 2741-2751.
[101] X. Zhang, M. Zhou, L. Lei, Preparation of photocatalytic TiO_2 coatings of nanosized particles on activated carbon by AP-MOCVD, Carbon 43(8) (2005) 1700-1708.
[102] M. Wojtoniszak, D. Dolat, A. Morawski, E. Mijowska, Carbon-modified TiO_2 for photocatalysis, Nanoscale Res Lett 7(1) (2012) 1-6.
[103] W. Li, S. Ismat Shah, C.P. Huang, O. Jung, C. Ni, Metallorganic chemical vapor deposition and characterization of TiO_2 nanoparticles, Materials Science and Engineering: B 96(3) (2002) 247-253.
[104] K.T. Raić, Formation of nanoparticles by CVD technique, Metalurgija 8(3) (2002) 191-200.
[105] C.-S. Kuo, Y.-H. Tseng, C.-H. Huang, Y.-Y. Li, Carbon-containing nano-titania prepared by chemical vapor deposition and its visible-light-responsive photocatalytic activity, Journal of Molecular Catalysis A: Chemical 270(1–2) (2007) 93-100.
[106] X. Zhang, M. Zhou, L. Lei, Preparation of an Ag–TiO_2 photocatalyst coated on activated carbon by MOCVD, Materials Chemistry and Physics 91(1) (2005) 73-79.
[107] X. Zhang, M. Zhou, L. Lei, TiO_2 photocatalyst deposition by MOCVD on activated carbon, Carbon 44(2) (2006) 325-333.
[108] G. Li Puma, A. Bono, D. Krishnaiah, J.G. Collin, Preparation of titanium dioxide photocatalyst loaded onto activated carbon support using chemical vapor deposition: A review paper, Journal of Hazardous Materials 157(2–3) (2008) 209-219.
[109] T.S.S. J.H Park, Chemical Vapor Deposition.
[110] A.C.J.a.P. O'Brien, Chemical Vapour Deposition: Precursors, Processes and Applications.
[111] Y. Cao, X. Zhang, W. Yang, H. Du, Y. Bai, T. Li, J. Yao, A Bicomponent TiO_2 /SnO_2 Particulate Film for Photocatalysis, Chemistry of Materials 12(11) (2000) 3445-3448.
[112] C.W.H. Dunnill, Z.A. Aiken, J. Pratten, M. Wilson, D.J. Morgan, I.P. Parkin, Enhanced photocatalytic activity under visible light in N-doped TiO_2 thin films produced by APCVD preparations using t-butylamine as a nitrogen source and their potential for antibacterial films, Journal of Photochemistry and Photobiology A: Chemistry 207(2–3) (2009) 244-253.
[113] R.Q. Cabrera, E.R. Latimer, A. Kafizas, C.S. Blackman, C.J. Carmalt, I.P. Parkin, Photocatalytic activity of needle-like TiO_2 /WO_{3-x} thin films prepared by chemical vapour deposition, Journal of Photochemistry and Photobiology A: Chemistry 239(0) (2012) 60-64.
[114] A. Sobczyk-Guzenda, B. Pietrzyk, H. Szymanowski, M. Gazicki-Lipman, W. Jakubowski, Photocatalytic activity of thin TiO_2 films deposited using sol–gel and plasma enhanced chemical vapor deposition methods, Ceramics International 39(3) (2013) 2787-2794.
[115] S.-C. Jung, N. Imaishi, Preparation, crystal structure, and photocatalytic activity of TiO_2 films by chemical vapor deposition, Korean J. Chem. Eng. 18(6) (2001) 867-872.
[116] H. Lee, M.Y. Song, J. Jurng, Y.-K. Park, The synthesis and coating process of TiO_2 nanoparticles using CVD process, Powder Technology 214(1) (2011) 64-68.
[117] Li W, Shah SI, Huang C-P, Jung O, N. C., Metalorganic chemical vapor deposition and characterization of TiO_2 nanoparticles, Mater Sci Eng B 96(3) (2002) 247-253.
[118] D.S. Bhachu, S. Sathasivam, C.J. Carmalt, I.P. Parkin, PbO-Modified TiO_2 Thin Films: A Route to Visible Light Photocatalysts, Langmuir 30(2) (2013) 624-630.
[119] L. Lei, H.P. Chu, X. Hu, P.-L. Yue, Preparation of Heterogeneous Photocatalyst (TiO_2 /Alumina) by Metallo-Organic Chemical Vapor Deposition, Industrial & Engineering Chemistry Research 38(9) (1999) 3381-3385.
[120] Z. Ding, X. Hu, G.Q. Lu, P.-L. Yue, P.F. Greenfield, Novel Silica Gel Supported TiO_2 Photocatalyst Synthesized by CVD Method, Langmuir 16(15) (2000) 6216-6222.
[121] G.H. Kim, S.D. Kim, S.H. Park, Plasma enhanced chemical vapor deposition of TiO_2 films on silica gel powders at atmospheric pressure in a circulating fluidized bed reactor, Chemical Engineering and Processing: Process Intensification 48(6) (2009) 1135-1139.
[122] P. Hajkova, P. Spatenka, J. Krumeich, P. Exnar, A. Kolouch, J. Matousek, The Influence of Surface Treatment on Photocatalytic Activity of PE CVD TiO_2 Thin Films, Plasma Processes and Polymers 6(S1) (2009) S735-S740.
[123] S. Mathur, P. Kuhn, CVD of titanium oxide coatings: Comparative evaluation of thermal and plasma assisted processes, Surface and Coatings Technology 201(3–4) (2006) 807-814.
[124] M.Y. Song, Y.-K. Park, J. Jurng, Direct coating of V_2O_5/TiO_2 nanoparticles onto glass beads by chemical vapor deposition, Powder Technology 231(0) (2012) 135-140.
[125] R.K. Bhakta, Rational development of precursors for MOCVD of TiO_2 : precursor chemistry, thin film deposition, mechanistic studies. <http://www-brs.ub.ruhr-uni-bochum.de/netahtml/HSS/Diss/BhaktaRaghunandanKrishna/diss.pdf>, 2005).
[126] A.C. Jones, Molecular design of improved precursors for the MOCVD of electroceramic oxides, Journal of Materials Chemistry 12(9) (2002) 2576-2590.
[127] L.G. Hubert-Pfalzgraf, H. Guillon, Trends in precursor design for conventional and aerosol-assisted CVD of high-Tc superconductors, Applied Organometallic Chemistry 12(3) (1998) 221-236.
[128] V.G. Bessergenev, R.J.F. Pereira, M.C. Mateus, I.V. Khmelinskii, D.A. Vasconcelos, R. Nicula, E. Burkel, A.M. Botelho do Rego, A.I. Saprykin, Study of physical and photocatalytic properties of titanium dioxide thin films prepared from complex precursors by chemical vapour deposition, Thin Solid Films 503(1–2) (2006) 29-39.
[129] X.T.Y. Y. XU, Chemical Vapour Deposition.
[130] X.-w. Zhang, M.-h. Zhou, L.-c. Lei, S. Xu, Synthesis of TiO_2 supported on activated carbon by MOCVD: operation parameters study, J. Zheijang Univ.-Sci. 5(12) (2004) 1548-1553.
[131] J.-O. Choo, R.A. Adomaitis, G.W. Rubloff, L. Henn-Lecordier, Y. Liu, Simulation-based design and experimental evaluation of a spatially controllable CVD reactor, AIChE Journal 51(2) (2005) 572-584.
[132] K.L. Choy, Chemical vapour deposition of coatings, Progress in Materials Science 48(2) (2003) 57-170.
[133] S. Bondi, W. Lackey, R. Johnson, X. Wang, Z. Wang, Laser assisted chemical vapor deposition synthesis of carbon nanotubes and their characterization, Carbon 44(8) (2006) 1393-1403.
[134] P. O'Brien, N.L. Pickett, D.J. Otway, Developments in CVD Delivery Systems: A Chemist's Perspective on the Chemical and Physical Interactions Between Precursors, Chemical Vapor Deposition 8(6) (2002) 237-249.
[135] M.W. Pyun, E.J. Kim, D.-H. Yoo, S.H. Hahn, Oblique angle deposition of TiO_2 thin films prepared by electron-beam evaporation, Applied Surface Science 257(4) (2010) 1149-1153.
[136] N.T. Khoa, M.W. Pyun, D.-H. Yoo, S.W. Kim, J.-Y. Leem, E.J. Kim, S.H. Hahn, Photodecomposition effects of graphene oxide coated on TiO_2 thin film prepared by electron-beam evaporation method, Thin Solid Films 520(16) (2012) 5417-5420.
[137] W.K. Lee, E.J. Kim, S.H. Hahn, Structural and photocatalytic properties of TiO_2 /SiO_x/TiO_x multi-layer prepared by electron-beam evaporation method, Vacuum 85(1) (2010) 30-33.
[138] T.-S. Yang, M.-C. Yang, C.-B. Shiu, W.-K. Chang, M.-S. Wong, Effect of N2 ion flux on the photocatalysis of nitrogen-doped titanium oxide films by electron-beam evaporation, Applied Surface Science 252(10) (2006) 3729-3736.

[139] S.-W. Hsu, T.-S. Yang, T.-K. Chen, M.-S. Wong, Ion-assisted electron-beam evaporation of carbon-doped titanium oxide films as visible-light photocatalyst, Thin Solid Films 515(7–8) (2007) 3521-3526.
[140] P. Eiamchai, P. Chindaudom, A. Pokaipisit, P. Limsuwan, A spectroscopic ellipsometry study of TiO_2 thin films prepared by ion-assisted electron-beam evaporation, Current Applied Physics 9(3) (2009) 707-712.
[141] T. Luttrell, S. Halpegamage, E. Sutter, M. Batzill, Photocatalytic activity of anatase and rutile TiO_2 epitaxial thin film grown by pulsed laser deposition, Thin Solid Films 564(0) (2014) 146-155.
[142] P.B. Nair, V.B. Justinvictor, G.P. Daniel, K. Joy, V. Ramakrishnan, P.V. Thomas, Effect of RF power and sputtering pressure on the structural and optical properties of TiO_2 thin films prepared by RF magnetron sputtering, Applied Surface Science 257(24) (2011) 10869-10875.
[143] C.H. Huang, C.C. Tsao, C.Y. Hsu, Study on the photocatalytic activities of TiO_2 films prepared by reactive RF sputtering, Ceramics International 37(7) (2011) 2781-2788.
[144] C. Ma, W. Dong, L. Fang, F. Zheng, M. Shen, Z. Wang, Synthesis of TiO_2 /Pt/TiO_2 multilayer films via radio frequency magnetron sputtering and their enhanced photocatalytic activity, Thin Solid Films 520(17) (2012) 5727-5732.
[145] M.-C. Wang, H.-J. Lin, C.-H. Wang, H.-C. Wu, Effects of annealing temperature on the photocatalytic activity of N-doped TiO_2 thin films, Ceramics International 38(1) (2012) 195-200.
[146] B. Barrocas, O.C. Monteiro, M.E.M. Jorge, S. Sério, Photocatalytic activity and reusability study of nanocrystalline TiO_2 films prepared by sputtering technique, Applied Surface Science 264(0) (2013) 111-116.
[147] Z. Wang, N. Yao, X. Hu, X. Shi, Structural and photocatalytic study of titanium dioxide films deposited by DC sputtering, Materials Science in Semiconductor Processing 21(0) (2014) 91-97.
[148] W. Zhang, K. Wang, S. Zhu, Y. Li, F. Wang, H. He, Yttrium-doped TiO_2 films prepared by means of DC reactive magnetron sputtering, Chemical Engineering Journal 155(1–2) (2009) 83-87.
[149] C. Zhang, W. Ding, H. Wang, W. Chai, D. Ju, Influences of working pressure on properties for TiO_2 films deposited by DC pulse magnetron sputtering, Journal of Environmental Sciences 21(6) (2009) 741-744.
[150] X. Yu, Z. Shen, Photocatalytic TiO_2 films deposited on cenosphere particles by pulse magnetron sputtering method, Vacuum 85(11) (2011) 1026-1031.
[151] V. Meille, Review on methods to deposit catalysts on structured surfaces, Applied Catalysis A: General 315(0) (2006) 1-17.
[152] A. Mubarak, E. Hamzah, M.R.M. Toff, REVIEW OF PHYSICAL VAPOUR DEPOSITION (PVD) TECHNIQUES FOR HARD COATING, Jurnal Mekanikal 20 (2005) 42-51.
[153] H.-U. Krebs, M. Weisheit, J. Faupel, E. Süske, T. Scharf, C. Fuhse, M. Störmer, K. Sturm, M. Seibt, H. Kijewski, D. Nelke, E. Panchenko, M. Buback, Pulsed Laser Deposition (PLD)- A Versatile Thin Film Technique, in: B. Kramer (Ed.), Advances in Solid State Physics, Springer Berlin Heidelberg2003, pp. 505-518.
[154] A. Perrone, A. Zocco, L. Cultrera, D. Guido, Detailed studies of the plume deflection effect during long laser irradiation of solid targets, Applied Surface Science 197–198(0) (2002) 251-256.
[155] Y. Suda, H. Kawasaki, T. Ueda, T. Ohshima, Preparation of high quality nitrogen doped TiO_2 thin film as a photocatalyst using a pulsed laser deposition method, Thin Solid Films 453–454(0) (2004) 162-166.
[156] A. Khodorov, S. Levichev, A. Chahboun, A.G. Rolo, S. Bernstorff, N.P. Barradas, E. Alves, M.J.M. Gomes, Growth and characterization of Mn-doped ZnO/TiO_2 multilayer nanostructures grown by pulsed laser deposition, physica status solidi (c) 7(11-12) (2010) 2724-2726.
[157] S.-S. Lin, Y.-H. Hung, S.-C. Chen, The Properties of TiO_2 Nanoceramic Films Prepared by Electron Beam Evaporation, Journal of Nanoscience and Nanotechnology 9(6) (2009) 3599-3605.
[158] Z. Lu, X. Jiang, B. Zhou, X. Wu, L. Lu, Study of effect annealing temperature on the structure, morphology and photocatalytic activity of Si doped TiO_2 thin films deposited by electron beam evaporation, Applied Surface Science 257(24) (2011) 10715-10720.
[159] R. Schmidt, M. Parlak, A.W. Brinkman, Control of the thickness distribution of evaporated functional electroceramic NTC thermistor thin films, Journal of Materials Processing Technology 199(1–3) (2008) 412-416.
[160] J. Singh, D.E. Wolfe, Review Nano and macro-structured component fabrication by electron beam-physical vapor deposition (EB-PVD), J Mater Sci 40(1) (2005) 1-26.
[161] J.Z. Shi, C.Z. Chen, H.J. Yu, S.J. Zhang, Application of magnetron sputtering for producing bioactive ceramic coatings on implant materials, Bull Mater Sci 31(6) (2008) 877-884.
[162] S.-S. Lin, The optical properties of Ti-doped TiO_2 nanoceramic films deposited by simultaneous rf and dc magnetron sputtering, Ceramics International 38(4) (2012) 3129-3134.
[163] Wenjie ZHANG, Shenglong ZHU, Y.L.a.F. WANG, Photocatalytic Property of TiO_2 Films Deposited by Pulse DC Magnetron Sputtering, J. Mater. Sci. Technol 20(1) (2004).
[164] V. Claudia, L. Francis, P.V. I, Photocatalytic degradation of acetone on ZnO-dopped TiO_2 films prepared by sputtering, Revue Roumaine de Chimie 51(7-8) (2006) 827-833.
[165] S.K. Zheng, T.M. Wang, G. Xiang, C. Wang, Photocatalytic activity of nanostructured TiO_2 thin films prepared by dc magnetron sputtering method, Vacuum 62(4) (2001) 361-366.
[166] P. Pansila, N. Witit-anun, S. Chaiyakun, Influence of sputtering power on structure and photocatalyst properties of DC magnetron sputtered TiO_2 thin film, Procedia Engineering 32(0) (2012) 862-867.
[167] Y. Song, J. Zhang, H. Yang, S. Xu, L. Jiang, Y. Dan, Preparation and visible light-induced photo-catalytic activity of H-PVA/TiO_2 composite loaded on glass via sol–gel method, Applied Surface Science 292(0) (2014) 978-985.
[168] M.Y. Abdelaal, R.M. Mohamed, Novel Pd/TiO_2 nanocomposite prepared by modified sol–gel method for photocatalytic degradation of methylene blue dye under visible light irradiation, Journal of Alloys and Compounds 576(0) (2013) 201-207.
[169] F. Oshani, R. Marandi, S. Rasouli, M.K. Farhoud, Photocatalytic investigations of TiO_2 –P_{25} nanocomposite thin films prepared by peroxotitanic acid modified sol–gel method, Applied Surface Science 311(0) (2014) 308-313.
[170] Y. You, S. Zhang, L. Wan, D. Xu, Preparation of continuous TiO_2 fibers by sol–gel method and its photocatalytic degradation on formaldehyde, Applied Surface Science 258(8) (2012) 3469-3474.
[171] T.S. Jamil, T.A. Gad-Allah, M.E.M. Ali, M.N.B. Momba, Utilization of nano size TiO_2 for degradation of phenol enrich water by solar photocatalytic oxidation, Desalination and Water Treatment (2013) 1-6.
[172] N. Abbas, G.N. Shao, M.S. Haider, S.M. Imran, S.S. Park, H.T. Kim, Sol–gel synthesis of TiO_2-Fe_2O_3 systems: Effects of Fe_2O_3 content and their photocatalytic properties, Journal of Industrial and Engineering Chemistry 39 (2016) 112-120.
[173] I. Singh, R. Kumar, B.I. Birajdar, Zirconium doped TiO_2 nano-powder via halide free non-aqueous solvent controlled sol-gel route, Journal of Environmental Chemical Engineering.
[174] S.I. Al-Mayman, M.S. Al-Johani, M.M. Mohamed, Y.S. Al-Zeghayer, S.M. Ramay, A.S. Al-Awadi, M.A. Soliman, TiO_2 ZnO photocatalysts synthesized by sol–gel auto-ignition technique for hydrogen production, International Journal of Hydrogen Energy 42(8) (2017) 5016-5025.
[175] A.C. Martins, A.L. Cazetta, O. Pezoti, J.R.B. Souza, T. Zhang, E.J. Pilau, T. Asefa, V.C. Almeida, Sol-gel synthesis of new TiO_2 /activated carbon photocatalyst and its application for degradation of tetracycline, Ceramics International 43(5) (2017) 4411-4418.
[176] W.-H. Yuan, Z.-L. Xia, L. Li, Synthesis and photocatalytic properties of core–shell TiO_2 @$ZnIn_2S_4$ photocatalyst, Chinese Chemical Letters 24(11) (2013) 984-986.
[177] N.R. Khalid, E. Ahmed, Z. Hong, M. Ahmad, Synthesis and photocatalytic properties of visible light responsive La/TiO_2-graphene composites, Applied Surface Science 263(0) (2012) 254-259.
[178] Z. He, W. Que, J. Chen, X. Yin, Y. He, J. Ren, Photocatalytic Degradation of Methyl Orange over Nitrogen–Fluorine Codoped TiO_2 Nanobelts Prepared by Solvothermal Synthesis, ACS Applied Materials & Interfaces 4(12) (2012) 6816-6826.
[179] H.R. Pant, B. Pant, R.K. Sharma, A. Amarjargal, H.J. Kim, C.H. Park, L.D. Tijing, C.S. Kim, Antibacterial and photocatalytic properties of Ag/TiO_2 /ZnO nano-flowers prepared by facile one-pot hydrothermal process, Ceramics International 39(2) (2013) 1503-1510.
[180] M. Yao, J. Zhao, S. Lv, K. Lu, Preparation and hydrogenation of urchin-like titania using a one-step hydrothermal method, Ceramics International 43(9) (2017) 6925-6931.
[181] S. Min, J. Hou, Y. Lei, X. Ma, G. Lu, Facile one-step hydrothermal synthesis toward strongly coupled TiO_2 /graphene quantum dots photocatalysts for efficient hydrogen evolution, Applied Surface Science 396 (2017) 1375-1382.
[182] R. Hao, G. Wang, C. Jiang, H. Tang, Q. Xu, In situ hydrothermal synthesis of g-C3N4/TiO_2 heterojunction photocatalysts with high specific surface area for Rhodamine B degradation, Applied Surface Science 411 (2017) 400-410.
[183] U. Alam, M. Fleisch, I. Kretschmer, D. Bahnemann, M. Muneer, One-step hydrothermal synthesis of Bi-TiO_2 nanotube/graphene composites: An efficient photocatalyst for spectacular degradation of organic pollutants under visible light irradiation, Applied Catalysis B: Environmental.

[184] Z. Tian, N. Yu, Y. Cheng, Z. Wang, Z. Chen, L. Zhang, Hydrothermal synthesis of graphene/TiO_2 /CdS nanocomposites as efficient visible-light-driven photocatalysts, Materials Letters 194 (2017) 172-175.
[185] C.C. Chen, W.J. Yang, C.Y. Hsu, Investigation into the effects of deposition parameters on TiO_2 photocatalyst thin films by rf magnetron sputtering, Superlattices and Microstructures 46(3) (2009) 461-468.
[186] S.-J. Shen, T.-S. Yang, M.-S. Wong, Co-sputtered boron-doped titanium dioxide films as photocatalysts, Surface and Coatings Technology 303 (2016) 184-190.
[187] M. Lelis, S. Tuckute, S. Varnagiris, M. Urbonavicius, G. Laukaitis, K. Bockute, Tailoring of TiO_2 film microstructure by pulsed-DC and RF magnetron co-sputtering, Surface and Coatings Technology 377 (2019) 124906.

Available online at www.jourcc.com

Journal homepage: www.JOURCC.com

Journal of Composites and Compounds

Application of different nanocatalysts in industrial effluent treatment: A review

Sara Eskandarinezhad [a] , Reza Khosravi [b], Mohamadamin Amarzadeh [c], Piyal Mondal [d], Fernando Jorge Correa Magalhães Filho [e]*

[a] *Department of Mining and Metallurgy, Yazd University, Yazd, Iran*
[b] *Department of Chemical Engineering, Faculty of Engineering, Ferdowsi University of Mashhad, Mashhad, Iran*
[c] *Department of Safety Engineering, Abadan Faculty of Petroleum Engineering, Petroleum University of Technology, Abadan, Iran*
[d] *Department of Chemical Engineering, Indian Institute of Technology Guwahati, Guwahati, 781039, India*
[e] *Departamento de Engenharia Sanitária e Ambiental, Universidade Católica Dom Bosco, Campo Grande, Brazil*

A B S T R A C T

The manufacturing, application, and design of chemical processes and products that minimize or remove waste and the use of dangerous and toxic reagents are referred to as green chemistry. Green chemistry is made up of twelve principles, one of which is catalysis. The role of catalysis is to accelerate the reaction by introducing a substance called a catalyst. Because of their high efficiency, productivity, activity, and selectivity, nanocatalysts have recently received many interests. Nanocatalysts are characterized by their high surface area to volume ratio, as well as their nanoscale forms and sizes. One of the significant applications of nanocatalysts is wastewater and wastewater purification. Green and bio-synthesized nanocatalysts could be used efficiently to remove heavy metals, medicinal, organic, and inorganic pollutants from the wastewater systems. This paper reviews nanocatalysts based on noble and magnetic nanocatalysts, as well as metal catalysts supported by organic polymers, and discusses their industrial effluent treatment mechanisms.

Peer review under responsibility of jourcc

A R T I C L E I N F O R M A T I O N

Article history:
Received 24 January 2021
Received in revised form 11 February 2021
Accepted 25 March 2021

Keywords:
Green chemistry
Magnetic nanocatalyst
Noble nanocatalysts
Organic polymer-supported metal catalysts

Table of contents

1. Introduction 43
2. Nanocatalysts 44
3. Application of various nanocatalysts in industrial effluent treatment 44
3.1. Nanocatalysts based on magnetic metals 44
3.2. Nanocatalysts based on noble metals 45
3.3. Nanocatalysts based on organic polymer-supported metal catalysts 47
4. Catalytic mechanisms 51
5. Conclusions and future insights 52

1. Introduction

The rapid expansion of various manufacturing sectors has adverse effects on the environment, particularly on the aquatic one, since most industries have wastewater composed of organic and inorganic pollutants with high concentration. As an example, various industries, including textile, paint, pharmaceutical, printing, leather, paper, and carpet, have produced daily a large number of aromatic pollutants, including many types of nitro compounds and dye. These industries would release large quantities of residual pollutants even if they were refined using conventional techniques [1-5]. Biodegradation of most of these aromatic pollutants dissolved in water is very hard, therefore becoming a long-term and direct toxic threat to aquatic and amphibian lives, animals, and microorganisms. Finally, this process affects humans since the lives on land depend on aquatic products and water, and some of these pollutants are extremely toxic, mutagenic, and carcinogenic [5-7].

Anastas and Warner in 1998 [8] proposed twelve principles called the principles of green chemistry to eliminate and reduce chemical substances and processes that are harmful to the environment. Fabrication and development of catalysts is an essential principle of green chemistry. These principles state that catalytic reagents are better than stoichiometric reagents since catalytic reagents are applied in small quantities and carry out one reaction several times, but stoichiometric reagents are

* *Corresponding author: Sara Eskandarinezhad; E-mail: s.eskandari.nezhad@gmail.com*
https://doi.org/10.52547/jcc.3.1.5

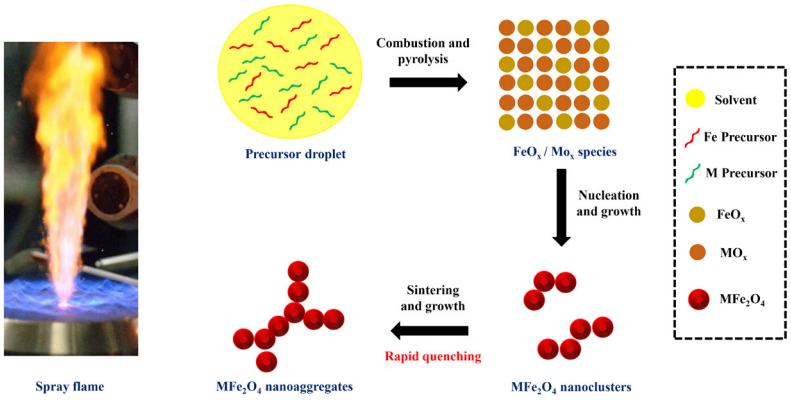

Fig. 1. Schematic illustration of the chainlike MFe_2O_4 nanoaggregates formation using spray flame.

applied further and work only once [9, 10]. The base of these twelve green chemistry principles is to work similarly to nature. If the catalyst is not used, humans' necessary products, such as lubricants, paints, fuels, fibers, polymers, fine chemicals, medicines, will not be produced. Catalysis is a process that helps chemical transformations take place, allowing for the industrial processing of required products [11, 12]. Therefore, applying catalyst fabrication methods can be rendered more sustainable, cost-effective, and environmentally friendly. Soft catalysts such as crown ethers (as phase transfer catalysts) and zeolites have more industrial applications than heavy metal catalysts, which are usually non-recoverable [13]. Enzymatic catalysis is the greenest and most effective catalysis in nature among three classifications of enzymatic, heterogeneous, and homogeneous catalysis. Heterogeneous and homogeneous catalysis has some advantages and limitations; therefore, it is crucial to create a novel catalytic mechanism that is easily recoverable and active, like heterogeneous and homogeneous catalysis, respectively [14].

Nanomaterials offer promising properties originating from their high surface area [15, 16]. Nanocatalysts have both advantages of the heterogeneous and homogeneous catalytic system [17, 18]. This system provides ease of catalyst recovery and separation as well as selective, and rapid chemical transformations with good product yield. One of the essential features of a catalyst is the ability to be recovered before being used in industry as green chemical manufacturing processes [19, 20]. One of the advantages of homogeneous catalysis is that the interaction between catalyst and reactants is significantly improved due to their nanosize and high surface area. Because of the catalyst's insolubility in the solvent, it is heterogeneous and hence it could be readily removed from the solution, which is one of the properties of heterogeneous catalysis [21]. Several authors have studied many magnetic [22-24], zinc [25, 26], cobalt [27, 28], and copper-based [29, 30] nanocatalysts. In this work, different nanocatalysts in industrial effluent treatment, including zinc-based nanocatalysts, cobalt-based nanocatalysts, copper-based nanocatalysts, and magnetic nanocatalysts, and their mechanism of action have been studied. Moreover, recent advancements have been reported.

2. Nanocatalysts

One of the first applications of nanoparticles is Catalysis. Several materials and elements such as silica, clays, titanium dioxide, iron, and aluminum have been applied as catalysts in nanoscale [31-35]. Nevertheless, there is no suitable explanation and the exact reason for nanoparticles' excellent catalytic behavior. The wide nanoparticles' surface area directly affects reaction rate and it can be a good reason for its catalytic performance [36]. The properties of structure, shape, and nanosize of any substance affect their catalytic performance. A better selectivity was achieved by well-adjusting nanocatalyst composition, including the use of supports, core-shell type, and bimetallic size and shape. By showing how the physical properties and preparation parameters associated with nanoparticles influence their catalytic characteristics, nanocatalysts with high activity, selectivity, and resilience can be designed. These advantages led to enabling industrial chemical reactions to produce less waste, consume less energy, and become more resource-efficient, reducing the environmental effect caused by applying chemical processes [37-39]. Nanoparticles are one of the most crucial catalysts for industrial purposes with many applications in chemical manufacturing, energy storage, and conversion. The heterogeneity and differences in shape and size of nanoparticles led to their special catalytic performance [40, 41].

According to the effect of nanomaterial intrinsic features on catalysis, the meaning and concept of nanocatalyst will be understood [42]. The intrinsic properties of nanomaterials that significantly affect the catalytic performance [21, 43] could be classified as follows: quantities directly connected with the bond length, including binding energy, atomic density, as well as mean lattice constant. Surface densification and relaxation are caused by lattice contraction in a nano solid.

Quantities that relied on the cohesive energy per atom, including diffusion, the activation energy for chemical reactions, atomic dislocation, evaporation in a nano solid, phase transitions, critical temperature, Coulomb blockade, thermal stability, and self-organization growth.

The Hamiltonian, which defines the whole band structure, as well as attributes like photoemission, core level energy, and bandgap differs by the binding energy density in the relaxed continuum zone.

Qualities that result from the combined influence of the density of binding energy and energy of atomic cohesiveness including the magnetic performance of a ferromagnetic nano-solid, compressibility of a nano-solid, extensibility, surface energy, surface stress, Young's modulus, and mechanical strength.

3. Application of various nanocatalysts in industrial effluent treatment

3.1. Nanocatalysts based on magnetic metals

Gawande et al. [14] investigated the application of surface-functionalized nano magnetite supported nanoparticles in pharmaceutically significant, green chemistry, and catalysis reactions. Magnetite-supported metal nanocatalysts have been effectively applied in organic synthesis for various crucial reactions and they act as the catalytically active site [44-46]. The most important examples of these catalysts are Ni, Co, and Ferrites metal alloys. Some researchers have applied spinel ferrites for

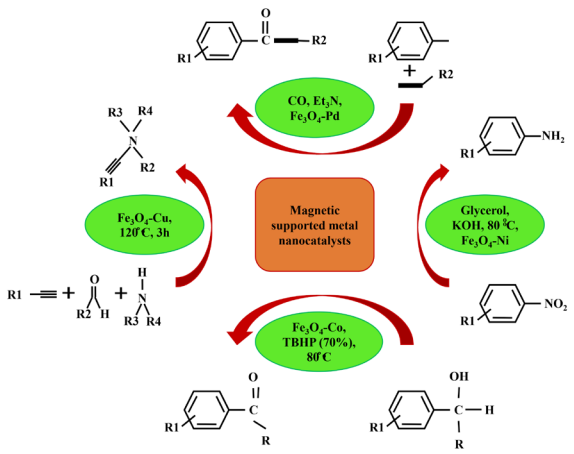

Fig. 2. Catalysis reactions of some organic components by metal nanoparticles supported by magnetite.

dyes and nitroarenes reduction. For example, Feng et al. [47] studied the $CuFe_2O_4$, which was prepared by hydrothermal technique; it has a high catalytic activity for nitrophenol reduction in the sodium borohydride presence. Li et al. [48] used the spray pyrolysis method to synthesize the chainlike spinel MFe2O4 (M = Cu, Ni, Co, and Zn). (Fig. 1). It was revealed that $CuFe_2O_4$ has the best catalytic performance for the nitroaromatic reduction compared to $ZnFe_2O_4$, $CoFe_2O_4$, and $NiFe_2O_4$.

Goyal et al. [49] have studied the catalytic efficiency of nano ferrites of MFe_2O_4 (M = Zn, Cu, Ni) as well as Mn-doped $CoFe_2O_4$ catalysts for the 4-NP catalytic reduction [50]. These samples were provided by the sol-gel process. $CuFe_2O_4$ presented higher catalytic performance between the synthesized ferrites while pure $CoFe_2O_4$ was not active, but the addition of Mn ions improved its catalytic efficiency. The synergistic effect of the Fe^{3+}, Mn^{3+}, and Co^{3+}, which were in the octahedral sites, could be accountable for improving catalytic activity. $CoMn_{0.2}Fe_{1.8}O_4$ showed the highest catalytic performance. Kiran et al. [51] studied the Bi^{2+} catalytic performance substituted nanoparticles of $CoFe_2O_4$, which were synthesized by co-precipitation and combustion methods, and revealed that the sample synthesized by combustion technique showed better catalytic activity in comparison with the nanoparticles synthesized using the co-precipitation technique. Singh et al. [52] synthesized Ni^{2+}-doped $CoFe_2O_4$ ($Ni_xCo_{1-x}Fe_2O_4$ nanoparticles by the reverse micelle method. Dey et al. [53] studied the cube-shaped magnetic $NiFe_2O_4$ nanoparticle for 4-nitrophenol (4-NP) catalytic reduction. Dhiman et al. [54] prepared several morphologies of $NiFe_2O_4$ hydrothermally using varying reaction conditions, solvents, additives, and precursors. It was reported that the catalytic performance of all the provided morphologies for reduction reactions depends on the surface area. The $NiFe_2O_4$ nano cord morphology showed the highest surface area and highest catalytic property. Papadas et al. [55] prepared three-dimensional mesoporous $BiFeO_3$ using a process of nanoparticle templating, which in the first step involved the synthesis of polymer-assisted aggregating formation of 3-aminopropanoic acid stabilized $BiFeO_3$ nanocrystals, accompanied by thermal decomposition to eliminate surfactant molecules . Catalysis reactions of some organic components by metal nanoparticles supported by magnetite are presented in Fig. 2.

Amir et al. [56] studied the degradation of organic dyes, including methylene blue (MB) and methyl orange (MO), using the recyclable magnetic nanocatalyst of Fe_3O_4@His@Ag in which histidine was applied as a linker. According to catalytic analysis, this nanocatalyst can lead to MB and MO degradation at the appropriate time. This material could also be recovered five times using magnetic separation while it maintains most of its activity. Kurtan et al. [57] prepared a magnetically recyclable nanocatalyst of $MnFe_2O_4$@SiO_2@Ag by chemical reduction and co-precipitation method. The reduction of several azo compounds, including rhodamine B (RhB), eosin Y (EY), MB, and MO, as well as aromatic nitro compounds like 4-NP and 2-nitroaniline (2-NA), 4-nitroaniline (4-NA), was catalyzed by a magnetically recyclable Mn-Fe_2O_4@SiO_2@Ag nanocatalyst. Furthermore, the magnetic nanocatalyst exhibits high recyclability, with qualities that are maintained after multiple using cycles. Mohammadi et al. [58] studied the *in situ* and green synthesis of Fe_3O_4@SiO_2Ag magnetic nanocatalysts employing safflower (Carthamus tinctorius L.) flower extract with no surfactants or stabilizers. For the reduction of MO, MB, and 4NP, the catalytic activity of the resulting nanocatalyst was investigated at room temperature. To reduce MB, MO, and 4NP, the noticeable rate constants were 0.09 s^{-1}, 0.064 $s^{-1,}$ and 0.756 min^{-1}, respectively. A magnet was used to recover the catalyst, which was then reused for multiple cycles without losing its function. Veisi et al. [59] studied the surface functionalization of Fe_3O_4 nanoparticles with thiol groups to immobilize Ag nanoparticles, resulting in Fe_3O_4/SiO_2-Pr-S-Ag nanoparticles. Fe_3O_4/SiO_2-Pr-S-Ag NPs have excellent catalytic efficiency as a reusable nanocatalyst for the MB, RhB, and 4-NP degradation in an aqueous solution at room temperature. Ghosh et al. [60] investigated a convenient procedure for the synthesis of a new nanocatalyst containing Ag, $CoFe_2O_4$, and mesoporous TiO_2 nanoparticles for three essential reactivities: (i) photocatalytic MB degradation, (ii) 4-NP reduction, and (iii) styrene epoxidation. The prepared catalyst showed a high catalytic performance to these three reactions. Within 10 hours, they recorded a 98 percent conversion of styrene and a 95 percent selectivity of styrene oxide. The result showed that this catalyst reduced 4-nitrophenol in 4 minutes with k_{app} = 1.08 min^{-1}. When exposed to visible light for 60 minutes, the catalyst exhibited total photodegradation of MB. In addition, the catalyst was readily restored using a permanent magnet externally as well as exhibited excellent reusability. Najafinejad et al. [61] prepared Au nanoparticles supported on Fe_3O_4@ polyaniline, and their activity in eliminating MB and MO from aqueous systems was investigated. Two nanocatalyst concentrations were applied at room temperature to examine the impact of nanocatalyst dosage on the degradation rate of azo dyes. When azo dyes are degraded with $NaBH_4$, the reaction is 10^3 to 10^4 times quicker than degrading without the nanocatalyst. A list of recent nanocatalysts based on magnetic metals for treating various industrial effluents is provided in Table. 1.

3.2. Nanocatalysts based on noble metals

The noble metals, such as Pt, Pd, Ag, and Au, make most catalysts for the reduction reaction, but their high cost has limited their practical applications [65-67]. Because metal-based catalysts can reduce their high surface energy, they can quickly aggregate with no effective protection or stabilization of the nanocatalysts, resulting in deterioration of their catalytic performance and decreased lifespan. [68-70]. For example, the aggregation of bimetallic NPs of Ag–Au occurs without protection by a surfactant of the triblock copolymer; at room temperature, the bimetallic NPs stabilized by surfactants can be stable for weeks [71, 72]. The results showed that Pd and Pt have excellent adsorption energy properties [73, 74]. The microwave-polyol process was used to create Pd, Pt, Pd@Ag, and Pt@Ag nanoparticles, and the nano boxes of these core/shell systems prepared by galvanic replacement reactions showed optical properties. [75, 76]. Besides, Gu et al. [77] reported the photochemical creation of Pd, Pt, and Ag monometallic NPs supported on graphene/ZnO and applied these multi-hybrid nano-architectures as electrocatalysts for H_2O_2. The free Ag NPs prepared by several various methods are also reported [78].

Salem et al. [79] prepared Pt@Ag and Pd@Ag core/shell nanoparticles using the citrate method in two steps (Fig. 3). To examine the catalytic performance of these nanostructures of core/shell, the Congo

Table 1.
Nanocatalysts based on magnetic metals for the degradation of pollutants in wastewater

Authors/Country	Nanocatalysts	Synthesis Methods	% removal/ reduction	Catalytic behaviors
Oliveira et al. [62] Brazil	TiO_2:$CoFe_2O_4$	$CoFe_2O_4$ via Combustion and TiO_2:$CoFe_2O_4$ via Pechini method	Degradation ~100% and efficient mineralization of diuron (DRN)	Reducing the concentration of $CoFe_2O_4$ improved the photocatalytic systems mineralization. The photocatalytic treatment decreased the toxicity of the system and amplified CE50 from 1.5% to 14%.
Mohamed et al. [63] Saudi Arabia	TiO_2/α-Fe_2O_3 nanocomposite	Co-precipitation	Degradation of MB~98%	TiO_2/α-Fe_2O_3 nanocomposites exhibited better photocatalytic performance compared to pure Fe_2O_3 or TiO_2 nanomaterials; increased α-Fe_2O_3 concentration enhanced the activity.
Feng et al. [47] China	$CoFe_2O_4$	Hydrothermal technique	Nitrophenol reduction~95%	Reduction happened in the presence of sodium borohydride.
Li et al. [48] China	Chainlike spinel MFe_2O_4 (M = Cu, Ni, Co, and Zn)	Spray pyrolysis method	Nitroaromatic reduction ~100%	$CoFe_2O_4$ has the best catalytic performance in reducing nitroaromatic compared to $ZnFe_2O_4$, $CoFe_2O_4$, and $NiFe_2O_4$
Goyal et al. [49] India	MFe_2O_4 nano ferrites (M = Zn, Cu, Ni), Mn-doped $CoFe_2O_4$	Sol-gel method	2-NP reduction~95%	Fe^{3+}, Mn^{3+}, and Co^{3+} enhanced the catalytic performance, $CoFe_2O_4$was the best ferrite catalyst, $CoMn_{0.2}Fe_{1.8}O_4$ was the best catalyst
Kiran et al. [51] India	Bi^{2+} substituted nanoparticles of $CoFe_2O_4$	Co-precipitation and combustion methods	4-NP to 4-AP reduction in 2.25 min	Combustion method results had better catalytic performance than co-precipitation process
Singh et al. [52] India	Ni^{2+}-doped $CoFe_2O_4$ ($Ni_xCo_{1-x}Fe_2O_4$) nanoparticles	Reverse micelle method	Reduction of 4-nitrophenol, degradation of Rhodamine B ~99%	Photo-oxidative degradation of Rhodamine B, $NaBH_4$ was used as the reducing agent.
Dey et al. [53] India	Cube-shaped magnetic $NiFe_2O_4$ nanoparticle	Novel method	4-nitrophenol (4-NP) catalytic reduction	Effective, reusable nickel ferrite magnetic nanocatalyst without implementing any functionalization,
Dhiman et al. [54] India	Several morphologies of $NiFe_2O_4$ hydrothermally	Varying reaction conditions, solvents, additives, and precursors	Degradation of anionic remazol brilliant yellow (RBY) ~90% and cationic safranine-O (SO)	$NiFe_2O_4$ nano cord morphology had the highest surface area and the best catalytic performance
Papadas et al. [55] USA	Three-dimensional mesoporous $BiFeO_3$	Nanoparticle templating	Reduction of p-nitrophenol to p-aminophenol with $NaBH_4$, ~98%	The MBFAs (kapp= 0.018 s^{-1}) reduction rate was two times quicker than arbitrary $BiFeO_3$ NP aggregates (0.009 s^{-1})
Amir et al. [56] Turkey	Fe_3O_4@His@Ag (histidine was applied as a linker)	Hydrothermal method	Complete degradation of MO and MB	Degradation of MB and MO at a reasonable time. Reusable five times.
Kurtan et al. [57] Turkey	$MnFe_2O_4$@SiO_2@Ag	Chemical reduction and co-precipitation method	Complete reduction of rhodamine B (RhB), eosin Y (EY), MB, MO. Reduction of 4-NP as well as 2-nitroaniline (2-NA), 4-nitroaniline (4-NA), and.	Remained unchanged after multiple uses
Mohammadi et al. [58] Iran	Magnetic nanocatalyst of Fe_3O_4@SiO_2-Ag	Green and in situ synthesis, prepared by safflower (Carthamus tinctorius L.) flower extract	Reduction of 4-NP, MO, and MB at ambient temperature ~98%	The apparent constant rate for MB, MO, and the 4-NP reduction was 0.09 s^{-1}, 0.064 s^{-1}, and 0.756 min^{-1}. Recoverable by the magnet and reusable.
Ghosh et al. [60] India	Nanoparticles of Ag, $CoFe_2O_4$, and mesoporous TiO_2	EDTA precursor-based method,	Complete photocatalytic degradation of MB, 4-NP reduction, styrene epoxidation ~98.1%	Reduction of 4-NP with kapp = 1.08 min^{-1} in 4 min, recoverable using magnet, reusable, and selectivity of styrene oxide.
Najafinejad et al. [61] Iran	Nanoparticles of Au supported on Fe_3O_4@ polyaniline	Reduction of Au^{3+} using a wild herbal extract (Allium Sp)	Reduce MB and MO from aqueous solutions	Degradation of azo dyes with $NaBH_4$ was 10^3 to 10^4 times quicker than degradation without employing the nanocatalyst.
Ranjith et al. [64] Taiwan	Hybrid rGO-TiO_2/Co_3O_4 nanocomposite	Co-precipitation	High reduction of MB and crystal violet dye	Compared to crystal violet dye, the decolorization of the MB dye was higher with reduced time. rGO/TiO_2/Co_3O catalyst could be applied to treat a variety of industrial dyes
Veisi et al. [59] Iran	Nanoparticles of Fe_3O_4/SiO_2-Pr-S-Ag. Fe_3O_4/SiO_2-Pr-S-Ag NPs	Surface modification of nanoparticles of Fe_3O_4 with thiol groups for the immobilization of Ag nanoparticles	Degradation of MB, RhB, and 4-NP high efficiently decolorized the dyes.	Significant catalytic performance with $NaBH_4$ in the water at ambient temperature, recyclable

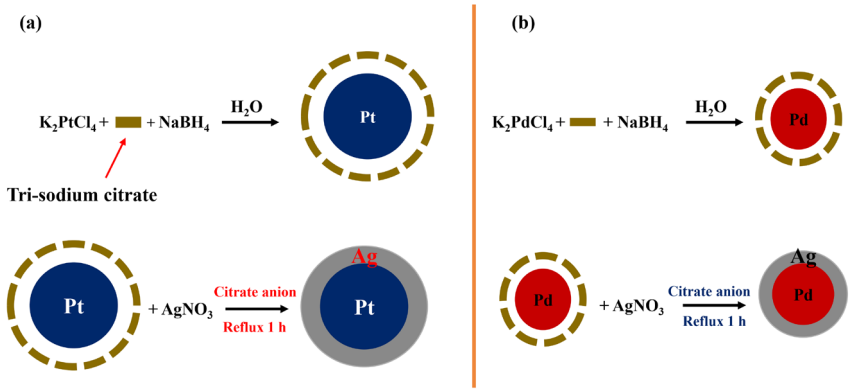

Fig. 3. Synthesis method of Pt@Ag and Pd@Ag core/shell.

red dye reductive degradation was selected. The electrons move from the reducing agent ($NaBH_4$) to the dye molecules through nanocatalysts, which serve as electron mediators. After four reaction cycles, the Pd@Ag nanocatalyst remained catalytically active. These results can be viewed as a cost-effective way to protect the environment by avoiding dye contamination in water supplies.

Moradi et al. [80] used the precipitation–decomposition method to create a range of Ag–ZnO/CNT nano photocatalysts with addition of multi-wall carbon nanotubes. The photocatalytic degradation of the Acid Orange 7 dye under visible light was used to determine the catalytic activity. As compared to the nanocomposite of Ag–ZnO and pure ZnO, the nano photocatalyst of Ag–ZnO/CNT with five wt. percent multi-wall carbon nanotubes loading had excellent photocatalytic activity. The efficient separation of pairs of electron hole on Ag–ZnO/CNT was related to improved photocatalytic performance. Duan et al. [81] synthesized the recyclable and high-performance nanocatalysts, which are composed of small, well-dispersed Ag nanoparticles that are immobilized on a Cu-based metal-organic substrate (MOF-199s) supported by CCFs (carboxymethylated cellulose fibers). The catalytic activity of AgNPs@MOF-199s/CCFs catalysts for the reduction of 4-nitrophenol to 4-aminophenol showed a high catalytic efficiency. Enhanced dispersion, the porous catalyst structures, and small particles of Ag stabilized by the MOF-199 s cause the high catalytic activity. Applying cellulose fiber led to the facilitation of the sustainability and reuse of nanohybrid catalysts revealing high and stable reusability of > 91% after five cycles.

Bao et al. [81] studied a one-pot method and used co-reduction growth in polyol mixture to synthesize amino-functionalized (-NH_2) graphene oxide (GO-) supported networked nanowires of Pd–Ag. The results showed effective catalytic activity with superior recovering efficiency at ambient temperature (25 ºC) for catalytic Cr(VI) reduction using the H_2 source of formic acid. The electron transfer from amino and Ag to Pd enhances Pd electron density, which improves the decomposition of formic acid and the reduction of Cr(VI). The catalytic reduction rate constant of Pd_3Ag_1/GO-NH_2 is 0.0768 min^{-1}, showing higher value compared to the monometallic Pd3Ag1/GO and Pd/GO-NH2 catalytic reduction rate constants. Iqbal et al. [82] created a new form of recyclable, ecologically safe, and convenient cerium-doped magnesium-aluminum-layered double hydroxide (MgAl-LDH) nanocatalyst, known as MgAlCe-LDH@Au. It was fabricated by adding Au nanoparticles with an approximate diameter of 3 nm on MgAlCe-LDH support by *in situ* reductions of $HAuCl_4$ utilizing $NaBH_4$. This nanocatalyst shows very considerable activity in the 4-nitrophenol reductive degradation by $NaBH_4$ with k_{app} = 0.041 s^{-1} (rate constant) and TOF= 1.2 × 10^6 h^{-1} (catalyst turnover frequency); at ambient temperature (25 ºC) and air pressure, the reactions took place in an aqueous system. MgAlCe-LDH@Au nanocatalysts can be recovered and they can keep their original performance after seven catalytic processes. MgAlCe-LDH@Au is also an effective catalyst for the reductive breakdown of usual organic dyes, such as rhodamine 6G (R6G), rhodamine B, methylene blue, methyl orange, and Congo red that led to increased values of TOFs to 3.2 × 10^4 h^{-1}. Sahoo et al. [83] applied a simple one-pot production of trimetallic porous Au@Pd@Ru nanoparticles at ambient temperature. The trimetallic nanoparticles exhibited excellent catalytic performance in reducing p-nitrophenol and the breakdown of many azo dyes. The method was applied to eliminate color from wastewater using catalytic degradation of azo dyes.

Nasrollahzadeh et al. [84] used a structurally described furfural with a 3-aminopropyltriethoxysilane long tail to immobilize palladium nanoparticles on NH_2-modified zeolite (Zeo) particles carrying a heterocyclic ligand. At room temperature (25 ºC) in aqueous solutions, NH_2 modified Zeo/Pd was produced as a reusable, highly active, and sustainable nanocatalyst to reduce Nigrosin (NS), MB, RhB, 4-NP, 2,4-dinitrophenylhydrazine (2,4-DNPH), potassium hexacyanoferrate(III) ($K_3[Fe(CN)_6]$), and Cr(VI). UV–Vis spectroscopy was used to evaluate the rate of removal of these toxicants with NH_2 modified nanocatalyst of Zeo/Pd using formic acid (HCOOH) and sodium borohydride ($NaBH_4$) at ambient temperature (25 ºC), as well as the nanocatalyst's ability to be recovered eight times without remarkable reduction of catalytic performance. Yan et al. [85] used the one-pot solvothermal method to make bimetallic Pt-rhodium alloyed (PtRh ANMPs) nanomultipods in oleylamine (OAm), using co-structure-directing agents of cetyltrimethylammonium chloride (CTAC) and creatinine. The prepared nanocatalyst showed remarkable catalytic properties to reduce RhB and 4-NP by $NaBH_4$. In similar conditions, the prepared catalyst exhibited a highly facilitated TOF=1.0 × 10^{-3}/0.44 × 10^{-3} mol g^{-1} min^{-1} and k=0.209/0.354 min^{-1} for RhB and 4-NP reduction versus industrial Pt black. Table 2 shows a list of recent nanocatalysts based on noble metals for treating various industrial effluents.

3.3. Nanocatalysts based on organic polymer-supported metal catalysts

Because of their porous network structures and functionalities, polymer hydrogels were used as metal nanoparticle carrier systems [104]. They could be produced by several polymerization techniques, including polymerizations [105, 106], free-radical [107, 108], and ionic [109, 110] based on convenient and low-cost solution routes. As an example, a core-shell microgel containing a shell of cross-linked poly(N-isopropyl acrylamide) (PNIPA) and solid polystyrene (PS) core was applied to stabilize a nanocatalyst of Pd [111]. A spherical polyelectrolyte brush-based scheme with poly ((2-methylpropenoyloxyethyl) trimethylammonium chloride) long chains as a shell and a solid PS core was quantitatively contrasted to the microgel-based process [112]. The results

Table 2.
Nanocatalysts based on noble metals for the degradation of pollutants in wastewater

Authors/ Country	Nanocatalysts	Synthesis methods	% removal/ reduction	Catalytic behaviors
Katoch et al. [87] India	Bi_2O_3	Microflow	Degradation of MO ~96 %	Bi_2O_3 nanoparticles exhibited excellent stability after three cycles indicating coated microreactors in photocatalysis reusability.
Dang et al. [88] China	$CuCl_2$ nanoflake film grown on the top surface of nanoporous anodic alumina substrate (nano-PAA-$CuCl_2$)	Self-assembly approach	Degradation of MO~95% and MB~100%	Applicable in Fenton-like reaction as an effective process for wastewater treatment.
Rehman et al. [89] Saudi Arabia	Ce & Zn doped CuO nanocatalyst	Co-precipitation	Degradation of MO ~81%	The photocatalyst of binary metal-doped CuO exhibited excellent photocatalytic performance for the treatment of toxic industrial effluents.
Dehghan et al. [90] Iran	ZnO/rGO	Chemical deposition	Removal of Metalaxyl (MX) ~ 90%	The MX toxicity was dropped from 51 to 15 within 96 h. The photocatalytic performance was reduced by nitrate and phosphate ions but remained constant in the presence of other water anions.
Dosti et al. [91] Iran	Pd NPs	-	Reduction of Cr(VI) ~99% and Cr(III) precipitation ~96%	Electrochemical cells could perform in-situ total free chlorine production and chromium removal concurrently.
Shelar et al. [92] India	Ag-doped ZnO	Co-precipitation	Degradation of MB ~65-95%	The photocatalytic performance increase with the increase of concentration of dopant.
Ikram et al. [93] Pakistan	Ag decorated MoS_2 nano pedals	Adopting hydrothermal approach	Dye degradation in the presence of $NaBH_4$ ~100%	Excellent potential for removing hazardous toxins, including tannery pollutants and synthetic dyes, from industrial effluents.
Nasrollahzadeh et al. [94] Iran	Ag/MgO nanocomposite	-	Complete and excellent reduction of MB, 4-$NPMO_2$, and 4-DNPH ~100%	The Ag/MgO system was reusable, highly stable, with excellent catalytic performance.
Khoshnamvand et al. [95] China	Ag NPs	Green synthesis	Reduction of 4-NP, and antioxidant activity against DPPH, and ABTS+ ~99%	Ag nanoparticles exhibited excellent antioxidant activity against ABTS and DPPH free radicals and efficient catalytic performance in 4-NP reduction to 4-AP.
Kumar et al. [96] Ecuador	Ag NPs	Biosynthesis	Reduction of MB ~29% in 1 hour	Exhibited effective photocatalytic activity to remove MB dye (5 $mg.L^{-1}$, k = 0.00707788 min^{-1}).
Garol et al. [97] India	Pd NPs	Green synthesis	Complete reduction of 4-NP, MO, and MB	Excellent catalytic reduction performance for all organic contaminants; the occurrence of complete reduction in 10 min.
Salehi et al. [98] Iran	Pd/RGO NPs	Chemical deposition	Reduction of MB, MO, and rhodamine B ~99%	These nanoparticles have excellent catalytic reduction activity.
Khan et al. [99] Pakistan	ZnO-NPs	Green synthesis	Synozol Navy Blue-KBF textile dye degradation ~91%	Removed the dye in 159 min, potential to have various photocatalytic and biological applications.
Ganesh et al. [100] South Korea	ZnO Np	Green synthesis	Reduction MB ~96%	These green prepared nanoparticles of ZnO could be effective photocatalysts and anti-microbial for dye degradation and eliminating pathogenic microbes in industrial effluents.
Prasad et al. [101] India	ZnO NPs	Green synthetic strategy using Abelmoschus esculentus	Degradation MB~100%, Complete degradation of rhodamine B. Degradation of Congo red, and MO	ZnO nanoparticles are applied in selective photodegradation of the target cationic dyes.
Rajaendaran et al. [102] India	Ag-Mo/CuO NPs	Biogenic synthesis	Photodegradation of MB~99%	The photocatalytic performance by AzI-MACO (99%) was higher than that of AzI-MCO (88%), AzI-ACO (74%), AzI-CO (52%), and CO (39%) nanoparticles.

Table 2. (Continued)

Authors/ Country	Nanocatalysts	Synthesis methods	% removal/ reduction	Catalytic behaviors
Salem et al. [79] Egypt	Pt@Ag and Pd@Ag core/shell	Citrate method in two steps	Congo red dye reductive degradation ~85%	NaBH4 was used as a reducing agent; nanocatalyst was catalytically stable after four cycles
Moradi et al. [80] Iran	Ag–ZnO/CNT	Method of precipitation–decomposition	Acid Orange 7 dye photocatalytic degradation under visible light ~100%	Improved photocatalytic activity due to effective separation of pairs of electron-hole on Ag–ZnO/CNT compared to the nanocomposite of Ag–ZnO and the pure ZnO reusable
Iqbal et al. [83] China	MgAlCe-LDH@Au	Au nanoparticles loading on MgAlCe-LDH by an in situ reductions of $HAuCl_4$	Degradation of 4-nitrophenol ~100%, Complete degradation of rhodamine 6G (R6G), RhB, Congo red, MO, and MB	The reactions were in an aqueous system at room temperature and atmospheric pressure, reusable for seven cycles,
Sahoo et al. [84] India	Trimetallic porous nanoparticles of Au@Pd@Ru	Facile ambient temperature one-pot synthesis	Efficient p-nitrophenol reduction and degradation of reactive black (RB-5) and reactive red (RR-120)	Color removal and elimination of produced amine from wastewater
Nasrollahzadeh et al. [85] Iran	Pd NPs@Zeo	Immobilization of structurally defined furfural with 3-aminopropyltriethoxysilane long tail, multi-step organic amine functionalization	Reduction of Nigrosin (NS), MB, RhB, 4-NP, 2,4-dinitrophenylhydrazine (2,4-DNPH), potassium hexacyanoferrate (III) Cr(VI) and (K3[Fe(CN)6]),	Highly active, recoverable, and reusable for eight times at room temperature, antibacterial activity against E. coli.
Yan et al. [86] China	Nanomultipods of bimetallic PtRh-ANMPs in OAM by adopting the co-structure-directing agents of cetyltrimethylammonium chloride (CTAC) and creatinine	A facile one-pot solvothermal method	RhB ~97% and 4-NP ~94% reduction by NaBH4	Highly effective for RhB and 4-NP reduction than commercial Pt black under similar conditions, recyclable
Mohammadi et al. [103] Iran	Fe_3O_4/SBA-16-Cit-Cya-Au nanocomposite	Chemical deposition	Reduction of MB and MO, the reaction mixture turned colorless.	Sustainable and highly efficient after eight cycles.
Memar et al. [104] Iran	CuO/CuZnO	Chemical deposition	Degradation of MO and MB	Excellent catalytic activity and high repeatability after the fifth cycle of degradation reaction.

showed that the polyelectrolyte brush-based catalyst had better catalytic efficiency than the one stabilized by microgel, which may be linked with the various diffusional barriers present in such stabilizing processes. A bottlebrush polymer tightly linked on a solid core of PS was also investigated as an Ag nanoparticle carrier platform. However, the synthesis method is complicated, which can lead to high costs and difficulties in raw materials personnel, and time, restricting broad realistic implementations [113, 114].

Using electrostatic attraction, a microgel of polymethacrylic acid was applied as a carrier device to accumulate the metal ions, which were then reduced to the resulting metal nanoparticles [115]. Moreover, a modified cryogel of poly(4-vinyl pyridine) was applied to adsorb metal ions and reduction treatment for the production of a compound catalyst for 4NP and MB dye reduction [116]. Besides, amidodiol was used as a reducing agent and a cross-linking agent to adsorb Ag nanoparticles in a poly(acrylic acid)–based hydrogel fibrillar system [117]. The cationic dyes such as crystal violet, MB, and R6G were catalytically reduced with the synthesized hydrogel immobilized Ag nanoparticles. Temperature and pH were observed to have a remarkable influence on the catalyzed process. To prepare the Au and Ag nanoparticles, gel beads of calcium alginate (CA) were applied as stabilizing and reducing agents [118]. The researchers hypothesized that metallic Ag might be a superior catalyst compared to Au throughout this catalytic reduction process because the as-synthesized CA-stabilized nanocatalyst of Ag has been more effective for transforming of 4NP to 4AP compared to the Au equivalent. Also, the volume of Ag nanoparticles loaded on alginate or the surface covering with Ag nanoparticles was assumed to be more desirable for the catalyzed process than Au nanoparticles [109].

Metal catalysts could also benefit from the use of polymer dendrimers as stabilization systems. As an example, poly (amidoamine) (PAMAM) and poly (propylene imine) (PPI) dendrimers were applied to stabilize nanoparticles of Au for the reduction of 4NP [119, 120]. The results showed that as the dendrimer concentration increased, the rate constants of catalytic reduction for all of the processes studied declined. PPI and PAMAM dendrimers with amino groups on their surfaces were analyzed for synthesis and stabilization of Au compound nanocatalysts via laser irradiation reduction rather than chemical reduction [121]. With increasing the irradiation time, the mean size of the Au nanoparticles declined. According to the previous report, the dendrimers were adsorbed on the surfaces of NPs as a monolayer, lowering the efficiency of the catalytic performance. Furthermore, a layer-by-layer nanoreactor film was fabricated for holding silver nanoparticles utilizing a PAMAM dendrimer with positive charge and negatively charged polyacrylic acid or polystyrene sulfonate [122].

Polyacrylonitrile (PAN) substrate was also applied to embed silver nanoparticles by immobilizing the Ag nanoparticles within the polymer matrix. However, because of the blocking influence of the polymer matrix, nanoparticles of PAN/Ag matrix are inappropriate for catalytic applications. In addition, Ag nanoparticles were applied to the PAN nanofiber surface to expose most of their surface [123]. The nanofiber of PAN had been pre-modified for binding site incorporation before applying Ag nanoparticles upon its surface. Hydroxylamine hydrochloride

Table 3.
Nanocatalysts based on organic polymer-supported metal catalysts for the degradation of pollutants in wastewater

Authors/Country	Nanocatalysts	Synthesis method	Application: % removal/ reduction	Catalytic behavior
Kaliraji et al. [131] Korea	ZnO nano-flowers	Green synthesis	Removal of Eosin Y (EY), Malachite green (MG), and MB ~99%	High efficiency and reusability after five cycles without any remarkable loss in degradation performance.
Duan et al. [81] China	AgNPs@MOF-199s/ CCFs	Ag nanoparticles immobilized on a Cu-based metal-organic framework (MOF-199s) supported by CCFs (carboxymethylated cellulose fibers)	The 4-nitrophenol reduction to 4-aminophenol ~95%	Better dispersion improved the catalytic activity; cellulose fiber increased sustainability and reusability of >91% after five cycles.
M. Ajmal et al. [116] Saudi Arabia	A microgel of polymethacrylic acid	Inverse suspension polymerization	Absorb and reduce metal ions ~100%	A carrier system that uses electrostatic interactions to adsorb metal ions and then reduces the adsorbed metal ions to metal nanoparticles
Bhat et al. [129] Malaysia	The Pd catalyst based on the framework of chitosan-tannin (CT)	Glutaraldehyde chitosan crosslinking	The reduction of Congo red~23% and nitrate~71% in the absence and presence of H2.	Catalyst is considerably thermally-stable compared to CT support
Samai et al. [130] India	Nanocomposite of polyaniline/cerium oxide	Hydrothermal method.	The removal of RhB~91% in wastewater under irradiation of the UV light.	Polyaniline polymer was employed as active catalyst support to enhance the cerium oxide nanoparticle photocatalytic activity.
Nasrollahzadeh et al. [132] Iran	Pd/reduced graphene oxide (RGO) nanocomposite	Chemical deposition	Degradation of Cr(VI), 4-NP, CR, MB, and MO, the disappearance of absorbance peaks	Reusability and recyclability after multiple employment with no alteration in catalytic performance.
Peng et al. [133] China	Pd truncated octahedrons (PdTOs) and Pd NPs	Biosynthesis	Excellent reduction of 4-NP	The apparent rate constant (Ka) over PdTOs was 0.358 min^{-1} in p-NP reduction, which is improved compared to spherical PdNPs-0 (0.08 min^{-1}).
Gu et al. [77] China	Pd, Pt, and Ag monometallic NPs supported on graphene/ZnO	Photochemical synthesis	Electrocatalysts for H_2O_2	Distinct electrocatalytic activity
Bao et al. [82]ÿ China	Pd3Ag1/GO-NH_2	One-pot method	Excellent catalytic reduction of Cr(VI)	Formic acid (a H2 source) at room temperature, reduction rate constant was higher compared to the monometallic Pd_3Ag1/GO and Pd/GO-NH_2.
Sahiner et al. [117] Saudi Arabia	Modifiable Poly(4-vinylpyridine) (p(4-VP)) cryogels	Cryogellation using free radical polymerization method	Complete degradation of MB dye and reduction of 4NP	The cryogel embedded with Fe, Cu, Ni, and Co nanoparticles employed in an aqueous solution with $NaBH_4$
Narayanan [118] India	Polyacrylic acid–amidodiol hydrogels (SPAGs) entrapped Ag nanoparticle	Acrylic acid in situ polymerization and silver nitrate reduction utilizing amidodiol as cross-linking agent	Complete reduction of crystal violet, MB, and R6G	Temperature and pH had a remarkable influence on the catalytic reaction, easy separation, promising reusability, and absence of induction period.

has been utilized as a modifier by reacting with the –CN groups existing in PAN to create numerous amine as well as hydroxyl groups that could chelate Ag ions and immobilize them. Reduction treatment was used to build the Ag-decorated catalyst on the modified PAN fiber. A poly-(3,4) ethylene dioxythiophene (PEDOT) substrate was also used as a support base for Pd nanoparticles. [124]. The sodium polystyrene sulfonate (Na–PSS) catalytic reduction of the PEDOT supported nanoparticles of Pd in the solution was employed to improve the distribution of the PEDOT supported nanoparticles of Pd. The destructive impact on the catalyzed process must be considered because the surfactant Na-PSS is inclined to position the Pd catalyst. To stabilize Au and Fe_3O_4 nanoparticles, the conducting polymer polypyrrole (PPy) was utilized [125]. However, these nanoparticles were wrapped or embedded in a polymer substrate, creating a great diffusion barrier to the catalyst impairing MB dye catalytic activity. The carrier platform for the Au nanocatalyst [126] was Poly(allylamine hydrochloride) which was modified with composite sub microspheres poly(glycidyl methacrylate). The results showed that the carrier system's positive charges and epoxy groups could improve the catalyzed process. Epoxy groups have a role as electron acceptors because of their electrophilicity; therefore, they capture electrons and create an electron-rich region at the Au nanoparticle-sphere interface. This area could represent an electron reservoir, allowing the electron to be transferred to the reactant 4-NP in catalytic reduction of 4-NP; in the meantime, 4-NP anions could be adsorbed onto the positively charged surfaces of the sphere with ionic attraction. Aside from the multistep procedures and complex preparing requirements that restrict wide implementations, the composite sphere catalyst's reusability and stability have not been studied. Furthermore, the electrons captured by epoxy groups may not be freed, and the reduction of the epoxy groups could occur in the catalyzed reduction process by the captured electrons [1].

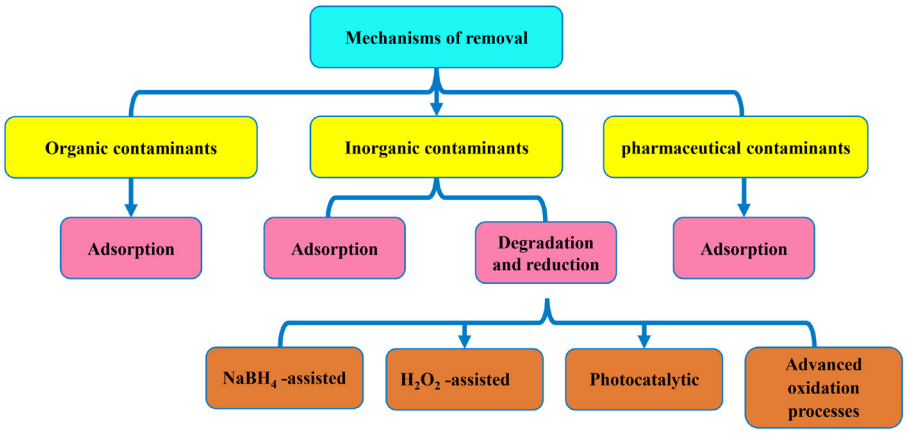

Fig. 4. Removal mechanisms by nanomaterials for different pollutants.

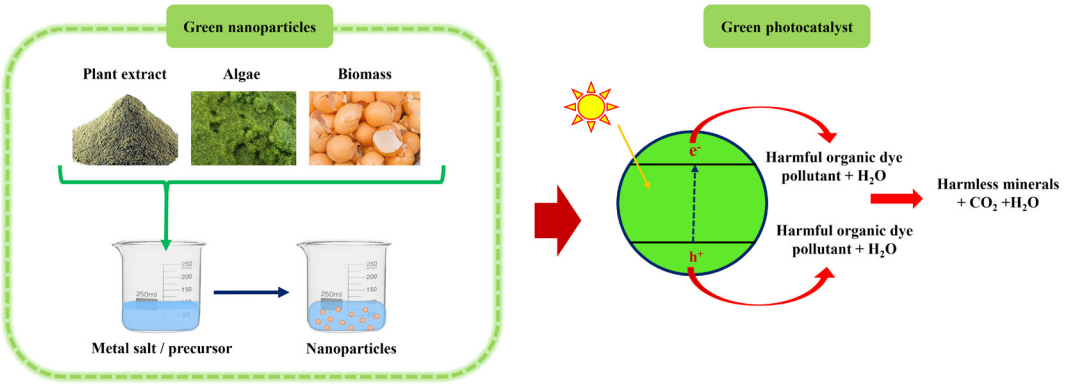

Fig. 5. Mechanism of dye photocatalytic degradation via green-synthesized nanoparticles.

To stabilize Au nanoparticles for the 4-NP reduction catalysis, quaternary ammonium resin beads of PS were used. The results showed that the tinier the Au nanoparticles, the quicker the catalyzed process. The Au nanoparticles immobilized on the surface of resin seem fragile because they could be dissociated with cationic surfactants, suggesting the composite catalyst's low endurance [127]. Bhat et al. [128] synthesized a Pd catalyst established on the chitosan-tannin (CT) framework. The catalyst's catalytic efficiency was investigated in the presence and absence of H_2 to reduce Congo red and nitrate. Within 60 and 20 minutes, respectively, the catalytic performances eliminated 23 percent and 71 percent of Congo red and nitrate.

Samai et al. [129] used a conducting polymer of polyaniline as active catalyst support to promote the cerium oxide nanoparticle photocatalytic activity. The as-prepared nanocomposite of polyaniline/cerium oxide shows significantly improved photocatalytic efficiency than some oxide nanoparticles or polyaniline for removing RhB in wastewater under the UV light irradiation. The results indicated that a nanocomposite containing cerium oxide nanoparticles and polyaniline in a 1:1 molar ratio degraded 91 percent of Rhodamine B in 2 hours, while cerium oxide nanoparticles only degraded 10%. Recent studies on applying various organic polymer-supported metal nanocatalysts for pollutant removal from wastewater are summarized in Table 3.

4. Catalytic mechanisms

Different types of biological, chemical, and physical technologies such as advanced oxidation processes (AOPs), ultra-filtration, membrane, sedimentation, flocculation, adsorption, oxidation, reverse osmosis, and ion-exchange are employed for treating wastewater. Because of their excellent performance, good reproducibility, convenience, and ease of handling, AOPs including photocatalysis, Fenton reaction, ozonation, or their variations are used to remove organic contaminants [134].

AOP is classified as remarkably nonselective and reactive chemical oxidants, including $\bullet O_2$, O_3, H_2O_2, and •OH to remove resistant and non-biodegradable organic pollutants.

As shown below, the Fenton reaction by radical of •OH is a low-cost, efficient, and sustainable wastewater treatment process. [135]:

$Fe^{2+} + H_2O_2 + H^+ \rightarrow Fe^{3+} + \bullet OH + H_2O$

Jaafar et al. [136] have studied some quantum calculations based on the ELF (electron localization function) and DFT (density functional theory) to investigate the removal process of Neutral Red dye (NR) in sewerage. In an aqueous medium, the Fenton reaction mechanism between free radicals (•OH) and the NR dye for its degradation was examined. For eliminating organic and inorganic pollutants and eradication of toxins (Fig. 4) from wastewater, freshwater sediments, groundwater, and other sites, a variety of pathways have been used, including reduction and (photo)degradation, adsorption, and UV photolysis/photocatalysis [137].

Nanomaterials can adsorb or degrade the contaminants using several catalytic approaches, including photocatalysis, H_2O_2, and $NaBH_4$, whereas green-synthesized nanoparticles are an excellent choice for photocatalytic wastewater treatment (Fig. 5) [138]. Toxic organic pollutants are broken down into other materials [139] or fully mineralized components, producing water, carbon dioxide, or other inorganic ions. In general, a semiconductor such as TiO_2 is capable of absorbing light with a wavelength equal to or greater than the wavelength of the semi-

conductor bandgap, resulting in the creation of electron-hole (e^--h^+) pairs [140, 141]. Reduction-oxidation reactions involve the interaction of nanocatalyst with adsorbate molecules. As shown in the equations below, h^+_{vb} interacts with surface-bound water to form •OH, and oxygen selects e-CB to form a superoxide radical anion..

New green prepared metal-organic framework-based photocatalytic materials have recently received a great deal of interest, particularly because of their capacity for environmentally friendly removal of toxic organic contaminants. [142-144]. Several studies have reported on the use of transition metals in MOF-based photocatalysts to remove extremely toxic contaminants under UV/vis, UV, and visible light. First, a MOF-5 was utilized to act as an efficient photocatalyst [145, 146]; these MOFs have a wide absorption band in the 500-840 nm range, which is related to the delocalized electron that lives on a time scale of microsecond and is most probably occupies a conduction band, with a value of conduction band energy equal to 0.2 V vs. NHE and a 3.4 eV bandgap. For the degradation of aqueous phenol, this method showed proportional performance with TiO_2 or ZnO. MOF-5 is an efficient photocatalyst since it is in a charge-separated state, with holes in the valence bands and electrons in the conduction band. As a result, phenol photodegradation can be accomplished by a series of reactions, including the primary formation of radical cations through transferring a phenol electron to the MOF-5 hole, or the oxygen active specie formation, including superoxide radical anions, by the interaction between photo-ejected electrons and oxygen. [147, 148]. Das et al. [149] prepared a double interpenetrated porous MOF (UTSA-38) containing Zn_4O with a bandgap of 2.85 eV, and its photocatalytic performance for the removal of MO in aqueous systems under UV/vis, visible light, as well as dark conditions was shown to be strong. According to the findings, under UV light for 120 minutes, methyl orange could be decayed into colorless smaller particles.

In reducing poisonous nitro compounds to useful and valuable amino compounds in aqueous systems, $NaBH_4$ has attracted much attention as a preferred alternative to hydrogen sources and a water-soluble reductant. Because metal hydride structures formed from BH_4-ions through π-π stacking interaction have been evaluated as intermediates in this reduction reaction, the activation of $NaBH_4$ is a major procedure that needs to take a metal material as the active site. The existence of a nanocatalyst of Pd stabilized amine-modified zeolite (Pd NPs@Zeo) with stacking interactions of π-π was found to explain the reduction of toxic 4-NP by $NaBH_4$ reductant [84]. Pd NPs@Zeo transform $NaBH_4$ to molecular H_2 and BO_2 dissociated on the nanocatalyst's surface, and the adsorbed 4-NP interacts with the dissociated H_2 gas to produce 4-aminophenol. Consequently, the as-synthesized aminophenol is eventually desorbed from the nanocatalyst base, resuming the catalytic process. The nanocatalyst also plays a part in facilitating simple reduction by adsorbing molecular H_2 or 4-NP nearby. Magnetically separable nano-bio hybrid catalysts, Fe_3O_4@Ch-PdNPs and Fe_3O_4@Ch-AuNPs, have been prepared and designed by a three-step procedure according to the process of biosynthetic mineralization [150]. Shewanella algae produced spherical Fe_3O_4 nanoparticles (35 nm) that were then coated or functionalized with chitosan, accompanied by modification with nanoparticles of Pd or Au to produce a reusable and water-dispersible nano-bio hybrid catalyst that showed significant functionality for 4-NP reduction and dye photodegradation (>99 percent) in contaminated water at ambient temperatures (25 ºC) [151].

This reaction was triggered by the adsorbent and reduction of methylene blue by Au or Pd nanoparticles via the electron transfer process. The reaction rates exhibited pseudo-second-order rate kinetics; under UV light, the Fe_3O_4@Ch-Pd and Au nanoparticles finished the methylene blue reduction in just 1 minute, with apparent rate constants (k_{app}) of 5.0 min^{-1} and 4.0 min^{-1}, respectively. Furthermore, the normalized rate constant (k_{nor}) values of the nanoparticles of Au and Fe_3O_4@Ch-Pd for the degradation of methylene blue are 1.14×10^2 and 1.72×10^2 $mmol^{-1}s^{-1}$, respectively, showing catalytic activities of the nanoparticles of Au and Fe_3O_4@Ch-Pd. For eliminating severely carcinogenic and toxic arsenic (As), green-fabricated amorphous nanoparticles of Fe with 51 m^2 g^{-1} Brunauer–Emmett–Teller (BET) area were employed [150].

Arsenate was reported to be evenly adsorbed on the surfaces of Fe nanoparticles; Fourier-transform infrared spectroscopy (FTIR) spectrometer analysis revealed that the adsorption was mainly due to a FeO-As bond, but X-ray photoelectron spectroscopy (XPS) findings show that only As(V) was adsorbed. Therefore, this method for eliminating arsenate relies on Fe nanoparticles interacting with arsenate to generate a monodentate chelating ligand, and then followed by a complex of bidentate binuclear. More studies showed that the synthesized nanoparticles' maximum arsenate adsorbent potential was about 14.6 mg g^{-1} and that the optimum range of pH for anionic arsenate adsorbent was around 4 to 6. [150]. The Langmuir adsorption isotherms showed that adsorption of As(V) by Fe nanoparticles matched their regression coefficient (R^2 = 0.99), confirming the suggested chemisorption; the adsorption yield matched the pseudo-second-order kinetic model favorably. As a result, the green synthesis of Fe nanoparticles is a promising option for removing arsenic while also being simple to synthesize.

5. Conclusions and future insights

This work focuses on organic polymer-supported metal catalysts, noble metals nanocatalysts, and magnetic nanocatalysts and then summarizes their mechanism in treating industrial effluent. Studies show the efficacy and promising application of these nanocatalysts for the removal of industrial effluents. Since low-cost preparation is critical for their uses in wastewater treatment, future research could focus on measurement of interactive mechanisms in the water treatment system of these nanomaterials and refining their economic viability. In addition, the toxicity of these nanomaterials for the environment and human health should be examined and (quali-quantitative) risk assessment evaluations are suggested in this regard. To ensure that their implementation is safe, general assessments of their harm are needed. More studies are required to compare the nanomaterials' relative performances to recognize favorable earth-abundant materials, resource utilization, and energy usage.

Some essential future perspectives should be considered for biogenic nanomaterials deployment for water purification and treatment. Comprehensive research is needed before these green-synthesized nanomaterials and nanocatalysts can be used on a commercial or industrial scale. Since these nanomaterials may result in secondary contamination, this critical problem must be thoroughly investigated. While the preparation of these nanomaterials is eco-friendly and simple, some challenging and essential factors, such as stability issues and the influence of reaction parameters, should be optimized and analyzed, as these factors can improve their pollutant removal activity, morphologies, and behavior of nanomaterials. Moreover, the extraction and purification of the synthesized biogenic nanomaterials are essential for additional applications. They should also be isolated as pure as possible for wastewater treatment. More studies are needed to find nanomaterials of multifunctional and innovative nanohybrids to improve their efficient utility. The cost-effectiveness of green-synthesized nanomaterials versus nanoparticles synthesized using traditional methods should be investigated. The assessment of restorative quality and efficacy issues is conducted in laboratory settings, simulating the parameter ranges of actual environmental levels, but it's vital to examine and analyze the outcomes from real-world scenarios.

Conflict of interest

The authors declare that there is no conflict of interest that would prejudice the impartiality of this scientific work.

REFERENCES

[1] H. Hu, J.H. Xin, H. Hu, X. Wang, D. Miao, Y. Liu, Synthesis and stabilization of metal nanocatalysts for reduction reactions–a review, Journal of materials chemistry A 3(21) (2015) 11157-11182.

[2] M. Kamranifar, T.J. Al-Musawi, M. Amarzadeh, A. Hosseinzadeh, N. Nasseh, M. Qutob, F.S. Arghavan, Quick adsorption followed by lengthy photodegradation using $FeNi_3$@SiO_2@ZnO: A promising method for complete removal of penicillin G from wastewater, Journal of Water Process Engineering 40 (2021) 101940.

[3] A. Tkaczyk, K. Mitrowska, A. Posyniak, Synthetic organic dyes as contaminants of the aquatic environment and their implications for ecosystems: a review, Science of The Total Environment 717 (2020) 137222.

[4] C.G. Awuchi, H. Twinomuhwezi, C.G. Awuchi, V.S. Igwe, I.O. Amagwula, Industrial Waste Management, Treatment, and Health Issues: Wastewater, Solid, and Electronic Wastes, European Academic Research 8(2) (2020) 1081-1119.

[5] M. de Oliveira, B.E.F. Frihling, J. Velasques, F.J.C. Magalhães Filho, P.S. Cavalheri, L. Migliolo, Pharmaceuticals residues and xenobiotics contaminants: occurrence, analytical techniques and sustainable alternatives for wastewater treatment, Science of The Total Environment 705 (2020) 135568.

[6] B.K. Ghosh, S. Hazra, B. Naik, N.N. Ghosh, Preparation of Cu nanoparticle loaded SBA-15 and their excellent catalytic activity in reduction of variety of dyes, Powder Technology 269 (2015) 371-378.

[7] D. Kim, H. Kim, J.Y. Chang, Designing internal hierarchical porous networks in polymer monoliths that exhibit rapid removal and photocatalytic degradation of aromatic pollutants, Small 16(22) (2020) 1907555.

[8] P.T. Anastas, J.C. Warner, Principles of green chemistry, Green chemistry: Theory and practice (1998) 29-56.

[9] G.E. Crisenza, P. Melchiorre, Chemistry glows green with photoredox catalysis, Nature communications 11(1) (2020) 1-4.

[10] Y. Ren, Y. Ma, G. Min, W. Zhang, L. Lv, W. Zhang, A mini review of multifunctional ultrafiltration membranes for wastewater decontamination: Additional functions of adsorption and catalytic oxidation, Science of The Total Environment (2020) 143083.

[11] T.-L. Chen, H. Kim, S.-Y. Pan, P.-C. Tseng, Y.-P. Lin, P.-C. Chiang, Implementation of green chemistry principles in circular economy system towards sustainable development goals: Challenges and perspectives, Science of the Total Environment 716 (2020) 136998.

[12] C.-H.C. Zhou, J.N. Beltramini, Y.-X. Fan, G.M. Lu, Chemoselective catalytic conversion of glycerol as a biorenewable source to valuable commodity chemicals, Chemical Society Reviews 37(3) (2008) 527-549.

[13] V. Polshettiwar, R.S. Varma, Green chemistry by nano-catalysis, Green Chemistry 12(5) (2010) 743-754.

[14] M.B. Gawande, P.S. Branco, R.S. Varma, Nano-magnetite (Fe_3O_4) as a support for recyclable catalysts in the development of sustainable methodologies, Chemical Society Reviews 42(8) (2013) 3371-3393.

[15] L. Bazli, A. Khavandi, M.A. Boutorabi, M. Karrabi, Morphology and viscoelastic behavior of silicone rubber/EPDM/Cloisite 15A nanocomposites based on Maxwell model, Iranian Polymer Journal 25(11) (2016) 907-918.

[16] L. Bazli, A. Khavandi, M.A. Boutorabi, M. Karrabi, Correlation between viscoelastic behavior and morphology of nanocomposites based on SR/EPDM blends compatibilized by maleic anhydride, Polymer 113 (2017) 156-166.

[17] N. Manojkumar, C. Muthukumaran, G. Sharmila, A. Aishwarya, Heterogeneous nanocatalysts for sustainable biodiesel production: A review, Journal of Environmental Chemical Engineering (2020) 104876.

[18] M. Shokouhimehr, Magnetically separable and sustainable nanostructured catalysts for heterogeneous reduction of nitroaromatics, Catalysts 5(2) (2015) 534-560.

[19] S. Tripathi, W. Boggs, Role of Nanocatalysts in Synthesis of Carbon Nanofiber, Carbon Nanofibers: Fundamentals and Applications (2021) 49.

[20] R. Naveenkumar, G. Baskar, Process optimization, green chemistry balance and technoeconomic analysis of biodiesel production from castor oil using heterogeneous nanocatalyst, Bioresource Technology 320 (2021) 124347.

[21] S.B. Singh, P.K. Tandon, Catalysis: a brief review on nano-catalyst, J Energy Chem Eng 2(3) (2014) 106-115.

[22] S. Kazemifard, H. Nayebzadeh, N. Saghatoleslami, E. Safakish, Application of magnetic alumina-ferric oxide nanocatalyst supported by KOH for in-situ transesterification of microalgae cultivated in wastewater medium, Biomass and Bioenergy 129 (2019) 105338.

[23] A. Marjani, M.H. Zare, M.H. Sadeghi, S. Shirazian, M. Ghadiri, Synthesis of alginate-coated magnetic nanocatalyst containing high-performance integrated enzyme for phenol removal, Journal of Environmental Chemical Engineering (2020) 104884.

[24] F. Sadegh, N. Politakos, E.G. de San Román, O. Sanz, I. Perez-Miqueo, S.E. Moya, R. Tomovska, A green synthesis of nanocatalysts based on reduced graphene oxide/magnetic nanoparticles for the degradation of Acid Red 1, RSC Advances 10(64) (2020) 38805-38817.

[25] A.S. Ethiraj, P. Uttam, K. Varunkumar, K.F. Chong, G.A. Ali, Photocatalytic performance of a novel semiconductor nanocatalyst: Copper doped nickel oxide for phenol degradation, Materials Chemistry and Physics 242 (2020) 122520.

[26] G.A. Ali, Photocatalytic performance of a novel semiconductor nanocatalyst: Copper doped nickel oxide for phenol degradation, (2019).

[27] T. Jayabalan, S. Naina Mohamed, M. Matheswaran, T. Radhakrishnan, A. Pugazhendhi, A. Alagarsamy, Enhanced biohydrogen production from sugar industry effluent using nickel oxide and cobalt oxide as cathode nanocatalysts in microbial electrolysis cell, International Journal of Energy Research (2020).

[28] A.S. Adekunle, J.A. Oyekunle, L.M. Durosinmi, O.S. Oluwafemi, D.S. Olayanju, A.S. Akinola, O.R. Obisesan, O.F. Akinyele, T.A. Ajayeoba, Potential of cobalt and cobalt oxide nanoparticles as nanocatalyst towards dyes degradation in wastewater, Nano-Structures & Nano-Objects 21 (2020) 100405.

[29] C.-O.O. Maureen, O.J. Nnaemeka, A.N. Basil, O.E. Emeka, Photocatalytic degradation of a basic dye using zinc oxide nanocatalyst, Int. Lett. Chem. Phys. Astron 81 (2019) 18-26.

[30] L. Pandian, R. Rajasekaran, P. Govindan, Synergistic effect of ozone on cadmium doped zinc oxide nanocatalyst for the degradation of textile dyeing wastewater, Materials Research Express 6(8) (2019) 085513.

[31] Q. Sun, X. Fu, R. Si, C.H. Wang, N. Yan, Mesoporous silica-encaged ultrafine bimetallic nanocatalysts for CO_2 hydrogenation to formates, ChemCatChem 11(20) (2019) 5093-5097.

[32] P.C.L. Muraro, S.R. Mortari, B.S. Vizzotto, G. Chuy, C. Dos Santos, L.F.W. Brum, W.L. da Silva, Iron oxide nanocatalyst with titanium and silver nanoparticles: Synthesis, characterization and photocatalytic activity on the degradation of Rhodamine B dye, Scientific reports 10(1) (2020) 1-9.

[33] Z. Cheng, X. Chu, J. Yin, B. Dai, W. Zhao, Y. Jiang, J. Xu, H. Zhong, P. Zhao, L. Zhang, Formation of composite fuels by coating aluminum powder with a cobalt nanocatalyst: Enhanced heat release and catalytic performance, Chemical Engineering Journal 385 (2020) 123859.

[34] G. Jaiswal, V.G. Landge, D. Jagadeesan, E. Balaraman, Iron-based nanocatalyst for the acceptorless dehydrogenation reactions, Nature communications 8(1) (2017) 1-13.

[35] K. Zhang, J.H. Cha, S.Y. Jeon, K.O. Kirlikovali, M. Ostadhassan, V. Rasouli, O.K. Farha, H.W. Jang, R.S. Varma, M. Shokouhimehr, Pd modified prussian blue frameworks: Multiple electron transfer pathways for improving catalytic activity toward hydrogenation of nitroaromatics, Molecular Catalysis 492 (2020) 110967.

[36] H. Suo, L. Xu, Y. Xue, X. Qiu, H. Huang, Y. Hu, Ionic liquids-modified cellulose coated magnetic nanoparticles for enzyme immobilization: improvement of catalytic performance, Carbohydrate polymers 234 (2020) 115914.

[37] K. Yan, C. Jarvis, T. Lafleur, Y. Qiao, X. Xie, Novel synthesis of Pd nanoparticles for hydrogenation of biomass-derived platform chemicals showing enhanced catalytic performance, RSC advances 3(48) (2013) 25865-25871.

[38] K. Yan, T. Lafleur, G. Wu, J. Liao, C. Ceng, X. Xie, Highly selective production of value-added γ-valerolactone from biomass-derived levulinic acid using the robust Pd nanoparticles, Applied Catalysis A: General 468 (2013) 52-58.

[39] M. Shokouhimehr, K. Hong, T.H. Lee, C.W. Moon, S.P. Hong, K. Zhang, J.M. Suh, K.S. Choi, R.S. Varma, H.W. Jang, Magnetically retrievable nanocomposite adorned with Pd nanocatalysts: efficient reduction of nitroaromatics in aqueous media, Green Chemistry 20(16) (2018) 3809-3817.

[40] S. Luo, Z. Zeng, G. Zeng, Z. Liu, R. Xiao, M. Chen, L. Tang, W. Tang, C. Lai, M. Cheng, Metal organic frameworks as robust host of palladium nanoparticles in heterogeneous catalysis: Synthesis, application, and prospect, ACS applied materials & interfaces 11(36) (2019) 32579-32598.

[41] M.J. Ndolomingo, N. Bingwa, R. Meijboom, Review of supported metal nanoparticles: synthesis methodologies, advantages and application as catalysts, Journal of Materials Science 55(15) (2020) 6195-6241.

[42] K. Yan, T. Lafleur, C. Jarvis, G. Wu, Clean and selective production of γ-valerolactone from biomass-derived levulinic acid catalyzed by recyclable Pd nanoparticle catalyst, Journal of cleaner production 72 (2014) 230-232.

[43] B.R. Cuenya, Synthesis and catalytic properties of metal nanoparticles: Size, shape, support, composition, and oxidation state effects, Thin Solid Films 518(12) (2010) 3127-3150.

[44] M.B. Gawande, A.K. Rathi, P.S. Branco, I.D. Nogueira, A. Velhinho, J.J. Shrikhande, U.U. Indulkar, R.V. Jayaram, C.A.A. Ghumman, N. Bundaleski, Regio-and Chemoselective Reduction of Nitroarenes and Carbonyl Compounds over Recyclable Magnetic Ferrite-Nickel Nanoparticles (Fe_3O_4/Ni) by Using Glycerol as a Hydrogen Source, Chemistry–A European Journal 18(40) (2012) 12628-

12632.
[45] M.B. Gawande, A. Rathi, I.D. Nogueira, C. Ghumman, N. Bundaleski, O. Teodoro, P.S. Branco, A Recyclable ferrite–Co magnetic nanocatalyst for the oxidation of alcohols to carbonyl compounds, ChemPlusChem 77(10) (2012) 865-871.
[46] F. Sharifianjazi, M. Moradi, N. Parvin, A. Nemati, A.J. Rad, N. Sheysi, A. Abouchenari, A. Mohammadi, S. Karbasi, Z. Ahmadi, Magnetic $CoFe_2O_4$ nanoparticles doped with metal ions: a review, Ceramics International (2020).
[47] J. Feng, L. Su, Y. Ma, C. Ren, Q. Guo, X. Chen, $CuFe_2O_4$ magnetic nanoparticles: A simple and efficient catalyst for the reduction of nitrophenol, Chemical engineering journal 221 (2013) 16-24.
[48] Y. Li, J. Shen, Y. Hu, S. Qiu, G. Min, Z. Song, Z. Sun, C. Li, General flame approach to chainlike MFe_2O_4 spinel (M= Cu, Ni, Co, Zn) nanoaggregates for reduction of nitroaromatic compounds, Industrial & Engineering Chemistry Research 54(40) (2015) 9750-9757.
[49] A. Goyal, S. Bansal, S. Singhal, Facile reduction of nitrophenols: Comparative catalytic efficiency of MFe_2O_4 (M= Ni, Cu, Zn) nano ferrites, International journal of hydrogen energy 39(10) (2014) 4895-4908.
[50] A. Goyal, S. Bansal, V. Kumar, J. Singh, S. Singhal, Mn substituted cobalt ferrites ($CoMnxFe_{2-x}O_4$ (x= 0.0, 0.2, 0.4, 0.6, 0.8, 1.0)): As magnetically separable heterogeneous nanocatalyst for the reduction of nitrophenols, Applied Surface Science 324 (2015) 877-889.
[51] V.S. Kiran, S. Sumathi, Comparison of catalytic activity of bismuth substituted cobalt ferrite nanoparticles synthesized by combustion and co-precipitation method, Journal of Magnetism and Magnetic Materials 421 (2017) 113-119.
[52] C. Singh, A. Goyal, S. Singhal, Nickel-doped cobalt ferrite nanoparticles: efficient catalysts for the reduction of nitroaromatic compounds and photo-oxidative degradation of toxic dyes, Nanoscale 6(14) (2014) 7959-7970.
[53] C. Dey, A. Chaudhuri, A. Ghosh, M. Mandal Goswami, Magnetic cube-shaped $NiFe_2O_4$ nanoparticles: an effective model catalyst for nitro compound reduction, (2017).
[54] M. Dhiman, A. Goyal, V. Kumar, S. Singhal, Designing different morphologies of NiFe 2 O 4 for tuning of structural, optical and magnetic properties for catalytic advancements, New Journal of Chemistry 40(12) (2016) 10418-10431.
[55] I. Papadas, K. Subrahmanyam, M.G. Kanatzidis, G. Armatas, Templated assembly of BiFeO 3 nanocrystals into 3D mesoporous networks for catalytic applications, Nanoscale 7(13) (2015) 5737-5743.
[56] M. Amir, U. Kurtan, A. Baykal, Rapid color degradation of organic dyes by Fe_3O_4@His@Ag recyclable magnetic nanocatalyst, Journal of Industrial and Engineering Chemistry 27 (2015) 347-353.
[57] U. Kurtan, M. Amir, A. Yıldız, A. Baykal, Synthesis of magnetically recyclable $MnFe_2O_4$@SiO_2@Ag nanocatalyst: Its high catalytic performances for azo dyes and nitro compounds reduction, Applied Surface Science 376 (2016) 16-25.
[58] P. Mohammadi, H. Sheibani, Green synthesis of Fe_3O_4@SiO_2-Ag magnetic nanocatalyst using safflower extract and its application as recoverable catalyst for reduction of dye pollutants in water, Applied Organometallic Chemistry 32(4) (2018) e4249.
[59] H. Veisi, S. Razeghi, P. Mohammadi, S. Hemmati, Silver nanoparticles decorated on thiol-modified magnetite nanoparticles (Fe_3O_4/SiO_2-Pr-S-Ag) as a recyclable nanocatalyst for degradation of organic dyes, Materials Science and Engineering: C 97 (2019) 624-631.
[60] B.K. Ghosh, D. Moitra, M. Chandel, H. Lulla, N.N. Ghosh, Ag nanoparticle immobilized mesoporous TiO_2-cobalt ferrite nanocatalyst: A highly active, versatile, magnetically separable and reusable catalyst, Materials Research Bulletin 94 (2017) 361-370.
[61] M.S. Najafinejad, P. Mohammadi, M. Mehdi Afsahi, H. Sheibani, Biosynthesis of Au nanoparticles supported on Fe_3O_4@polyaniline as a heterogeneous and reusable magnetic nanocatalyst for reduction of the azo dyes at ambient temperature, Materials Science and Engineering: C 98 (2019) 19-29.
[62] P.L.d. Oliveira, N.S. Lima, A.C.F.d.M. Costa, E.B. Cavalcanti, L.d.S. Conrado, Obtaining TiO2:CoFe2O4 nanocatalyst by Pechini method for diuron degradation and mineralization, Ceramics International 46(7) (2020) 9421-9435.
[63] H.H. Mohamed, N.A. Alomair, S. Akhtar, T.E. Youssef, Eco-friendly synthesized α-Fe2O3/TiO2 heterojunction with enhanced visible light photocatalytic activity, Journal of Photochemistry and Photobiology A: Chemistry 382 (2019) 111951.
[64] R. Ranjith, V. Renganathan, S.-M. Chen, N.S. Selvan, P.S. Rajam, Green synthesis of reduced graphene oxide supported TiO2/Co3O4 nanocomposite for photocatalytic degradation of methylene blue and crystal violet, Ceramics International 45(10) (2019) 12926-12933.
[65] V. Vetere, A.B. Merlo, M.L. Casella, Chemoselective hydrogenation of aromatic ketones with Pt-based heterogeneous catalysts. Substituent effects, Applied Catalysis A: General 491 (2015) 70-77.
[66] W. Jin, L. Pastor-Pérez, J.J. Villora-Pico, M.M. Pastor-Blas, A. Sepúlveda-Escribano, S. Gu, N.D. Charisiou, K. Papageridis, M.A. Goula, T.R. Reina, Catalytic conversion of palm oil to bio-hydrogenated diesel over novel N-doped activated carbon supported Pt nanoparticles, Energies 13(1) (2020) 132.
[67] H.M.A. Sharif, A. Mahmood, H.-Y. Cheng, R. Djellabi, J. Ali, W.-L. Jiang, S.-S. Wang, M.R. Haider, N. Mahmood, A.-J. Wang, Fe_3O_4 nanoparticles coated with EDTA and Ag nanoparticles for the catalytic reduction of organic dyes from wastewater, ACS Applied Nano Materials 2(8) (2019) 5310-5319.
[68] G.P. Sahoo, D.K. Bhui, D. Das, A. Misra, Synthesis of anisotropic gold nanoparticles and their catalytic activities of breaking azo bond in sudan-1, Journal of Molecular Liquids 198 (2014) 215-222.
[69] Z.-H. Xie, H.-Y. Zhou, C.-S. He, Z.-C. Pan, G. Yao, B. Lai, Synthesis, application and catalytic performance of layered double hydroxide based catalysts in advanced oxidation processes for wastewater decontamination: A review, Chemical Engineering Journal (2021) 128713.
[70] X.-Y. Zhang, W.-L. Yu, J. Zhao, B. Dong, C.-G. Liu, Y.-M. Chai, Recent development on self-supported transition metal-based catalysts for water electrolysis at large current density, Applied Materials Today 22 (2021) 100913.
[71] M.S. Holden, K.E. Nick, M. Hall, J.R. Milligan, Q. Chen, C.C. Perry, Synthesis and catalytic activity of pluronic stabilized silver–gold bimetallic nanoparticles, RSC advances 4(94) (2014) 52279-52288.
[72] S.G. Babu, M. Gopiraman, D. Deng, K. Wei, R. Karvembu, I.S. Kim, Robust Au–Ag/graphene bimetallic nanocatalyst for multifunctional activity with high synergism, Chemical Engineering Journal 300 (2016) 146-159.
[73] N.V. Long, M. Ohtaki, T.D. Hien, J. Randy, M. Nogami, A comparative study of Pt and Pt–Pd core–shell nanocatalysts, Electrochimica Acta 56(25) (2011) 9133-9143.
[74] Z. Bo, X. Guo, X. Wei, H. Yang, J. Yan, K. Cen, Density functional theory calculations of NO_2 and H_2S adsorption on the group 10 transition metal (Ni, Pd and Pt) decorated graphene, Physica E: Low-dimensional Systems and Nanostructures 109 (2019) 156-163.
[75] K. Patel, S. Kapoor, D.P. Dave, T. Mukherjee, Synthesis of Pt, Pd, Pt/Ag and Pd/Ag nanoparticles by microwave-polyol method, Journal of Chemical Sciences 117(4) (2005) 311-316.
[76] B.H. Susanto, J.R.V. Siallagan, Analysis of NiMoP/γ-Al_2O_3 Catalyst Preparation with Impregnation and Microwave Polyol Methods for Bio-Jet Production, Materials Science Forum, Trans Tech Publ, 2020, pp. 257-264.
[77] H. Gu, Y. Yang, J. Tian, G. Shi, Photochemical synthesis of noble metal (Ag, Pd, Au, Pt) on graphene/ZnO multihybrid nanoarchitectures as electrocatalysis for H_2O_2 reduction, ACS applied materials & interfaces 5(14) (2013) 6762-6768.
[78] T. Iqbal, S. Tufail, S. Ghazal, Synthesis of silver, chromium, manganese, tin and iron nano particles by different techniques, International Journal of Nanoscience and Nanotechnology 13(1) (2017) 19-52.
[79] M.A. Salem, E.A. Bakr, H.G. El-Attar, Pt@ Ag and Pd@ Ag core/shell nanoparticles for catalytic degradation of Congo red in aqueous solution, Spectrochimica Acta Part A: Molecular and Biomolecular Spectroscopy 188 (2018) 155-163.
[80] M. Moradi, M. Haghighi, S. Allahyari, Precipitation dispersion of Ag–ZnO nanocatalyst over functionalized multiwall carbon nanotube used in degradation of Acid Orange from wastewater, Process Safety and Environmental Protection 107 (2017) 414-427.
[81] C. Duan, C. Liu, X. Meng, W. Lu, Y. Ni, Fabrication of carboxymethylated cellulose fibers supporting Ag NPs@MOF-199s nanocatalysts for catalytic reduction of 4-nitrophenol, Applied Organometallic Chemistry 33(5) (2019) e4865.
[82] K. Iqbal, A. Iqbal, A.M. Kirillov, B. Wang, W. Liu, Y. Tang, A new Ce-doped MgAl-LDH@ Au nanocatalyst for highly efficient reductive degradation of organic contaminants, Journal of Materials Chemistry A 5(14) (2017) 6716-6724.
[83] A. Sahoo, S.K. Tripathy, N. Dehury, S. Patra, A porous trimetallic Au@ Pd@ Ru nanoparticle system: synthesis, characterisation and efficient dye degradation and removal, Journal of Materials Chemistry A 3(38) (2015) 19376-19383.
[84] M. Nasrollahzadeh, T. Baran, N.Y. Baran, M. Sajjadi, M.R. Tahsili, M. Shokouhimehr, Pd nanocatalyst stabilized on amine-modified zeolite: Antibacterial and catalytic activities for environmental pollution remediation in aqueous medium, Separation and Purification Technology 239 (2020) 116542.
[85] Q. Yan, X.-Y. Wang, J.-J. Feng, L.-P. Mei, A.-J. Wang, Simple fabrication of bimetallic platinum-rhodium alloyed nano-multipods: A highly effective and recyclable catalyst for reduction of 4-nitrophenol and rhodamine B, Journal of Colloid and Interface Science 582 (2021) 701-710.
[86] V. Katoch, N. Sharma, M. Sharma, M. Baghoria, J.J. Panda, M. Singh, B. Prakash, Microflow synthesis and enhanced photocatalytic dye degradation performance of antibacterial Bi 2 O 3 nanoparticles, Environmental Science and Pollution Research (2021) 1-11.

[87] Y. Dang, Y. Cheng, Y. Zhou, Y. Huang, K. Wang, Nano-PAA-CuCl2 Composite as Fenton-like Reusable Catalyst to Enhanced Degrade Organic Pollutant MB/MO, Catalysts 11(1) (2021) 10.
[88] A. ur Rehman, M. Aadil, S. Zulfiqar, P.O. Agboola, I. Shakir, M.F. Aly Aboud, S. Haider, M.F. Warsi, Fabrication of binary metal doped CuO nanocatalyst and their application for the industrial effluents treatment, Ceramics International (2020).
[89] S. Dehghan, M. Tahergorabi, S. Norzaee, E. Boorboor Azimi, M. Hasham Firooz, Y. Dadban Shahamat, Preparation and photocatalytic performance of reduced graphene oxide/ ZnO nanocatalyst for degradation of metalaxyl from aqueous solution: effect of operational parameters, mineralisation and toxicity bioassay, International Journal of Environmental Analytical Chemistry (2020) 1-23.
[90] M. Dorosti, M. Baghdadi, S. Nasimi, A continuous electroreduction cell composed of palladium nanocatalyst immobilized on discarded cigarette filters as an active bed for Cr(VI) removal from groundwater, Journal of Environmental Management 264 (2020) 110409.
[91] S.G. Shelar, V.K. Mahajan, S.P. Patil, G.H. Sonawane, Effect of doping parameters on photocatalytic degradation of methylene blue using Ag doped ZnO nanocatalyst, SN Applied Sciences 2 (2020) 1-10.
[92] M. Ikram, M.I. Khan, A. Raza, M. Imran, A. Ul-Hamid, S. Ali, Outstanding performance of silver-decorated MoS2 nanopetals used as nanocatalyst for synthetic dye degradation, Physica E: Low-dimensional Systems and Nanostructures 124 (2020) 114246.
[93] M. Nasrollahzadeh, R. Akbari, Z. Issaabadi, S.M. Sajadi, Biosynthesis and characterization of Ag/MgO nanocomposite and its catalytic performance in the rapid treatment of environmental contaminants, Ceramics International 46(2) (2020) 2093-2101.
[94] M. Khoshnamvand, C. Huo, J. Liu, Silver nanoparticles synthesized using Allium ampeloprasum L. leaf extract: Characterization and performance in catalytic reduction of 4-nitrophenol and antioxidant activity, Journal of Molecular Structure 1175 (2019) 90-96.
[95] B. Kumar, K.S. Vizuete, V. Sharma, A. Debut, L. Cumbal, Ecofriendly synthesis of monodispersed silver nanoparticles using Andean Mortiño berry as reductant and its photocatalytic activity, Vacuum 160 (2019) 272-278.
[96] V. Garole, B. Choudhary, S. Tetgure, D. Garole, A. Borse, Palladium nanocatalyst: green synthesis, characterization, and catalytic application, International Journal of Environmental Science and Technology 16(12) (2019) 7885-7892.
[97] M. Hashemi Salehi, M. Yousefi, M. Hekmati, E. Balali, Application of palladium nanoparticle-decorated Artemisia abrotanum extract-modified graphene oxide for highly active catalytic reduction of methylene blue, methyl orange and rhodamine B, Applied Organometallic Chemistry 33(10) (2019) e5123.
[98] Z.U.H. Khan, H.M. Sadiq, N.S. Shah, A.U. Khan, N. Muhammad, S.U. Hassan, K. Tahir, F.U. Khan, M. Imran, N. Ahmad, Greener synthesis of zinc oxide nanoparticles using Trianthema portulacastrum extract and evaluation of its photocatalytic and biological applications, Journal of Photochemistry and Photobiology B: Biology 192 (2019) 147-157.
[99] M. Ganesh, S.G. Lee, J. Jayaprakash, M. Mohankumar, H.T. Jang, Hydnocarpus alpina Wt extract mediated green synthesis of ZnO nanoparticle and screening of its anti-microbial, free radical scavenging, and photocatalytic activity, Biocatalysis and agricultural biotechnology 19 (2019) 101129.
[100] A.R. Prasad, J. Garvasis, S.K. Oruvil, A. Joseph, Bio-inspired green synthesis of zinc oxide nanoparticles using Abelmoschus esculentus mucilage and selective degradation of cationic dye pollutants, Journal of Physics and Chemistry of Solids 127 (2019) 265-274.
[101] K. Rajendaran, R. Muthuramalingam, S. Ayyadurai, Green synthesis of Ag-Mo/CuO nanoparticles using Azadirachta indica leaf extracts to study its solar photocatalytic and antimicrobial activities, Materials Science in Semiconductor Processing 91 (2019) 230-238.
[102] P. Mohammadi, H. Daneshafruz, H. Sheibani, Gold nanoparticles on cyanuric citric acid functionalized magnetic SBA-16 as an effective catalyst for dye reduction, Physica E: Low-dimensional Systems and Nanostructures 126 (2021) 114392.
[103] M. Memar, A.R. Rezvani, S. Saheli, Synthesis, characterization, and application of CuO nanoparticle 2D doped with Zn 2+ against photodegradation of organic dyes (MB & MO) under sunlight, Journal of Materials Science: Materials in Electronics (2021) 1-19.
[104] A. Nouri, B. Faraji Dizaji, N. Kianinejad, A. Jafari Rad, S. Rahimi, M. Irani, F. Sharifian Jazi, Simultaneous linear release of folic acid and doxorubicin from ethyl cellulose/chitosan/g-C_3N_4/MoS_2 core-shell nanofibers and its anticancer properties, Journal of Biomedical Materials Research Part A (2020).
[105] S. Yuan, G. Zhang, J. Zhu, N. Mamrol, S. Liu, Z. Mai, P. Van Puyvelde, B. Van der Bruggen, Hydrogel assisted interfacial polymerization for advanced nanofiltration membranes, Journal of Materials Chemistry A 8(6) (2020) 3238-3245.
[106] X. Li, S. Ye, Y.C. Zhang, H.P. Zhao, Y. Huang, B. Zhang, T. Cai, Magnetic Janus nanocomposites with iridium (III) complexes for heterogeneous catalysis of logic controlled RAFT polymerization using multiplexed external switching, Nanoscale 12(14) (2020) 7595-7603.
[107] H. Hu, J.H. Xin, H. Hu, PAM/graphene/Ag ternary hydrogel: synthesis, characterization and catalytic application, Journal of Materials Chemistry A 2(29) (2014) 11319-11333.
[108] F. Gorginpour, H. Zali-Boeini, H.A. Rudbari, A quinoxaline-based porous organic polymer containing copper nanoparticles CuNPs@ Q-POP as a robust nanocatalyst toward C–N coupling reaction, RSC Advances 11(6) (2021) 3655-3665.
[109] L. Ai, J. Jiang, Catalytic reduction of 4-nitrophenol by silver nanoparticles stabilized on environmentally benign macroscopic biopolymer hydrogel, Bioresource technology 132 (2013) 374-377.
[110] M. Norouzi, D. Elhamifar, Ionic liquid-modified magnetic mesoporous silica supported tungstate: A powerful and magnetically recoverable nanocatalyst, Composites Part B: Engineering 176 (2019) 107308.
[111] Y. Mei, Y. Lu, F. Polzer, M. Ballauff, M. Drechsler, Catalytic activity of palladium nanoparticles encapsulated in spherical polyelectrolyte brushes and core–shell microgels, Chemistry of Materials 19(5) (2007) 1062-1069.
[112] M.I. Din, R. Khalid, Z. Hussain, T. Hussain, A. Mujahid, J. Najeeb, F. Izhar, Nanocatalytic assemblies for catalytic reduction of nitrophenols: a critical review, Critical reviews in analytical chemistry 50(4) (2020) 322-338.
[113] M. J. Thiele, M.D. Davari, M. Konig, I. Hofmann, N.O. Junker, T. Mirzaei Garakani, L. Vojcic, J.r. Fitter, U. Schwaneberg, Enzyme–polyelectrolyte complexes boost the catalytic performance of enzymes, ACS catalysis 8(11) (2018) 10876-10887.
[114] C. Nagahama, A. Zinchenko, Small DNA additives to polyelectrolyte multilayers promote formation of ultrafine gold nanoparticles with enhanced catalytic activity, Colloid and Polymer Science 297(3) (2019) 363-369.
[115] M. Ajmal, M. Siddiq, H. Al-Lohedan, N. Sahiner, Highly versatile p (MAc)–M (M: Cu, Co, Ni) microgel composite catalyst for individual and simultaneous catalytic reduction of nitro compounds and dyes, RSC Advances 4(103) (2014) 59562-59570.
[116] N. Sahiner, S. Yildiz, H. Al-Lohedan, The resourcefulness of p (4-VP) cryogels as template for in situ nanoparticle preparation of various metals and their use in H_2 production, nitro compound reduction and dye degradation, Applied Catalysis B: Environmental 166 (2015) 145-154.
[117] R.K. Narayanan, S.J. Devaki, T.P. Rao, Robust fibrillar nanocatalysts based on silver nanoparticle-entrapped polymeric hydrogels, Applied Catalysis A: General 483 (2014) 31-40.
[118] S. Saha, A. Pal, S. Kundu, S. Basu, T. Pal, Photochemical green synthesis of calcium-alginate-stabilized Ag and Au nanoparticles and their catalytic application to 4-nitrophenol reduction, Langmuir 26(4) (2010) 2885-2893.
[119] D. Hu, Y. Huang, H. Liu, H. Wang, S. Wang, M. Shen, M. Zhu, X. Shi, The assembly of dendrimer-stabilized gold nanoparticles onto electrospun polymer nanofibers for catalytic applications, Journal of Materials Chemistry A 2(7) (2014) 2323-2332.
[120] S. Gatard, L. Salmon, C. Deraedt, J. Ruiz, D. Astruc, S. Bouquillon, Gold Nanoparticles Stabilized by Glycodendrimers: Synthesis and Application to the Catalytic Reduction of 4-Nitrophenol, European Journal of Inorganic Chemistry 2014(16) (2014) 2671-2677.
[121] K. Kuroda, T. Ishida, M. Haruta, Reduction of 4-nitrophenol to 4-aminophenol over Au nanoparticles deposited on PMMA, Journal of Molecular Catalysis A: Chemical 298(1-2) (2009) 7-11.
[122] P. Kannan, F.A. Rahim, X. Teng, R. Chen, H. Sun, L. Huang, D.-H. Kim, Enhanced emission of $NaYF_4$: Yb, Er/Tm nanoparticles by selective growth of Au and Ag nanoshells, RSC advances 3(21) (2013) 7718-7721.
[123] C. Zhang, Q. Yang, N. Zhan, L. Sun, H. Wang, Y. Song, Y. Li, Silver nanoparticles grown on the surface of PAN nanofiber: Preparation, characterization and catalytic performance, Colloids and Surfaces A: Physicochemical and Engineering Aspects 362(1-3) (2010) 58-64.
[124] S. Harish, J. Mathiyarasu, K. Phani, V. Yegnaraman, Synthesis of conducting polymer supported Pd nanoparticles in aqueous medium and catalytic activity towards 4-nitrophenol reduction, Catalysis letters 128(1) (2009) 197-202.
[125] T. Yao, T. Cui, H. Wang, L. Xu, F. Cui, J. Wu, A simple way to prepare Au@ polypyrrole/Fe 3 O 4 hollow capsules with high stability and their application in catalytic reduction of methylene blue dye, Nanoscale 6(13) (2014) 7666-7674.
[126] K.Ö. Hamaloğlu, E. Sağ, Ç. Kip, E. Şenlik, B.S. Kaya, A. Tuncel, Magnetic-porous microspheres with synergistic catalytic activity of small-sized gold nanoparticles and titania matrix, Frontiers of Chemical Science and Engineering

13(3) (2019) 574-585.
[127] S. Panigrahi, S. Basu, S. Praharaj, S. Pande, S. Jana, A. Pal, S.K. Ghosh, T. Pal, Synthesis and size-selective catalysis by supported gold nanoparticles: study on heterogeneous and homogeneous catalytic process, The Journal of Physical Chemistry C 111(12) (2007) 4596-4605.
[128] I.U.H. Bhat, M.N.K. Anwar, J.N. Appaturi, Polymer based palladium nanocatalyst for the degradation of nitrate and Congo Red, Journal of Polymers and the Environment 27(7) (2019) 1475-1487.
[129] B. Samai, S.C. Bhattacharya, Conducting polymer supported cerium oxide nanoparticle: Enhanced photocatalytic activity for waste water treatment, Materials Chemistry and Physics 220 (2018) 171-181.
[130] L. Kaliraj, J.C. Ahn, E.J. Rupa, S. Abid, J. Lu, D.C. Yang, Synthesis of panos extract mediated ZnO nano-flowers as photocatalyst for industrial dye degradation by UV illumination, Journal of Photochemistry and Photobiology B: Biology 199 (2019) 111588.
[131] M. Nasrollahzadeh, B. Jaleh, T. Baran, R.S. Varma, Efficient degradation of environmental contaminants using Pd-RGO nanocomposite as a retrievable catalyst, Clean Technologies and Environmental Policy 22(2) (2020) 325-335.
[132] X. Peng, X. Bai, Z. Cui, X. Liu, Green synthesis of Pd truncated octahedrons using of firmiana simplex leaf extract and their catalytic study for electro-oxidation of methanol and reduction of p-nitrophenol, Applied Organometallic Chemistry 33(8) (2019) e5045.
[133] S. Bao, H. Liu, Y. Liu, W. Yang, Y. Wang, Y. Yu, Y. Sun, K. Li, Amino-functionalized graphene oxide-supported networked Pd–Ag nanowires as highly efficient catalyst for reducing Cr(VI) in industrial effluent by formic acid, Chemosphere 257 (2020) 127245.
[134] M.N. Chong, B. Jin, C.W. Chow, C. Saint, Recent developments in photocatalytic water treatment technology: a review, Water research 44(10) (2010) 2997-3027.
[135] A. Jaafara, A. Driouichb, Z. Lakbaibib, H.B. El Ayouchiac, K. Azzaouid, A. Boussaouda, S. Jodehe, Central composite design for the optimization of Basic Red V degradation in aqueous solution using Fenton reaction, Desalination and Water Treatment 158 (2019) 364-371.
[136] A. Jaafar, H.B. El Ayouchia, Z. Lakbaibi, A. Boussaoud, S. Jodeh, K. Azzaoui, M. Tabyaoui, Degradation of Pollutant Dye in Aqueous Solution using Fenton Reaction: A DFT Study, GP GLOBALIZE RESEARCH JOURNAL OF CHEMISTRY (2019).
[137] H. Eskandarloo, A. Kierulf, A. Abbaspourrad, Nano-and micromotors for cleaning polluted waters: focused review on pollutant removal mechanisms, Nanoscale 9(37) (2017) 13850-13863.
[138] K. Shivaji, E.S. Monica, A. Devadoss, D.D. Kirubakaran, C.R. Dhas, S.M. Jain, S. Pitchaimuthu, Synthesizing Green Photocatalyst Using Plant Leaf Extract for Water Pollutant Treatment, Green Photocatalysts, Springer2020, pp. 25-46.
[139] A.A. Yaqoob, T. Parveen, K. Umar, M.N. Mohamad Ibrahim, Role of nanomaterials in the treatment of wastewater: A review, Water 12(2) (2020) 495.
[140] A. Moghanian, F. Sharifianjazi, P. Abachi, E. Sadeghi, H. Jafarikhorami, A. Sedghi, Production and properties of Cu/TiO_2 nano-composites, Journal of Alloys and Compounds 698 (2017) 518-524.
[141] S. Kabra, S. Gharde, P. Gore, S. Jain, V.H. Khire, B. Kandasubramanian, Recent trends in nanothermites: Fabrication, characteristics and applications, Nano Express (2020).
[142] T. Toyao, M. Saito, Y. Horiuchi, K. Mochizuki, M. Iwata, H. Higashimura, M. Matsuoka, Efficient hydrogen production and photocatalytic reduction of nitrobenzene over a visible-light-responsive metal–organic framework photocatalyst, Catalysis Science & Technology 3(8) (2013) 2092-2097.
[143] Y. Pi, X. Li, Q. Xia, J. Wu, Y. Li, J. Xiao, Z. Li, Adsorptive and photocatalytic removal of Persistent Organic Pollutants (POPs) in water by metal-organic frameworks (MOFs), Chemical Engineering Journal 337 (2018) 351-371.
[144] T. Saeed, A. Naeem, I.U. Din, M.A. Alotaibi, A.I. Alharthi, I.W. Khan, N.H. Khan, T. Malik, Structure, nomenclature and viable synthesis of micro/nanoscale metal organic frameworks and their remarkable applications in adsorption of organic pollutants, Microchemical Journal (2020) 105579.
[145] M. Nasrollahzadeh, M. Sajjadi, S. Iravani, R.S. Varma, Green-synthesized nanocatalysts and nanomaterials for water treatment: Current challenges and future perspectives, Journal of Hazardous Materials 401 (2021) 123401.
[146] A. Mukhtar, S. Ullah, A.G. Al-Sehemi, M.A. Assiri, S. Saqib, R. Amen, M. Babar, M.A. Bustam, T. Ahmad, Synthesis and Stability of Metal-organic Frameworks (MOFs) Photocatalysts for the Removal of Persistent Organic Pollutants (POPs) from Wastewater, Current Analytical Chemistry 17(1) (2021) 61-81.
[147] F.S. Jazi, N. Parvin, M. Rabiei, M. Tahriri, Z.M. Shabestari, A.R. Azadmehr, Effect of the synthesis route on the grain size and morphology of ZnO/Ag nanocomposite, Journal of Ceramic Processing Research 13(5) (2012) 523-526.
[148] Y. Zhang, J. Zhou, X. Chen, Q. Feng, W. Cai, MOF-derived C-doped ZnO composites for enhanced photocatalytic performance under visible light, Journal of Alloys and Compounds 777 (2019) 109-118.
[149] M.C. Das, H. Xu, Z. Wang, G. Srinivas, W. Zhou, Y.-F. Yue, V.N. Nesterov, G. Qian, B. Chen, A Zn 4 O-containing doubly interpenetrated porous metal–organic framework for photocatalytic decomposition of methyl orange, Chemical Communications 47(42) (2011) 11715-11717.
[150] T. Parandhaman, N. Pentela, B. Ramalingam, D. Samanta, S.K. Das, Metal nanoparticle loaded magnetic-chitosan microsphere: water dispersible and easily separable hybrid metal nano-biomaterial for catalytic applications, ACS Sustainable Chemistry & Engineering 5(1) (2017) 489-501.
[151] M. Abdeen, S. Sabry, H. Ghozlan, A.A. El-Gendy, E.E. Carpenter, Microbial-physical synthesis of Fe and Fe_3O_4 magnetic nanoparticles using Aspergillus niger YESM1 and supercritical condition of ethanol, Journal of Nanomaterials 2016 (2016).

Available online at www.jourcc.com

Journal homepage: www.JOURCC.com

Journal of Composites and Compounds

Sol-gel: Uncomplicated, routine, and affordable synthesis procedure for utilization of composites in drug delivery: Review

Reyhaneh Nasr Azadani [a], Milad Sabbagh [b], Haniye Salehi [c], Amir Cheshmi [d], Ali Raza [e], Beena Kumari [f], Gisou Erabi [g]*

[a] *Department of Biomaterials Nanotechnology and Tissue engineering, School of Advanced Technology in Medicine, Isfahan University of Medical Sciences, Isfahan, Iran*

[b] *Lecturer at Dept. Biomedical Eng. & Dept. Laboratory Instrumentation Eng. Principal Investigator at ""Ebn-e-Sina Micro-Engineering Group"", ""ESMS"" group, Tehran, Iran*

[c] *Department of Physical Education and Sport Science, Faculty of Literature and Humanities, Islamic Azad University, Kerman Branch, Kerman, Iran*

[d] *Department of Materials Engineering, Babol Noshirvani University of Technology, Shariati Avenue, Babol, Iran*

[e] *School of Biomedical Engineering, Shanghai Jiaotong University, Shanghai, China*

[f] *Department of Pharmaceutical Sciences, Indira Gandhi University, Meerpur, Rewari, Haryana, India*

[g] *Student Research Committee, School of Medicine, Urmia University of Medical Sciences, Urmia, Iran*

ABSTRACT

Drug delivery is known as an approach for transporting a pharmaceutical compound in animals and the human body to achieve effective therapy. Drug carriers are usually based on nanoparticles synthesized by several methods. The sol-gel method is an inexpensive and simple process to prepare drug carriers that can produce particles with a high degree of homogeneity and purity. The process of sol-gel involves hydrolysis, polymerization/condensation of monomers, particle growth, and gel formation. The properties of materials including composition and morphology are affected by several factors and can be controlled by the process parameters. Due to the advantages of this method, it is widely used for drug carriers' preparation. In this study, the definition and advantages of the sol-gel process are discussed. Moreover, drug carriers such as organic-inorganic, silica, and calcium composites, as well as bioactive glass synthesized by this method are reviewed.

Peer review under responsibility of jourcc

ARTICLE INFORMATION

Article history:
Received 24 January 2021
Received in revised form 11 February 2021
Accepted 25 March 2021

Keywords:
Drug carriers
Organic-inorganic composites
Silica composites
Calcium composites
Bioactive glass

Table of contents

1. Introduction 57
2. Principle of the sol-gel method 58
3. Advantages of the sol-gel method 59
4. Synthesis of drug carriers by the sol-gel method 60
4.1. Organic-inorganic composite drug carriers 60
4.2. Silica composite drug carriers 61
4.3. Calcium composite drug carriers 62
4.4. Bioactive glass drug carriers 63
5. In-vitro and in vivo drug release studies 64
6. Conclusions and future insight 66

1. Introduction

The drug delivery system (DDS) is presented as a technology or method that enables drugs to achieve optimized therapeutic benefits by accurately managing their body distribution profiles. Numerous methods to accomplish an effective treatment since at least the 1970s have been introduced by scientists such as Gregoriadis [1], Zafaroni [2], and Theeuwes [3]. These methods were also explored concisely in the conference held during the same period [4]. The drug delivery system's aims

* *Corresponding author: Amir Cheshmi; E-mail: amir_cheshomi@yahoo.com*

https://doi.org/10.52547/jcc.3.1.6

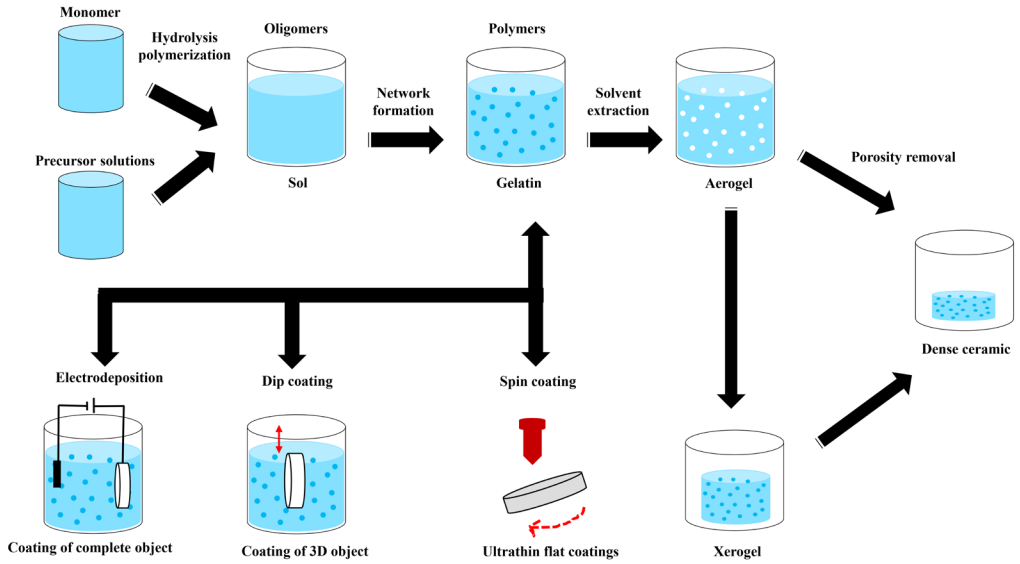

Fig. 1. Synthesis method of sol-gel.

and strategies are often divided into three main areas, i.e., 1) preference of route of administration and improvement of absorption, 2) controlling the release from formulations, and 3) targeting specific site of operation. Different drug delivery techniques for improving absorption [5] and regulated release [6] have been introduced in these respects. In the case of drug targeting, macromolecules including antibodies [7] and particulate vehicles such as liposomes [8] have also been used to build multiple carrier mechanisms for the targeted delivery of specific organs and cells [9]. Many composites have been created and assessed for various biomedical applications, such as tissue engineering, cardiac prosthesis, and drug delivery in the last few years [10-14]. For example, the composite's composition must contain an acid-resistant lipids exterior protecting the lactate dehydrogenase (LDH) interlayers for supplying medicine to the intestines [15].

Many synthesis approaches have been introduced for producing these biomaterials, such as co-precipitation, in-situ gelling, microemulsion, electrospinning, solvothermal, microwave emission, and double emulsion of water-in-oil-in-water (w/o/w), free polymerization of radicals, and sol-gel. The sol-gel procedure is flexible and straightforward among the afore-mentioned methods; the components of the process are cheap, inert, resilient to light and heat, and harmless to the ecosystem or humans [16, 17]. The sol-gel approach allows the manufacturing of homogeneous drug delivery nanoparticles and enables the processing of optimum temperature required for the treatment of biological products, to regulate the size and releasing rate [18]. The sol-gel system has attracted the attention of many scientists in the medical sector in recent years [19-21]. The term refers to a low-temperature process that uses chemical components that can create uniform and pure glasses and ceramics [22].

In biotechnology applications in which biomolecules, including proteins, enzymes, and antibodies, are incorporated into the sol-gel matrix have lately been widely investigated [23]. The notion was proposed in 1983 by Unger et al. [24] using sol-gel-based silica in drug delivery applications. Furthermore, numerous sol-gel-based compounds are bioactive; they can bind to human tissues such as bone. These remarkable biomaterials have osteoconductive qualities and can be used *in vivo*. For both therapeutic strategies (gene/drug delivery) as well as diagnosis (imaging), nanoparticles are proven to have potential to be used as intravascular or cellular probes which could play a crucial role in bio-medicine [25]. However, the efficiency of synthetic biomaterials relies significantly on the synthesized powders' overall features and qualities. These characteristics include purity, the structure of the phase, density, crystallinity, size of the particle, particle size arrangement, specific surface area, and geometry of particles [26].

The sol-gel methodologies have been used during the last few decades to produce several mixed-metal oxides, nanoporous oxides, nanomaterials, nanoscale structures, organic-inorganic hybrids, nanocoatings, glasses, amorphous, monolithic and structured composite, organic metal assemblies, and bioinspired materials [27-30]. It is an interesting strategy for the preparation of hybrid materials as it occurs in a solution, effortlessly implementing organic phases into an inorganic material, and at the same time, inhibiting degradation [31]. The reactions that happen during the sol-gel procedure are (i) solution-forming by hydrolysis of alkoxide precursors (sol phase) and (ii) condensation of the transitional species causing 3D network formation (gel phase) [32]. In this paper, the sol-gel synthesis method for applying composites in drug delivery, the fabrication of drug carriers through this technique, and its benefits are described in depth.

2. Principle of the sol-gel method

The science of sol-gel dates back to more than 150 years ago. During his experiments on silica sols, Graham first invented the word "sol-gel" in 1864 [33]. While van Helmont discovered "water glass" in 1640 by dissolving silicate substance in alkali and followed by precipitating silica gel in the acidic environment, it was in 1846 that Ebelmen witnessed transparent glass creation. After exposure to a silane atmosphere derived from $SiCl_4$ and ethanol [34, 35], real sol-gel research was started for the first time. During the doctoral courses at the University of Goettingen in 1912-1915, Patrick developed a cost-effective and fast sol-gel process to manufacture massive silica gel amounts from sodium silicate (Na_2SiO_3) [36]. Besides, by supercritical drying of the gel produced by hydrolytic polycondensation of $Si(OH)_4$, Kistler [37] presented the first synthesis of a highly porous silica form (SiO_2), which he called "aerogel". Sol-gel techniques also allow for powderless manufacturing, directly from solution, glasses, thin fibers or films, and ceramics. Precursors are combined at the molecular level, and alternately structured materials can be formed at far lower temperatures than conventional processing methods can offer [38].

Generally, in the sol-gel procedure, the phase transformation from a liquid "sol" (mostly colloidal) to a solid "gel" of a system is required. For the sol's preparation, metal-organic compounds or inorganic metal salts like metal alkoxides [M (OR) n] are used as the initial materials. M demonstrates network-forming elements like B, Al, Zr, Ti, Si, etc. and R is commonly an alkyl group. Tetramethyl-orthosilicate (TMOS) and Tetraethyl-orthosilicate (TEOS) in the sol-gel method are the most widely utilized precursors. Since metal alkoxide is combined with a mutual solvent (often alcohol) and water in the base/acid catalyst presence leading to the initiation of the simple sol-gel reaction [39-41].

Normally, after the hydrolysis process is triggered, the condensation and hydrolysis reactions proceed simultaneously. The hydrolysis contributes to creating siloxane bonds (Si-O-Si) and silanol groups (Si-OH) formed by condensation reactions, leading to the water and alcohol production as by-products. The final material characteristics and composition are considerably affected by the chemical reactions that happen throughout the sol-gel process. Additional processing of the sol allows one to render materials of sol-gel in various configurations. With dip, spin, and spray coating, thin films could be formed on a substrate [42, 43].

The solution's viscosity increases steadily during the sol-gel transition as the sol begins to become interconnected to make a stable and porous gel network. The gel may be transformed into rigid glass particles or ceramic with more drying and heat processing (at atmospheric pressure) resulting in considerable shrinkage due to the solvent liquid removal. The obtained substance is recognized as "xerogel". The network does not get smaller and an extremely porous, low-density substance called aerogel is processed if solvent elimination happens within hypercritical (supercritical) settings [44, 45]. Viscous sintering (xerogel shrinkage because of a limited viscous flow) is caused by thermal processing of the xerogel at high temperatures, and the porous gel is appropriately converted into a thick glass [46] (Fig. 1).

When the sol viscosity is calibrated to a suitable viscosity level, it is possible to obtain ceramic fibers from the sol. Through precipitation, emulsion methods, or spray pyrolysis, ultra-fine, and homogenous ceramic powders are produced. Applications such as using sol-gel as the porous membrane to the encapsulation of enzymes, sensor molecules, and several other substances are most prevalent, while many applications of sol-gel-derived composites are rapidly developing in biomedical uses [47, 48].

The creation of new biomaterials is needed for biomedical applications, and it can be accomplished by combining sol-gel biochemistry and chemistry. Gel-derived substances are ideal platforms for analyzing and regulating biochemical interactions due to their micro-pores, broad specific surface, and residual hydroxyl ions inside constrained matrices with boosted bioactivity [49]. The coating of medical instruments is an essential factor in all biomedical applications. Materials utilized in medical tools must have suitable structural and technical qualities and they preferably facilitate the healing response with no triggering severe physiological reactions [50]. Medical device manufacturers use different surface treatments, like coatings, to improve or alter characteristics, including hydrophobicity/hydrophilicity, biocompatibility, functionality, and lubricity. For diverse biomedical uses, sol-gel processing provides an alternative strategy for creating bioactive surfaces. A variety of benefits are provided by sol-gel thin film development, such as low-temperature production, simplicity of manufacturing process, and accurate chemical and microstructural regulation [51].

The sol-gel-derived layers or films have substantial biocompatibility, large specific surface areas (they can be utilized as an adsorbed drug carrier), and an outer surface where rich chemistry facilitates appropriate biomolecules for effective functionalization [52]. The regulation of the silica coating's thickness and pore-size distribution also offers a systematic approach to control the duration and amount of drug release [53]. The drug diffusion and release rate are associated with both the porosity and thickness of coated films, which can be managed by the sol-gel dip-coating method by the sol composition and withdrawal speed. The benefits of applying the sol-gel dip-coating approach are that it is not reliant on the morphology of the material and it is possible to manage surface characteristics and a high level of homogeneity of thickness [54, 55].

One of the most promising drug delivery platforms is the sol-gel approach. In general, the formation of sol-gel is known as a chemical processing technique for the development of ceramic materials through implementing three significant steps: (i) solvent formulation, (ii) solvent gelation, and (iii) solvent elimination. Currently, the sol-gel method is proved to be a potential technological area, as its multifunctionality enables scientists to produce a wide variety of materials characterized by specific microstructures and nanostructures [38], ideal for the development of many innovative products, such as fibers [56], industrial coatings [57], and films. Actually, by employing lower manufacturing temperatures than those implicated in conventional ceramic powder consolidation or glass melting methods, the sol-gel approach allows highly uniform and chemically pure materials to be obtained [58].

In the biomedical industry, the sol-gel approach reveals its potential specifically to manufacture bioactive glasses in the form of inherently nanoporous materials capable of optimizing bioactivity and cellular response due to its distinctive material characteristics, including large specific surface area than conventional methods used products [20, 59]. Besides, sol-gel technology provides the opportunity to generate hybrid materials firmly bonded at the nanoscale consisting of inorganic and organic basis, eliminating the shortcomings of conventional multiphasic composites [60, 61].

3. Advantages of the sol-gel method

The sol-gel method is a significant development in science demanding a multidisciplinary strategy with its numerous uses. It produces ceramic and glass materials at comparably lower temperatures that enable the loading of different organic and inorganic materials and biomolecules during the glass structuring. The sol-gel method was recognized since the 1800s, but the uses of sol-gel have expanded several times over the last two decades. It has been employed for the manufacturing of optical coatings, optical fibers, electro-optic products, powders of colloidal silica for stationary as catalytic support and chromatographic phase, nanoporous carbon xerogels, and aerogels as hydrogen storing substances, nanocrystalline semiconductor-doped xerogels, luminescence concentrators, active waveguides, semiconducting tools, adjustable lasers, and sunscreen. Precise sol-gel technology uses are continually evolving in nanotechnology, biomedical equipment, environmental control, and defense [39, 62].

The sol-gel process, which enables the regulation of complex oxides stoichiometry and the development of high-purity, uniform, and crystalline nanoparticles under mild reaction conditions, is among the most flexible synthesis methods [63]. The sol-gel technique has many benefits, such as the pure quality of products and the potential of incorporating thermolabile molecules, among the most significant ones. In reality, inorganic-organic hybrid materials [64] can be obtained in which the organic and inorganic phases are linked to sub-micrometer levels at the nanometer [65].

Fascinating biomaterials for a range of clinical and biomedical applications have been suggested in the past few years for ceramics, drug delivery systems, and glasses provided by integrating polymers or drugs into the inorganic matrix [64, 66], or nanocomposites generated from hybrid materials, all designed by this model. For example, they have been used as knee and hip implants or cardiac valves [55, 67].

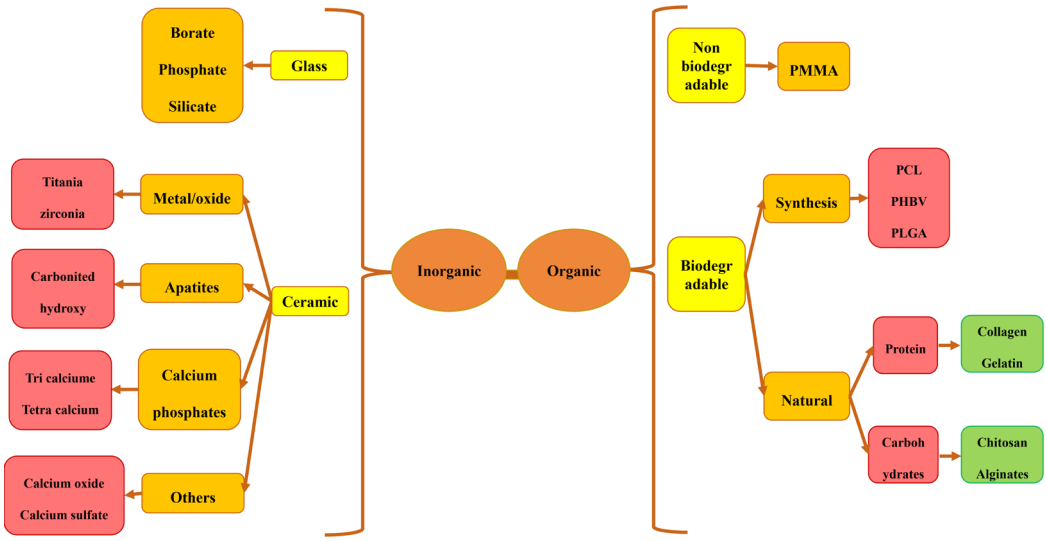

Fig. 2. Possible organic-inorganic combinations for drug delivery.

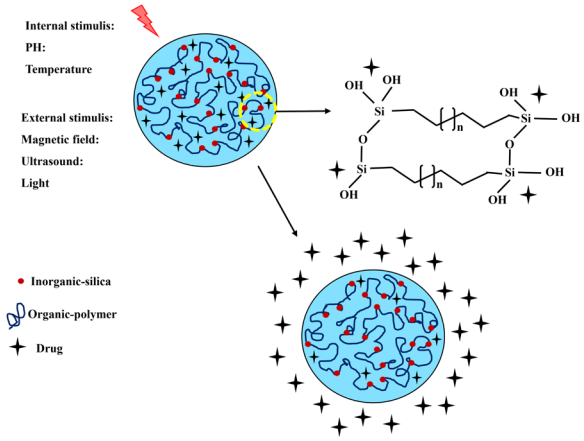

Fig. 3. Mechanism of organic-inorganic systems of drug delivery.

4. Synthesis of drug carriers by the sol-gel method

4.1. Organic-inorganic composite drug carriers

Recently, various prospective composites have been prepared, developed, and investigated for biomedical applications such as biosensors, artificial blood vessels, stem cell therapy, cancer therapy, immunotherapy, antimicrobial properties, enzyme immobilization, wound dressings, cardiac prosthesis, tissue engineering, drug delivery, and etc.[68-71]. The choice of an inorganic-organic composite would be more logical than that of a single type carrier material. Composites are supposed to provide required mechanical strength, boosted tissue integration, and prolonged and effective drug release, consisting of several phases combined to provide better performance. Fig. 2 demonstrates several potential formulations for bone drug delivery in the creation of inorganic-organic composites.

Organic-inorganic hybrid composites produced through the sol-gel method are of great interest. Firstly, a uniform sol that converts into a gel is provided. After that, the controlled drying process happen to produce a monolith or powder. The sol-gel composition is stablished on polycondensation and metal alkoxides $M(OR)_x$ hydrolysis, where M = Si, Zr, Ti, Al. and R = any alkyl group. Hydrolysis that causes OR group replacement connected to M by M-OH groups, is the initial reaction. As before, these chemical species can interact together to build M-O-M bonds, leading to metal network establishment. This stage creates a three-dimensional network with the solvent used in these processes residing inside the structure's pores. Organic-inorganic composites were produced by Catauro et al. [72] through the sol-gel technique. The drug was applied throughout the sol-gel procedure, with TiO_2 and poly (ε-caprolactone) (PCL) glass acting as inorganic and organic phases. A similar technique was developed to produce composite films of silica and Poly(methyl methacrylate) (PMMA) by Lin et al. [73] and zirconia and PCL by Catauro et al. [74]. However, the sol-gel interactions are influenced by several factors, including composition and concentration of the solvents, reactants, catalysts, process temperature, solvent elimination speed, and drug release pace by inorganic material and binding operative material. The procedure is sluggish and requires hazardous chemicals to be used [73]. Fig. 3 illustrates the general mechanism of organic-inorganic systems of drug delivery.

Sakai's [75] process obtained organic-inorganic core-shell beads. The aminopropyl silane's positively charged ammonium electrostatically bound to the alginate, after that the outer silanols attached the hydrolyzed TMOS to create the three-dimensional inorganic shell covering the calcium alginate center. The membrane shell permeability is being regulated by changing the molar ratio among TMOS and aminopropyl silane or increasing the shell thickness.

Silicates are known to avoid macrophage attraction, and following immersions in calcium-rich, and sodium alginate solutions the beads, would cover by the outer calcium alginate coating. Many inorganic-organic hybrid nanocomposites, consisting of indomethacin (IND), have been produced as a modeling drug by M. Catauro et al. [76] by utilizing inorganic (TEOS) and organic (polyethylene glycol, PEG) precursors through sol-gel technology. Indomethacin interaction with the inorganic material and its concentration appear to play a part in release kinetic models. In particular, it was found that the discs with the smallest dosage of indomethacin had a sigmoid-shaped release graph; the discs with the largest dosage of indomethacin (15 and10% wt) had a time-dependent exponential drug release rate throughout the saline solution.

The incorporation of the polymer regulates the release of the drug in a different way. To achieve therapeutic techniques for utilization in iron deficiency anemia treatment, M. Catauro et al. [77] integrated various

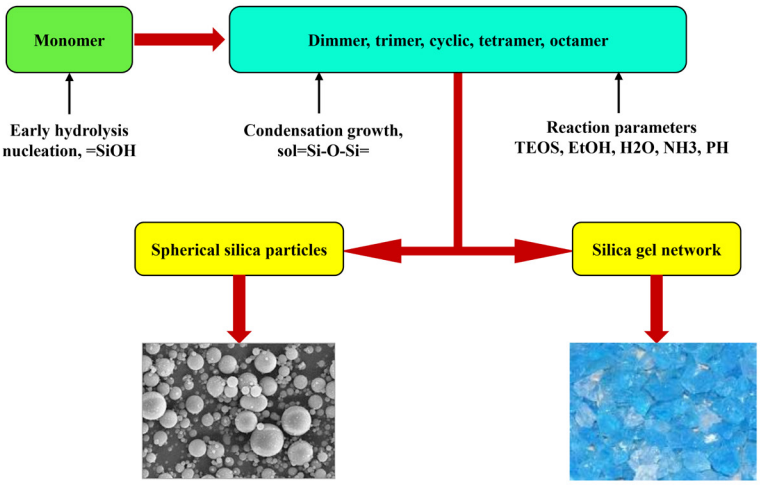

Fig. 4. Schematic of silica formation by the sol-gel process.

quantities of pure Fe(II)C in n a silica matrix by a sol-gel method. The bioactivity analysis indicates that the existence of Fe(II)C does not influence the silica matrix's bioactivity. Hence, the obtained results promote the release kinetic assessment of Fe(II)C from SiO_2/Fe(II)C hybrids to determine their possible application as drug delivery tools.

Cataura et al. [78] developed organic-inorganic hybrids based on chlorogenic acid/PEG using the sol-gel process in other experiments. The findings suggest that this biomaterial could be employed in multiple biomedical uses, including drug delivery, because of its flexibility and biocompatibility. Bollino et al. [79] produced organic hybrid (OIH) compounds for the regulated release of anti-inflammatory factors via the sol-gel system. The materials explored are SiO_2- PCL OIH wherein ketoprofen (SiO_2/PCL/KET) or indomethacin (SiO_2/PCL/IND) is introduced. The findings demonstrate that the drug release relies on the amount of PCL and the drug molecule framework. Sol-gel polystyrene/silica nanocomposites (PS/Si NCs) were produced by Mezan et al. [80]. The experimental result shows the potential for using PS/SiO_2 as coating, catalyst, and biomaterials such as drug carriers.

4.2. Silica composite drug carriers

Across multiple fields, including surface science and synthesis, the design of ceramic nanoparticles with enhanced characteristics has been investigated with remarkable progress. Silica, silicon carbide, titania, zirconia, alumina, silicon nitride are different ceramics types. Developments in nanotechnology have resulted in the advance of nanosized SiO_2a, which has been extensively utilized as a filler in composite engineering. Metal impurities are found in silica particles derived from natural sources and are not useful for advanced science and industrial purposes.

Synthetic silica (pyrogenic silica, precipitated silica, colloidal silica, and silica gels), which is refined and often manufactured in amorphous powder shapes, is therefore predominant in comparison with natural mineral SiO_2 (tridymite, quartz, cristobalite) in the crystalline build. Reversed microemulsion, flame synthesis, and the sol-gel system are commonly employed techniques to generate silica nanoparticles. Due to its capability to regulate morphology, size distribution, and particle size by comprehensive control of process parameters, the sol-gel system is extensively employed to manufacture pure silica particles [81].

Modern medicine focuses on local therapy [82] and it is believed that employing silica composites in local drug distribution has some benefits including: (1) the capacity to integrate significant quantities of broadly scattered or dissolved drugs at low temperatures during solidification procedures, (2) the assurance of efficient stabilization of the drug load towards deterioration due to moderately well host-guest interactions, (3) the regulated kinetics of drug release by adjusting the porous silica structure characteristics. Medicinal drugs such as molsidomine [83], bisphosphonate [84], itraconazole [85], ibuprofen, doxorubicin (DOX) [86], and vancomycin [87] have also been integrated into silica compounds, providing many potentials for both regulated deliveries of medicines and effective local therapy [88].

Because of its capability to create pure and uniform materials under moderate conditions, the sol-gel system is commonly used to manufacture glass, ceramic, and silica materials for decades. The mechanism involves hydrolysis as well as metal alkoxides ($Si(OR)_4$) condensation including tetraethylorthosilicate (TEOS, $Si(OC_2H_5)_4$) or inorganic salts including sodium silicate (Na_2SiO_3) using as a catalyst in the presence of mineral base (e.g., NH_3) or acid (e.g., HCl) [89, 90]. In the sol-gel system, the fundamental interactions of TEOS that result in the forming of SiO_2 particles can be formulated as [39, 91]:

$$Si(OC_2H_5)_4 + H_2O \xrightarrow{\text{hydrolysis}} Si(OC_2H_5)_3OH + C_2H_5OH$$

$$\equiv Si-O-H + H-O-Si\equiv \xrightarrow{\text{water condensation}} \equiv Si-O-Si\equiv + H_2O \quad (1)$$

$$\equiv Si-OC_2H_5 + H-O-Si\equiv \xrightarrow{\text{alcohol condensation}} \equiv Si-O-Si\equiv + C_2H_5OH$$

Hydrolysis of the molecules of TEOS produces silanol groups. Siloxane bridges (Si-O-Si) forming the whole silica construct are formed by polymerization/condensation among the groups of silanol or the groups of silanol and ethoxy [81, 92]. It is possible to separate silica particle creation into two steps: (i) nucleation, (ii) growth. The two models, including monomer addition [93] and controlled aggregation [94], have been suggested to explain the silica growth process. The model of monomer addition shows that the particle growth happens after an initial nucleation burst by adding hydrolyzed monomers to the (primary) particles exterior. On the other hand, the model of aggregation describes that nucleation happens continuously during the process and that the resultant nuclei (primary particles) are aggregated together for the formation of dimmer, trimmer, and bigger particles (secondary particles). Based on the reaction parameters, illustrated in Fig. 4, both models contribute to creating either a gel network or spherical product [81].

The impact of hydroxy-terminated polydimethylsiloxane (PDMS)

with (10, 20, 30, and 40 percent (w/w)) upon the physicochemical features of composites manufactured by low-temperature sol-gel polydimethylsiloxane/calcium phosphate/silica (PDMS-modified CaP/SiO_2) was described by Prokopowicz et al. [88]. The release study indicates that 20 percent PDMS in the composite was adequate to reduce the water-soluble molecule's burst release and resulted in zero-order drug release. This study suggests that the coefficient of drug partition and coefficient of permeability and its release did not alter with time.

An innovative warfarin-silica composite was designed by Parfenyuk et al. [95] for managed drug release using the sol-gel processing method. The kinetic parameters and release mechanisms for both drugs are identical in general. Nevertheless, unlike sol-gel molsidomine-SiO_2 composites that displayed drug release kinetics near zero-order kinetics just in a strongly acidic medium, warfarin sol-gel composite with phenyl-modified SiO_2 releases warfarin at roughly equal rates in the medium mimicking various sections of the gastrointestinal system according to zero-order kinetic law. The suggested warfarin-silica composite is a prospect for the continued processing of innovative oral warfarin SiO_2-based framework with regulated drug release. Stergar [96] presented a novel promising mechanism of drug delivery, that is, composites of Ni67.5Cu32.5 magnetic nanoparticles (MNPs) made by the sol-gel process. Using paracetamol (PCM), bupivacaine hydrochloride (BPC), and pentoxifylline (PTX) as model drugs, its ability to distribute drugs in a managed way was evaluated. NiCu particle release activity of PCM, BPC, and PTX verified that the base nanoparticles could release (and thus deliver) different drugs independent of their base characteristics.

Vlasenkova et al. [97] have developed a sol-gel/emulsion system to produce silica microcapsules to regulate release without losing their original form of the encapsulated protein. The processing parameters were observed to affect the unloaded silica particles' porous nature, the silica particle release qualities filled with bovine serum albumin (BSA), and encapsulated and released protein structural status significantly. Boffito et al. [98] suggested a different approach to this complex objective by mixing mesoporous SiO_2 nanoparticles coated with a pH acid-sensitive self-immolating polymer (MSN-CS-SIP) with custom-made amphiphilic poly (ether urethane)s (PEUs) based thermo-sensitive hydrogels. The hybrid injectable compositions developed in this way could constitute a significant step in producing drug carriers that are responsive to multi-stimuli. These formulations can efficiently activate the release of their content appropriate to medical requirements by changing their behavior following biochemical signals from the surrounding physio-pathological setting.

4.3. Calcium composite drug carriers

Because of being potential candidates for decades of drug encapsulation and their biodegradability and biocompatibility, calcium-based nanostructured and calcium composites are extensively used in biomedicine [99, 100]. Considering its broad uses for drug delivery and even tissue engineering, calcium carbonate, $CaCO_3$, is currently one of the most described nanomaterials. This substance's appealing characteristic is that it stays slightly soluble in a neutral or basic medium but dissolves quickly in an acid medium, like cytosol (pH = 5.5), allowing for selective release of uptake into the cells [101].

Kolanthai et al. [102] developed composite scaffolds of 3D porous calcium phosphate ((hydroxyapatite/β-tricalcium phosphate)/agarose, (HAp/β-TCP)/agarose) by sol-gel methodology with solvents of ethanol (EBS) and water (WBS). The growing bone could be supported by microporous scaffolds (WBS), while nanopores (EBS) could increase the degradation process. WBS and EBS could also be employed as scaffolds for drug delivery and tissue engineering. Palmqvist et al. [103] controlled nucleation and growth of produced nano by the sol-gel process to generate nanocomposites for drug delivery purposes by CO_2 sequestration by a calcium alkoxide solution. In neutral aqueous conditions, the composite particles are stable but are readily dissolved at pH = 7.40 in an acid media or also in phosphate-buffered saline (PBS), releasing the hydrophobic organic part in the form of a reasonably stable colloid solution. In both acidic and PBS media, successful ibuprofen release as a model drug was obtained and could be attenuated by including β-carotene as a hydrophobic portion.

In the endodontic materials design that facilitates regeneration of bone/cementum tissue and prevents bacterial growth, calcium silicate (CS)-based structures are useful. The mesoporous CS (MesoCS) nanocomposites were produced by Huang et al.[104] by employing sol-gel techniques. MesoCS nanoparticles could be used to retain the constant gentamicin release and fibroblast growth factor-2 as drug carriers (FGF-2). Due to the release of FGF-2, the MesoCS-loaded FGF-2 can stimulate other odontogenic-related proteins than CS. In a study by Ghadiri et al. [105] in both acidic and alkaline media types, mesoporous calcium-magnesium-silicate was produced using the cetyltrimethylammonium bromide (CTAB)-assisted sol-gel process. The findings suggest that the reversal phase, the releasing of drug molecules, relies heavily on the surface area. The drug molecules have more accessible space during the diffusion stage to connect with specimens with larger surface area, facilitating more host-guest contact during the diffusion phase, thereby decreasing the release kinetics.

CaP as bioactive carriers produced in different kinds, such as thin coatings, ceramics, composites, and cement, appear to be an appropriate and widely used option in prosthesis for bone regeneration, [106]. The recent biphasic composites of mesoporous silica and calcium phosphate material (CaP@MSi) in powder and pellet form were produced by Prokopowicz et al. [107] as a promising bone drug delivery method for doxycycline hydrochloride (DOX). The collected pellets retained CaP@MSi permeability capacity and supported the sustained release of DOX for five days. The produced biphasic CaP@MSi composites tend to have the usage capacity of a bone-specific drug carrier. Szewczyk et al. [108] generated a MSi-CaP composite in the shape of spherical granules (pellets) filled with cefazolin as a model antibiotic. In comparison to the burst release of cefazolin-loaded MSi-CaP powders, the burst release of cefazolin from the pellets was decreased by 3 (90 and 30 percent after 15 min of release test, respectively). After 60 days of the mineralization potential assessment in the modeled body fluid, the experiments showed that the pellets' entire surface was coated with carbonated hydroxyapatite in line with the preferred morphology.

Through the sol-gel technique, Tsai et al. [109] developed mesoporous hydroxyapatite-CaO composite nanofibers (p-HApFs) by utilizing Pluronic P123 as an electrospinning procedure and a porogen and discovered that p-HApFs had sufficient drug loading capacity and could prolong the burst of tetracycline release (TC). A similar discovery relating to the creation of CaO in the synthesis of HAp by the sol-gel was also published by Lopatin et al. [110]. Nevertheless, several experiments have shown that the biocompatibility of HAp is adversely affected by CaO [111].

Kanchana et al. [42] have shown that introducing strontium to biphasic calcium phosphate synthesis by the sol-gel process could reduce the forming CaO impurities. In this context, Tsai et al. [112] manufactured mesoporous composition strontium-substituted hydroxyapatite-CaO-CO_3 nanofibers (mSrHANFs) using an electrospinning system that relies on a sol-gel precursor with CTAB as porogen and assessed the impact of varying quantities of Sr doping on mSrHANF components. The mSrHANFs had a remarkable drug-loading capacity and could prolong TC burst release to sustain antibacterial function for over three weeks. Therefore, in bone tissue engineering, mSrHANFs could be used as drug carriers. The protein carrier was encapsulated by Purushothaman et al. [113], and casein was hybridized with superparamagnetic calcium ferrite nanoparticles (CFNP) (fabricated by the sol-gel technique) in

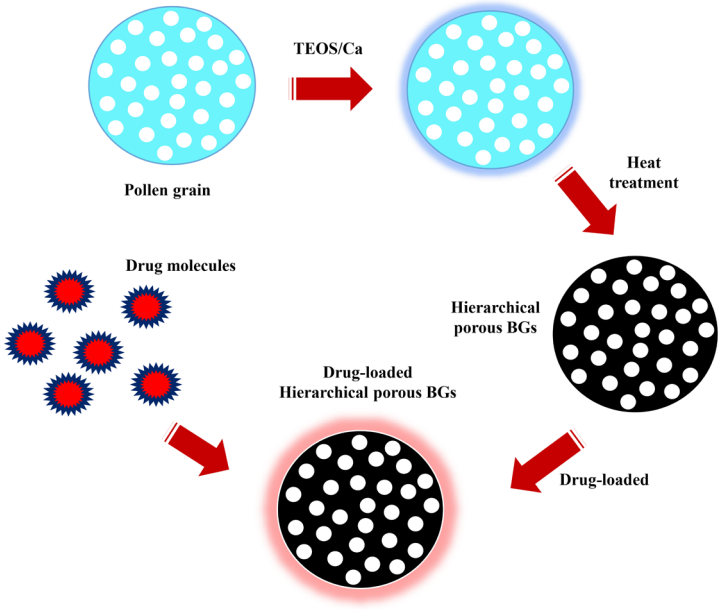

Fig. 5. Drug delivery systems based on porous BGs.

which the anti-cancer drug, curcumin (Cur), was included. Eventually, to make receptor-mediated endocytosis effective, folic acid (FA) was conjugated. In an acidic environment, elevated drug concentration, and magnetic field impact conditions, the drug release rate was higher. For casein-Cur with FA conjugation in contrast to the carrier lacking FA, the IC50 value decreased almost six-fold for MCF-7 cells. The casein-CFNP-Cur-FA was explicitly observed in the analysis as an innovative possible formulation for targeted drug delivery.

4.4. Bioactive glass drug carriers

Synthetic biomaterials of bioactive glasses (BGs) were first produced in the late 1960s [114] and they, by the apatite layer creation on their surface, are capable of binding to the bone. BGs are dissolvable under physiological conditions to various levels, being osteoinductive, osteoconductive, and angiogenic in specific compositions [115, 116]. These unique characteristics significantly enhance the BGs use in the regeneration/repair of bone [117].

Their potential has lately been illustrated in the field of soft tissue regeneration [118], with a focus on their biological activity to facilitate angiogenesis and to function as antibacterial agents. The biologically active ions release, stimulates specific healing mechanisms in soft tissue repair and wound healing [119], thus causes specific biological effects. BGs are amorphous in origin and have intermediate oxides, network modifiers, and network formers, in their framework [120]. Without external materials, the network designers could shape glasses independently [121].

B_2O_3, SiO_2, P_2O_5 are the most studied network formers in BGs; network modifiers affect the glass structure by binding to non-bridging oxygen atoms such as Si-O-M+ in which M+ is a modifier cation; intermediate oxides could either perform as network modifiers or join the glass structure such as network formers [22]. SiO_2, P_2O_5, and B_2O_3 could typically serve as network formers for generating BGs [122]. Nevertheless, regarding BGs generated by the sol-gel system, many of them are silicate glasses, and extensive research has focused on them since their emergence in the early 1990s [123]. By properly regulating the condensation and hydrolysis of borate precursors, borate BGs have lately been produced. The biological and physicochemical characteristics of BGs could be regulated by adjusting the composition [124]. Bioactive glass nanoparticles (BGN) are appealing biomaterials among the different morphologies of BGs for a significant variety of biomedical uses owing to their tiny scale, large surface-to-volume ratio, and high specific surface area that grant unique qualities to them [125].

Because of these desirable morphological features, in some uses, like drug delivery, BGN has significant benefits over its micron-sized counterparts. In general, BGNs are a good foundation for composites, as their morphological properties make their uniform integration into polymer matrices much simple [126, 127]. In addition, the use of structure-forming agents allows complicated morphologies including hollow or mesoporous structures to be accomplished by BGN. In effect, this improved porosity and surface area enhance BGN capacity to serve as drug carriers and other biomolecules for regulated release [128]. TEOS is the most commonly employed silicate precursor for the sol-gel production of BGN, whereas ethanol and/or water are used as solvents [129]. Under acidic or basic environments, the sol-gel process could occur, and those conditions influence the properties of the resulting materials. For instance, BGs with various morphologies could be accomplished by merely adjusting the solvent's pH. TEOS initially precedes condensation and hydrolysis in the catalysts presence to form nanoparticles of SiO_2 in a standard sol-gel procedure for BGN [130]. During the condensation and hydrolysis of TEOS or after the development of SiO_2 nanoparticles, metal ion precursors could be included. To create BGN, the generated nanoparticles are then dried and calcinated. Organic substances could also be included during the production to form the particles or increase dispersity [129]. Moreover, to promote the processing of BGN [130], other methods, such as microemulsion [131], could be coupled with the sol-gel system. Drug delivery systems based on porous BGs are schematically presented in Fig. 5.

Wang et al. [132] effectively produced terbium-containing mesoporous bioactive glass nanospheres (Tb/MBG) by the sol-gel process. Findings have demonstrated that the developed nanospheres of Tb/MBG show excellent biocompatibility, rapid degradation, and regulated delivery of DOX. The release of DOX from nanospheres of Tb/MBG could be effectively adjusted by doping ion concentrations and modifying the pH condition. Hassanzadeh-Tabrizi et al. [133] have established an easy and efficient technique for preparing forsterite nanopowder via a surfactant-assisted sol-gel process as a novel drug delivery mechanism. During loading and releasing processes, ibuprofen molecules could be adsorbed onto mesoporous composites' surface in the impregnation phase and get released through diffusion-controlled mechanisms. The solvent reaches the ibuprofen-matrix phase via the pores during the release step. It could be shown that drug delivery is quicker in the early testing period reach-

ing a slower pattern after around ten hours.

These findings are in line with the report by Horcajada et al. [134]. They studied the impact of MCM-41 pore size on drug delivery rate and demonstrated that the rate of ibuprofen delivery in a mimicking solution of body fluid declines as the pore size reduces. A composite formulated from hydroxyapatite forms MBG granules and bone cement, a promising carrier for biologically active proteins was investigated by Schumacher et al. [135]. Sol-gel technique was used, and mesoporous bioactive $CaO\text{-}SiO_2$ glass was produced. The feasibility of MBG particles to regulate the enzyme Lyz release and the growth factor VEGF from CaP cement (CPC) has been proven. Composites of CPC/MBG appear to be a useful material for the growth factors delivery into bone fractures with a slightly improved porosity and mechanical strength that enhances over time. They could demonstrate that MBG improves and regulate the proteins release from the cement matrix.

Hollow mesoporous bioglass (HMBG) nanoparticles were produced by Wang et al. [136]. The HMBG nanoparticles had more significant potential for drug retention and stable drug release than the unique mesoporous architecture of HMBG. Furthermore, *in vivo* tests revealed that the nanoparticles of HMBG could facilitate regeneration of bone and the drug-loading nanoparticles of HMBG had a more remarkable ability to repair. Sayed et al. [137] examined hematite-doped chitosan/bioglass substrates as an alternate implant method to restore damaged root canals by delivering 2% chlorhexidine gluconate (CHX). As indicated by *in vitro* drug release and antibacterial experiments, the utilization of hematite (Fe_2O_3) increased drug release and entirely removed bacterial growth within 14 days. A list of the composites produced by the sol-gel method is provided in Table 1.

5. In vitro and in vivo drug release studies

It is possible to test the bioactivity of a composite and its specific components *in vitro*. Experiments are conducted by immersing specimens in SBF with a human plasma-like composition and ion concentration at 37 °C [146]. The *in vitro* approach for bioactivity analysis receives further appreciation due to concern for animal use in experiments. *In vitro* biodegradation of drug-releasing composites is investigated by detecting a decline in sample weight and molecular weight of the decaying polymer following immersion in a medium at 37 °C over varying periods with liquids as a sterile solution of pH 7.4 PBS [147] or simulated body fluid (SBF) [148] implementing as a condition of deterioration. While both liquids are not entirely appropriate for replicating the condition *in vivo*, SBF is a better option versus PBS. SBF simulates pH and ionic concentrations more precisely to plasma and supports the research sample with bioactivity. Therefore, when a composite is exposed to biodegradation tests, bioactivity will also be exhibited in SBF, and degradation will be affected, simulating better *in vivo* conditions. A composite's *in vivo* examination is not only limited to the release of drugs but also extended to its bioactivity [149, 150].

In vivo animal experiments are performed after radical debriding of localized osteomyelitis and estimating drug concentrations by collecting the drug from bone specimens. Commonly, in and near the places where the composites were in contact, the drug content was high, and the concentration reduced as the distance increased. Thus, there may be a strong need for organized administration of medications to protect the nearby bones and tissues under therapeutic circumstances of use, at least in the beginning for a limited duration. However, composites seem sufficiently appropriate and in their active state during the study period to release the drugs. It is not, however, a situation peculiar to composites. Drug delivery systems, either polymeric or inorganic, have identical conditions [151].

The mouse Langerhans islets encapsulation in sol-gel silicates was reported by Pope et al. [152] in 1997. *In vitro* experiments have shown that insulin could be produced and secreted by sol-gel encapsulated cells. In some diabetic mice, silica gel encapsulated islets have been transplanted inter-peritoneally and have been shown to lower their urinary sugar level significantly. These initial findings were promising since they proved that the sol-gel encapsulation offers a solution to overcome immune system rejection. Carturan et al. [153] resurrected this area of research systematically, beginning with conventional sol-gel procedures and later improving the Biosil gas phase deposition technique. They showed that by changing the silicate deposit's thickness or modifying its porosity, they could retain Langerhans cell viability in the silicates and regulate the barrier of mass transport.

Lately, the group has focused more on prosperous biohybrid transplantation in 10 glycemic rats. The results showed that 60% of the rats were alive after two months, but more significantly, their blood glucose level reduced from about 400 mg/l 100 mg/l after transplantation. This trend remained for over a month at this level [154]. The authors reported that the encapsulation did not deteriorate the function of the islets. Moreover, Sakai et al. [155] showed that the inner alginate polymer could be liquefied by introducing citrate to chelate and remove the calcium binder. In another study by Sakai et al. [156], it was shown that the *in vitro* proliferation of pancreatic islets inside the siliceous pancreas was enabled by liquefication. The bioartificial pancreas capability to decrease and regulate the diabetic mice's blood glucose level from more than 400 mg/l to a healthy level of 200 mg/l for weeks was shown by *in vivo* experiments with diabetic mice.

Hu et al. [157] announced manufacturing of graphene oxide (GO)-integrated highly sensitive amphiphilic copolymer-based nanocomposite that displayed a low-intensity UV light-triggered sol-gel transformation. GO material could make the nucleation and unpleasant symptoms more apparent. An *in vitro* analysis examined the continuous drug release output of the hydrogel samples. The findings revealed that our drug carrier's release characteristics, namely the increased release rate within the acidic microenvironment of tumor conditions, are highly promising in improving patients with malignant tumors, cancer, and other diseases.

Dolinina et al. [134] have developed composites of molsidomine-silica. The SiO_2 composites with the cardiovascular drug molsidomine were produced through sol-gel and adsorption in their research. In the *in vitro* study, the cumulative release rate of the drug was evaluated using the following expressions:

V is the complete release medium volume, C_t is the drug concentration at time t, C_{t-1} is the concentration of the drug at the time (t-1), n is the removed release medium volume, w is the drug content in the composite. As an instrumental error and sum of precision error, the relative variability in full release (percent) was not more than 4 percent. The findings achieved in this study show that the production process of composites of adsorption, molsidomine-silica, or sol-gel technology has a significant impact on the composites' release qualities. The composites have a variable drug distribution over the SiO_2 matrixes and diverse durability of the composite structure in neutral media and acid due to different concepts of their creation.

Using sol-gel processing, Kolanthai et al. [158] developed nanosized (80×23 nm^2) and porous (17 ± 1 nm) HAp/agarose composite rods. The composite exhibited an initial burst release of around 60 percent within ten hours regarding *in vitro* drug release. The regulated release of drugs was subsequently reported. A strong interaction of the HAp mesoporous surface with the drug was associated with sustained release. Finally, for reconstructive surgery uses, bone filling, and drug delivery, the composite powder could be used. A smart pH-responsive nano-carrier (P.4-VP@MCM-41) by utilizing P.4-VP as reversible pH-sensitive gatekeepers and MCM-41 as drug nano-containers has been effectively developed by Abbaszad Rafi et al. [159]. The polymerizable functional groups (3-(Trimethoxysilyl)propylmethacrylate) were mostly grafted

Table 1.
Composites Studied for Drug Delivery via sol-gel method

Carrier	Cytotoxicity behavior of carrier	Drug	Experimental medium	Drug release behavior	Reference
Bioactive glass ceramics	-	Gentamicin	PBS	The drug release outcome exhibited that both 45S5 and S53P4 showed a gradually continuous gentamicin release.	Auniq et al. [134]
Calcium ferrite nanoparticles (CFNP)	Cytotoxicity test performed MCF-7 breast cancer cells, and results showed The IC50 value reduced nearly six-fold for MCF-7 cells	Curcumin	Acidic conditions and under the influence of magnetic field	The drug release rate was higher in acidic conditions, increased drug concentrations, and under the influence of the magnetic field.	Purushothaman et al. [109]
Magnetite (Fe_3O_4)-doped nanoparticles of mesoporous bioactive glass (Fe_3O_4-MBG NPs)	No considerable normal human fibroblast (NHFB) cell death was detected during in vitro analysis. For nanoparticles of Mc-Fe_3O_4-MBG significant inhibitory influences on the cancer cells (MG-63) viability were observed.	Mitomycin	SBF	Nanoparticles of Fe_3O_4-MBG expressed low cytotoxicity, good biocompatibility, and controlled release thus, for drug delivery, they are a safe biomaterial.	Rahman et al. [135]
Ag_2O-MBG NPs	At 11.88 µg/mL of nanoparticles of DOX-Ag_2O-MBG, significant inhibitory influence on the viability of the MG-63 osteosarcoma cancer cells was detected.	DOX	SBF	Doxorubicin (DOX) was encapsulated with 84% efficiency. The release of DOX was affected by release media pH (6.4–8.4) and the drug loading concentration (0.2–1.0 mg/mL). DOX release was 93% was witnessed almost for two weeks at a little acidic 6.4 pH.	Rahman et al. [136]
SiO_2/PCL OIHs (organic-inorganic)	The compatibility with the organic solvent, the starting liquid state, and the slow processing temperatures make the sol-gel an ideal method to synthesize OIHs.	Anti-inflammatory IND or KET	SBF	The IND speed release reduces with increasing PCL the wt%, whereas the speed release of KET increases with PCL increasing of wt%.	Bollino et al. [75]
Terbium doped mesoporous bioactive glasses (Tb/MBG)	The Tb/MBG cytotoxicity assessed by a cell counting kit-8 (CCK-8), and results revealed that the carrier at low concentration had no notable cytotoxicity in MC3T3 cells.	DOX	SBF	Nanospheres of Tb/MBG exhibited controlled release property of anti-cancer drugs (DOX) and distinct degradation in PBS with various pH values. Their mechanism of release can be described by Fickian diffusion according to the model of Higuchi.	Wang et al. [128]
Polymethyl methyl acrylate/polystyrene/silica composite	The cytotoxicity studies by RAW macrophage cells exhibited that all the samples showed good cell viability.	5-Fluorouracil	PBS	The kinetics of drug release showed that the drug was released in a sustained manner for a period of 180 h in PBS at a pH of 6.8.	Shanmugasundar et al. [137]
Silica-calcium phosphate composite (MSi-CaP)	-	Cefazolin	SBF	The burst release of cefazolin from the pellets was reduced by 3 when compared to the burst release of cefazolin-loaded MSi-CaP powders (90 and 30% after 15 min of release studies, respectively).	Szewczyk et al. [104]
HMBG	Nanoparticles had good biocompatibility and they could promote MG-63 cell proliferation considerably.	Ibuprofen	SBF	MBG nanoparticles had sustained drug release ability and higher drug loading due to their special hollow structure and penetrative mesopores on the shell.	Wang et al. [138]
$Ca_3Mg(SiO_4)_2$)	The cytocompatibility, mechanical properties, and bioactivity of the compound have been comprehensively assessed.	Ibuprofen	SBF	The synthesized calcium-magnesium-silicate samples' potential application as a drug delivery agent is investigated by estimating the ibuprofen release properties of them up to 180 h.	Bigham et al. [139]
MBG/polyurethanes (PUs) nanocomposite	The nanocomposites showed high cell viability (96–100%) and are thus designated as biocompatible.	Imatinib	SBF	There was no burst influence and 52–84% of the drug was released during 3 weeks	Shoaib et al. [140]
Samarium incorporated mesoporous bioactive glasses (Sm/MBG)	-	DOX	SBF	The results exhibited that the Sm/MBG/alginate microspheres show sustained DOX delivery, and their mechanism of release is controlled by Fickian diffusion according to the model of Higuchi.	Zhang et al. [141]

onto MCM-41 pore entrants to provide the silica-based nano-container following MSNs synthesis through the surfactant-assisted sol-gel system, with no surfactant removal. The release of the drug could be limited at pH 7.4 in the bloodstream based on the current *in vitro* results; nevertheless, due to the cancerous cell acidic microenvironment, an accelerated release would be found in cancerous tissues. Accordingly, this nano-carrier could have a possible use for anti-cancer drugs in pH-sensitive delivery systems.

A new technique was applied by Ghazaiea [160] to monitor various drug releases by encapsulating them using sol-gel in organic-inorganic hybrids. By utilizing UV-visible spectrophotometry (UV-Vis), the drug release of the composites of N-triethylchitosan/sodium naproxen@SiO_2 was examined. At a physiological temperature of 37 °C and a pH of 7.4, this research was carried out. This sort of sol-gel process could develop composites of different sizes and porous shells. Dynamic light scattering (DLS) and zeta potential analysis results indicate that particles of various sizes and shapes are possible. Kumaresan's [161] synthetic saponite has been effectively produced using the sol-gel hydrothermal process and Quinine (QU) as a guest molecule. During controlled release experiments, they also compared the natural (NSAP) and synthetic (SSAP) saponite clay with QU nanocomposite and pure QU. Normal QU and drug-loaded QNSAP and QSSAP nanocomposite *in vitro* drug release experiments have been successfully performed by employing dialysis bag procedure using the pH gradient process in the physiological setting. The study proved that the SSAP presented better-controlled release patterns than NSAP and pure QU. The current result also shows that the natural/synthetic saponite clay minerals are more efficient materials to be employed as simplistic and effective drug release vehicles.

An innovative biodegradable thermosensitive composite hydrogel based on PEG-PCL-PEG (PECE) and Pluronic F127 copolymer undergoing thermosensitive sol-gel transformation was produced by Gong et al. [162]. The composite hydrogel cytotoxicity was tested through utilizing human HEK293 cells through a cell viability method. The viability of 293 cells in the presence of composite hydrogel copolymers, even though the input copolymers was 500 μg per well, was still greater than 71.4 percent. The sample drugs used were BSA, vitamin B12 (VB12), honokiol (HK) to study the *in vitro* release activity of protein drugs, hydrophilic small molecular drugs, hydrophobic small molecular drugs, and the composite hydrogel. The higher Pluronic F127 quantity, lower concentration of hydrogel, or less initial drug loading led to a higher cumulative rate of release.

Kundu et al. [163] produced a novel localized drug delivery method focused on drug-loaded porous hydroxyapatite ceftriaxone-sulbactam composite. It was found that the lower percentage of pores with a range of mostly micro-pores was better than the higher percentage of pores both *in vitro* and *in vivo*. CFS (combination of b-lactam antibiotic and b-lactamase inhibitor) release from HAp prosthetics was quicker than SBF in PBS. Besides, both *in vivo* and *in vitro* drug elution findings after six weeks revealed that the CFS release against Staphylococcus aureus was more significant than the minimum inhibitory dosage. The advantages of CFS loaded HAp implants over the parenteral group are on pathogen elimination and new bone development, which was also shown *in-vivo* experiments.

Safari et al.[164] synthesized dopamine (DOP)/chitosan (CIS)@TiO_2 nanohybrid composites by the sol-gel process. In comparison to the DOP/CIS composites, TiO_2 integration significantly increased drug trapping and decreased drug release. After 10 min in a pH 7.4 solution, the DOP/CIS composites lacking TiO_2 coating released the entire drug, whereas the TiO_2 coated composites released the trapped drug after 16 h. The effects are quite promising and could be used to adjust DOP usage from injection to oral. Rahman et al. [81] doped nanoparticles of silver oxide mesoporous bioactive glass (Ag_2O-MBG NPs) for the regulated doxorubicin release as a model drug by the sol-gel process. Through MTT assay and *in vivo* tissue histopathology, the as-synthesized nanoparticles of Ag_2O-MBG did not present any adverse impact, and drug release was regulated by adjusting the pH of the released medium, and dosage of drug loading. These properties have shown that the Ag_2O-MBG NPs method is beneficial for the bone cancer medication of bone tissue regeneration.

6. Conclusions and future insight

Lately, given the simplicity and usefulness of sol-gel approaches in regulating the structure and characteristics of BGN, sol-gel production of BGN has been gradually studied. Because of their qualities, BGN can be great transporters of drugs. Even though impressive improvement has been accomplished in the manufacturing of BGN, many other challenges remain, particularly regarding the accurate control of composition and size that must be addressed to achieve efficient BGN usage. By changing production parameters, including catalyst concentration and TEOS, the BGN size may be easily adjusted, but smaller particles are prone to aggregate to shape larger clusters, particularly in the salts presence. This restriction complicates the development of highly scattered BGN smaller than 100 nm. The critical challenge found by a variety of research is that the inclusion of metallic salts usually causes nanoparticles to be aggregated. On the other hand, in drug delivery, organic-inorganic composites and porous inorganic materials, including calcium carbonates, mesoporous silica, calcium phosphates, and other silica and calcium-based structures, have been commonly used as carriers. Such carriers can also be produced using the sol-gel process. These technologies have several qualities, such as high bioactive drug loading, *in vivo* navigating and visualization, and remote content release by internal and external stimuli.

The morphological and surface qualities of silica and calcium configurations enable organic functionalization to be carried out to innovative and effective hybrid carriers with improved multimodal characteristics being created. In addition, there are several options for co-encapsulating of different bioactive compounds in situ (fluorescent molecule, drug, protein, and gene). These products, however, can also have some limitations related to their stability and safety. While these materials are known to be non-toxic, it is always necessary to monitor and control the concentration of particles utilized to prevent harmful impacts. Further considerations relating to particle stability should be addressed when dealing with biological fluids (blood plasma, cell culture media). For example, in biological fluids, organic compounds appear to bind to drug carriers' surface, creating so-called coronas across the particles. This corona could modify the physicochemical characteristics of particles dramatically, leading to the aggregation of particles. They should therefore be characterized not only in aqueous solutions, but also in biological fluids. More studies on the design of these comparatively high capacity carriers seem to be essential to minimize the shortcomings of each as much as possible.

REFERENCES

[1] G. Gregoriadis, Targeting of drugs, Nature 265(5593) (1977) 407-411.
[2] A. Zaffaroni, Therapeutic systems: the key to rational drug therapy, Drug metabolism reviews 8(2) (1978) 191-221.
[3] M. Hashida, Role of pharmacokinetic consideration for the development of drug delivery systems: A historical overview, Advanced drug delivery reviews (2020).
[4] H. Bundgaard, M. Johansen, Pro-drugs as drug delivery systems XX. Oxazolidines as potential pro-drug types for β-aminoalcohols, aldehydes or ketones, International Journal of Pharmaceutics 10(2) (1982) 165-175.
[5] B.B. Patel, N.A. Patel, Brain targeting drug delivery system through nasal cavity, Pharma News (2021).
[6] L. Li, Y. He, X. Zheng, L. Yi, W. Nian, Progress on Preparation of pH/Temperature-Sensitive Intelligent Hydrogels and Applications in Target Transport and Con-

trolled Release of Drugs, International Journal of Polymer Science 2021 (2021).
[7] J. Zhuang, L. Zhou, W. Tang, T. Ma, H. Li, X. Wang, C. Chen, P. Wang, Tumor targeting antibody-conjugated nanocarrier with pH/thermo dual-responsive macromolecular film layer for enhanced cancer chemotherapy, Materials Science and Engineering: C 118 (2021) 111361.
[8] N.T.T. Le, D.T.D. Nguyen, N.H. Nguyen, C.K. Nguyen, D.H. Nguyen, Methoxy polyethylene glycol–cholesterol modified soy lecithin liposomes for poorly water-soluble anticancer drug delivery, Journal of Applied Polymer Science 138(7) (2021) 49858.
[9] M. Abniki, A. Moghimi, F. Azizinejad, Fabrication of bionanocomposite based on LDH using biopolymer of gum arabic and chitosan-coating for sustained drug-release, Journal of the Serbian Chemical Society 85(9) (2020) 1223-1235.
[10] J. Daraei, Production and characterization of PCL (Polycaprolactone) coated TCP/nanoBG composite scaffolds by sponge foam method for orthopedic applications, Journal of Composites and Compounds 2(2) (2020) 44-49.
[11] E. Asadi, A.F. Chimeh, S. Hosseini, S. Rahimi, B. Sarkhosh, L. Bazli, R. Bashiri, A.H.V. Tahmorsati, A review of clinical applications of graphene quantum dot-based composites, Journal of Composites and Compounds 1(1) (2019) 31-40.
[12] H.W. Jang, A. Zareidoost, M. Moradi, A. Abuchenari, A. Bakhtiari, R. Pouriamanesh, B. Malekpouri, A.J. Rad, D. Rahban, Photosensitive nanocomposites: environmental and biological applications, Journal of Composites and Compounds 2(2) (2020) 50-60.
[13] Y. Zamania, A. Zareeinb, L. Bazlic, R. NasrAzadanid, B.P. Mahammode, S. Nasibi, A.M. Chahardehig, Journal of Composites and Compounds, (2020).
[14] Y. Zamani, A. Zareein, L. Bazli, R. Nasr Azadani, B.P. Mahammod, S. Nasibi, A.M. Chahardehi, Nanodiamond-containing composites for tissue scaffolds and surgical implants: A review, Journal of Composites and Compounds 2(5) (2020) 215-227.
[15] A. Czajkowska-Kośnik, M. Szekalska, K. Winnicka, Nanostructured lipid carriers: A potential use for skin drug delivery systems, Pharmacological Reports 71(1) (2019) 156-166.
[16] F. Niazvand, A. Cheshmi, M. Zand, R. NasrAzadani, B. Kumari, A. Raza, S. Nasibi, An overview of the development of composites containing Mg and Zn for drug delivery, Journal of Composites and Compounds 2(5) (2020) 193-204.
[17] M. Abniki, A. Moghimi, F. Azizinejad, Synthesis of calcium-layered double hydroxide based nanohybrid for controlled release of an anti-inflammatory drug, Journal of the Chinese Chemical Society (2020).
[18] C. Tipa, M.T. Cidade, T. Vieira, J.C. Silva, P.I. Soares, J.P. Borges, A New Long-Term Composite Drug Delivery System Based on Thermo-Responsive Hydrogel and Nanoclay, Nanomaterials 11(1) (2021) 25.
[19] A. Moghanian, A. Ghorbanoghli, M. Kazem-Rostami, A. Pazhouheshgar, E. Salari, M. Saghafi Yazdi, T. Alimardani, H. Jahani, F. Sharifian Jazi, M. Tahriri, Novel antibacterial Cu/Mg-substituted 58S-bioglass: Synthesis, characterization and investigation of in vitro bioactivity, International Journal of Applied Glass Science 11(4) (2020) 685-698.
[20] M.S.N. Shahrbabak, F. Sharifianjazi, D. Rahban, A. Salimi, A comparative investigation on bioactivity and antibacterial properties of sol-gel derived 58S bioactive glass substituted by Ag and Zn, Silicon 11(6) (2019) 2741-2751.
[21] A. Esmaeilkhanian, F. Sharifianjazi, A. Abouchenari, A. Rouhani, N. Parvin, M. Irani, Synthesis and characterization of natural nano-hydroxyapatite derived from turkey femur-bone waste, Applied biochemistry and biotechnology 189(3) (2019) 919-932.
[22] L. Bazli, B. Eftekhari Yekta, A. Khavandi, Preparation and Characterization of Sn-Containing Glasses for Brachytherapy Applications, Transactions of the Indian Ceramic Society 76(4) (2017) 242-246.
[23] Q. Lei, J. Guo, A. Noureddine, A. Wang, S. Wuttke, C.J. Brinker, W. Zhu, Sol–Gel-Based Advanced Porous Silica Materials for Biomedical Applications, Advanced Functional Materials 30(41) (2020) 1909539.
[24] K. Unger, H. Rupprecht, B. Valentin, W. Kircher, The use of porous and surface modified silicas as drug delivery and stabilizing agents, Drug Development and Industrial Pharmacy 9(1-2) (1983) 69-91.
[25] P.P. Nampi, V.S. Mohan, A.K. Sinha, H. Varma, High surface area sol–gel nano silica as a novel drug carrier substrate for sustained drug release, Materials Research Bulletin 47(6) (2012) 1379-1384.
[26] A. Rajaeiyan, M. Bagheri-Mohagheghi, Comparison of sol-gel and co-precipitation methods on the structural properties and phase transformation of γ and α-Al 2 O 3 nanoparticles, Advances in Manufacturing 1(2) (2013) 176-182.
[27] V.S. Rizi, F. Sharifianjazi, H. Jafarikhorami, N. Parvin, L.S. Fard, M. Irani, A. Esmaeilkhanian, Sol–gel derived SnO_2/Ag_2O ceramic nanocomposite for H_2 gas sensing applications, Materials Research Express 6(11) (2019) 1150g2.
[28] F. Sharifianjazi, M. Moradi, A. Abouchenari, A.H. Pakseresht, A. Esmaeilkhanian, M. Shokouhimehr, M.S. Asl, Effects of Sr and Mg dopants on biological and mechanical properties of SiO_2–CaO–P_2O_5 bioactive glass, Ceramics International 46(14) (2020) 22674-22682.
[29] F. Sharifianjazi, M. Moradi, N. Parvin, A. Nemati, A.J. Rad, N. Sheysi, A. Abouchenari, A. Mohammadi, S. Karbasi, Z. Ahmadi, Magnetic $CoFe_2O_4$ nanoparticles doped with metal ions: a review, Ceramics International (2020).
[30] L. Bazli, M. Siavashi, A. Shiravi, A review of carbon nanotube/TiO_2 composite prepared via sol-gel method, Journal of Composites and Compounds 1(1) (2019).
[31] M.A. Zadeh, S. Van Der Zwaag, S. Garcia, Routes to extrinsic and intrinsic self-healing corrosion protective sol-gel coatings: a review, Self-Healing Materials 1 (2013) 1-18.
[32] M. Catauro, E. Tranquillo, R. Risoluti, S. Vecchio Ciprioti, Sol-Gel synthesis, spectroscopic and thermal behavior study of SiO_2/PEG composites containing different amount of chlorogenic acid, Polymers 10(6) (2018) 682.
[33] T. Graham, XXXV.—On the properties of silicic acid and other analogous colloidal substances, Journal of the Chemical Society 17 (1864) 318-327.
[34] J.D. Wright, N.A. Sommerdijk, Sol-gel materials: chemistry and applications, CRC press2000.
[35] Ebelmen, Recherches sur les combinaisons des acides borique et silicique avec les éthers, 1846.
[36] W.A. Patrick, Silica gel and process of making same, Google Patents, 1919.
[37] S.S. Kistler, Coherent expanded aerogels and jellies, Nature 127(3211) (1931) 741-741.
[38] G.J. Owens, R.K. Singh, F. Foroutan, M. Alqaysi, C.-M. Han, C. Mahapatra, H.-W. Kim, J.C. Knowles, Sol–gel based materials for biomedical applications, Progress in Materials Science 77 (2016) 1-79.
[39] L.L. Hench, J.K. West, The sol-gel process, Chemical Reviews 90(1) (1990) 33-72.
[40] D. Wang, G.P. Bierwagen, Sol–gel coatings on metals for corrosion protection, Progress in organic coatings 64(4) (2009) 327-338.
[41] A.R. Rouhani, A.H. Esmaeil-Khanian, F. Davar, S. Hasani, The effect of agarose content on the morphology, phase evolution, and magnetic properties of $CoFe_2O_4$ nanoparticles prepared by sol-gel autocombustion method, International Journal of Applied Ceramic Technology 15(3) (2018) 758-765.
[42] B. Riegel, S. Blittersdorf, W. Kiefer, S. Hofacker, M. Müller, G. Schottner, Kinetic investigations of hydrolysis and condensation of the glycidoxypropyltrimethoxysilane/aminopropyltriethoxy-silane system by means of FT-Raman spectroscopy I, Journal of non-crystalline solids 226(1-2) (1998) 76-84.
[43] C. Brinker, K. Keefer, D. Schaefer, C. Ashley, Sol-gel transition in simple silicates, Journal of Non-Crystalline Solids 48(1) (1982) 47-64.
[44] N. Job, R. Pirard, J. Marien, J.-P. Pirard, Porous carbon xerogels with texture tailored by pH control during sol–gel process, Carbon 42(3) (2004) 619-628.
[45] S. Askari, M. Ghashang, G. Sohrabi, Synthesis and mechanical properties of Bi_2O_3-$Al_4Bi_2O_9$ nanopowders, Journal of Composites and Compounds 2(5) (2020).
[46] G.W. Scherer, C.J. Brinker, E.P. Roth, Sol→ gel→ glass: III. Viscous sintering, Journal of non-crystalline solids 72(2-3) (1985) 369-389.
[47] L. Ding, X. Zhu, Y. Wang, B. Shi, X. Ling, H. Chen, W. Nan, A. Barrett, Z. Guo, W. Tao, J. Wu, X. Shi, Intracellular Fate of Nanoparticles with Polydopamine Surface Engineering and a Novel Strategy for Exocytosis-Inhibiting, Lysosome Impairment-Based Cancer Therapy, Nano Letters 17(11) (2017) 6790-6801.
[48] X. Zhu, X. Ji, N. Kong, Y. Chen, M. Mahmoudi, X. Xu, L. Ding, W. Tao, T. Cai, Y. Li, T. Gan, A. Barrett, Z. Bharwani, H. Chen, O.C. Farokhzad, Intracellular Mechanistic Understanding of 2D MoS_2 Nanosheets for Anti-Exocytosis-Enhanced Synergistic Cancer Therapy, ACS Nano 12(3) (2018) 2922-2938.
[49] Y.V. Solovev, A.Y. Prilepskii, E.F. Krivoshapkina, A.F. Fakhardo, E.A. Bryushkova, P.A. Kalikina, E.I. Koshel, V.V. Vinogradov, Sol-gel derived boehmite nanostructures is a versatile nanoplatform for biomedical applications, Scientific Reports 9(1) (2019) 1176.
[50] B. Ben-Nissan, A.H. Choi, Sol-gel production of bioactive nanocoatings for medical applications. Part 1: an introduction, Nanomedicine 1(3) (2006) 311-319.
[51] Q. Lei, J. Guo, A. Noureddine, A. Wang, S. Wuttke, C.J. Brinker, W. Zhu, Sol–Gel-Based Advanced Porous Silica Materials for Biomedical Applications, Advanced Functional Materials 30(41) (2020) 1909539.
[52] F. Sharifianjazi, A. Esmaeilkhanian, M. Moradi, A. Pakseresht, M.S. Asl, H. Karimi-Maleh, H.W. Jang, M. Shokouhimehr, R.S. Varma, Biocompatibility and mechanical properties of pigeon bone waste extracted natural nano-hydroxyapatite for bone tissue engineering, Materials Science and Engineering: B 264 (2021) 114950.
[53] M. Radmansouri, E. Bahmani, E. Sarikhani, K. Rahmani, F. Sharifianjazi, M. Irani, Doxorubicin hydrochloride - Loaded electrospun chitosan/cobalt ferrite/titanium oxide nanofibers for hyperthermic tumor cell treatment and controlled drug release, International Journal of Biological Macromolecules 116 (2018) 378-384.

[54] Y.-T. Xie, J.-R. Chen, Y.-T. Chen, B.-C. Jiang, Z.-H. Sie, H.-Y. Hsu, T.-L. Chen, Y.-Y. Chiang, H.-Y. Hsueh, Sol–gel-derived hierarchically wrinkled mesoporous ceramics for enhancement of cell alignment, Chemical Engineering Journal 405 (2021) 126572.
[55] L. Bazli, H. Nargesi khoramabadi, A. Modarresi Chahardehi, H. Arsad, B. Malekpouri, M. Asgari Jazi, N. Azizabadi, Factors influencing the failure of dental implants: a systematic review, Journal of Composites and Compounds 2(2) (2020).
[56] C. Gong, D. Chen, X. Jiao, Q. Wang, Continuous hollow α-Fe_2O_3 and α-Fe fibers prepared by the sol–gel method, Journal of Materials Chemistry 12(6) (2002) 1844-1847.
[57] H.-W. Kim, H.-E. Kim, J.C. Knowles, Fluor-hydroxyapatite sol–gel coating on titanium substrate for hard tissue implants, Biomaterials 25(17) (2004) 3351-3358.
[58] F. Baino, E. Fiume, M. Miola, E. Verné, Bioactive sol-gel glasses: Processing, properties, and applications, International Journal of Applied Ceramic Technology 15(4) (2018) 841-860.
[59] Z. Goudarzi, N. Parvin, F. Sharifianjazi, Formation of hydroxyapatite on surface of SiO_2– P_2O_5–CaO–SrO–ZnO bioactive glass synthesized through sol-gel route, Ceramics International 45(15) (2019) 19323-19330.
[60] Z. Amini, S.S. Rudsary, S.S. Shahraeini, B.F. Dizaji, P. Goleij, A. Bakhtiari, M. Irani, F. Sharifianjazi, Magnetic bioactive glasses/Cisplatin loaded-chitosan (CS)-grafted- poly (ε-caprolactone) nanofibers against bone cancer treatment, Carbohydrate Polymers 258 (2021) 117680.
[61] Z. Goudarzi, A. Ijadi, A. Bakhtiari, S. Eskandarinezhad, N. Azizabadi, M.A. Jazi, Sr-doped bioactive glasses for biological applications, Journal of Composites and Compounds 2(3) (2020) 105-109.
[62] R. Gupta, A. Kumar, Bioactive materials for biomedical applications using sol–gel technology, Biomedical Materials 3(3) (2008) 034005.
[63] T. Dippong, E.A. Levei, O. Cadar, A. Mesaros, G. Borodi, Sol-gel synthesis of $CoFe_2O_4$:SiO_2 nanocomposites – insights into the thermal decomposition process of precursors, Journal of Analytical and Applied Pyrolysis 125 (2017) 169-177.
[64] L. Zhao, Y. Wu, S. Chen, T. Xing, Preparation and characterization of cross-linked carboxymethyl chitin porous membrane scaffold for biomedical applications, Carbohydrate Polymers 126 (2015) 150-155.
[65] M. Catauro, F. Bollino, F. Papale, S. Marciano, S. Pacifico, TiO_2/PCL hybrid materials synthesized via sol–gel technique for biomedical applications, Materials Science and Engineering: C 47 (2015) 135-141.
[66] H. Ghazanfari, S. Hasanizadeh, S. Eskandarinezhad, S. Hassani, M. Sheibani, A. Dordsheikh Torkamani, B. Fakić, Recent progress in materials used towards corrosion protection of Mg and its alloys, Journal of Composites and Compounds 2(5) (2020).
[67] M. Catauro, S. Vecchio Ciprioti, Sol-Gel Synthesis and Characterization of Hybrid Materials for Biomedical Applications, in: C. Demetzos, N. Pippa (Eds.), Thermodynamics and Biophysics of Biomedical Nanosystems: Applications and Practical Considerations, Springer Singapore, Singapore, 2019, pp. 445-475.
[68] M.E. Astaneh, A. Goodarzi, M. Khanmohammadi, A. Shokati, S. Mohandesnezhad, M.R. Ataollahi, S. Najafipour, M.S. Farahani, J. Ai, Chitosan/gelatin hydrogel and endometrial stem cells with subsequent atorvastatin injection impact in regenerating spinal cord tissue, Journal of Drug Delivery Science and Technology 58 (2020) 101831.
[69] M.S. Hasnain, A.K. Nayak, Alginate-inorganic composite particles as sustained drug delivery matrices, Applications of Nanocomposite Materials in Drug Delivery, Elsevier2018, pp. 39-74.
[70] H. Ullah, F. Wahid, H.A. Santos, T. Khan, Advances in biomedical and pharmaceutical applications of functional bacterial cellulose-based nanocomposites, Carbohydrate polymers 150 (2016) 330-352.
[71] S. Ebrahimi-Barough, J. Ai, M. Payab, S. Alavi-Moghadam, A. Shokati, H.R. Aghayan, B. Larijani, B. Arjmand, Standard Operating Procedure for the Good Manufacturing Practice-Compliant Production of Human Endometrial Stem Cells for Multiple Sclerosis, (2020).
[72] M. Catauro, M.G. Raucci, D. de Marco, L. Ambrosio, Release kinetics of ampicillin, characterization and bioactivity of TiO_2/PCL hybrid materials synthesized by sol–gel processing, Journal of Biomedical Materials Research Part A 77A(2) (2006) 340-350.
[73] M. Lin, H. Wang, S. Meng, W. Zhong, Z. Li, R. Cai, Z. Chen, X. Zhou, Q. Du, Structure and Release Behavior of PMMA/Silica Composite Drug Delivery System, Journal of Pharmaceutical Sciences 96(6) (2007) 1518-1526.
[74] M. Catauro, M. Raucci, G. Ausanio, Sol–gel processing of drug delivery zirconia/polycaprolactone hybrid materials, Journal of Materials Science: Materials in Medicine 19(2) (2008) 531-540.
[75] S. Sakai, T. Ono, H. Ijima, K. Kawakami, Proliferation and Insulin Secretion Function of Mouse Insulinoma Cells Encapsulated in Alginate/Sol-Gel Synthesized Aminopropyl-Silicate/Alginate Microcapsule, Journal of Sol-Gel Science and Technology 28(2) (2003) 267-272.
[76] M. Catauro, F. Bollino, F. Papale, M. Gallicchio, S. Pacifico, Synthesis and chemical characterization of new silica polyethylene glycol hybrid nanocomposite materials for controlled drug delivery, Journal of Drug Delivery Science and Technology 24(4) (2014) 320-325.
[77] M. Catauro, D. Naviglio, R. Risoluti, S. Vecchio Ciprioti, Sol–gel synthesis and thermal behavior of bioactive ferrous citrate–silica hybrid materials, Journal of Thermal Analysis and Calorimetry 133(2) (2018) 1085-1092.
[78] M. Catauro, F. Barrino, G.D. Poggetto, F. Pacifico, S. Piccolella, S. Pacifico, Chlorogenic acid/PEG-based organic-inorganic hybrids: A versatile sol-gel synthesis route for new bioactive materials, Materials Science and Engineering: C 100 (2019) 837-844.
[79] F. Bollino, M. Catauro, Organic Inorganic Hybrid Materials Synthesized via Sol–Gel for Controlled Drug Delivery, Macromolecular Symposia 389(1) (2020) 1900059.
[80] S.O. Mezan, A.H. Jabbar, M.Q. Hamzah, A.N. Tuama, N.N. Hasan, M.S. Roslan, M.A. Agam, Synthesis, characterization, and properties of polystyrene/SiO_2 nanocomposite via sol-gel process, AIP Conference Proceedings 2151(1) (2019) 020034.
[81] I.A. Rahman, V. Padavettan, Synthesis of Silica Nanoparticles by Sol-Gel: Size-Dependent Properties, Surface Modification, and Applications in Silica-Polymer Nanocomposites—A Review, Journal of Nanomaterials 2012 (2012) 132424.
[82] K. Krukiewicz, J.K. Zak, Biomaterial-based regional chemotherapy: Local anticancer drug delivery to enhance chemotherapy and minimize its side-effects, Materials Science and Engineering: C 62 (2016) 927-942.
[83] E.V. Parfenyuk, E.S. Dolinina, Design of silica carrier for controlled release of molsidomine: Effect of preparation methods of silica matrixes and their composites with molsidomine on the drug release kinetics in vitro, European Journal of Pharmaceutics and Biopharmaceutics 88(3) (2014) 1038-1045.
[84] M. Iafisco, N. Margiotta, Silica xerogels and hydroxyapatite nanocrystals for the local delivery of platinum–bisphosphonate complexes in the treatment of bone tumors: A mini-review, Journal of Inorganic Biochemistry 117 (2012) 237-247.
[85] R. Mellaerts, J.A.G. Jammaer, M. Van Speybroeck, H. Chen, J.V. Humbeeck, P. Augustijns, G. Van den Mooter, J.A. Martens, Physical State of Poorly Water Soluble Therapeutic Molecules Loaded into SBA-15 Ordered Mesoporous Silica Carriers: A Case Study with Itraconazole and Ibuprofen, Langmuir 24(16) (2008) 8651-8659.
[86] M. Prokopowicz, Formulation, characterisation and in vitro studies of doxorubicin-loaded silica–polydimethylsiloxane granules, European Journal of Pharmaceutical Sciences 66 (2015) 10-19.
[87] H. Qu, S. Bhattacharyya, P. Ducheyne, Silicon oxide based materials for controlled release in orthopedic procedures, Advanced Drug Delivery Reviews 94 (2015) 96-115.
[88] M. Prokopowicz, A. Szewczyk, R. Łunio, W. Sawicki, Monolithic polydimethylsiloxane-modified silica composites prepared by a low-temperature sol–gel micromolding technique for controlled drug release, Reactive and Functional Polymers 114 (2017) 136-145.
[89] K.J. Klabunde, J. Stark, O. Koper, C. Mohs, D.G. Park, S. Decker, Y. Jiang, I. Lagadic, D. Zhang, Nanocrystals as Stoichiometric Reagents with Unique Surface Chemistry, The Journal of Physical Chemistry 100(30) (1996) 12142-12153.
[90] W. Stöber, A. Fink, E. Bohn, Controlled growth of monodisperse silica spheres in the micron size range, Journal of Colloid and Interface Science 26(1) (1968) 62-69.
[91] T. Matsoukas, E. Gulari, Monomer-addition growth with a slow initiation step: A growth model for silica particles from alkoxides, Journal of Colloid and Interface Science 132(1) (1989) 13-21.
[92] H. Nargesi khoramabadi, M. Arefian, M. Hojjati, I. Tajzad, A. Mokhtarzade, M. Mazhar, A. Jamavari, A review of Polyvinyl alcohol / Carboxiy methyl cellulose (PVA/CMC) composites for various applications, Journal of Composites and Compounds 2(3) (2020).
[93] T. Matsoukas, E. Gulari, Dynamics of growth of silica particles from ammonia-catalyzed hydrolysis of tetra-ethyl-orthosilicate, Journal of Colloid and Interface Science 124(1) (1988) 252-261.
[94] G.H. Bogush, C.F. Zukoski, Studies of the kinetics of the precipitation of uniform silica particles through the hydrolysis and condensation of silicon alkoxides, Journal of Colloid and Interface Science 142(1) (1991) 1-18.
[95] E.V. Parfenyuk, E.S. Dolinina, Development of Novel Warfarin-Silica Composite for Controlled Drug Release, Pharmaceutical Research 34(4) (2017) 825-835.
[96] J. Stergar, U. Maver, M. Bele, L. Gradišnik, M. Kristl, I. Ban, NiCu-silica nanoparticles as a potential drug delivery system, Journal of Sol-Gel Science and

Technology (2020).
[97] M.I. Vlasenkova, E.S. Dolinina, E.V. Parfenyuk, Preparation of mesoporous silica microparticles by sol–gel/emulsion route for protein release, Pharmaceutical Development and Technology 24(2) (2019) 243-252.
[98] M. Boffito, A. Torchio, C. Tonda-Turo, R. Laurano, M. Gisbert-Garzarán, J.C. Berkmann, C. Cassino, M. Manzano, G.N. Duda, M. Vallet-Regí, K. Schmidt-Bleek, G. Ciardelli, Hybrid Injectable Sol-Gel Systems Based on Thermo-Sensitive Polyurethane Hydrogels Carrying pH-Sensitive Mesoporous Silica Nanoparticles for the Controlled and Triggered Release of Therapeutic Agents, Frontiers in Bioengineering and Biotechnology 8(384) (2020).
[99] Y. Zamani, A. Zareein, L. Bazli, R. NasrAzadani, B. Pasha Mahammod, S. Nasibi, A. Modarresi Chahardehi, Nanodiamond-containing composites for tissue scaffolds and surgical implants: A review, Journal of Composites and Compounds 2(5) (2020).
[100] S. Gao, M. Fan, Z. Li, K. Ge, X.-J. Liang, J. Zhang, Smart calcium peroxide with self-sufficience for biomedicine, Sci China Life Sci 63 (2020) 152-156.
[101] R. Sun, M. Åhlén, C.-W. Tai, É.G. Bajnóczi, F. de Kleijne, N. Ferraz, I. Persson, M. Strømme, O. Cheung, Highly porous amorphous calcium phosphate for drug delivery and bio-medical applications, Nanomaterials 10(1) (2020) 20.
[102] E. Kolanthai, V.S. Dikeshwar Colon, P.A. Sindu, V.S. Chandra, K.R. Karthikeyan, M.S. Babu, S.M. Sundaram, M. Palanichamy, S.N. Kalkura, Effect of solvent; enhancing the wettability and engineering the porous structure of a calcium phosphate/agarose composite for drug delivery, RSC Advances 5(24) (2015) 18301-18311.
[103] N.G.M. Palmqvist, J.-M. Nedelec, G.A. Seisenbaeva, V.G. Kessler, Controlling nucleation and growth of nano-$CaCO_3$ via CO_2 sequestration by a calcium alkoxide solution to produce nanocomposites for drug delivery applications, Acta Biomaterialia 57 (2017) 426-434.
[104] C.-Y. Huang, T.-H. Huang, C.-T. Kao, Y.-H. Wu, W.-C. Chen, M.-Y. Shie, Mesoporous Calcium Silicate Nanoparticles with Drug Delivery and Odontogenesis Properties, Journal of Endodontics 43(1) (2017) 69-76.
[105] S. Ghadiri, S.A. Hassanzadeh-Tabrizi, A. Bigham, The effect of synthesis medium on structure and drug delivery behavior of CTAB-assisted sol–gel derived nanoporous calcium–magnesium–silicate, Journal of Sol-Gel Science and Technology 83(1) (2017) 229-236.
[106] S. Nasibi, K. Alimohammadi, L. Bazli, S. Eskandarinezhad, A. Mohammadi, N. Sheysi, TZNT alloy for surgical implant applications: A systematic review, Journal of Composites and Compounds 2(3) (2020).
[107] M. Prokopowicz, A. Szewczyk, A. Skwira, R. Sądej, G. Walker, Biphasic composite of calcium phosphate-based mesoporous silica as a novel bone drug delivery system, Drug Delivery and Translational Research 10(2) (2020) 455-470.
[108] A. Szewczyk, A. Skwira, M. Prokopowicz, Drug-loaded mesoporous silica/calcium phosphate composites for bone regeneration, Engineering of Biomaterials 22 (2019).
[109] S.-W. Tsai, S.-S. Huang, W.-X. Yu, Y.-W. Hsu, F.-Y. Hsu, Fabrication and Characteristics of Porous Hydroxyapatite-CaO Composite Nanofibers for Biomedical Applications, Nanomaterials 8(8) (2018) 570.
[110] C.M. Lopatin, V. Pizziconi, T.L. Alford, T. Laursen, Hydroxyapatite powders and thin films prepared by a sol-gel technique, Thin Solid Films 326(1) (1998) 227-232.
[111] M.H. Fathi, A. Hanifi, V. Mortazavi, Preparation and bioactivity evaluation of bone-like hydroxyapatite nanopowder, Journal of Materials Processing Technology 202(1) (2008) 536-542.
[112] S.-W. Tsai, W.-X. Yu, P.-A. Hwang, S.-S. Huang, H.-M. Lin, Y.-W. Hsu, F.-Y. Hsu, Fabrication and Characterization of Strontium-Substituted Hydroxyapatite-CaO-$CaCO_3$ Nanofibers with a Mesoporous Structure as Drug Delivery Carriers, Pharmaceutics 10(4) (2018) 179.
[113] B. K. Purushothaman, M. Harsha S, P.U. Maheswari, K.M.M. Sheriffa Begum, Magnetic assisted curcumin drug delivery using folate receptor targeted hybrid casein-calcium ferrite nanocarrier, Journal of Drug Delivery Science and Technology 52 (2019) 509-520.
[114] P. Ducheyen, L.L. Hench, The processing and static mechanical properties of metal fibre reinforced bioglass, Journal of Materials Science 17(2) (1982) 595-606.
[115] H. Duan, C. Cao, X. Wang, J. Tao, C. Li, H. Xin, J. Yang, Y. Song, F. Ai, Magnesium-alloy rods reinforced bioglass bone cement composite scaffolds with cortical bone-matching mechanical properties and excellent osteoconductivity for load-bearing bone in vivo regeneration, Scientific Reports 10(1) (2020) 18193.
[116] A. Bakhtiari, A. Cheshmi, M. Naeimi, S.M. Fathabad, M. Aliasghari, A.M. Chahardehi, S. Hassani, V. Elhami, Synthesis and characterization of the novel 80S bioactive glass: bioactivity, biocompatibility, cytotoxicity, Journal of Composites and Compounds 2(4) (2020) 110-114.
[117] L. Zhou, L. Fan, F.-M. Zhang, Y. Jiang, M. Cai, C. Dai, Y.-A. Luo, L.-J. Tu, Z.-N. Zhou, X.-J. Li, C.-Y. Ning, K. Zheng, A.R. Boccaccini, G.-X. Tan, Hybrid gelatin/oxidized chondroitin sulfate hydrogels incorporating bioactive glass nanoparticles with enhanced mechanical properties, mineralization, and osteogenic differentiation, Bioactive Materials 6(3) (2021) 890-904.
[118] M. Miola, E. Verné, C. Vitale-Brovarone, F. Baino, Antibacterial Bioglass-Derived Scaffolds: Innovative Synthesis Approach and Characterization, International Journal of Applied Glass Science 7(2) (2016) 238-247.
[119] C. Wu, Z. Zhang, K. Zhou, W. Chen, J. Tao, C. Li, H. Xin, Y. Song, F. Ai, Preparation and characterization of borosilicate-bioglass-incorporated sodium alginate composite wound dressing for accelerated full-thickness skin wound healing, Biomedical Materials 15(5) (2020) 055009.
[120] D. Durgalakshmi, R. Ajay Rakkesh, B. Subramanian, Bioactive assessment of bioactive glass nanostructures synthesized using synthetic and natural silica resources, International Journal of Applied Ceramic Technology 17(4) (2020) 1976-1984.
[121] M.S. Araujo, A.C. Silva, J.F. Bartolomé, S. Mello-Castanho, Structural and thermal behavior of 45S5 Bioglass®-based compositions containing alumina and strontium, Journal of the American Ceramic Society 103(6) (2020) 3620-3630.
[122] A. Moghanian, A. Ghorbanoghli, M. Kazem-Rostami, A. Pazhouheshgar, E. Salari, M. Saghafi Yazdi, T. Alimardani, H. Jahani, F. Sharifian Jazi, M. Tahriri, Novel antibacterial Cu/Mg-substituted 58S-bioglass: Synthesis, characterization and investigation of in vitro bioactivity, International Journal of Applied Glass Science 11(4) (2020) 685-698.
[123] R. Li, A.E. Clark, L.L. Hench, An investigation of bioactive glass powders by sol-gel processing, Journal of Applied Biomaterials 2(4) (1991) 231-239.
[124] F. Sharifianjazi, M. Moradi, A. Abouchenari, A.H. Pakseresht, A. Esmaeilkhanian, M. Shokouhimehr, M. Shahedi Asl, Effects of Sr and Mg dopants on biological and mechanical properties of SiO_2–CaO–P_2O_5 bioactive glass, Ceramics International 46(14) (2020) 22674-22682.
[125] F. Sharifianjazi, N. Parvin, M. Tahriri, Synthesis and characteristics of sol-gel bioactive SiO_2-P_2O_5-CaO-Ag_2O glasses, Journal of Non-Crystalline Solids 476 (2017) 108-113.
[126] A.R. Boccaccini, M. Erol, W.J. Stark, D. Mohn, Z. Hong, J.F. Mano, Polymer/bioactive glass nanocomposites for biomedical applications: A review, Composites Science and Technology 70(13) (2010) 1764-1776.
[127] K. Zhang, Q. Van Le, Bioactive glass coated zirconia for dental implants: a review, Journal of Composites and Compounds 2(2) (2020).
[128] F. Sharifianjazi, N. Parvin, M. Tahriri, Formation of apatite nano-needles on novel gel derived SiO_2-P_2O_5-CaO-SrO-Ag_2O bioactive glasses, Ceramics International 43(17) (2017) 15214-15220.
[129] C. Vichery, J.-M. Nedelec, Bioactive Glass Nanoparticles: From Synthesis to Materials Design for Biomedical Applications, Materials 9(4) (2016) 288.
[130] K. Zheng, A.R. Boccaccini, Sol-gel processing of bioactive glass nanoparticles: A review, Advances in Colloid and Interface Science 249 (2017) 363-373.
[131] A. Lukowiak, J. Lao, J. Lacroix, J.-M. Nedelec, Bioactive glass nanoparticles obtained through sol–gel chemistry, Chemical Communications 49(59) (2013) 6620-6622.
[132] X. Wang, Y. Zhang, C. Lin, W. Zhong, Sol-gel derived terbium-containing mesoporous bioactive glasses nanospheres: In vitro hydroxyapatite formation and drug delivery, Colloids and Surfaces B: Biointerfaces 160 (2017) 406-415.
[133] S.A. Hassanzadeh-Tabrizi, A. Bigham, M. Rafienia, Surfactant-assisted sol–gel synthesis of forsterite nanoparticles as a novel drug delivery system, Materials Science and Engineering: C 58 (2016) 737-741.
[134] P. Horcajada, A. Rámila, J. Pérez-Pariente, R. Vallet, x, M., Influence of pore size of MCM-41 matrices on drug delivery rate, Microporous and Mesoporous Materials 68(1) (2004) 105-109.
[135] M. Schumacher, L. Reither, J. Thomas, M. Kampschulte, U. Gbureck, A. Lode, M. Gelinsky, Calcium phosphate bone cement/mesoporous bioactive glass composites for controlled growth factor delivery, Biomaterials Science 5(3) (2017) 578-588.
[136] Y. Wang, H. Pan, X. Chen, The Preparation of Hollow Mesoporous Bioglass Nanoparticles With Excellent Drug Delivery Capacity for Bone Tissue Regeneration, Frontiers in Chemistry 7(283) (2019).
[137] S.A.M. El-Sayed, M. Mabrouk, M.E. Khallaf, B.M. Abd El-Hady, E. El-Meliegy, M.R. Shehata, Antibacterial, drug delivery, and osteoinduction abilities of bioglass/chitosan scaffolds for dental applications, Journal of Drug Delivery Science and Technology 57 (2020) 101757.
[138] R.B.Z. Auniq, N. Hirun, U. Boonyang, Three-Dimensionally Ordered Macroporous-Mesoporous Bioactive Glass Ceramics for Drug Delivery Capacity and Evaluation of Drug Release, Ceramic Materials, IntechOpen2020.
[139] M.S.U. Rahman, M.A. Tahir, S. Noreen, M. Yasir, I. Ahmad, M.B. Khan, K.W. Ali, M. Shoaib, A. Bahadur, S. Iqbal, Magnetic mesoporous bioactive glass

for synergetic use in bone regeneration, hyperthermia treatment, and controlled drug delivery, RSC Advances 10(36) (2020) 21413-21419.
[140] M.S. ur Rahman, M.A. Tahir, S. Noreen, M. Yasir, M.B. Khan, T. Mahmood, A. Bahadur, M. Shoaib, Osteogenic silver oxide doped mesoporous bioactive glass for controlled release of doxorubicin against bone cancer cell line (MG-63): In vitro and in vivo cytotoxicity evaluation, Ceramics International 46(8, Part A) (2020) 10765-10770.
[141] S. Shanmugasundar, N. Kannan, E. Sundaravadivel, S. Zsolt, K. Mukunthan, J. Manokaran, J. Narendranath, V. Kamalakannan, P. Kavitha, V. Prabhu, Study on the inflammatory response of PMMA/polystyrene/silica nanocomposite membranes for drug delivery and dental applications, PloS one 14(3) (2019) e0209948.
[142] Y. Wang, H. Pan, X. Chen, The preparation of hollow mesoporous bioglass nanoparticles with excellent drug delivery capacity for bone tissue regeneration, Frontiers in chemistry 7 (2019) 283.
[143] A. Bigham, S. Hassanzadeh-Tabrizi, A. Khamsehashari, A. Chami, Surfactant-assisted sol–gel synthesis and characterization of hierarchical nanoporous merwinite with controllable drug release, Journal of Sol-Gel Science and Technology 87(3) (2018) 618-625.
[144] M. Shoaib, M.S. ur Rahman, A. Saeed, M.M. Naseer, Mesoporous bioactive glass-polyurethane nanocomposites as reservoirs for sustained drug delivery, Colloids and Surfaces B: Biointerfaces 172 (2018) 806-811.
[145] Y. Zhang, X. Wang, Y. Su, D. Chen, W. Zhong, A doxorubicin delivery system: Samarium/mesoporous bioactive glass/alginate composite microspheres, Materials Science and Engineering: C 67 (2016) 205-213.
[146] P. Abasian, M. Radmansouri, M. Habibi Jouybari, M.V. Ghasemi, A. Mohammadi, M. Irani, F.S. Jazi, Incorporation of magnetic NaX zeolite/DOX into the PLA/chitosan nanofibers for sustained release of doxorubicin against carcinoma cells death in vitro, International Journal of Biological Macromolecules 121 (2019) 398-406.
[147] C. Soundrapandian, B. Sa, S. Datta, Organic–Inorganic Composites for Bone Drug Delivery, AAPS PharmSciTech 10(4) (2009) 1158-1171.
[148] A. Ratier, I.R. Gibson, S.M. Best, M. Freche, J.L. Lacout, F. Rodriguez, Setting characteristics and mechanical behaviour of a calcium phosphate bone cement containing tetracycline, Biomaterials 22(9) (2001) 897-901.
[149] A. Bordbar-Khiabani, S. Ebrahimi, B. Yarmand, In-vitro corrosion and bioactivity behavior of tailored calcium phosphate-containing zinc oxide coating prepared by plasma electrolytic oxidation, Corrosion Science 173 (2020) 108781.
[150] E. Jablonská, D. Horkavcová, D. Rohanová, D.S. Brauer, A review of in vitro cell culture testing methods for bioactive glasses and other biomaterials for hard tissue regeneration, Journal of Materials Chemistry B 8(48) (2020) 10941-10953.
[151] T.J. Mäkinen, M. Veiranto, P. Lankinen, N. Moritz, J. Jalava, P. Törmälä, H.T. Aro, In vitro and in vivo release of ciprofloxacin from osteoconductive bone defect filler, Journal of Antimicrobial Chemotherapy 56(6) (2005) 1063-1068.
[152] E.J.A. Pope, K. Braun, C.M. Peterson, Bioartificial organs I: Silica gel encapsulated pancreatic islets for the treatment of diabetes mellitus, Journal of Sol-Gel Science and Technology 8(1) (1997) 635-639.
[153] G. Carturan, R. Campostrini, S. Dire, V. Scardi, E. De Alteriis, Inorganic gels for immobilization of biocatalysts: inclusion of invertase-active whole cells of yeast (Saccharomyces cerevisia) into thin layers of SiO_2 gel deposited on glass sheets, J. mol. catal 57(1) (1989) L13-L16.
[154] G. Carturan, R. Dal Toso, S. Boninsegna, R. Dal Monte, Encapsulation of functional cells by sol–gel silica: actual progress and perspectives for cell therapy, Journal of Materials Chemistry 14(14) (2004) 2087-2098.
[155] S. Sakai, T. Ono, H. Ijima, K. Kawakami, Modification of porous aminopropyl-silicate microcapsule membrane by electrically-bonded external anionic polymers, Journal of Biomaterials Science, Polymer Edition 14(7) (2003) 643-652.
[156] S. Sakai, T. Ono, H. Ijima, K. Kawakami, MIN6 cells-enclosing aminopropyl-silicate membrane templated by alginate gels differences in guluronic acid content, International Journal of Pharmaceutics 270(1) (2004) 65-73.
[157] H. Hu, X. Wang, K.I. Lee, K. Ma, H. Hu, J.H. Xin, Graphene oxide-enhanced sol-gel transition sensitivity and drug release performance of an amphiphilic copolymer-based nanocomposite, Scientific Reports 6(1) (2016) 31815.
[158] E. Kolanthai, K. Ganesan, M. Epple, S.N. Kalkura, Synthesis of nanosized hydroxyapatite/agarose powders for bone filler and drug delivery application, Materials Today Communications 8 (2016) 31-40.
[159] A. Abbaszad Rafi, M. Mahkam, S. Davaran, H. Hamishehkar, A Smart pH-responsive Nano-Carrier as a Drug Delivery System: A hybrid system comprised of mesoporous nanosilica MCM-41 (as a nano-container) & a pH-sensitive polymer (as smart reversible gatekeepers): Preparation, characterization and in vitro release studies of an anti-cancer drug, European Journal of Pharmaceutical Sciences 93 (2016) 64-73.
[160] M. Ghazaie, P. Ghiaci, M. Ghiaci, Study on release of naproxen and metformin encapsulated in biopolymer-inorganic mesoporous matrices as controlled drug-delivery systems, Microporous and Mesoporous Materials 244 (2017) 291-300.
[161] K. S, R. Rama Pawar, B. D Kevadiya, H. C Bajaj, Synthesis of Saponite Based Nanocomposites to Improve the Controlled Oral Drug Release of Model Drug Quinine Hydrochloride Dihydrate, Pharmaceuticals (Basel) 12(3) (2019) 105.
[162] C.Y. Gong, S. Shi, P.W. Dong, X.L. Zheng, S.Z. Fu, G. Guo, J.L. Yang, Y.Q. Wei, Z.Y. Qian, In vitro drug release behavior from a novel thermosensitive composite hydrogel based on Pluronic f127 and poly(ethylene glycol)-poly(ε-caprolactone)-poly(ethylene glycol) copolymer, BMC Biotechnology 9(1) (2009) 8.
[163] B. Kundu, C. Soundrapandian, S.K. Nandi, P. Mukherjee, N. Dandapat, S. Roy, B.K. Datta, T.K. Mandal, D. Basu, R.N. Bhattacharya, Development of New Localized Drug Delivery System Based on Ceftriaxone-Sulbactam Composite Drug Impregnated Porous Hydroxyapatite: A Systematic Approach for In Vitro and In Vivo Animal Trial, Pharmaceutical Research 27(8) (2010) 1659-1676.
[164] M. Safari, M. Ghiaci, M. Jafari-Asl, A.A. Ensafi, Nanohybrid organic–inorganic chitosan/dopamine/TiO_2 composites with controlled drug-delivery properties, Applied Surface Science 342 (2015) 26-33.

Available online at www.jourcc.com

Journal homepage: www.JOURCC.com

Journal of Composites and Compounds

A review of additive manufacturing of Mg-based alloys and composite implants

Yasamin Zamani [a], Hadi Ghazanfari [b], Gisou Erabi [c], Amirhossein Moghanian [d], Belma Fakić [e], Seyed Mohammad Hosseini [f], Babar Pasha Mahammod [g]*

[a] *Department of Biology, Tehran Medical Sciences Branch, Islamic Azad University, Tehran, Iran*
[b] *Department of Mining, Metallurgical and Materials Engineering, Université Laval, Québec G1V 0A6, QC, Canada*
[c] *Student Research Committee, School of Medicine, Urmia University of Medical Sciences, Urmia ,Iran*
[d] *Department of Materials Engineering, Imam Khomeini International University, Qazvin 34149-16818, Iran*
[e] *Metallographic laboratory, Institute "Kemal Kapetanović" in Zenica, University of Zenica, B and H*
[f] *School of Mechanical Engineering, College of Engineering, University of Tehran, Tehran, 11155-4563, Iran*
[g] *National Institute of Technology Warangal, Warangal, India*

ABSTRACT

Magnesium based materials are considered promising biodegradable metals for orthopedic bone implant applications as they exhibit similar density and elastic modulus to that of bone, biodegradability, and excellent osteogenic properties. The use of Mg based biomaterials eliminates the limitations of currently used implant materials such as stress shielding and the need for the second surgery. Recently, the development of Mg-based implants has attracted significant attention. Additive manufacturing is one of the effective techniques to develop Mg based implants. Additive manufacturing which could be named 3D printing is a transformative and rapid method of producing industrial parts with in the acceptable dimensional range. Therefore, recent investigations have tried to apply this method for the development of Mg-based implants. This state-of-the-art review focuses on the additive manufacturing of Mg biodegradable materials and their *in-vitro* corrosion and degradation, and mechanical properties. The future directions to develop Mg biodegradable materials are reported through summarization of current achievements.

Peer review under responsibility of jourcc

ARTICLE INFORMATION

Article history:
Received 24 January 2021
Received in revised form 11 February 2021
Accepted 25 March 2021

Keywords:
Additive manufacturing
Magnesium alloys
3D printing
Composite implants

Table of contents

1. Introduction 71
2. Application of biodegradable Mg alloys in orthopedic implants 72
3. Additive manufacturing of Mg-based alloys and composite implants 73
3.1. Selective laser melting 73
3.2. Electron beam melting 75
4. Characteristics of Mg alloy and composite implants produced by AM 76
4.1. Mechanical properties 76
4.2. Biodegradability behavior 77
4.3. Biocompatibility 77
5. Conclusions and future insights 79

1. Introduction

Since 1988, when the first system (SLA-1) founded on stereolithography (SL) processes was launched, additive manufacturing, rapid prototyping, or 3D printing has been introduced to the market. Since the patent for fused deposition modeling (FDM) was granted in 2009, additive manufacturing technologies started to develop significantly. This technique is already recognized by various names including fused filament fabrication (FFF), 3D printing, or the standard title of material extrusion (ME). The democratization of 3D printing resulted in significant advancements in AM machine software and hardware, as well as the introduction of a diverse variety of construction materials (feedstock used in AM) [1, 2].

The AM technology is applied in many medical applications including customized implants, tissue engineering scaffolds, and anatomical mockups for surgery simulation, planning, and training [3, 4], person-

* *Corresponding author: Yasamin Zamani; E-mail: yasaminzamani181@gmail.com*
https://doi.org/10.52547/jcc.3.1.7

alized surgical guides [5, 6]. As an example, the implants of the metal alloy have been prepared by selective electron beam melting (EBM) or laser melting (SLM), but for anatomical mockups, the processes of SL and PolyJet have been preferred. SLM and EBM according to ASTM F2792-12a, are categorized as technologies of powder bed fusion in which thermal energy fuse specifically powder bed regions [7]. Magnesium alloy due to its comparable mechanical properties, good biocompatibility, and natural degradability, has attracted much attention for application in the bone repair field. Once the Mg implants are placed at the fracture site, the degradation of these implants starts by the electrochemical corrosion mechanism. The released Mg ions contribute to new bone formation and excess magnesium ions will be excreted through the kidneys. In addition, Mg alloy has Young's modulus of approximately 45 GPa as well as density of about 1.79 g/cm^3 which are close to that of human cortical bone (15–30 GPa, 1.75 g/cm^3). However, the fast degradation of Mg leads to excess release of hydrogen gas and structural integrity loss is an important issue [8]. Hence, for a successful bone regeneration, Mg bone-implants should degrade slowly by maintaining good structural integrity and releasing less H_2.

The methodology of additive manufacturing demonstrates much potential in terms of preparing complicated bone implants quickly. Additive processing of Mg-based composites and alloys for the application of bone implants has been studied [9]. Using additive processing, a few researchers prepared Mg-based composites and alloys for bioapplication [10-12]. Due to its capacity for producing biodegradable implants and allowing development possibilities not possible with conventional manufacturing, AM of Mg alloys is gaining prominence in the industry. Magnesium composites have been developed as a potential biomaterial for applications in urology, respiratory medicine, cardiology, and orthopedics. Since the device degrades, the primary benefit of Magnesium is that long-term issues could be reduced or eliminated [13]. Researchers showed that additive produced specimens had stronger mechanical properties and consistency than hot extrude techniques and die cast and base material specimens. In addition, researchers discovered that the mechanical properties of 3D printed Magnesium specimens were superior to those of base materials. [14].

This article reviews the application of additive manufacturing in the preparation of Mg-based materials for bone implants. Besides, the properties of additively manufactured Mg-based materials such as composite's corrosion behavior, in-vito biodegradability, biocompatibility, and mechanical properties are reported and finally, the recent advancements in additive manufacturing are discussed as well.

2. Application of biodegradable Mg alloys in orthopedic implants

In biomedical research, biodegradable metals including Mg, Zn, and Fe have attracted significant attention. Many researchers have been carried to develop biodegradable materials using these metal alloys. Mg and its alloys are the lightest structural alloys, with appealing properties like good damping capacity, high strength to weight ratio, good castability and machinability, and a wide range of uses in industries including aerospace defense, automotive, and electronics [15]. In the physiological medium, however, pure Mg has very low corrosion resistance. Copper, zirconium, manganese, zinc, aluminum, and silicon are used to enhance the corrosion resistance and mechanical characteristics of pure Mg alloys. [16, 17].

Cast magnesium composites are the most popular magnesium alloys used currently in the automobile industry's powertrain and interior parts. Wrought magnesium alloys, on the other hand, are less commonly utilized due to their high cost and low formability [18]. In cast magnesium alloys, rare earth elements such as Gd, Ce, Y, and Nd are used as main alloying components These materials have a high magnesium solubility and are efficient in creep resistance and precipitation hardening [19]. The prevailing cast Mg alloys are Elektron 21, WE43, WE54, QH21, QE22, HZ32, HK31, ZC63, ZE41, ZK61, ZK51, AM50, AZ91, AZ81, and AZ63 while typical wrought Mg alloys are ZC71, ZE41, HM21, HK31, M1A, ZK60, Elektron 675, AZ80, AZ61, and AZ31. Z (Zinc), W (Yttrium), T (Tin), S (Silicon), R (Chromium), O (Silver), N (Nickel), M (Manganese), L (Lithium), K (Zirconium), H (Thorium), F (Iron), E (Rare earth metals), D (Cadmium), C (Copper), B (Bismuth), and A (Aluminum) are the prefix letters for two main alloying metals in Mg composites formed based on ASTM B275. [20].

In biomedicine applications, the generally practiced technique for controlling the Mg degradation rate is alloying. Magnesium can be effectively modified by alloying with an additional suitable amount of other elements to boost its mechanical properties and resistance [21]. Mg alloys are classified into two main categories: austenite and hypereutectate. Magnesium alloys are classified into two major categories. The first category contains between 2 and 10% wt% Al with a small amount of Zn and Mn, showing increased tolerance and mechanics. The second group is the combination of scarce earth elements and another metal including Ag, Zn, Y, and a lesser amount of Zr, leading to improved degradation resistance, finer grain structure, and mechanical performance [20]. Most researches showed that alloying is an appropriate method to control the Mg degradation rate but it does not influence its fundamental qualities. As an example, AZ31B, formed using mixing Al, Zn, and Mg and led to the improvement in the degradation resistance inside the rabbits' femora [22].

Hampp et al. [23] investigated the LANd442 alloy, which is composed of 2 wt percent Nd, 4 wt percent Al, 4 wt percent Li, and 90 wt% Mg. In the examined rabbit model, the results revealed an increase in corrosion resistance with the formation of new bone tissue. A small quantity of subcutaneous gas was also found in the area of the implant. Wu et al. [24] investigated the influences of alloying various amounts of Al and Li on the Mg–Li–Al–Zn quaternary alloy system. Their results revealed that alloying with Li considerably enhanced the ductility while Al improved the Li–Al–Zn alloys strength. The experiment of indirect *in vitro* cytotoxicity exhibited lower cytotoxicity for the alloys showing higher corrosion resistance. *In vivo* corrosion rates in the mouse subcutaneous model demonstrated different corrosion rates than the *in vitro* tests.

According to Li et al. [25], adding <2wt% Sr to Mg–Sr and Mg–Zr–Sr alloys significantly improved corrosion resistance. The addition of Sr improves the corrosion resistance of Mg–5Al alloys. Bone development may be aided by incorporating calcium into magnesium alloys, and the corrosive and mechanical characteristics of Mg–Ca alloys can be regulated by varying the amount of calcium. The dual Mg–Ca alloy of 1-20wt% Ca was tested by Li et al. [26], and the alloy of Mg–1Ca demonstrated no cell toxicity. The corrosion resistance of the Mg–1Ca alloy was increased due to the creation of an apatite layer on the surface. Comparably, Rad et al. [27] discovered that increasing the Ca content of Mg by 0.5 percent improved corrosion. The biodegradable magnesium alloys with different compositions were studied and revealed no favorable results. The appropriate choice of the content and the type of the alloying element can remarkably enhance the Mg without compromising its mechanical function and biocompatibility.

Magnesium and its composites have received a great deal of recognition for temporary implant applications such as screws, orthopedic bone plates, and coronary stents. Ghanbari et al. [28] investigated the wear behavior of biodegradable Mg–5Zn–1Y–(0–1)Ca alloys in simulated body fluid. Because of the improved corrosion resistance caused by the formation of intermetallic Ca2Mg6Zn3 particles, the friction coefficient and wear rate of the Mg–5Zn–1Y–1Ca alloy show more instability than the other alloys. In general, Ca-free alloy gives the best wear resis-

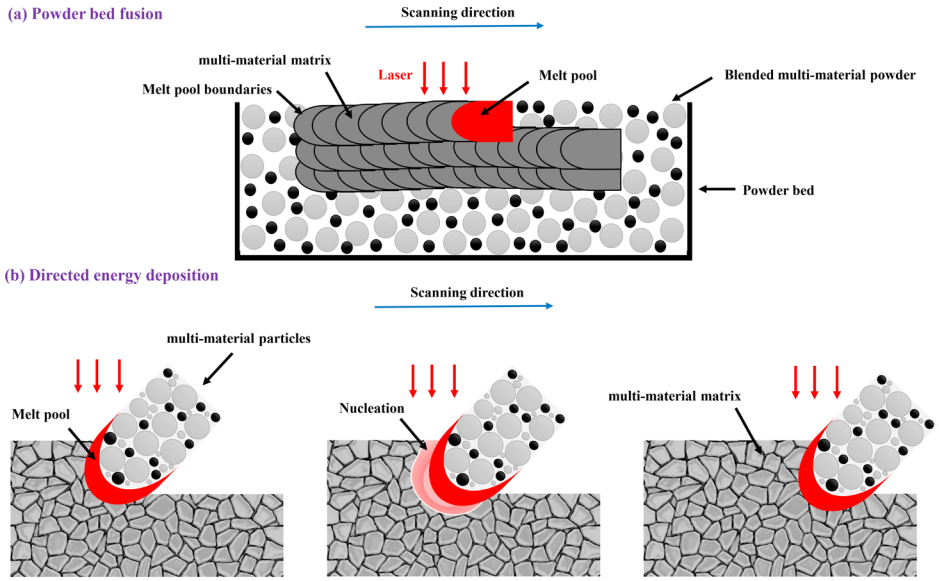

Fig. 1. DED and PBF additive manufacturing.

tance, particularly at the higher load of wear. Wang et al. [29] applied magnesium alloy (Mg–Zn–Y–Nd) stent in esophageal cancer therapy. In comparison to 317 L stainless steel, the Mg alloy inhibited the growth of esophageal cancer cells and had a milder hardness and good biodegradability. In addition, Liu et al. [30] studied the fatigue behavior of an extruded Mg–Zn–Y–Nd alloy for vascular stents in simulated body fluid (SBF) and air. Their findings indicated that the as-extruded alloy of Mg–Zn–Y–Nd in the air has a fatigue limit of 65 MPa after 10^7 cycles, and it has a linear association between stress amplitudes and fatigue life as well, and with no limit in SBF. Zhao et al. [31] investigated the use of pure magnesium screws to fix a vascularized bone graft in patients with femoral head osteonecrosis (ONFH). The findings indicated that using a magnesium screw to support a bone flap is both efficient and biocompatible. The rate of biodegradation is tolerable in comparison to the rate of tissue healing, and the discharged magnesium ions promote new bone formation. Airway stentings can be made from a variety of materials, including hybrid tubes and silicone. These stents, however, do not provide adequate long-term efficacy. Metallic stents, as well as mucociliary clearance, resulted in unfavorable tissue growth and drastic granulation. The large percentage of these side effects necessitates the use of secondary surgical methods to remove the stents. Because of a clear shortage of currently existing stents, there is a significant therapeutic need for biodegradable airway stents that would maintain airway patency and then be completely degrade overtime after achieving the intended goals [32].

The effectiveness of biodegradable Mg composites for the application of tracheal stents was investigated by Wu et al. [33]. This research reveals that magnesium alloys (Mg-Al-Zn-Ca-Mn) have excellent cytocompatibility and that (Mg-Al-Zn-Ca-Mn) is a useful choice for tracheal stent applications. Magnesium and its composites are sorts of biomaterials that, with proper manufacturing and design, will play a significant role in innovating biomedical applications. Wei et al. [34] implanted $COOH^+$ ion to decrease the ZK60 Mg alloy degradation and enhance its application in the physiological environment. *In vitro* cytotoxicity tests and corrosion, experiments show that the treatment of ion implantation can improve the alloy biocompatibility and reduce the corrosion rate. Dai et al. [24] performed Ti, Ni, and Ti/Ni plasma immersion ion implantation on the AM60 Mg composite. In a 3.5 percent solution of NaCl, the corrosion resistance of the Ni- and Ti/Ni-implanted AM60 samples was significantly reduced.

3. Additive manufacturing of Mg-based alloys and composite implants

AM, 3D printing, and solid free-form fabrication are interchangeable terms, and they've been used to create complex 3D porous architectures with precise pore topology control [35]. AM may create a variety of scaffolds with complex geometries that can improve cell diffusion and extracellular matrix (ECM). It uses a layer-by-layer preparation method based on computer-aided design (CAD) models [36]. Depending on the heat source (arc, electron beam, or laser), wire or powder, and feedstock materials used, different kinds of additive manufacturing procedures exist. As shown in Fig. 1, ASTM Standard F2792 categorizes additive manufacturing processes into two categories: powder bed fusion (PBF) and directed energy deposition (DED) [20]. PBF is one of the near net shape strategies of preparation [37] and the most preferred method of additive manufacturing for the fabrication of metallic scaffolds. It uses thermal energy to preferentially fuse and melt metal powders together in layers in a powder bed to produce solid patterns using multiple techniques such as EBM and SLM [38]. The first study on the efficacy of laser powder bed fusion (L-PBF) of magnesium powder was published by Ng et al. [39]. In an insulating gas atmosphere at atmospheric pressure, a mini L-PBF system with a Nd: YAG laser was used to melt single tracks of pure magnesium powders. Great regions of sintered powder were noticed around the tracks, expelling from the molten pool due to extreme evaporation. Oxidation occurs within the track and afterward, the same team investigated the influence of manufacturing variables on the microstructure and structure efficiency of pure magnesium powders using multi-layer melting [40].

3.1. Selective laser melting (SLM)

SLM applies a fiber laser system for energy supply. The entire process occurs in a chamber consisting of inert gas to diminish the surrounding oxygen and decrease absorption of hydrogen, thereby maintaining high purity. Fig. 2 represents a schematic of the SLM system. SLM's fiber laser has a power output of up to 1 kW, depending on the package used in the device [7]. The galvanometer keeps track of the beam's focus, whilst the F-theta changes the beam's displacement on

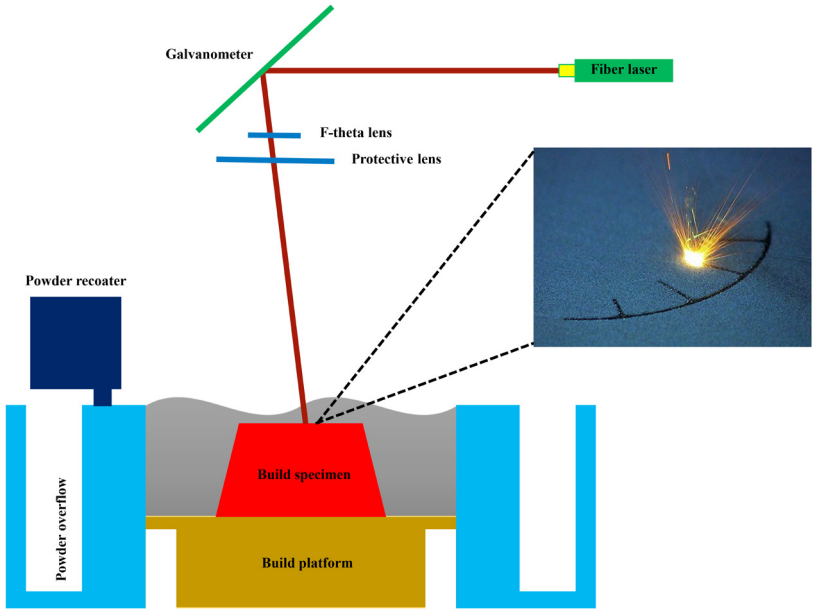

Fig. 2. Schematic illustration of an SLM system.

the build table. The powder reactor carries and spreads a 20-100 mm thick powder film on top of the table. The build table can be preheated up to 200 degrees Celsius. The laser selectively melts the powder layer according to the geometry defined in the CAD file. Each layer of a component is built in two steps using SLM. The part's surface boundaries are first formed, which is referred to as contouring, and then the powder within the contour is melted to create a full single layer. This process continues until the entire three-dimensional template is finished [41]. Applications of SLM are manufacturing orthopedic implants such as zygomatic bone replacements [42] and finger [43].

In fabricating metallic biomaterials, SLM is the most popular technology for powder bed fusion. In SLM, rapid heating and cooling processes exist which normally surpasses 105 K/s [44]. Hence, because of such cooling haste, solidification happens quickly and the grain growth is prevented [45]. Moreover, it decreases the heterogeneity of the composition due to a cohesive microstructure across the substrate. Concerning stage dynamics and grain size, the compact and homogeneous microstructure prefers improved stability, densification, and mechanical properties. Typically, except when a multi-material compound is provided in advance, using one single powder bed dispenser for a single metal powder is challenging in the process of *in-situ* delivery of several substances [46, 47].

Multi-material design using mixed metal or metal-ceramic powder mixtures in the powder bed, SLM has been applied to multi-material production of Mg-based [48-50] and Ti-based [51, 52] biomaterials. The correlation between Mg-Zn structure, deficiencies, and mechanical properties was examined during in situ adsorption of Magnesium combined with Zinc during SLM [51]. The magnesium alloy WE43 developed by Esmaily et al. [53] was accomplished by SLM. The findings indicate that corrosion of prepared Mg alloys with SLM could be excellently improved once the effect of powder characteristics is more controlled and understood. In contrast to conventional construction techniques, Zumdick et al. [54] studied the characteristics of WE43 developed by SLM. The SLM samples had incredibly fine grains with the size of about 1 µm and uniform microstructure, and very delicate secondary stages, while the as-cast specimen had a grain size of 44.3 µm and various stages. Tensile testing of additively produced samples revealed an increased maximum tensile strength of 308 MPa and a 12 percent elongation to break. Further analysis of the WE43 compound developed by the SLM was performed by Qin et al to create porous Zn-xWE43 (x=0 percent, 2 percent, 5 percent, and 8 percent) substrates by SLM mechanically mixing WE43 and pure Zn powders. For the as-fabricated ZnWE43 substrates, elevated densification over 99.9 percent was recorded.

Using SLM, Chen et al. [55] developed double MgZn composites, and the mechanical and harmful properties were analyzed. With a mean range of 15µm, the SLM manufactured compound showed homogeneous grains. The precipitation of the MgZn phase and quick solidification have effectively prevented grain enlargement. Smaller grains decreased the speed of deterioration and increased the microhardness. Wei et al. [51] analyzed Mg-Zn binary composites with differing Zn proportions using the SLM technique. At Zn amount of 1 wt percent, almost full dense parts were acquired. The specimen of Mg-1Zn had comparable mechanical characteristics with that of the as-cast equivalents. Furthermore, pre-alloyed biomaterials consisting of Mg such as Mg–3 Zn and ZK60 were alloyed *in situ* throughout SLM using scarce elements of the earth (for example Nd [56] and Dy [52]) for increased sustainability and persistent coherence of biomaterials.

Mg-3Zn-xDy (x=0-5 w%) composites were produced by Long et al. [52] using the SLM technique. The speed of deterioration and hydrogen evolution of the Mg-3Zn-1Dy composite was greatly decreased due to the combined effect of smaller particle size, uniform microstructure, as well as the inclusion of the second step. Wu et al. produced Mg-Zn-Zr (ZK60) magnesium compound formulations. [57] by SLM. Experimental findings indicated that laser strength and speed of the scan played a key role in the efficiency determination of SLM ZK60.

SLM ZK60 with limited deficiencies and high structural precision could be achieved at a laser strength of 50 W and a scanning velocity of 500-800 mm/s. SLM ZK60 in Hanks' formulation has increased strength and corrosion stability, particularly as compared to cast ZK60. Thus, the developed SLM ZK60 holds great promise for biomedical applications due to its favorable mechanical characteristics and low degradable quality.

The in situ compounds of ZK60 with Cu [58] were found to have antibacterial properties and improved compressive strength in the main composite material. Shuai et al. [58] used the SLM technique to create the ZK60-Cu alloy, which has excellent antibacterial qualities and favorable corrosion in body fluid. The ZK60–0.4Cu compound has improved compressive strength attributable to grain accuracy improvement, dispersion bolstering, and precipitate boosting. The ZK60-Cu compound has a high level of cytocompatibility, according to experiments in cell culture. Another way to enhance the corrosion protection of MgZn alloys is to incorporate hydroxyapatite (HAp; Ca10(PO4)6(OH)2). [59, 60]. In this regard, Mg-3 Zn/xHAp blends were synthesized by Shuai

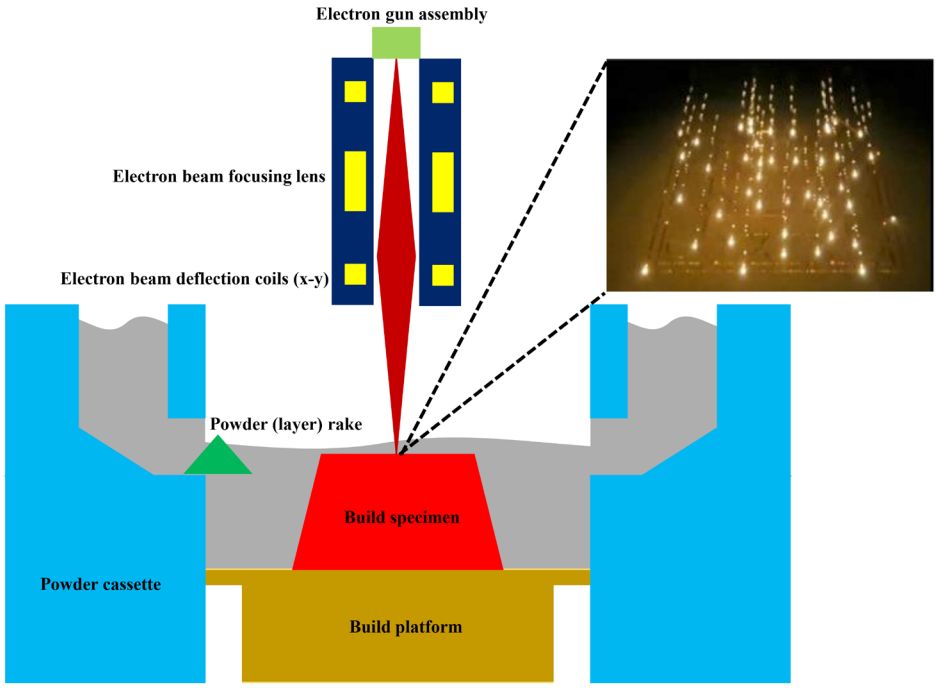

Fig. 3. Schematic illustration of an EBM system.

et al.[61] using the SLM technique. The relative density ranged from 95.5% to 97.9% for the as-built specimens. Fast solidification avoided HAp particle agglomeration and facilitated homogenous distribution. Increasing the amount of HAp contributed to the production of finer grains. Along with the development of the apatite coating sheet, finer grains contribute to increased resilience to biodegradation. Furthermore, by fine-grain reinforcement and second phase enhancement, the hardness of the Mg-3 Zn composite was strengthened.

Liu et al. [62] studied the SLM development of porous Mg-Ca alloys. Because of the grain refining and solid solution enhancement, the microhardness of the SLM-manufactured specimens was better than that of as-cast pure magnesium. Yao et al. [63] used SLM to change the surface of such Magnesium composites (Mg-Zn-Ca and Mg-Ca) to improve the corrosion effect and micro-hardness simultaneously. The corrosion ratio decreased and the microhardness increased in both Mg-0.5Zn-0.3Ca and Mg-0.6Ca. On the other hand, managing laser power density, and therefore avoiding the formation of unwanted pore spaces and unnecessary melting is challenging due to the widely divergent thermal characteristics of various components. Since certain additives have higher melting temperature, they cannot be fully melted and distributed, but they remain partially melted next to the matrix [64]. The grain size proportions of multi-material powders could be adjusted to account for variations in thermal properties, with a smaller size for a substance with a higher melting point [65].

Post-AM heating might be needed to enhance multi-material distribution and chemical property uniformity [50]. The availability of multi-material powders supply to the powder bed is also a critical factor in maintaining a consistent multi-material distribution within the resulting composite. Powder bed fusion is prone to strong thermal currents and may induce fractures and defects in the multi-material substrate since it uses large thermal powers. To allow successful application of laser power as well as other process parameters that should be synchronized with each material's physical characteristics and powder features, powder bed fusion for in situ versatile AM alloys or ceramic substrates necessitates robust and complicated enhancement. Furthermore, it is essential to consider the measures taken for the reuse and recycling of the remaining substances in the powder bed [66, 67].

3.2. Electron beam melting

EBM is another composite fabrication process that is expected to transform the implant- manufacturing sector. This device was developed and patented by Arc am AB, a Swedish company. The metal powder is liquefied using the energy of an electron stream [68]. The procedure is carried out in a vacuum chamber where the electron beam is the power supply. The vacuum by offering an atmosphere void of oxygen guarantees high purity and decreases the chance of picking up hydrogen. This function is highly helpful in the manufacture of titanium-6aluminium-4vanadium (Ti6Al4V) parts since it is possible to monitor the small amounts of interstitial components during manufacturing [69]. Besides, a high temperature of around 700 degrees Celsius is established in the system throughout the construction of the component to decrease excess tensions and thereby warpage and distortion [70].

Fig.3 shows the mechanism of the EBM process. The EBM device consists of a 60 kW electron gun that produces a guided energy intensity beam over 100 kW/cm2 (equivalent to an electron beam-welding unit or electron gun in a scanning electron microscope). Electromagnetic lenses control the beam concentration, and deflection coils direct the beam's motion on the building table. A powder layer with a thickness of 100 m is dispersed over the table to make a part. Two hoppers placed within the construction chamber supply the powder. From both ends, a running rake brings in powder and spreads it across the table. During EBM, initially, the electron beam heat up the powder layer with faster scanning, accompanied by powder layer melting according to the CAD model's geometry. Each layer of a component is built in two phases. The outer boundary of the part is first built, known as contouring, and then the powder inside the contour begins to melt, forming a single sheet. [71, 72].

EBM was employed to manufacture orthopedic parts including jaw, hip, knee, substitutes, and maxillofacial plates [73]. This procedure continues until the required three-dimensional portion is entirely completed The implants developed by EBM, such as acetabular cups, have also been approved by the Food and Drug Administration (FDA) of the United States and have been CE accredited since 2010 and 2007, respectively [74, 75]. Both of these procedures share common benefits and are actively taken into account in the manufacturing of orthopedic implants.

These benefits include complex product processing, innovative designs, hollow systems, and products with practical gradients. A cost-effective strategy that causes lowering manufacturing costs and shortening the period to market for high-value products. Some of the benefits include superior structural properties, virtually no porosity, the ability to mix different components, reduced material waste dramatically. Exclusion of costly instrumentation. Because of these benefits, various scholars have performed multiple studies to confirm the merit of these methods in implant production. As an artificial bone that is implanted inside the corpus, orthopedic implants are often used for structural strengthening. Temporary implants, including screws and plates, as well as permanent implants, can be utilized to repair body sections such as fingers, knees, and hips. [76, 77]. Permanent implants rely more on resilience, durability, and tolerance to corrosion in joint replacements and tribology.

A study of the Magnesium alloy AZ91HP processed using High Current Pulsed Electron Beam (electron energy of 30 keV, a pulse length of 1 μs, and energy density of 3 J/cm^2) has been reported by Gao et al. [78] After treatment, as demonstrated by sliding pressure, corrosion, and immersion tests, the wear and corrosion tolerance of the alloy was substantially increased. Schmid et al. [79] developed AZ91 Mg alloy using the EBM process. While treating magnesium under typical laser beam melting conditions, the findings revealed keyhole melting happens, and modifying energy input by changing the layer thickness has a lesser influence than changing the distance of the hatch, scan rate, or laser strength.

4. Characteristics of Mg alloy and composite implants produced by AM

4.1. Mechanical properties

Implants must be immune to anatomical loads. Thus, mechanical properties including stiffness, tensile and compressive strength, hardness flexibility, durability, and ductility must be evaluated prior to therapeutic implementation. [80]. The alleged stress shielding, that happens when the external pressures are acting upon the implant instead of bone, results in a substantial discrepancy between the elastic moduli of the body tissue and implant. Stress shielding induces bone necrosis that leads to the implant/scaffold destabilization and ultimately the implant/premature scaffold collapse. The cancellous and cortical bones have an elastic modulus in the range of 22.4 to 132.3 MPa and 7.7 to 21.8 GPa, respectively. An elastic modulus imitating the normal human bone elastic modulus [81, 82] should be demonstrated by implants. Adapting the elastic modulus to the proper rate is also vital for the nature of the implant.Accordingly, multiple methods could be used to avoid the implant/scaffold and bone from mismatching mechanical characteristics. Mixing with β stabilizers is one method for reducing the elastic moduli of the implant by applying a β step in the structure. Together with porosity, elastic moduli also can be efficiently decreased [83-85].

Based on Gibson and Ashby model [86], relative density is the most significant design feature of a porous structure that affects Young's module. The ratio of the density of the elastic substance (ρ) to the density of the solid material (ρ_s) is known as relative density. The given formulas describe the relations between the elastic modulus, plastic failure strength, and relative density [20]:

$$\sigma_{pl} = 0.3\left(\rho / \rho_s\right)^{1.5} \rho_{ys} \tag{1}$$

$$E = \rho(\rho_s)^2 E_s \tag{2}$$

Where σ_{pl} is the intensity of the plastic failure, ρ/ρ_s the relative density, the yield strength is ρ_{ys}. E is Young's modulus; the subscript (s) reflects the substrate material features. Provided formulas show that increasing porosity reduces the elastic modulus' strength and causes plastic breakdown. However, by grain refining as per the Hall-Petch model, the mechanical properties of an implant/scaffold can be increased as follows [87]:

$$\sigma_y = \sigma_0 + \frac{k}{\sqrt{d}} \tag{3}$$

Here yield stress is σ_y, σ_0 is a material constant for the starting stress for dislocation movement, k is a material constant known as strengthening coefficient, and d denotes the size of the grain. In a related way as reported by the Hall-Petch equation, grain refining greatly increases the hardness of the products according to Eq. 4 [87];

$$H = H_0 + \frac{k}{\sqrt{d}} \tag{4}$$

Where H is the material hardness, H_0 and k are suitable constants correlated with the material hardness, and d is the particle size.

As earlier described, SLM-manufactured composites retain refined grains because of quick cooling and solidification. Researchers examined the processing of biodegradable Magnesium composites of different compositions using SLM.

Sing et al. [88] reported multi-material production in SLM employing AlSi10Mg and UNS C18400 copper alloy. Under a three-point bending examination, the tensile strength of Cu at the root was determined to be 176 ±31 MPa, and the flexural strength of Al at the root was assessed about 200 MPa for Cu and 500 MPa for Al.

According to the Hall-Petch formula, a single track of pure Magnesium demonstrated grain sophistication and increased hardness in the study by Ng et al. [40]. Yang et al. [44] used the SLM technique to create pure Magnesium cubes, which was then verified by them. SLM then produced a variety of Mg alloys with increased toughness cause of the high cooling and solidification speeds [62]. The yield strength, elastic modulus, compressive strength, and tensile strength of the SLM-generated Magnesium models outperformed widely manufactured equivalents and they were favored for orthopedic applications. Research work shows that in compliance with the Hall-Petch model, grain refining increases the hardness of the biodegradable Mg sections. The hardness of the Mg generated by the SLM varied from 0.4 to 1.2 GPa [89].

Mg-Zn dual composites with seven varied formulas (Zn = 1, 2, 4, 6, 8, 10, and 12 wt%) were produced by Wei et al. [51] by employing SLM. The hardness and tensile measurements revealed that with the as-cast equivalent, only the Mg-1Zn sample had equivalent mechanical properties. Mechanical characteristics of the SLM-processed alloys were substantially weakened at higher Zn content primarily due to the decline in the level of densification. In addition, Qin et al. [90] manufactured AM Zn-xWE43 porous scaffolds containing various WE43 volume ratios. Zn-5WE43 had the maximum tensile strength of 335.4 MPa, but the elongation was just 1%. The compressive strength and Young's modulus of Zn-5WE43 porous substrates were 73.2 MPa and 2480 MPa, respectively, while pure Zn porous substrates were 22.9 MPa and 950 MPa. Li et al. [91] developed geometrically organized porous Mg (WE43) substrates through the SLM process based upon the diamond unit cell. Substrates were constructed to yield 67 percent porosity with a pore size of 600 μm and strut size of 400 μm, whereas the scaffolds that have already been developed had an approximate 64 percent porosity and strut size of 420 μm. The mechanical properties of the porous WE43 (E=0.7–0.8 GPa) substrates were also found to remain within the limit reported for trabecular bone (E=0.5–20 GPa) after 4 weeks of biodegradation. The modeled configuration accurately aligned the real topology of the porous architectures, which included a completely entangled porous construct, elevated porosity, and explicitly regulated geometry of the unit cells. A

desirable biodegradation activity was demonstrated by additively produced porous Mg samples with around 20 percent volume reduction after 4 weeks. Small cytotoxicity was registered at less than 25 percent.

4.2. Biodegradability behavior

The Mg-based substances are recommended for medical applications due to their biodegradability. The objective of biodegradable Mg is to establish a functional interaction in vitro and in vivo involving biodegradable specimens of magnesium and the natural biological setting while traditional metals are utilized as biocompatible substances to enhance mechanical characteristics, decrease production costs, and improving corrosion resistance. [92]. Different studies have been conducted regarding the cellular mechanisms and biological environment-biomaterial interaction to emphasize the biological effect of corrosion byproducts[93, 94]. Many research groups have focused on Mg to develop new medical applications, particularly after it was discovered that implanting magnesium tools causes no noticeable alterations in blood content. [95-97].

Because of the increased content of grain borders, grain refining potentially accelerates the amount of corrosion. Gollapudi et al. defined the effect of particle sizes on the corrosion rate [98] as given in Eq. 5:

$$i_{corr} = A + B(d)^{1/2} \exp\left(-9/8S_n^2\right) \quad (5)$$

The corrosion current is i_{corr}, *A,* and *B* are constants that depend on the impurity level or material composition, the grain size distribution is S_n and the mean grain size is d in this equation.

Many corrosion materials have a significant influence on the rate of corrosion of biodegradable metals. [99, 100]. Fine-grain, because of the formation of corrosion products can lead to a decrease in the rate of corrosion in a passivated environment. According to various studies, the corrosion rate of magnesium and its composites declines as grain size reduces [89]. The manufacturing process, architecture, and material selected all affect the biodegradation efficiency of additively processed magnesium. In addition, the condition of processing has a prevailing influence on the as-built parts' biodegradation characteristics. Niu et al. [101] studied the bulk pure magnesium's corrosion behavior, which was prepared by the SLM method. The results of the study highlighted the significance of selecting proper parameters for the magnesium SLM processing to minimize corrosion rate and processing pores. The rate of corrosion (r) is calculated by the following equation:

$$r = (M_1 - M_2)/t_i \quad (6)$$

In this equation, M_1 is the material mass before corrosion and M_2 is the material mass after corrosion, and t_i is the immersion time. Researches exhibit that the corrosion rate of magnesium alloys can be decreased by grain refinement [102]. As noted, the SLM process involves fast cooling causes homogenized microstructure formation and fine grains leading to the improvement in corrosion resistance [103]. Li et al. [91] prepared WE43 scaffolds by the SLM method. The as-fabricated scaffolds showed improved biodegradation resistance of 0.17 ml/cm^2·day compared with the as-extruded and as-cast counterparts of 0.3 ml/cm^2·day. Xie et al. [104] investigated SLMed Mg-xMn with various content of Mn. The XPS spectra of the corrosion surface exhibited that alloying manganese into magnesium by SLM produced a protective film of manganese oxide, which reduced the biodegradation rate. All the results of the corrosion surface morphologies, immersion test, and electrochemistry test coincided well. The SLMed Mg-0.8Mn had the lowest rate of biodegradation. When manganese content was more than 0.8 wt.%, the effect of the undissolved manganese phase on the reduction of the biodegradation resistance counteracted the effect of the relatively protective layer of manganese oxide on the enhancement of the biodegradation resistance.

The corrosive behavior of pure Fe and AM WE43-based porous scaffolds was investigated by Li et al. [91]. The corrosive behavior was studied in SBF for 7 days and the results showed that the weight losses of AM porous WE43 and the bulk WE43 plates (10×10×2 mm^3) were almost 9% and 5%, respectively. The process of SLM was used by Shuai et al. [105] to promote the ZK60 corrosion resistance for potential applications as biodegradable implants. The extended solid solution, homogenized microstructure, and grain refinement improved ZK60 alloy corrosion resistance because of the fast grain refinement in the SLM process. Nd was incorporated into ZK60 alloy with the SLM process by Shuai et al. [56]. The as-prepared sample had intermetallic phases and fine grains of α-Mg along the grain boundaries. The resistance to degradation increased with the dense surface layer formation promoted by the Nd_2O_3, besides the structure of the 3D honeycomb of intermetallic phases resulted in the formation of a tight barrier for corrosion prevention.

Rakesh et al. [106] studied Mg-1Zn-2Dy alloy by SLM and their results exhibited that the surface energy was changed with LSM because of changes in the chemical composition, microstructure, and surface morphology of the material. The detailed degradation research was performed in Hank's balanced salt solution (HBSS). The enhancement in the degradation behavior followed by laser surface melting is attributed to the microstructural refinement because of the fast cooling and heating of the melted zone. Besides the grain size, an essential factor is the intermetallic phase, which affects the Mg alloy's biodegradation behavior [107]. Shuai et al. [108] investigated various intermetallic phase volume fractions and grain size by adding different concentrations of Al into Mg–Zn alloy. In this experiment, ZK30-xAl cubes with the dimensions of 5 mm×5 mm×5 mm were prepared using the SLM method. Based on the results, with an increase in the content of Al, the refinement of the grain size occurred and the volume fraction of intermetallic phase was reduced. When the Al content was lower than 3 wt%, the main factor that affected the degradation performance was the grain refinement. Many grain boundaries were generated by the finer grains causing readily passivation of the alloy leading to an enhanced resistance to degradation. Nevertheless, by increasing the content of Al, the major factor affecting the degradation behavior was the intermetallic phase even though the size of grain was more refined.

In another work conducted by Yang et al. [109], mesoporous SiO_2 was incorporated into ZK60 alloy for the enhancement of the degradation resistance using SLM. Since the rapid cooling and heating occur in SLM, mesoporous silica particles homogeneously dispersed in the magnesium matrix and led to the formation of a decent interface binding. Mesoporous SiO_2 can be used for magnesium surface passivation because of its positive corrosion potential. Besides, the exceptional bioactivity and mesoporous structure of SiO_2 promoted the apatite layer deposition, which has a role as a protection film against corrosion of the Mg matrix. Table 1 summarizes previously studied work regarding the biodegradation behavior of magnesium prepared by AM. Improved biodegradation resistance is achieved by the improved microstructure resulting in the rapid cooling and fast solidification involved in the SLM process.

4.3. Biocompatibility

The chemical composition and degradation products mostly specify the biocompatibility of biodegradable metal-based implants. Therefore, the strict usage of biocompatible powders should be the main attention. The information gathered from the biodegradable bulk material design can help with the primary design of powder composition [89, 110-112]. For the enhancement of biocompatibility and mechanical integrity of bulk magnesium alloys during biodegradation, surface biofunctionalization has been carried out [113].

Table 1.
Properties of biodegradable Mg manufactured by AM

Material	AM method	Mechanical performance	Biodegradation behavior	Biocompatibility	Reference
TiTa	SLM	Elastic modulus of ~75 GPa and tensile strength of ~924 MPa	Corrosion resistance	In contrast to other SLM titanium alloys, this alloy is highly biocompatible and has no toxic materials like aluminum or vanadium.	Sing et al. [64]
WE43	L-PBF	With the increase of the strut diameter from 275 μm to 800 μm, the increase in the elastic modulus was from 0.2 to 0.8 GPa, and also the yield strength was improved from 8 to 40 MPa.	The solution treated and as-printed scaffolds showed the lowest rate of corrosion of 2–3 mm/year and the corrosion rate could be decreased to ~0.1 mm/year with plasma electrolytic oxidation surface treatments.	Scaffolds based on WE43 magnesium alloy with the PEO surface treatment presented acceptable biocompatibility.	Li et al. [127]
SLM-prepared ZK60 and cast ZK60	SLM	The hardness of cast and SLM ZK60 was 0.78 and 0.55 GPa, respectively, while their elastic moduli were similar.	Higher corrosion resistance in Hanks' solution was exhibited by SLM ZK60 compared to cast ZK60 so that the corrosion current density and hydrogen evolution rate reductions were 50 % and 30 %, respectively.	-	Wu et al. [57]
ZK60/BG	LPBF	Mechanical properties were improved due to the refined grains in which reinforcing particles were orderly dispersed.	LPBF with a fast process of solidification resulted in a homogenized and refined microstructure. This feature was also considered responsible for the improved corrosion resistance of ZK60/BG.	ZK60/BG with improved biocompatibility promoted differentiation and cell growth, which led to accelerating healing of bones as an in vivo implant.	Yang et al. [9]
Fe-Mg	SLM	-	After immersion for 21 days the rate of degradation improved by 2.74 times.	The MG-63 cells proliferated faster, showing excellent cytocompatibility.	Shuai et al. [128]
Mg-Ca and Mg-Zn-Ca	SLM	The improvement of microhardness (HV0.1(for Mg–0.6Ca and Mg–0.5Zn–0.3Ca was from 46 ± 1 HV to 56 ± 1 HV and from 47 ± 3 HV to 55 ± 3 HV, respectively.	The rate of corrosion for laser-processed Mg–0.5Zn–0.3Ca and the laser-processed Mg–0.6Ca reduced from 1.6 ± 0.1 mm/y to 0.7 ± 0.2 mm/y and from 2.1 ± 0.2 mm/y to 1.0 ± 0.1 mm/y, respectively.	The laser processed magnesium alloys showed excellent biocompatibility.	Yao et al. [63]
Ti+Mg	Inkjet 3D printing	Composite of Ti+Mg showed high UCS (418MPa) and low modulus (5.2GPa) matching bone.	After 5 days of immersion, porous Ti showed a poor corrosion rate of ~1.14 μm/year, while Ti + Mg composites exhibited a corrosion rate of <1 mm/year.	The results of cell viability showed the absence of mild cytotoxicity improved the proliferation rate of SAOS-2 osteoblastic bone cells.	Meenashisundaram et al. [129]
AZ31B-HA composites	Friction stir AM	-	Corrosion resistance was higher in the composites compared to untreated AZ31B because of an optimum balance between positive influences of grain size refinement and the limited number of local galvanic couples.	-	Ho et al. [130]
ZK30-xCu	SLM	-	Biodegradation rate order was as follows: ZK30 < ZK30-0.1Cu < ZK30-0.2Cu < ZK30-0.3Cu	The alloys show good cytocompatibility and antibacterial ability.	Xu et al. [45]
Mg-5.9Zn-0.13Zr	3D printing	With sintering process conducted at 573 °C and holding time up to 60 h, comparable elastic modulus, compressive properties, and density, close to that of human cortical bone were obtained.	-	-	Salehi et al. [131]
AZ61	SLM	The ultimate tensile strength of the as-synthesized alloy was measured to be 93% higher compared to the as-cast alloy, the increase in the yield strength was 136%, and the decrease in the surface roughness was from 18.95 to 7.49 μm.	-	-	Liu et al. [132]
WE43	L-PBF	-	It can be shown that, because of high process-induced surface roughness, which supports corrosion of locally intensified, several crack initiation sites are appearing, which is one of the major reasons for the intense decrease in fatigue strength.	-	Wegner et al. [133]

Table 1. (Continued)

Material	AM method	Mechanical performance	Biodegradation behavior	Biocompatibility	Reference
Zn-xWE43	L-PBF	The highest tensile strength was 335.4 MPa relating to Zn-5WE43, while the elongation was only 1%. Young's modulus and compressive strength of Zn-5WE43 porous scaffolds were 2480 MPa and 73.2 MPa, respectively, but for pure Zn porous scaffolds, these values accounted for 950 MPa and 22.9 MPa respectively.	The powders of Zn-Mg alloy based exhibited hopeful prospects for applications of biodegradable.	-	Qin et al. [90]
ZK30/BG composites	SLM	-	The rate of degradation of the ZK30 matrix declined with the BG introduction.	Cytocompatibility was enhanced with the BG addition.	Yin et al. [122]
ZK60-xCu	SLM	Because of the refinement of the grains and uniform dispersion of MgZnCu phases with short-bar shapes, the compressive strength improved.	ZK60-Cu alloys show an excellent biodegradation rate.	ZK60-Cu alloys showed good cytocompatibility and strong antibacterial ability.	Shuai et al. [58]

Desirable results have been obtained for biodegradable magnesium alloys having different compositions. When the content and type of the alloying element(s) are selected carefully, the biodegradation resistance of magnesium can be remarkably increased without scarifying its mechanical function as well as its biocompatibility. The in vivo and in vitro tests have many differences. Sanchez et al. [114] reported the lower rate of corrosion (1-4 times) for magnesium alloys in the in vivo test in comparison with the in vitro test. Some of the results are attributed to the in vivo evaluations of vascular stents based on biodegradable metals [115]. In addition, in microstructure and chemical composition, the biocompatibility results are attributed to time, implantation position together with structure design [89, 116]. The potential of using pure magnesium-based screws to fix vascularized bone graft in ONFH patients was studied by Zhao et al. [31]. The results showed the biocompatibility of the magnesium screw and its efficiency in bone flap stabilization. Its degradation rate was comparable to the tissue-healing rate; also, the released magnesium ions could stimulate the formation of new bone.

$Mg_3(PO_4)_2$ is a bioceramic exhibiting special bioactivity, biodegradability, and biocompatibility [20]. A composite scaffold based on gelatin/$Mg_3(PO_4)_2$ with binder jetting was fabricated by Farag and Yun [117]. Dense struts were formed by the addition of gelatin into $Mg_3(PO_4)_2$ up to 6 wt%; therefore, it considerably enhanced the mechanical performance of the scaffolds. In addition, the composite scaffolds showed good cell affinity and wettability. Binder jetting was also used on $Mg_3(PO_4)_2$ powder by Vorndran et al. [118]. The binder liquid used in this study composed of K_2HPO_4 (2 M), 20% H_3PO_4 or $(NH_4)_2HPO_4$ (0.5 M) for the formation of a matrix of, newberyite ($MgHPO_4 \cdot 3H_2O$), struvite-(K) ($MgKPO_4 \cdot 6H_2O$), or struvite ($MgNH_4PO_4 \cdot 6H_2O$) by employing a hydraulic setting reaction.

In order to inhibit infections inside the human body, it is essential to incorporate antibacterial properties into implants. As *in vitro* studies show, antibacterial features are not presented by Mg metal and alloys [58]. By coupling 3D printed and traditionally manufactured Mg alloys with Cu, bacterial activity decreased. However, traditional methods of manufacturing cannot deliver Mg-Cu components with good quality due to galvanic corrosion issues. For low levels of Cu in Mg alloys that are below the limit of solid solubility, additive manufacturing has been shown to be able to handle this challenge [45]. Studies show that after 72 h under normal pH conditions, *Escherichia Coli* colony count was reduced to zero by the addition of 0.4 wt% Cu powder to ZK60. Moreover, blending bioactive glass with Mg-based alloys has demonstrated the enhancement of cytocompatibility [119, 120]. Besides, resistance to degradation in the ZK30 Mg alloy was found to be improved in simulated body fluid by the increase in the bioactive glass content in the ZK30 powder mixture. This is due to magnesium ion release limitations within the body. Using laser additive manufacturing, Yang et al. [9] reinforced Mg with bioglass. To compare the biocompatibility of the composite with ZK60 as control, the as-prepared part acquired at a volumetric energy density of 185.19 J/mm^3 was used. Generally, observed dead cells were very few. Briefly, improved biocompatibility provided by ZK60/BG enhanced differentiation and cell growth leading to accelerated bone healing.

Mg–Y–RE–Zr alloy prepared by conventional methods has been stated to exhibit good osteoconductivity and biocompatibility and no toxicity [121]. This alloy is being used for the fabrication of screws to treat hallux valgus and bone fractures in the European Union. Y is an important alloying element, which enhances the overall behavior of the alloy and its degradation because this element decreases galvanic coupling due to the formation of intermetallic phases. It also produces a net improvement in the corrosion resistance by protective surface oxide layer formation, depending on the environment [122]. Bär et al. [121] created implants made of WE43 by additive manufacturing. The results demonstrated that the sample has good osteoconductivity and biocompatibility. Yao et al. [63] studied the SLM magnesium alloys such as Mg–0.5Zn–0.3Ca and Mg–0.6Ca and according to the results good biocompatibility was found in laser processed magnesium alloys. In addition, the enhanced properties are related to the modified surface chemistry, residual stress, confined impurity elements, and laser-induced grain refinement. The dual alloying influence of manganese and/or Sn on the performance of magnesium alloys prepared by SLM was investigated by Gao et al. [123]. The alloys of Mn- and/or Sn-containing exhibited good cytocompatibility as indicated by increased viability of MG-63 cells and the normal morphology revealing that the developed alloy of AZ61-Mn-Sn is a promising choice for biodegradable bone implants. Table 1 exhibits the biocompatibility, biodegradation, and mechanical properties of different materials produced by AM.

5. Conclusions and future insights

Mg-based implants with personalized designs consistent with the patient's anatomic data can be created using additive manufacturing. Although the probability of sacrificial material elimination has been exhibited by recent studies, as-prepared magnesium components still lack sufficient formation quality. EBM seems to be inappropriate because severe evaporation of magnesium affects the propagation of electron beam in the vacuum environment within the build chamber. In the SLM process, high densification is achieved because of the efficient infiltration as well as complete melting of magnesium resulting in the elimination of voids in the bulk struts/material. The fast solidification and high rates of cooling in the SLM process are favored to obtain improved microstruc-

ture with an enhanced solid solution, homogenized phase distribution, and refined grains. Therefore, the corrosive and mechanical properties of magnesium produced by SLM are superior to their traditionally produced counterparts. Powder properties and processing conditions notably affect the mechanical and biological performance of the as-prepared magnesium implants and scaffolds, microstructure, dimensional accuracy, and formation quality. The optimal processing conditions and powder properties led to higher energy efficiency and material densification. The topology of scaffolds notably influences differentiation, proliferation, and new cells' attachment. Studies concentrating on the manufacturing of Mg with various lattice structures by the AM process are quite limited.

It is required to conduct more studies for comparative investigation regarding the influence of pore porosity, topology, and various lattice structures, to recognize the ideal design for scaffolds to render the best performance. There might be some differences in the biological properties of the as-prepared magnesium in vivo and in vitro. There are wide in vitro studies to evaluate the biodegradation characteristics of additively manufactured Mg alloys, however, limited reports are focusing on the in vivo performance of these alloys. Therefore, it is recommended to carry out more in vivo investigations to shed light on the biodegradation performance of magnesium implants manufactured by AM. Eventually, based on the period required for the healing of the defected tissues, the in vivo performance of additively manufactured magnesium implants in terms of time (up to ~2 months) is needed to be investigated to ultimately succeed of the implants in clinical applications.

REFERENCES

[1] I. Antoniac, D. Popescu, A. Zapciu, A. Antoniac, F. Miculescu, H. Moldovan, Magnesium filled polylactic acid (PLA) material for filament based 3D printing, Materials 12(5) (2019) 719.

[2] T.Y. Kwak, J.Y. Yang, Y.B. Heo, S.J. Kim, S.Y. Kwon, W.J. Kim, D.H. Lim, Additive manufacturing of a porous titanium layer structure Ti on a Co–Cr alloy for manufacturing cementless implants, Journal of Materials Research and Technology 10 (2021) 250-267.

[3] J.B. Hochman, J. Kraut, K. Kazmerik, B.J. Unger, Generation of a 3D printed temporal bone model with internal fidelity and validation of the mechanical construct, Otolaryngology–Head and Neck Surgery 150(3) (2014) 448-454.

[4] E.K. O'Brien, D.B. Wayne, K.A. Barsness, W.C. McGaghie, J.H. Barsuk, Use of 3D printing for medical education models in transplantation medicine: a critical review, Current Transplantation Reports 3(1) (2016) 109-119.

[5] D. Popescu, D. Laptoiu, Rapid prototyping for patient-specific surgical orthopaedics guides: A systematic literature review, Proceedings of the Institution of Mechanical Engineers, Part H: Journal of Engineering in Medicine 230(6) (2016) 495-515.

[6] D. Popescu, D. Laptoiu, R. Marinescu, I. Botezatu, Design and 3D printing customized guides for orthopaedic surgery–lessons learned, Rapid Prototyping Journal (2018).

[7] S.L. Sing, J. An, W.Y. Yeong, F.E. Wiria, Laser and electron-beam powder-bed additive manufacturing of metallic implants: A review on processes, materials and designs, Journal of Orthopaedic Research 34(3) (2016) 369-385.

[8] A. Masoudian, A. Tahaei, A. Shakiba, F. Sharifianjazi, J.A. Mohandesi, Microstructure and mechanical properties of friction stir weld of dissimilar AZ31-O magnesium alloy to 6061-T6 aluminum alloy, Transactions of nonferrous metals society of China 24(5) (2014) 1317-1322.

[9] Y. Yang, C. Lu, S. Peng, L. Shen, D. Wang, F. Qi, C. Shuai, Laser additive manufacturing of Mg-based composite with improved degradation behaviour, Virtual and Physical Prototyping (2020) 1-16.

[10] C. Wu, W. Zai, H. Man, Additive manufacturing of ZK60 magnesium alloy by selective laser melting: Parameter optimization, microstructure and biodegradability, Materials Today Communications (2020) 101922.

[11] D. Carluccio, C. Xu, J. Venezuela, Y. Cao, D. Kent, M. Bermingham, A.G. Demir, B. Previtali, Q. Ye, M. Dargusch, Additively manufactured iron-manganese for biodegradable porous load-bearing bone scaffold applications, Acta biomaterialia 103 (2020) 346-360.

[12] V.S. Telang, R. Pemmada, V. Thomas, S. Ramakrishna, P. Tandon, H.S. Nanda, Harnessing Additive Manufacturing for Magnesium Based Metallic Bioimplants: Recent Advances and Future Perspectives, Current Opinion in Biomedical Engineering (2021) 100264.

[13] R. Karunakaran, S. Ortgies, A. Tamayol, F. Bobaru, M.P. Sealy, Additive manufacturing of magnesium alloys, Bioactive Materials 5(1) (2020) 44-54.

[14] M.N. Jahangir, M.A.H. Mamun, M.P. Sealy, A review of additive manufacturing of magnesium alloys, AIP Conference Proceedings, AIP Publishing LLC, 2018, p. 030026.

[15] T. Trang, J. Zhang, J. Kim, A. Zargaran, J. Hwang, B.-C. Suh, N. Kim, Designing a magnesium alloy with high strength and high formability, Nature communications 9(1) (2018) 1-6.

[16] A. Dehghanghadikolaei, H. Ibrahim, A. Amerinatanzi, M. Elahinia, Biodegradable magnesium alloys, Metals for Biomedical Devices, Elsevier2019, pp. 265-289.

[17] A. Moghanian, A. Ghorbanoghli, M. Kazem-Rostami, A. Pazhouheshgar, E. Salari, M. Saghafi Yazdi, T. Alimardani, H. Jahani, F. Sharifian Jazi, M. Tahriri, Novel antibacterial Cu/Mg-substituted 58S-bioglass: Synthesis, characterization and investigation of in vitro bioactivity, International Journal of Applied Glass Science 11(4) (2020) 685-698.

[18] B.R. Powell, P.E. Krajewski, A.A. Luo, Chapter 4 - Magnesium alloys for lightweight powertrains and automotive structures, in: P.K. Mallick (Ed.), Materials, Design and Manufacturing for Lightweight Vehicles (Second Edition), Woodhead Publishing2021, pp. 125-186.

[19] A. Sheikhani, R. Roumina, R. Mahmudi, Hot deformation behavior of an extruded AZ31 alloy doped with rare-earth elements, Journal of Alloys and Compounds 852 (2021) 156961.

[20] N. Sezer, Z. Evis, M. Koç, Additive manufacturing of biodegradable magnesium implants and scaffolds: Review of the recent advances and research trends, Journal of Magnesium and Alloys (2020).

[21] Y. Luan, P. Mao, L. Tan, J. Sun, M. Gao, Z. Ma, Optimising the mechanical properties and corrosion resistance of biodegradable Mg-2Zn-0.5Nd alloy by solution treatment, Materials Technology (2021) 1-10.

[22] J. Huang, Y. Ren, Y. Jiang, B. Zhang, K. Yang, In vivo study of degradable magnesium and magnesium alloy as bone implant, Frontiers of Materials Science in China 1(4) (2007) 405-409.

[23] C. Hampp, B. Ullmann, J. Reifenrath, N. Angrisani, D. Dziuba, D. Bormann, J.M. Seitz, A. Meyer-Lindenberg, Research on the biocompatibility of the new magnesium alloy LANd442—an in vivo study in the rabbit tibia over 26 weeks, Advanced Engineering Materials 14(3) (2012) B28-B37.

[24] J. Dai, Z. Liu, B. Yu, Q. Ruan, P.K. Chu, Effects of Ti, Ni, and Dual Ti/Ni Plasma Immersion Ion Implantation on the Corrosion and Wear Properties of Magnesium Alloy, Coatings 10(4) (2020) 313.

[25] Y. Li, C. Wen, D. Mushahary, R. Sravanthi, N. Harishankar, G. Pande, P. Hodgson, Mg–Zr–Sr alloys as biodegradable implant materials, Acta biomaterialia 8(8) (2012) 3177-3188.

[26] Z. Li, X. Gu, S. Lou, Y. Zheng, The development of binary Mg–Ca alloys for use as biodegradable materials within bone, Biomaterials 29(10) (2008) 1329-1344.

[27] H.R.B. Rad, M.H. Idris, M.R.A. Kadir, S. Farahany, Microstructure analysis and corrosion behavior of biodegradable Mg–Ca implant alloys, Materials & Design 33 (2012) 88-97.

[28] A. Ghanbari, H. Jafari, F.A. Ghasemi, Wear Behavior of Biodegradable Mg–5Zn–1Y–(0–1) Ca Magnesium Alloy in Simulated Body Fluid, Metals and Materials International 26(3) (2020) 395-407.

[29] S. Wang, X. Zhang, J. Li, C. Liu, S. Guan, Investigation of Mg–Zn–Y–Nd alloy for potential application of biodegradable esophageal stent material, Bioactive Materials 5(1) (2020) 1-8.

[30] M. Liu, J. Wang, S. Zhu, Y. Zhang, Y. Sun, L. Wang, S. Guan, Corrosion fatigue of the extruded Mg–Zn–Y–Nd alloy in simulated body fluid, Journal of Magnesium and Alloys 8(1) (2020) 231-240.

[31] D. Zhao, S. Huang, F. Lu, B. Wang, L. Yang, L. Qin, K. Yang, Y. Li, W. Li, W. Wang, Vascularized bone grafting fixed by biodegradable magnesium screw for treating osteonecrosis of the femoral head, Biomaterials 81 (2016) 84-92.

[32] F. Sharifianjazi, A. Esmaeilkhanian, M. Moradi, A. Pakseresht, M.S. Asl, H. Karimi-Maleh, H.W. Jang, M. Shokouhimehr, R.S. Varma, Biocompatibility and mechanical properties of pigeon bone waste extracted natural nano-hydroxyapatite for bone tissue engineering, Materials Science and Engineering: B 264 (2021) 114950.

[33] J. Wu, B. Lee, P. Saha, P. N Kumta, A feasibility study of biodegradable magnesium-aluminum-zinc-calcium-manganese (AZXM) alloys for tracheal stent application, Journal of Biomaterials Applications 33(8) (2019) 1080-1093.

[34] X. Wei, P. Liu, S. Ma, Z. Li, X. Peng, R. Deng, Q. Zhao, Improvement on corrosion resistance and biocompability of ZK60 magnesium alloy by carboxyl ion implantation, Corrosion Science 173 (2020) 108729.

[35] I. Gibson, D. Rosen, B. Stucker, M. Khorasani, Design for Additive Manufacturing, in: I. Gibson, D. Rosen, B. Stucker, M. Khorasani (Eds.), Additive Manufacturing Technologies, Springer International Publishing, Cham, 2021, pp. 555-607.
[36] Z. Wang, W. Wu, G. Qian, L. Sun, X. Li, J.A. Correia, In-situ SEM investigation on fatigue behaviors of additive manufactured Al-Si10-Mg alloy at elevated temperature, Engineering Fracture Mechanics 214 (2019) 149-163.
[37] H. Rezaeifar, M.A. Elbestawi, On-line melt pool temperature control in L-PBF additive manufacturing, The International Journal of Advanced Manufacturing Technology 112(9) (2021) 2789-2804.
[38] S.Y. Choy, C.-N. Sun, W.J. Sin, K.F. Leong, P.-C. Su, J. Wei, P. Wang, Superior energy absorption of continuously graded microlattices by electron beam additive manufacturing, Virtual and Physical Prototyping (2021) 1-15.
[39] C. Ng, M. Savalani, H. Man, I. Gibson, Layer manufacturing of magnesium and its alloy structures for future applications, Virtual and physical prototyping 5(1) (2010) 13-19.
[40] C. Ng, M. Savalani, M. Lau, H. Man, Microstructure and mechanical properties of selective laser melted magnesium, Applied Surface Science 257(17) (2011) 7447-7454.
[41] L. Thijs, F. Verhaeghe, T. Craeghs, J. Van Humbeeck, J.-P. Kruth, A study of the microstructural evolution during selective laser melting of Ti–6Al–4V, Acta materialia 58(9) (2010) 3303-3312.
[42] H. Rotaru, R. Schumacher, S.-G. Kim, C. Dinu, Selective laser melted titanium implants: a new technique for the reconstruction of extensive zygomatic complex defects, Maxillofacial plastic and reconstructive surgery 37(1) (2015) 1.
[43] S. Merkt, A. Kleyer, A.J. Hueber, The Additive Manufacture of Patient-tailored Finger Implants: Feasibility study: implants based on XtremeCT technique, Laser Technik Journal 11(2) (2014) 54-56.
[44] Y. Yang, P. Wu, X. Lin, Y. Liu, H. Bian, Y. Zhou, C. Gao, C. Shuai, System development, formability quality and microstructure evolution of selective laser-melted magnesium, Virtual and Physical Prototyping 11(3) (2016) 173-181.
[45] R. Xu, M.-C. Zhao, Y.-C. Zhao, L. Liu, C. Liu, C. Gao, C. Shuai, A. Atrens, Improved biodegradation resistance by grain refinement of novel antibacterial ZK30-Cu alloys produced via selective laser melting, Materials Letters 237 (2019) 253-257.
[46] F. de Oliveira Campos, A.C. Araujo, A.L. Jardini Munhoz, S.G. Kapoor, The influence of additive manufacturing on the micromilling machinability of Ti6Al4V: A comparison of SLM and commercial workpieces, Journal of Manufacturing Processes 60 (2020) 299-307.
[47] D. Yang, H. Li, S. Liu, C. Song, Y. Yang, S. Shen, J. Lu, Z. Liu, Y. Zhu, In situ capture of spatter signature of SLM process using maximum entropy double threshold image processing method based on genetic algorithm, Optics & Laser Technology 131 (2020) 106371.
[48] T. Larimian, T. Borkar, Additive manufacturing of in situ metal matrix composites, Additive Manufacturing of Emerging Materials, Springer2019, pp. 1-28.
[49] C. Cai, C. Radoslaw, J. Zhang, Q. Yan, S. Wen, B. Song, Y. Shi, In-situ preparation and formation of TiB/Ti-6Al-4V nanocomposite via laser additive manufacturing: microstructure evolution and tribological behavior, Powder technology 342 (2019) 73-84.
[50] J. Wang, Y. Liu, P. Qin, S. Liang, T. Sercombe, L. Zhang, Selective laser melting of Ti–35Nb composite from elemental powder mixture: Microstructure, mechanical behavior and corrosion behavior, Materials Science and Engineering: A 760 (2019) 214-224.
[51] K. Wei, X. Zeng, Z. Wang, J. Deng, M. Liu, G. Huang, X. Yuan, Selective laser melting of Mg-Zn binary alloys: Effects of Zn content on densification behavior, microstructure, and mechanical property, Materials Science and Engineering: A 756 (2019) 226-236.
[52] T. Long, X. Zhang, Q. Huang, L. Liu, Y. Liu, J. Ren, Y. Yin, D. Wu, H. Wu, Novel Mg-based alloys by selective laser melting for biomedical applications: microstructure evolution, microhardness and in vitro degradation behaviour, Virtual and Physical Prototyping 13(2) (2018) 71-81.
[53] M. Esmaily, Z. Zeng, A.N. Mortazavi, A. Gullino, S. Choudhary, T. Derra, F. Benn, F. D'Elia, M. Müther, S. Thomas, A. Huang, A. Allanore, A. Kopp, N. Birbilis, A detailed microstructural and corrosion analysis of magnesium alloy WE43 manufactured by selective laser melting, Additive Manufacturing 35 (2020) 101321.
[54] N.A. Zumdick, L. Jauer, L.C. Kersting, T.N. Kutz, J.H. Schleifenbaum, D. Zander, Additive manufactured WE43 magnesium: A comparative study of the microstructure and mechanical properties with those of powder extruded and as-cast WE43, Materials Characterization 147 (2019) 384-397.
[55] J. Chen, P. Wu, Q. Wang, Y. Yang, S. Peng, Y. Zhou, C. Shuai, Y. Deng, Influence of alloying treatment and rapid solidification on the degradation behavior and mechanical properties of Mg, Metals 6(11) (2016) 259.
[56] C. Shuai, Y. Yang, S. Peng, C. Gao, P. Feng, J. Chen, Y. Liu, X. Lin, S. Yang, F. Yuan, Nd-induced honeycomb structure of intermetallic phase enhances the corrosion resistance of Mg alloys for bone implants, Journal of Materials Science: Materials in Medicine 28(9) (2017) 130.
[57] C.L. Wu, W. Zai, H.C. Man, Additive manufacturing of ZK60 magnesium alloy by selective laser melting: Parameter optimization, microstructure and biodegradability, Materials Today Communications 26 (2021) 101922.
[58] C. Shuai, L. Liu, M. Zhao, P. Feng, Y. Yang, W. Guo, C. Gao, F. Yuan, Microstructure, biodegradation, antibacterial and mechanical properties of ZK60-Cu alloys prepared by selective laser melting technique, Journal of Materials Science & Technology 34(10) (2018) 1944-1952.
[59] B.R. Sunil, T.S. Kumar, U. Chakkingal, V. Nandakumar, M. Doble, Friction stir processing of magnesium–nanohydroxyapatite composites with controlled in vitro degradation behavior, Materials Science and Engineering: C 39 (2014) 315-324.
[60] R. Del Campo, B. Savoini, A. Muñoz, M. Monge, G. Garcés, Mechanical properties and corrosion behavior of Mg–HAP composites, Journal of the mechanical behavior of biomedical materials 39 (2014) 238-246.
[61] C. Shuai, Y. Zhou, Y. Yang, P. Feng, L. Liu, C. He, M. Zhao, S. Yang, C. Gao, P. Wu, Biodegradation resistance and bioactivity of hydroxyapatite enhanced Mg-Zn composites via selective laser melting, Materials 10(3) (2017) 307.
[62] C. Liu, M. Zhang, C. Chen, Effect of laser processing parameters on porosity, microstructure and mechanical properties of porous Mg-Ca alloys produced by laser additive manufacturing, Materials Science and Engineering: A 703 (2017) 359-371.
[63] X. Yao, J. Tang, Y. Zhou, A. Atrens, M.S. Dargusch, B. Wiese, T. Ebel, M. Yan, Surface modification of biomedical Mg-Ca and Mg-Zn-Ca alloys using selective laser melting: Corrosion behaviour, microhardness and biocompatibility, Journal of Magnesium and Alloys (2020).
[64] S.L. Sing, W.Y. Yeong, F.E. Wiria, Selective laser melting of titanium alloy with 50 wt% tantalum: Microstructure and mechanical properties, Journal of Alloys and Compounds 660 (2016) 461-470.
[65] R. Rahmani, M. Brojan, M. Antonov, K.G. Prashanth, Perspectives of metal-diamond composites additive manufacturing using SLM-SPS and other techniques for increased wear-impact resistance, International Journal of Refractory Metals and Hard Materials 88 (2020) 105192.
[66] N. Putra, M. Mirzaali, I. Apachitei, J. Zhou, A. Zadpoor, Multi-material additive manufacturing technologies for Ti-, Mg-, and Fe-based biomaterials for bone substitution, Acta Biomaterialia (2020).
[67] R. Singh, A. Gupta, O. Tripathi, S. Srivastava, B. Singh, A. Awasthi, S.K. Rajput, P. Sonia, P. Singhal, K.K. Saxena, Powder bed fusion process in additive manufacturing: An overview, Materials Today: Proceedings 26 (2020) 3058-3070.
[68] S.M.J. Razavi, B. Van Hooreweder, F. Berto, Effect of build thickness and geometry on quasi-static and fatigue behavior of Ti-6Al-4V produced by Electron Beam Melting, Additive Manufacturing 36 (2020) 101426.
[69] J. Parthasarathy, B. Starly, S. Raman, A. Christensen, Mechanical evaluation of porous titanium (Ti6Al4V) structures with electron beam melting (EBM), Journal of the mechanical behavior of biomedical materials 3(3) (2010) 249-259.
[70] A. Casadebaigt, J. Hugues, D. Monceau, High temperature oxidation and embrittlement at 500–600° C of Ti-6Al-4V alloy fabricated by Laser and Electron Beam Melting, Corrosion Science 175 (2020) 108875.
[71] V. Lunetto, M. Galati, L. Settineri, L. Iuliano, Unit process energy consumption analysis and models for Electron Beam Melting (EBM): Effects of process and part designs, Additive Manufacturing 33 (2020) 101115.
[72] M. Cronskär, M. Bäckström, L.E. Rännar, Production of customized hip stem prostheses–a comparison between conventional machining and electron beam melting (EBM), Rapid Prototyping Journal (2013).
[73] M. Touri, F. Kabirian, M. Saadati, S. Ramakrishna, M. Mozafari, Additive manufacturing of biomaterials− the evolution of rapid prototyping, Advanced Engineering Materials 21(2) (2019) 1800511.
[74] B.R. Luce, M. Drummond, B. Jönsson, P.J. Neumann, J.S. Schwartz, U. Siebert, S.D. Sullivan, EBM, HTA, and CER: clearing the confusion, The Milbank Quarterly 88(2) (2010) 256-276.
[75] L.E. Rännar, A. Glad, C.G. Gustafson, Efficient cooling with tool inserts manufactured by electron beam melting, Rapid Prototyping Journal (2007).
[76] G. Manivasagam, D. Dhinasekaran, A. Rajamanickam, Biomedical implants: corrosion and its prevention-a review, Recent patents on corrosion science (2010).
[77] M. Radmansouri, E. Bahmani, E. Sarikhani, K. Rahmani, F. Sharifianjazi, M. Irani, Doxorubicin hydrochloride - Loaded electrospun chitosan/cobalt ferrite/titanium oxide nanofibers for hyperthermic tumor cell treatment and controlled drug release, International Journal of Biological Macromolecules 116 (2018) 378-384.

[78] B. Gao, S. Hao, J. Zou, W. Wu, G. Tu, C. Dong, Effect of high current pulsed electron beam treatment on surface microstructure and wear and corrosion resistance of an AZ91HP magnesium alloy, Surface and Coatings Technology 201(14) (2007) 6297-6303.
[79] D. Schmid, J. Renza, M.F. Zaeh, J. Glasschroeder, Process influences on laser-beam melting of the magnesium alloy AZ91, Physics Procedia 83 (2016) 927-936.
[80] X. Tong, D. Zhang, X. Zhang, Y. Su, Z. Shi, K. Wang, J. Lin, Y. Li, J. Lin, C. Wen, Microstructure, mechanical properties, biocompatibility, and in vitro corrosion and degradation behavior of a new Zn–5Ge alloy for biodegradable implant materials, Acta biomaterialia 82 (2018) 197-204.
[81] M.-S. Song, R.-C. Zeng, Y.-F. Ding, R.W. Li, M. Easton, I. Cole, N. Birbilis, X.-B. Chen, Recent advances in biodegradation controls over Mg alloys for bone fracture management: a review, Journal of materials science & technology 35(4) (2019) 535-544.
[82] E. Sharifi Sedeh, S. Mirdamadi, F. Sharifianjazi, M. Tahriri, Synthesis and Evaluation of Mechanical and Biological Properties of Scaffold Prepared From Ti and Mg With Different Volume Percent, Synthesis and Reactivity in Inorganic, Metal-Organic, and Nano-Metal Chemistry 45(7) (2015) 1087-1091.
[83] M. Vlasea, Y. Shanjani, A. Basalah, E. Toyserkani, Additive manufacturing of scaffolds for tissue engineering of bone and cartilage, International Journal of Advanced Manufacturing Technology 13 (2011) 124-141.
[84] R. Narayan, Fundamentals of medical implant materials, ASM handbook (2012).
[85] L. Shi, L. Wang, Y. Duan, W. Lei, Z. Wang, J. Li, X. Fan, X. Li, S. Li, Z. Guo, The improved biological performance of a novel low elastic modulus implant, PLoS one 8(2) (2013) e55015.
[86] L.J. Gibson, Biomechanics of cellular solids, Journal of biomechanics 38(3) (2005) 377-399.
[87] E. Hall, Yield point phenomena in metals and alloys, Springer Science & Business Media2012.
[88] S.L. Sing, L.P. Lam, D.Q. Zhang, Z.H. Liu, C.K. Chua, Interfacial characterization of SLM parts in multi-material processing: Intermetallic phase formation between AlSi10Mg and C18400 copper alloy, Materials Characterization 107 (2015) 220-227.
[89] Y. Qin, P. Wen, H. Guo, D. Xia, Y. Zheng, L. Jauer, R. Poprawe, M. Voshage, J.H. Schleifenbaum, Additive manufacturing of biodegradable metals: current research status and future perspectives, Acta biomaterialia 98 (2019) 3-22.
[90] Y. Qin, P. Wen, M. Voshage, Y. Chen, P.G. Schückler, L. Jauer, D. Xia, H. Guo, Y. Zheng, J.H. Schleifenbaum, Additive manufacturing of biodegradable Zn-xWE43 porous scaffolds: Formation quality, microstructure and mechanical properties, Materials & Design 181 (2019) 107937.
[91] Y. Li, J. Zhou, P. Pavanram, M. Leeflang, L. Fockaert, B. Pouran, N. Tümer, K.-U. Schröder, J. Mol, H. Weinans, Additively manufactured biodegradable porous magnesium, Acta biomaterialia 67 (2018) 378-392.
[92] F. Witte, The history of biodegradable magnesium implants: a review, Acta biomaterialia 6(5) (2010) 1680-1692.
[93] D. Mareci, G. Bolat, J. Izquierdo, C. Crimu, C. Munteanu, I. Antoniac, R. Souto, Electrochemical characteristics of bioresorbable binary MgCa alloys in Ringer's solution: Revealing the impact of local pH distributions during in-vitro dissolution, Materials Science and Engineering: C 60 (2016) 402-410.
[94] P. Abasian, M. Radmansouri, M. Habibi Jouybari, M.V. Ghasemi, A. Mohammadi, M. Irani, F.S. Jazi, Incorporation of magnetic NaX zeolite/DOX into the PLA/chitosan nanofibers for sustained release of doxorubicin against carcinoma cells death in vitro, International Journal of Biological Macromolecules 121 (2019) 398-406.
[95] R. Radha, D. Sreekanth, Insight of magnesium alloys and composites for orthopedic implant applications–a review, Journal of magnesium and alloys 5(3) (2017) 286-312.
[96] J. Kubasek, D. Dvorsky, M. Cavojsky, M. Roudnicka, D. Vojtech, WE43 magnesium alloy-material for challenging applications, Kov. Mater 57 (2019) 159-165.
[97] J. Trinidad, I. Marco, G. Arruebarrena, J. Wendt, D. Letzig, E. Sáenz de Argandoña, R. Goodall, Processing of magnesium porous structures by infiltration casting for biomedical applications, Advanced Engineering Materials 16(2) (2014) 241-247.
[98] S. Gollapudi, Grain size distribution effects on the corrosion behaviour of materials, Corrosion Science 62 (2012) 90-94.
[99] X. Zhao, L.-l. Shi, J. Xu, A comparison of corrosion behavior in saline environment: rare earth metals (Y, Nd, Gd, Dy) for alloying of biodegradable magnesium alloys, Journal of Materials Science & Technology 29(9) (2013) 781-787.
[100] Z. Zhen, T.-f. Xi, Y.-f. Zheng, A review on in vitro corrosion performance test of biodegradable metallic materials, Transactions of Nonferrous Metals Society of China 23(8) (2013) 2283-2293.
[101] X. Niu, H. Shen, J. Fu, J. Yan, Y. Wang, Corrosion behaviour of laser powder bed fused bulk pure magnesium in hank's solution, Corrosion Science 157 (2019) 284-294.
[102] G. Argade, S. Panigrahi, R. Mishra, Effects of grain size on the corrosion resistance of wrought magnesium alloys containing neodymium, Corrosion Science 58 (2012) 145-151.
[103] J. Zhang, B. Song, Q. Wei, D. Bourell, Y. Shi, A review of selective laser melting of aluminum alloys: Processing, microstructure, property and developing trends, Journal of Materials Science & Technology 35(2) (2019) 270-284.
[104] B. Xie, M.-C. Zhao, Y.-C. Zhao, Y. Tian, D. Yin, C. Gao, C. Shuai, A. Atrens, Effect of Alloying Mn by Selective Laser Melting on the Microstructure and Biodegradation Properties of Pure Mg, Metals 10(11) (2020) 1527.
[105] C. Shuai, Y. Yang, P. Wu, X. Lin, Y. Liu, Y. Zhou, P. Feng, X. Liu, S. Peng, Laser rapid solidification improves corrosion behavior of Mg-Zn-Zr alloy, Journal of Alloys and Compounds 691 (2017) 961-969.
[106] R. K.R, S. Bontha, R. M.R, M. Das, V.K. Balla, Laser surface melting of Mg-Zn-Dy alloy for better wettability and corrosion resistance for biodegradable implant applications, Applied Surface Science 480 (2019) 70-82.
[107] M. Gieseke, C. Noelke, S. Kaierle, V. Wesling, H. Haferkamp, Selective laser melting of magnesium and magnesium alloys, Magnesium Technology 2013, Springer2013, pp. 65-68.
[108] C. Shuai, Y. Cheng, Y. Yang, S. Peng, W. Yang, F. Qi, Laser additive manufacturing of Zn-2Al part for bone repair: Formability, microstructure and properties, Journal of Alloys and Compounds 798 (2019) 606-615.
[109] Y. Yang, X. Guo, C. He, C. Gao, C. Shuai, Regulating degradation behavior by incorporating mesoporous silica for Mg bone implants, ACS Biomaterials Science & Engineering 4(3) (2018) 1046-1054.
[110] M.M. Saleh, A. Touny, M.A. Al-Omair, M. Saleh, Biodegradable/biocompatible coated metal implants for orthopedic applications, Bio-medical materials and engineering 27(1) (2016) 87-99.
[111] Y. Ding, C. Wen, P. Hodgson, Y. Li, Effects of alloying elements on the corrosion behavior and biocompatibility of biodegradable magnesium alloys: a review, Journal of materials chemistry B 2(14) (2014) 1912-1933.
[112] K. Munir, J. Lin, C. Wen, P.F. Wright, Y. Li, Mechanical, corrosion, and biocompatibility properties of Mg-Zr-Sr-Sc alloys for biodegradable implant applications, Acta biomaterialia 102 (2020) 493-507.
[113] M. Rahman, N.K. Dutta, N. Roy Choudhury, Magnesium Alloys With Tunable Interfaces as Bone Implant Materials, Frontiers in Bioengineering and Biotechnology 8 (2020) 564.
[114] A.H.M. Sanchez, B.J. Luthringer, F. Feyerabend, R. Willumeit, Mg and Mg alloys: how comparable are in vitro and in vivo corrosion rates? A review, Acta biomaterialia 13 (2015) 16-31.
[115] C. Xiao, L. Wang, Y. Ren, S. Sun, E. Zhang, C. Yan, Q. Liu, X. Sun, F. Shou, J. Duan, Indirectly extruded biodegradable Zn-0.05 wt% Mg alloy with improved strength and ductility: In vitro and in vivo studies, Journal of materials science & technology 34(9) (2018) 1618-1627.
[116] L. Murr, Metallurgy principles applied to powder bed fusion 3D printing/additive manufacturing of personalized and optimized metal and alloy biomedical implants: An overview, Journal of Materials Research and Technology 9(1) (2020) 1087-1103.
[117] M. Farag, H.-s. Yun, Effect of gelatin addition on fabrication of magnesium phosphate-based scaffolds prepared by additive manufacturing system, Materials Letters 132 (2014) 111-115.
[118] M. Castilho, M. Dias, U. Gbureck, J. Groll, P. Fernandes, I. Pires, B. Gouveia, J. Rodrigues, E. Vorndran, Fabrication of computationally designed scaffolds by low temperature 3D printing, Biofabrication 5(3) (2013) 035012.
[119] Y. Yin, Q. Huang, L. Liang, X. Hu, T. Liu, Y. Weng, T. Long, Y. Liu, Q. Li, S. Zhou, In vitro degradation behavior and cytocompatibility of ZK30/bioactive glass composites fabricated by selective laser melting for biomedical applications, Journal of Alloys and Compounds 785 (2019) 38-45.
[120] F. Sharifianjazi, N. Parvin, M. Tahriri, Synthesis and characteristics of sol-gel bioactive SiO_2-P_2O_5-CaO-Ag_2O glasses, Journal of Non-Crystalline Solids 476 (2017) 108-113.
[121] F. Bär, L. Berger, L. Jauer, G. Kurtuldu, R. Schäublin, J.H. Schleifenbaum, J.F. Löffler, Laser additive manufacturing of biodegradable magnesium alloy WE43: A detailed microstructure analysis, Acta Biomaterialia 98 (2019) 36-49.
[122] A.C. Hänzi, P. Gunde, M. Schinhammer, P.J. Uggowitzer, On the biodegradation performance of an Mg–Y–RE alloy with various surface conditions in simulated body fluid, Acta biomaterialia 5(1) (2009) 162-171.
[123] C. Gao, S. Li, L. Liu, S. Bin, Y. Yang, S. Peng, C. Shuai, Dual alloying improves the corrosion resistance of biodegradable Mg alloys prepared by selective

laser melting, Journal of Magnesium and Alloys (2020).
[124] M. Li, F. Benn, T. Derra, N. Kröger, M. Zinser, R. Smeets, J.M. Molina-Aldareguia, A. Kopp, J. Llorca, Microstructure, mechanical properties, corrosion resistance and cytocompatibility of WE43 Mg alloy scaffolds fabricated by laser powder bed fusion for biomedical applications, Materials Science and Engineering: C 119 (2021) 111623.
[125] C. Shuai, S. Li, C. Gao, Y. Yang, Z. Zhao, W. Liu, Y. Hu, Supersaturated Solid Solution of Mg in Fe Produced by Mechanical Alloying Followed by Selective Laser Melting (SLM) to Accelerate Degradation for Biomedical Applications, Lasers in Engineering (Old City Publishing) 47 (2020).
[126] G.K. Meenashisundaram, N. Wang, S. Maskomani, S. Lu, S.K. Anantharajan, S.T. Dheen, S.M.L. Nai, J.Y.H. Fuh, J. Wei, Fabrication of Ti + Mg composites by three-dimensional printing of porous Ti and subsequent pressureless infiltration of biodegradable Mg, Materials Science and Engineering: C 108 (2020) 110478.
[127] B. Ghotbi, S. Navkhasi, S. Ghobadi, Z. Shahsavari, N. Kahrizi, A Review of the Novel Corona Virus Disease (2019-nCoV), Health Research Journal 5(3) (2020) 180-187.
[128] M. Salehi, S. Maleksaeedi, M.A.B. Sapari, M.L.S. Nai, G.K. Meenashisundaram, M. Gupta, Additive manufacturing of magnesium–zinc–zirconium (ZK) alloys via capillary-mediated binderless three-dimensional printing, Materials & Design 169 (2019) 107683.
[129] S. Liu, W. Yang, X. Shi, B. Li, S. Duan, H. Guo, J. Guo, Influence of laser process parameters on the densification, microstructure, and mechanical properties of a selective laser melted AZ61 magnesium alloy, Journal of Alloys and Compounds 808 (2019) 151160.
[130] N. Wegner, D. Kotzem, Y. Wessarges, N. Emminghaus, C. Hoff, J. Tenkamp, J. Hermsdorf, L. Overmeyer, F. Walther, Corrosion and Corrosion Fatigue Properties of Additively Manufactured Magnesium Alloy WE43 in Comparison to Titanium Alloy Ti-6Al-4V in Physiological Environment, Materials 12(18) (2019) 2892.